Novel Single Source Integral Equation for Analysis of Electromagnetic Scattering by Penetrable Objects

by

Farhad Sheikh Hosseini Lori

A Thesis Submitted to the Faculty of Graduate Studies of

The University of Manitoba

in partial fulfilment of the requirements of the degree of

DOCTOR OF PHILOSOPHY

Department of Electrical and Computer Engineering
University of Manitoba
Winnipeg, Manitoba, Canada

Abstract

This thesis presents a novel single source surface electric field integral equation (EFIE) for the full-wave scattering problems by homogeneous dielectric objects and magneto-quasi-static characterization of the multiconductor transmission lines (MTLs) to determine inductance and resistance. Both the low and higher order method of moments (MoM) schemes are developed for numerical solution of this novel equation. The required theorems and derivations are given in detail. Numerical validations of this equation are conducted for various formulations such as scalar and vector 2D scattering problems, full-wave 3D scattering problems, and the problems of current flow in the 2D conductors of complex cross-sections. Error controllability of the numerically computed fields confirms that the proposed equation is rigorous in nature and may be an advantageous alternative to the other known single and double source surface integral equations (SIEs). The proposed single source integral equation (SSIE) features only electric type Green's functions, which distinguishes it from the previously know SSIE formulations. As such the new equation can be formulated in the form free of derivatives acting on the kernels. The new SSIE also features only one unknown surface function instead of two unknown functions as featured in the traditional SIEs. Unlike previously known single source surface integral equations derived through restricting of the single source field representation with surface equivalence principle, the new equation is obtained by constraining of the such representation with the volume equivalence principle. As a result, the new equation features integral operators that translate the fields from the surface of the scatterer to its volume and then back to its surface, lending it the name of Surface-Volume-Surface Electric Field Integral Equation (SVS-EFIE).

Contributions

The author contributed to the following publications while working towards the Ph.D. degree

- F. Sheikh Hosseini Lori, and V. Okhmatovski, "A Method and Apparatus for Determination of 3D Electromagnetic Fields Interacting with Complex Shaped Objects," Patent USSN 62/332045, 2016.
- F. Sheikh Hosseini Lori, M. S. Hosen, and V. Okhmatovski, "Higher Order Method of Moments Solution of the New Vector Single-Source Surface Integral Equation for 2D TE Scattering by Dielectric Objects," *IEEE NEMO2017,* Sevilla, Spain.
- F. Sheikh Hosseini Lori, M. S. Hosen, A. Menshov, M. Shafieipour, and V. Okhmatovski, "Accurate Transmission Lines Characterization via Higher Order Moment Method Solution of Novel Single-Source Integral Equation," *IEEE IMS2017,* Hawaii, USA.
- F. Sheikh Hosseini Lori, M. S. Hosen, A. Menshov, M. Shafieipour, and V. Okhmatovski, "Accurate Characterization of Coaxial Transmission Line via Higher Order Moment Method Solution of Novel Single-Source Surface Integral Equation,"in *IEEE 21st Work. Signal Power Integr.*, Lake Maggiore, Italy, May 2017, pp. 1–4.
- F. Sheikh Hosseini, V. Okhmatovski, "Novel Single-Source Surface Integral Equation for 3D Scattering Problems on Homogeneous Dielectric Objects," *IEEE Trans. Antennas Propag.,* (accepted with Minor Revision).
- F. Sheikh Hosseini, A. Menshov, V. Okhmatovski, "New Vector Single-Source Surface Integral Equation for Scattering Problems on Dielectric Objects in 2D,"*IEEE Trans. Antennas Propag.*, vo. 65, issue 7, pp. 3794–3799, 2017.
- F. Sheikh Hosseini, A. Menshov, V. Okhmatovski, "Novel Surface-Volume-Surface Electric Field Integral Equation for Solution of Scattering Problems on

Penetrable Objects," *URSI IEEE Int. Symp. Antenna and Propagation (APS)*, Puerto Rico, USA, 2016.

- F. Sheikh Hosseini, A. Menshov, V. Okhmatovski, "New Single-Source Integral Equation for Solution of Scattering Problems on Homogeneous Dielectric Objects," *IEEE Workshop on Finite Elements for Microwave Engineering (FEM)*, Florence, Italy, 2016.

- V. Okhmatovski, A. Menshov, F. L. Sheikh Hosseini, S. Zheng, "Novel single-source integral equation in electromagnetics," *URSI Intl. Symp. Electromagnetic Theory (EMTS)*, Espoo, Finland, pp.484–487, 2016.

- F. Sheikh Hosseini, A. Menshov, V. Okhmatovski, "Method of Moment Solution of Surface-Volume-Surface Electric Field Integral Equation for 2D TM and TE Scattering On Penetrable Cylinders of Arbitrary Cross-Section," *URSI IEEE Int. Symp. Antenna and Propagation (APS)*, Vancouver, Canada, 2015.

- Farhad Sheikh Hosseini Lori, Mohammad Shakander Hosen, Anton Menshov, Mohammad Shafieipour, and Vladimir Okhmatovski, "New Higher-Order Method of Moments for Accurate Inductance Extraction in Transmission Lines of Complex Cross-Sections, "IEEE Trans. Microw. Theory Techn., Under Review.

- Farhad Sheikh Hosseini Lori, Mohammad Shakander Hosen, and Vladimir Okhmatovski, "Higher Order Method of Moments Solution of the New Single-Source Surface Integral Equation for 2D TM and TE Scattering by Dielectric Cylinders, "IEEE Trans. Microw. Theory Techn., Under Review.

Acknowledgments

There is nothing like a dream to create the future.–Victor Hugo(1802-1885)

I would like to give the most credit of this work to my advisor Professor Vladimir Okhmatovski. Every story starts with an idea. I remember how four years ago at the beginning of my Ph.D. program, he told me that we will develop a new integral equation which can be used for computations of the electromagnetic fields in a different way. The idea resonated with me and I was convinced that such new equation can be developed. Throughout the remaining part of my doctoral research I tried to be the character it takes to move the idea forward. In the dark moments when everything seemed to have gone wrong with our formulations and it looked like our equation may not even be valid, he pushed me further and guided me to make the idea work. Thanks to Prof. Vladimir Okhmatovski for his expertise and time. In every sense, none of this work would have been possible without him.

I would like to thank my examining committee: Dr. Ian Jeffrey, Dr. Jason Morrison, and Dr. Ahmed Kishk for evaluation of this work.

I would like to acknowledge my colleagues Anton Menshov, Dr. Mohammad Shafieipour, Dr. Ali Yazdanpanah, and Shakander Hosen for all the support and discussions we had together. I learned a lot from you and hopefully will continue our collaboration in the future.

I wish to extend my gratitude to the Natural Sciences and Engineering Research Council of Canada, University of Manitoba, University of Manitoba Graduate Students Association, and MITACS for their financial support and funding my research.

Last but not the least, thanks to my parents, family and friends for all their support, help, and patience. Thanks also to all others who offered help.

The family is one of nature's masterpieces.–George Santayana (1863 - 1952)

Dedicated to my beautiful wife and daughter, Nefeli and Melissa, my parents Ebrahim and Azar, my brother and sister Iman and Shirin.

Table of Contents

List of Tables

List of Figures

Notation, Symbols and Acronyms

Herein some general remarks about the notations used throughout the thesis as well as a list of commonly used symbols and acronyms are provided.

- **Spatial-vectors:** continuous functions or data-vectors and matrices with entries that have more than one component in the Cartesian coordinates are denoted with a bold face letter such as $\boldsymbol{E}$, $\boldsymbol{H}$, and $\boldsymbol{J}$.
- **Scalar integral operators:** are denoted by upper-case calligraphic letters such as $\mathcal{T}$.
- **Vector integral operators:** are denoted by upper-case bold calligraphic letters such as $\boldsymbol{\mathcal{T}}$.
- **Vector matrices:** are denoted by upper-case bold calligraphic letters such as $\boldsymbol{Z}$.
- **Scalar matrices:** are denoted by upper-case calligraphic letters such as Z.
- **Dyads:** are denoted with upper-case letters with two overhead lines such as $\overline{\overline{I}}$ and $\overline{\overline{G}}_{e\epsilon}$.
- **Spatial derivative operators:** spatial gradient, divergence, and curl operators are given as $(\boldsymbol{\nabla})$,$(\boldsymbol{\nabla}\cdot)$ and $(\boldsymbol{\nabla}\times)$.
- **Integration differentials:** the differential element for line integrals is denoted by dl; for three-dimensional (3D) problems the boundary elements are surface patches which is denoted by ds. The differential volumetric (domain) element is denoted by dv.

Table 0.1: Common Symbols and Notations

Symbol	**Description**
$\hat{\mathbf{x}}$, $\hat{\mathbf{y}}$, $\hat{\mathbf{z}}$	Unit vectors in the x, y and z directions.
$\hat{\mathbf{n}}$	Normal unit vector outward to the boundary.
$\hat{\mathbf{t}}$	Tangential unit vector to the boundary.
$\boldsymbol{r}$, $\boldsymbol{r}'$	Position vectors in the 3D Cartesian coordinate system.
$\boldsymbol{\rho}$, $\boldsymbol{\rho}'$	Position vectors in the 2D Cartesian coordinate system.
ϵ_0	Permittivity of free-space.
ϵ	Relative complex permittivity of the scatterer.
σ	Conductivity of the scatterer.
μ_0	Permeability of free-space.
μ_r	Relative permeability of the scatterer.
k_0	Wavenumber of free-space.
k_ϵ	Wavenumber inside the scatterer.
ω	Radial frequency.
f	Frequency of operation.
$\mathtt{t}$	Time variable.
λ	Wavelength.
Γ	Gram matrix.
$\vec{E}(\boldsymbol{r}, \mathtt{t})$	Time domain electric-field intensity.
$\vec{H}(\boldsymbol{r}, \mathtt{t})$	Time domain magnetic-field intensity.
$\vec{B}(\boldsymbol{r}, \mathtt{t})$	Time domain magnetic-field density.
$\vec{D}(\boldsymbol{r}, \mathtt{t})$	Time domain electric-field density.
$\vec{M}^{\mathrm{i}}(\boldsymbol{r}, \mathtt{t})$	Time domain impinging magnetic current density.
$\vec{J}^{\mathrm{i}}(\boldsymbol{r}, \mathtt{t})$	Time domain impinging electric current density.
$\vec{J}^{\mathrm{c}}(\boldsymbol{r}, \mathtt{t})$	Time domain conductivity current density.
$\rho_e(\boldsymbol{r}, \mathtt{t})$	Time domain total electric charge density.
$\rho_e^c(\boldsymbol{r}, \mathtt{t})$	Time domain electric charge density of the electric current of conductivity.
$\rho_e^i(\boldsymbol{r}, \mathtt{t})$	Time domain electric charge density of the impressed electric current.

$\rho_m(\boldsymbol{r}, \mathtt{t})$	Time domain magnetic charge density.
$\rho_m^i(\boldsymbol{r}, \mathtt{t})$	Time domain magnetic charge density of the impressed magnetic current.
$\boldsymbol{E}^{\text{inc}}$	Time-harmonic incident electric-field for a transmitter.
$\boldsymbol{H}^{\text{inc}}$	Time-harmonic incident magnetic-field for a transmitter.
$\boldsymbol{E}^{\text{scat}}$	Time-harmonic scattered electric-field.
$\boldsymbol{E}$	Time-harmonic total electric-field.
$\boldsymbol{j}$	Polarization current density.
$\boldsymbol{J}$	Fictitious SVS surface source density.
$\overline{\overline{G}}_{e0}$	Dyadic electric Green's function of free space.
$\overline{\overline{G}}_{e\epsilon}$	Dyadic electric Green's function of the scatterer.
Ψ	The maximum order of 2D basis function.
Ω	The maximum order of 1D basis function.
∂S	Boundary of the 2D object.
S	Surface of the 2D object.
∂V	Boundary of the 3D object.
V	Volume of the 3D object.
ℓ	Length variable.
Re	Real part operator.
Im	Imaginary part operator.
$\boldsymbol{\nabla}$	Gradient operator.
$\boldsymbol{\nabla}\cdot$	Divergence operator.
$\boldsymbol{\nabla}\times$	Curl operator.
$\boldsymbol{\nabla}\times\boldsymbol{\nabla}\times$	Curl curl operator.
∇^2	The Laplacian.
$(\cdot)^{-1}$	Inverse operator.
$\|\cdot\|$	L_2- norm or Euclidean norm.
$\langle\cdot\,,\cdot\rangle$	Inner product.

Acronym	**Description**

EM	Electromagnetic
DC	Direct Current
BC	Boundary Condition
CEM	Computational Electromagnetic
CAD	Computer Aid Design
FEM	Finite Element Method
IE	Integral Equation
MoM	Method of Moments
FFT	Fast Fourier Transform
LO	Low Order
HO	Higher Order
SVS-IE	Surface Volume Surface Integral Equation
SIE	Surface Integral Equation
SSIE	Single Source Surface Integral Equation
VIE	Volume Integral Equation
V-EFIE	Volume Electric Field Integral Equation
PEC	Perfect Electric Conductor
EFIE	Electric Field Integral Equation
SVS-EFIE	Surface Volume Surface Electric Field Integral Equation
MFIE	Magnetic Field Integral Equation
TM	Transverse Magnetic Field Mode
TE	Transverse Electric Field Mode
TLs	Transmission Lines
RWG	Rao-Wilton-Glisson basis functions
SLAE	System of Linear Algebra Equation

1

Introduction

The most exciting phrase to hear in science, the one that heralds new discoveries, is not 'Eureka!' (I found it!) but 'That's funny ...'–Isaac Asimov (1920 - 1992)

Dynamic laws of electromagnetism, prediction of electromagnetic waves with speed of propagation near the speed of light and suggestion of light being in relation to the electric and magnetic phenomena were theorized by James Clerk Maxwell [1]. Maxwell's theory involves 20 equations, which Oliver Heaviside later reformulated them in the modern form by adopting complex numbers and vector analysis [2]. Time domain Maxwell's equations in differential form are:

$$\boldsymbol{\nabla} \times \vec{E}(\boldsymbol{r}, \mathtt{t}) = -\vec{M}^{\mathrm{i}}(\boldsymbol{r}, \mathtt{t}) - \frac{\partial}{\partial \mathtt{t}} \vec{B}(\boldsymbol{r}, \mathtt{t}), \tag{1.1}$$

$$\boldsymbol{\nabla} \times \vec{H}(\boldsymbol{r}, \mathtt{t}) = \vec{J}^{\mathrm{i}}(\boldsymbol{r}, \mathtt{t}) + \vec{J}^{\mathrm{c}}(\boldsymbol{r}, \mathtt{t}) + \frac{\partial}{\partial \mathtt{t}} \vec{D}(\boldsymbol{r}, \mathtt{t}), \tag{1.2}$$

$$\boldsymbol{\nabla} \cdot \vec{D}(\boldsymbol{r}, \mathtt{t}) = \rho_e(\boldsymbol{r}, \mathtt{t}), \tag{1.3}$$

$$\boldsymbol{\nabla} \cdot \vec{B}(\boldsymbol{r}, \mathtt{t}) = \rho_m(\boldsymbol{r}, \mathtt{t}), \tag{1.4}$$

indeed, through the notion of the continuity equation, that is the manifestation of the conservation of charge

$$\boldsymbol{\nabla} \cdot \vec{J}^{\mathrm{c}}(\boldsymbol{r}, \mathtt{t}) = -\frac{\partial}{\partial \mathtt{t}} \rho_e^i(\boldsymbol{r}, \mathtt{t}). \tag{1.5}$$

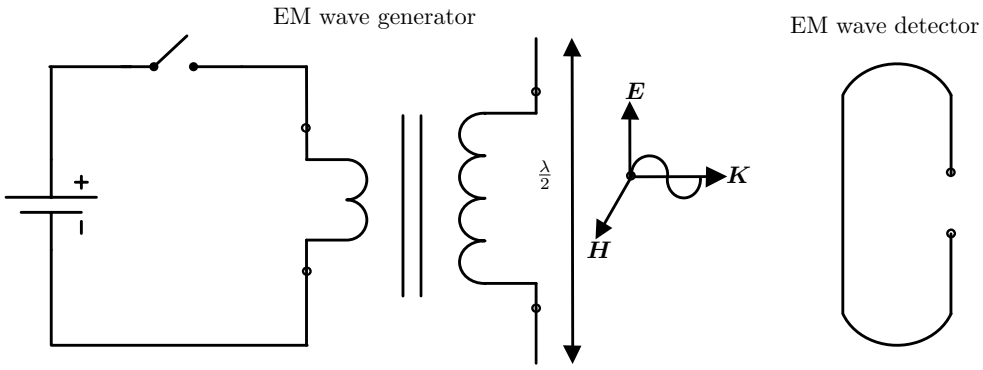

Figure 1.1: Schematic of Hertz device.

$$\boldsymbol{\nabla} \cdot \vec{J}^{\mathrm{i}}(\boldsymbol{r}, \mathtt{t}) = -\frac{\partial}{\partial \mathtt{t}} \rho_e^c(\boldsymbol{r}, \mathtt{t}). \tag{1.6}$$

$$\boldsymbol{\nabla} \cdot \vec{M}^{\mathrm{i}}(\boldsymbol{r}, \mathtt{t}) = -\frac{\partial}{\partial \mathtt{t}} \rho_m^i(\boldsymbol{r}, \mathtt{t}). \tag{1.7}$$

the 3rd and 4th Maxwell equations are directly obtained from the 1st and the 2nd equations. In (1.5) and (1.6), the total electric charge density $\rho_e(\boldsymbol{r}, \mathtt{t})$ is the sum of the electric charge density of the conductivity current $\vec{J}^{\mathrm{c}}(\boldsymbol{r}, \mathtt{t}) = \vec{E}(\boldsymbol{r}, \mathtt{t})\sigma$, σ being bulk conductivity, and impressed electric current $\vec{J}^{\mathrm{i}}(\boldsymbol{r}, \mathtt{t})$ of extraneous sources. In (1.7), the total magnetic charge density $\rho_m^i(\boldsymbol{r}, \mathtt{t})$ is associated with the magnetic charge density of the impressed magnetic current $\vec{M}^{\mathrm{i}}(\boldsymbol{r}, \mathtt{t})$ by extraneous sources. The magnetic current of conductivity is assumed to be zero.

Maxwell's theoretical predictions were confirmed experimentally by David Edward Hughes in 1879. Unfortunately, he didn't publish his results and wasn't credited with the first controlled radiation and reception of the electromagnetic wave. Later in 1883 Thomas Edison displayed his set up for 'conductivity of continuous currents through high vacuo' at the International Electrical Exhibition. He wasn't credited for the first practical demonstration of the electromagnetic waves either as he didn't attribute proper significance to his experiments. It wasn't until 1886-1888 period

when Heinrich Hertz performed his experiment that harnessing of electromagnetic waves was widely recognized [3]. Hence, it was Hertz who is the person credited with the discovery of generation and detection of the electromagnetic waves in laboratory. His device included an EM wave generator and a detector as simple as the one shown in Fig. 1.1. His EM wave generator consisted of a DC power supply, a mechanical switch, and a transformer that had primary coil of thick wire (low resistance) with few turns to take as much current from the DC power supply as possible, and a secondary coil with a large number of turns made of the thin wires. He connected two straight metal bars to terminals of the secondary coil. He created a standing wave pattern in the secondary coil by periodically turning the switch on and off. As a detector he used a loop wire with small gap in middle and length of $(\lambda/2)$. He showed existence of EM waves by observing sparks in the gap on a detector situated up to 20m away from the generator.

Later on by modifying Hertz's system into Fig. 1.2 humankind found the first application of EM waves for the radio broadcasts. The first broadcasts were demonstrated by Oliver Lodge and Alexander Popov in 1894 and 1895. The first transatlantic broadcast, by Guglielmo Marconi, followed in 1901. Instead of using a DC power supply, a sinusoidal power supply connected to a microphone to modulate the current in the primary circuit is still used to carry sounds on EM waves. On the receiver side a low pass filter was added to the gap along with an amplifier and a speaker. Using an amplitude modulated sinusoidal wave as carrier for information is still with us and most commonly seen in the AM radio broadcasting.

To simplify Maxwell's equation it is common to transfer them from four dimensional space-time domain (1.1)–(1.5) to the spectral domain using the Fourier transform. The resulting time-harmonic Maxwell's equations are:

$$\boldsymbol{\nabla} \times \boldsymbol{E}(\boldsymbol{r}) = -\boldsymbol{M}^i(\boldsymbol{r}) - i\omega \boldsymbol{B}(\boldsymbol{r}), \tag{1.8}$$

$$\boldsymbol{\nabla} \times \boldsymbol{H}(\boldsymbol{r}) = \boldsymbol{J}^i(\boldsymbol{r}) + \boldsymbol{J}^c(\boldsymbol{r}) + i\omega \boldsymbol{D}(\boldsymbol{r}), \tag{1.9}$$

$$\boldsymbol{\nabla} \cdot \boldsymbol{D}(\boldsymbol{r}) = \rho_e(\boldsymbol{r}), \tag{1.10}$$

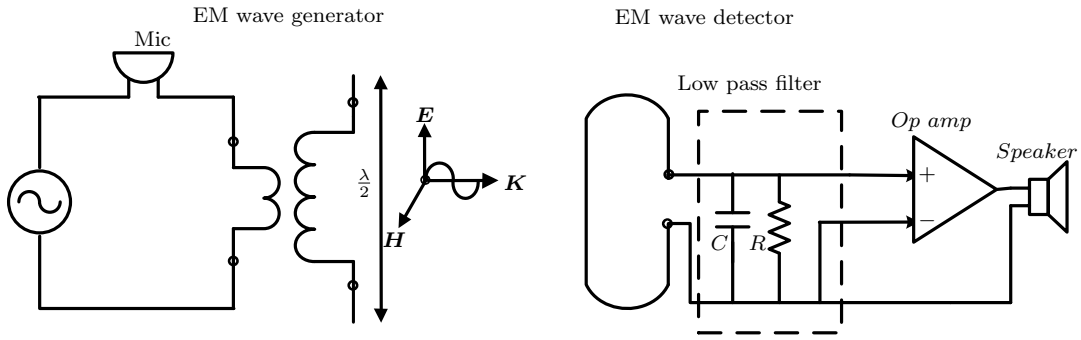

Figure 1.2: Simple radio device.

$$\boldsymbol{\nabla} \cdot \boldsymbol{B}(\boldsymbol{r}) = \rho_m(\boldsymbol{r}), \tag{1.11}$$

and the continuity equation becomes

$$\boldsymbol{\nabla} \cdot \boldsymbol{J}^{ic}(\boldsymbol{r}) = -i\omega\rho_e(\boldsymbol{r}). \tag{1.12}$$

Here and throughout this thesis, the $e^{i\omega\mathtt{t}}$ time convention is implied. What follows in the rest of the thesis is a discussion of manipulated field quantities in the spectral domain. No special notations are used to distinguish them from the time domain quantities. In this thesis we use the above time-harmonic form of Maxwell's equations to build our new theory. The medium is considered to be non-dispersive and homogeneous with the homogeneous relative permittivity, ϵ, and relative permeability, μ and independent of either the frequency or the intensity of the applied field. Therefore, the phase velocity of the wave is constant and the signal is propagated without distortion (dispersion). For lossless medium ϵ and μ are real numbers and for lossy medium ϵ and μ have real and imaginary parts.

After invention of the radio more advanced devices were constructed with advent of the vacuum tubes in 1906, diode in 1906, and triode in 1907. By 1910 all key com-

ponents for commercial use of EM waves were in place. Radio and TV broadcasting, satellite communication, Internet, remote sensing, GPS navigation and cellphones followed in the decades after as natural consequences of Maxwell's discovery. The theory of EM waves is a sophisticated branch of theoretical physics and its application has undoubtedly made a most profound impact on humanity.

Today devices that use EM waves make human life easier and more connected. However, this is not the end of story for EM waves. They will stay with us and continue enabling new technologies such as brain-machine interfaces, artificial intelligence, and others as researchers continue to look for new applications of EM waves and theory. What was impossible is becoming fathomable and fathomable becomes possible as EM theory and practice continue to evolve and solve more complicated problems and enable new applications.

With the advent of digital computers physical experiments can now be replaced by computer simulations to virtually explore phenomena in various branches of physics including electromagnetics [4–8]. Numerical experiments are widely used because physical experimentations are expensive and sometimes impossible [9,10]. This gives researchers and designers the flexibility to gain insight, to design and to optimize their prototypes before they are built. Real world electromagnetic problems such as scattering due to electrically large targets, radiation of sophisticated antennas, and modelling of wave guides all involve interaction of electromagnetic fields with physical objects and are governed by Maxwell's equations. These equations can now be solved numerically in realistic scenarios [9,11–14]. For these reasons the importance of computer-aided design (CAD) tools has grown significantly over the past decades. In a vast number of applications, the use of accurate numerical simulations reduces fabrication expenses and drastically enhances design efficiency [15–17]. Significant reduction in computational complexity associated with the numerical solution of the Maxwell equations, can be achieved when they are cast into the form of integral equations (IEs) [10,18]. Integral equations of electromagnetics have a relatively long history [19–22] dating back to the pioneering works of V. A. Fock in 1945. They are formed using the equivalence principles that allows the electromagnetic field in a volume to be expressed by its tangential components on the boundary. These tan-

gential components weigh the elementary waves emanating from vector point sources situated at the boundaries. Such elementary waves are knows as the Green's functions [23, 24] and correspond to the solution of the Maxwell equations with the Dirac delta-function as a source. When the fields produced by elementary point sources (Green's functions) are known, the fields due to an arbitrary source can be obtained using the superposition principle [10, 18]. This is because Maxwell's equations are linear in nature and field produced by general sources could be constructed as a superposition of fields emanating from the point sources forming them. The advantage of integral equation based solutions compared to the techniques relying on direct discretization of the Maxwell equations, such as finite-element method (FEM) [25] and finite-difference solutions [26], is that they allow a reduction of dimensionality of the boundary value problems by introducing the unknown field quantities only at the boundaries of the pertinent models [27, 29]. Discretization of the boundaries only, instead of volumetric discretization of the entire space, often leads to substantial reduction of computational effort required for evaluation of the sought electromagnetic (EM) field quantities [30]. Furthermore, in many important practical applications the IE formulations allow for abstraction of the complex environment [31] associated with the model into pertinent Green's function [23] associated with a particular IE formulation [32]. For stratified environment surrounding the model of interest, such abstraction has been a key to development of efficient EM solvers including commercial applications such as Sonnet [33], COMSOL [34], FEKO [35], and other products.

First numerical solutions of the integral equations were pioneered by E. N. Vasil'ev in Russia in 1958-1959 [36] as digital computers started becoming more widely available. He applied Krylov-Bogolyubov's method (a version of what is widely known as Method of Moments (MoM)) for reducing the integral equation in the problem of scattering on metallic cylinder to a system of linear algebraic equations. Subsequent works by R.F. Harrington followed in the United States who largely popularized MoM in the computational electromagnetics (CEM) community [37]. My advisor V. Okhmatovski was the last doctoral student of E. N. Vasil'ev which makes me in a way connected to the early history of integral equations in electromagnetics and their

MoM solutions. This doctoral work builds on this tradition.

The MoM technique got improved in the early 80s in the original works of S. Rao, D. Wilton, and A. Glisson [38]. For the first time it was shown how such MoM solutions can be formulated in conjunction with the flexible geometry representation using triangular patches and specially designed basis functions defined on pairs of adjacent triangles. Since then the integral equations of CEM and their MoM solutions have been widely used for solution of complex problems in computational electromagnetics in various important practical applications such as prediction of scattering signatures of the aircrafts [39], characterization of microwave and radio-frequency integrated circuits [40], construction of new materials [19], design of optical systems [41], and various other areas [42, 43].

For the solution of time-harmonic scattering problems on penetrable objects, there are three known classes of integral equations. For homogeneous and piecewise homogeneous scatterers, the standard formulations are the electric field integral equation (EFIE) and magnetic field integral equation (MFIE) or their spurious resonances free linear combination known as the combined field integral equation (CFIE) [27, 28]. Other linear combinations of the EFIE and MFIE equations and their associated extinction theorem forms are also commonly used to formulate the Müller IEs [44] and the Pogglio-Miller-Chu-Harrington-Wu-Tai (PMCHWT) IEs [32, 45]. In relation to the introduction of the new IE formulation in this work: all of the above IEs feature two unknown surface functions, namely equivalent electric and magnetic surface current densities, at the material interfaces of the penetrable scatterers.

A new contribution to the theory of integral equations arrived with the paper by Maystre and Vincent [46] who showed that only one fictitious current source is needed to represent both the electric and magnetic equivalent currents. This gave rise to the new class of the IEs suitable for solution of scattering problems on penetrable homogeneous objects. Such formulations are now known as single-source IEs (SSIE) [47], and they have been extensively studied by both engineers and mathematicians [48–55]. The benefit of having only one unknown current in the SSIEs comes at the expense of a large number of integral operator products (18 operator products in the SSIE for 2D transverse electric (TE) scattering problem, see (1.32) as an example) associ-

ated with the equations substantially more difficult MoM implementations [47], and a larger associated computational complexity. This work proposes a new type of the SSIE that features fewer integral operators (5 operator products) than traditional formulations. It also contains only electric field operators, which allows for its derivative free formulation.

A third type of integral equations known as the volumetric IE (VIE) formulations can also be used for solution of scattering problems on penetrable objects [27, 56, 57]. While such VIEs are applicable for both homogeneous and inhomogeneous scatterers they may be advantageous only in a limited number of particular scenarios (e.g. handling thin dielectric objects) [30] due to high computational complexity associated with the discretization of the volumetric unknown polarization currents and solution of the resultant dense matrix equations.

Computational and memory complexity associated with the numerical solution of Maxwell's equations can undergo further exponential reduction when higher-order (HO) discretization methods are employed for the numerical solution of the pertinent integral equations. Such methods include higher-order MoM discretization [58–61], and Locally Corrected Nystrom method (LCN) [62–64]. Demonstration of the proposed new SSIE solution with the HO MoM scheme is demonstrated in chapters 4, 5, and 6 of this thesis.

1.1 Motivation

This work introduces a new type of surface integral equation applicable to the solution of scattering problems on homogeneous non-magnetic 2D and 3D scatterers. Unlike the existing surface IE (SIE) formulations, which are derived using either the surface equivalence principle [27], [65] or Green's theorems [23], the proposed new surface equation is derived using both the surface and volume equivalence principles. Assuming that a non-magnetic scatterer is homogeneous, we represent the electric field at any point inside of it using the generalized surface equivalence principle featuring a single source [47] and applied to the interior of the scatterer (with the exterior electric field being unconstrained). The electric field representation, as a result, is

in the form of the surface integral of an unknown fictitious surface current density multiplied with Green's function of the homogeneous unbounded medium having the same permittivity as the scatterer. This representation can be also thought of as a superposition of the cylindrical waves emanating from the scatterer boundary for which the magnitudes are determined by an unknown function defined on the boundary of the scatterer. The unknown weighting function (fictitious electric surface current density) on the surface of the scatterer is not directly related to the conventional equivalent electric surface current density equal to the tangential components of the true magnetic fields. This is because it represents the jump in the tangential component of the true magnetic field inside the scatterer and unconstrained magnetic field outside of it. Traditional SSIE's constrain this interior surface equivalent principle field representation with the extinction theorem form of the exterior surface equivalence principle. In this work we constrain this interior surface equivalence principle with the volume equivalence principle instead, which is enforced on the interior of the scatterer boundary for the tangential component of the electric field. The resultant equation features a single surface unknown function similarly with previously known SSIEs, which is a main advantage of the proposed equation compared to it's traditional SIE counterparts such as PMCHWT or Müller formulations. Another advantage of the new equation is that it only features the electric field dyadic Green's functions. This property is beneficial if the scatterer is situated in a multilayered media [68–70]. The above listed benefits of the proposed SSIE, however, come at the expense of the field translations that take place from the scatterer's boundary to its volume and then from the volume to its boundary. Due to such field translations the new equation is termed the Surface-Volume-Surface (SVS) EFIE. As a result of such translations, the MoM [71] solution of the proposed SSIE equation requires both surface and volumetric discretizations of the scatterer. While it adds computational and memory costs, it also makes the new equation particularly suitable for acceleration with FFT-based fast algorithms [30] where such extra cost is already incurred due to the use of 3D FFT operations for computation of unknown surface field quantities. The proposed integral equation is rigorous in nature as it satisfies all pertinent equations and boundary conditions. Specifically, the wave equations and the radiation

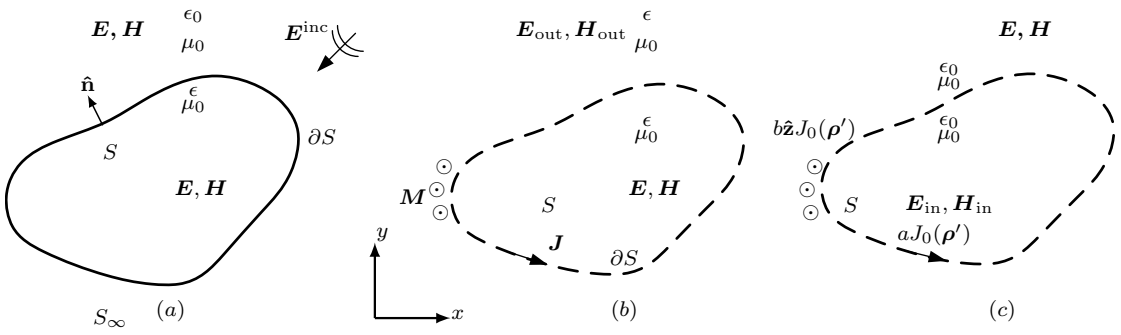

Figure 1.3: (a) The scattering problem of TE-polarized incident field $\boldsymbol{E}^{\text{inc}}$ on a non-magnetic dielectric cylinder with cross-section area S. (b) Equivalent problem for the interior field. (c) Equivalent problem for the exterior field.

condition are satisfied directly through construction of the field representations in the form of interior surface equivalence principle and the exterior volume equivalence principle, while the continuity of the tangential components on the boundary of the scatterer is satisfied implicitly due to the use of the volume equivalence principle [72].

1.2 Single and Double Source Integral Equations

For simplicity, consider a time-harmonic scattering of the TE-polarized incident field $\boldsymbol{E}^{\text{inc}}$ on a 2D homogeneous dielectric cylinder with relative permittivity ϵ directed along z-axis and having arbitrary cross-section with area S and boundary ∂S in the xy-plane (Fig. 1.3 (a)). The time convention $e^{i\omega \mathtt{t}}$ is assumed and suppressed throughout the thesis, $\mathtt{t}$ being time variable, ω cyclic frequency, and $i = \sqrt{-1}$. It is assumed that the incident electric field has no z component, that is $\boldsymbol{E}^{\text{inc}} = E_x^{\text{inc}}\hat{\mathbf{x}} + E_y^{\text{inc}}\hat{\mathbf{y}}$. Below, we overview conventional integral representations of the electric field inside volume S of the scatterer [27].

1.2.1 Traditional surface equivalence principle

In the most commonly used form [27] the equivalence principle integral representation of the electric field outside the volume S is obtained via application of the second

dyadic Green's theorem [23] applied to the volume S_∞ outside the scatterer [27, 29]

$$\begin{aligned} &\boldsymbol{E}^{\text{inc}}(\boldsymbol{\rho}) - i\omega\mu_0 \int\limits_{\partial S} \overline{\overline{G}}_{e0}(\boldsymbol{\rho},\boldsymbol{\rho}') \cdot \boldsymbol{J}^e(\boldsymbol{\rho}')\, d\rho' \\ &- \int\limits_{\partial S} \overline{\overline{G}}_{m0}(\boldsymbol{\rho},\boldsymbol{\rho}') \cdot \boldsymbol{J}^m(\boldsymbol{\rho}')\, d\rho' = \begin{cases} \boldsymbol{E}(\boldsymbol{\rho}), & \boldsymbol{\rho} \in S_\infty \setminus \partial S, \\ \mathbf{0}, & \boldsymbol{\rho} \in S \setminus \partial S, \end{cases} \end{aligned} \tag{1.13}$$

$$\begin{aligned} &\boldsymbol{H}^{\text{inc}}(\boldsymbol{\rho}) + \int\limits_{\partial S} \overline{\overline{G}}_{m0}(\boldsymbol{\rho},\boldsymbol{\rho}') \cdot \boldsymbol{J}^e(\boldsymbol{\rho}')\, d\rho' \\ &- i\omega\epsilon_0 \int\limits_{\partial S} \overline{\overline{G}}_{e0}(\boldsymbol{\rho},\boldsymbol{\rho}') \cdot \boldsymbol{J}^m(\boldsymbol{\rho}')\, d\rho' = \begin{cases} \boldsymbol{H}(\boldsymbol{\rho}), & \boldsymbol{\rho} \in S_\infty \setminus \partial S, \\ \mathbf{0}, & \boldsymbol{\rho} \in S \setminus \partial S, \end{cases} \end{aligned} \tag{1.14}$$

where $\boldsymbol{J}^e = \hat{\mathbf{n}} \times \boldsymbol{H}$ is the equivalent electric current defined on boundary ∂S as the tangential component of the true magnetic field $\boldsymbol{H}$, $\boldsymbol{J}^m = -\hat{\mathbf{n}} \times \boldsymbol{E}$ is the equivalent magnetic current defined on ∂S as the tangential component of the true electric field $\boldsymbol{E}$, $\overline{\overline{G}}_{e0}$ is the electric field dyadic Green's function

$$\overline{\overline{G}}_{e0}(\boldsymbol{\rho},\boldsymbol{\rho}') = \left(\frac{\boldsymbol{\nabla}\boldsymbol{\nabla}}{k_0^2} + \overline{\overline{I}}\right) G_0(\boldsymbol{\rho},\boldsymbol{\rho}'), \tag{1.15}$$

which satisfies inhomogeneous dyadic wave equation

$$\boldsymbol{\nabla} \times \boldsymbol{\nabla} \times \overline{\overline{G}}_{e0}(\boldsymbol{\rho},\boldsymbol{\rho}') - k_0^2 \overline{\overline{G}}_{e0}(\boldsymbol{\rho},\boldsymbol{\rho}') = \overline{\overline{I}}\delta(\boldsymbol{\rho} - \boldsymbol{\rho}'). \tag{1.16}$$

In (1.15), $G_0(\boldsymbol{\rho},\boldsymbol{\rho}') = \frac{1}{4i} H_0^{(2)}\left(k_0 \left|\boldsymbol{\rho} - \boldsymbol{\rho}'\right|\right)$ is the scalar Green's function of free-space satisfying inhomogeneous scalar Helmholtz equation $\nabla^2 G_0 + k_0^2 G_0 = -\delta(\boldsymbol{\rho} - \boldsymbol{\rho}')$, k_0 is the wave number in free space, $H_0^{(2)}$ is the second-kind Hankel function of 0th order, $\boldsymbol{\rho}$ and $\boldsymbol{\rho}'$ are vectors of the observation and source points, respectively, $\overline{\overline{I}}$ is the idem-factor. In (1.13), $\overline{\overline{G}}_{m0} = \boldsymbol{\nabla} \times \overline{\overline{G}}_{e0}$ is the free space magnetic field dyadic Green's function.

Similarly, the equivalence principle integral representation of the electric field inside the volume S is obtained via application of the second dyadic Green's theorem

[23] to the volume S inside the scatterer [27]

$$\begin{aligned} & i\omega\mu_0 \int_{\partial S} \overline{\overline{G}}_{e\epsilon}(\boldsymbol{\rho},\boldsymbol{\rho}') \cdot \boldsymbol{J}^e(\boldsymbol{\rho}')\, d\rho' \\ & + \int_{\partial S} \overline{\overline{G}}_{m\epsilon}(\boldsymbol{\rho},\boldsymbol{\rho}') \cdot \boldsymbol{J}^m(\boldsymbol{\rho}')\, d\rho' = \begin{cases} \mathbf{0}, & \boldsymbol{\rho} \in S_\infty \setminus \partial S, \\ \boldsymbol{E}(\boldsymbol{\rho}), & \boldsymbol{\rho} \in S \setminus \partial S, \end{cases} \end{aligned} \tag{1.17}$$

$$\begin{aligned} & - \int_{\partial S} \overline{\overline{G}}_{m\epsilon}(\boldsymbol{\rho},\boldsymbol{\rho}') \cdot \boldsymbol{J}^e(\boldsymbol{\rho}')\, d\rho' \\ & + i\omega\epsilon \int_{\partial S} \overline{\overline{G}}_{e\epsilon}(\boldsymbol{\rho},\boldsymbol{\rho}') \cdot \boldsymbol{J}^m(\boldsymbol{\rho}')\, d\rho' = \begin{cases} \mathbf{0}, & \boldsymbol{\rho} \in S_\infty \setminus \partial S, \\ \boldsymbol{H}(\boldsymbol{\rho}), & \boldsymbol{\rho} \in S \setminus \partial S, \end{cases} \end{aligned} \tag{1.18}$$

$\overline{\overline{G}}_{e\epsilon}$ is the electric field dyadic Green's function

$$\overline{\overline{G}}_{e\epsilon}(\boldsymbol{\rho},\boldsymbol{\rho}') = \left(\frac{\boldsymbol{\nabla}\boldsymbol{\nabla}}{k_0^2\epsilon} + \overline{\overline{I}} \right) G_\epsilon(\boldsymbol{\rho},\boldsymbol{\rho}'), \tag{1.19}$$

which satisfies inhomogeneous dyadic wave equation

$$\boldsymbol{\nabla} \times \boldsymbol{\nabla} \times \overline{\overline{G}}_{e\epsilon}(\boldsymbol{\rho},\boldsymbol{\rho}') - k_0^2\epsilon\overline{\overline{G}}_{e\epsilon}(\boldsymbol{\rho},\boldsymbol{\rho}') = \overline{\overline{I}}\delta(\boldsymbol{\rho}-\boldsymbol{\rho}'). \tag{1.20}$$

where $G_\epsilon(\boldsymbol{\rho},\boldsymbol{\rho}') = \frac{1}{4i}H_0^{(2)}\left(k_0\sqrt{\epsilon}\,|\boldsymbol{\rho}-\boldsymbol{\rho}'|\right)$ is the scalar Green's function of free-space satisfying inhomogeneous scalar Helmholtz equation $\nabla^2 G_\epsilon + k_0^2\epsilon G_\epsilon = -\delta(\boldsymbol{\rho}-\boldsymbol{\rho}')$. In (1.17), $\overline{\overline{G}}_{m\epsilon} = \boldsymbol{\nabla} \times \overline{\overline{G}}_{e\epsilon}$ is the magnetic field dyadic Green's function of homogeneous space with relative permittivity ϵ.

For the purpose of the subsequent discussions take note that the field is zero in the right-hand side of (1.13), when the observation point is located inside the scatterer volume S. This is a result of the so-called *extinction theorem* [27] that demonstrates inside the scatterer the equivalent electric and magnetic currents cancel the incident field to zero. Similarly, the field is zero in the right-hand side of (1.17), when the observation point is located outside the scatterer volume S.

1.2.2 Generalized surface equivalence principle

The equivalent external integral field representation (1.13) requiring zero fields inside the object and the equivalent internal field representation (1.17) requiring a vanishing field outside the object are just a particular case of a general form of the equivalent field representation. Detailed discussions on generalized equivalence principle can be found in [47], [51], and [71]. In the case of the field representation in the exterior region the field inside the object can be allowed to be arbitrary, instead of being forced to vanish as in (1.13) providing the following equivalent integral representation

$$\begin{aligned} &\boldsymbol{E}^{\text{inc}}(\boldsymbol{\rho}) - i\omega\mu_0 \int\limits_{\partial S} \overline{\overline{G}}_{e0}(\boldsymbol{\rho},\boldsymbol{\rho}') \cdot \boldsymbol{J}(\boldsymbol{\rho}')\, d\rho' \\ &- \int\limits_{\partial S} \overline{\overline{G}}_{m0}(\boldsymbol{\rho},\boldsymbol{\rho}') \cdot \boldsymbol{M}(\boldsymbol{\rho}')\, d\rho' = \begin{cases} \boldsymbol{E}(\boldsymbol{\rho}), & \boldsymbol{\rho} \in S_\infty \setminus \partial S, \\ \boldsymbol{E}_{in}(\boldsymbol{\rho}), & \boldsymbol{\rho} \in S \setminus \partial S. \end{cases} \end{aligned} \tag{1.21}$$

$$\begin{aligned} &\boldsymbol{H}^{\text{inc}}(\boldsymbol{\rho}) + \int\limits_{\partial S} \overline{\overline{G}}_{m0}(\boldsymbol{\rho},\boldsymbol{\rho}') \cdot \boldsymbol{J}(\boldsymbol{\rho}')\, d\rho' \\ &- i\omega\epsilon_0 \int\limits_{\partial S} \overline{\overline{G}}_{e0}(\boldsymbol{\rho},\boldsymbol{\rho}') \cdot \boldsymbol{M}(\boldsymbol{\rho}')\, d\rho' = \begin{cases} \boldsymbol{H}(\boldsymbol{\rho}), & \boldsymbol{\rho} \in S_\infty \setminus \partial S, \\ \boldsymbol{H}_{in}(\boldsymbol{\rho}), & \boldsymbol{\rho} \in S \setminus \partial S. \end{cases} \end{aligned} \tag{1.22}$$

In (1.21) and (1.22), $\boldsymbol{J} = \hat{\mathbf{n}} \times (\boldsymbol{H} - \boldsymbol{H}_{in})$ is the fictitious electric current defined on the boundary ∂S equal to the difference of the tangential component of the true magnetic field $\boldsymbol{H}$ outside the object on ∂S and arbitrary (unconstrained) Maxwellian magnetic field $\boldsymbol{H}_{in}$ inside the scatterer on ∂S and $\boldsymbol{M} = -\hat{\mathbf{n}} \times (\boldsymbol{E} - \boldsymbol{E}_{in})$ is the fictitious magnetic current defined on ∂S as the difference between the tangential component of the true electric field $\boldsymbol{E}$ outside the object on ∂S and arbitrary (undefined) Maxwellian electric field $\boldsymbol{E}_{in}$ inside the scatterer on ∂S.

Similarly, the generalized integral representation of the true electric field inside

the volume S (see Fig. 1.3 (b)) is given by

$$\begin{aligned} & i\omega\mu_0 \int\limits_{\partial S} \overline{\overline{G}}_{e\epsilon}(\boldsymbol{\rho},\boldsymbol{\rho}') \cdot \boldsymbol{J}(\boldsymbol{\rho}')\ d\rho' \\ & + \int\limits_{\partial S} \overline{\overline{G}}_{m\epsilon}(\boldsymbol{\rho},\boldsymbol{\rho}') \cdot \boldsymbol{M}(\boldsymbol{\rho}')\ d\rho' = \begin{cases} \boldsymbol{E}_{out}(\boldsymbol{\rho}), & \boldsymbol{\rho} \in S_\infty \setminus \partial S, \\ \boldsymbol{E}(\boldsymbol{\rho}), & \boldsymbol{\rho} \in S \setminus \partial S, \end{cases} \end{aligned} \tag{1.23}$$

$$\begin{aligned} & - \int\limits_{\partial S} \overline{\overline{G}}_{m\epsilon}(\boldsymbol{\rho},\boldsymbol{\rho}') \cdot \boldsymbol{J}(\boldsymbol{\rho}')\ d\rho' \\ & + i\omega\epsilon \int\limits_{\partial S} \overline{\overline{G}}_{e\epsilon}(\boldsymbol{\rho},\boldsymbol{\rho}') \cdot \boldsymbol{M}(\boldsymbol{\rho}')\ d\rho' = \begin{cases} \boldsymbol{H}_{out}(\boldsymbol{\rho}), & \boldsymbol{\rho} \in S_\infty \setminus \partial S, \\ \boldsymbol{H}(\boldsymbol{\rho}), & \boldsymbol{\rho} \in S \setminus \partial S, \end{cases} \end{aligned} \tag{1.24}$$

where $\boldsymbol{J} = \hat{\mathbf{n}} \times (\boldsymbol{H} - \boldsymbol{H}_{out})$ is the fictitious electric current defined on boundary ∂S equal to the difference of the tangential component of the true magnetic field $\boldsymbol{H}$ inside the object on ∂S and arbitrary (unconstrained) Maxwellian magnetic field $\boldsymbol{H}_{out}$ outside the scatterer on ∂S and $\boldsymbol{M} = -\hat{\mathbf{n}} \times (\boldsymbol{E} - \boldsymbol{E}_{out})$ is the fictitious magnetic current defined on ∂S as the difference between the tangential component of the true electric field $\boldsymbol{E}$ inside the object on ∂S and arbitrary (undefined) Maxwellian electric field $\boldsymbol{E}_{out}$ outside the scatterer on ∂S.

It's important to make the following observations in regard to the generalized equivalent field representations (1.21), (1.22) and (1.23), (1.24): a) Since the unconstrained internal fields $\boldsymbol{E}_{in}$, $\boldsymbol{H}_{in}$ and external fields $\boldsymbol{E}_{out}$, $\boldsymbol{H}_{out}$ are arbitrary, there are infinite number of different fictitious currents $\boldsymbol{J}$ and $\boldsymbol{M}$, which can reproduce both the true internal and the true external fields $\boldsymbol{E}$ and $\boldsymbol{H}$; b) Since the uniqueness theorem requires that true field inside a region (interior or exterior) must be defined either by the tangential component of the true electric field or the true magnetic field on the region boundary, the tangential components of the true field must be included in the formation of the fictitious equivalent currents $\boldsymbol{J}$ and $\boldsymbol{M}$; c) The equivalent fictitious currents $\boldsymbol{J}$ and $\boldsymbol{M}$ can determined numerically or analytically through solution of an appropriate integral equation. They have no apparent local relationship to the tangential components of the true fields $\boldsymbol{H}$ and $\boldsymbol{E}$ until the unconstrained

fields $\boldsymbol{E}_{in}$, $\boldsymbol{H}_{in}$ or $\boldsymbol{E}_{out}$, $\boldsymbol{H}_{out}$ are determined. Thus, true fields $\boldsymbol{H}$ and $\boldsymbol{E}$ including their tangential components on ∂S can only be determined from $\boldsymbol{J}$ and $\boldsymbol{M}$ using the integral field representations (1.21) and (1.23).

1.2.3 Single-source representation

In the generalized exterior equivalent field representation (1.21) the ambiguity in the definition of the internal fields $\boldsymbol{E}_{in}$ and $\boldsymbol{H}_{in}$ enables the expression of the fictitious equivalent electric $\boldsymbol{J}$ and fictitious equivalent magnetic current $\boldsymbol{M}$ in terms of a single fictitious current J_0 as $\boldsymbol{J} = aJ_0\hat{\mathbf{t}}$ and $\boldsymbol{M} = bJ_0\hat{\mathbf{z}}$, where a and b are arbitrary constants (see Fig. 1.3 (c)) [47]. These constants a and b are selected based on convenience or such that spurious resonances are avoided [47]. Substituting fictitious current representations into the generalized outer equivalence principle (1.21), (1.22) produces single-source field representation in volume S_∞, as follows:

$$\begin{aligned} &\boldsymbol{E}^{\text{inc}}(\boldsymbol{\rho}) - i\omega\mu_0 \int\limits_{\partial S} \overline{\overline{G}}_{e0}(\boldsymbol{\rho},\boldsymbol{\rho}') \cdot a\hat{\mathbf{t}}(\boldsymbol{\rho}')J_0(\boldsymbol{\rho}')\ d\rho' \\ &- \int\limits_{\partial S} \overline{\overline{G}}_{m0}(\boldsymbol{\rho},\boldsymbol{\rho}') \cdot b\hat{\mathbf{z}}J_0(\boldsymbol{\rho}')\ d\rho' = \begin{cases} \boldsymbol{E}(\boldsymbol{\rho}),\ \boldsymbol{\rho} \in S_\infty \setminus \partial S, \\ \boldsymbol{E}_{in}(\boldsymbol{\rho}), \boldsymbol{\rho} \in S \setminus \partial S, \end{cases} \end{aligned} \tag{1.25}$$

$$\begin{aligned} &\boldsymbol{H}^{\text{inc}}(\boldsymbol{\rho}) + \int\limits_{\partial S} \overline{\overline{G}}_{m0}(\boldsymbol{\rho},\boldsymbol{\rho}') \cdot a\hat{\mathbf{t}}(\boldsymbol{\rho}')J_0(\boldsymbol{\rho}')\ d\rho' \\ &-i\omega\epsilon_0 \int\limits_{\partial S} \overline{\overline{G}}_{e0}(\boldsymbol{\rho},\boldsymbol{\rho}') \cdot b\hat{\mathbf{z}}J_0(\boldsymbol{\rho}')\ d\rho' = \begin{cases} \boldsymbol{H}(\boldsymbol{\rho}),\ \boldsymbol{\rho} \in S_\infty \setminus \partial S, \\ \boldsymbol{H}_{in}(\boldsymbol{\rho}), \boldsymbol{\rho} \in S \setminus \partial S, \end{cases} \end{aligned} \tag{1.26}$$

Similarly, the single-source electric field representations inside the scatterer follow

from (1.23) and (1.24) upon substitution in it of $\boldsymbol{J} = aJ_0\hat{\mathbf{t}}$ and $\boldsymbol{M} = bJ_0\hat{\mathbf{z}}$

$$\begin{aligned} &i\omega\mu_0 \int\limits_{\partial S} \overline{\overline{G}}_{e\epsilon}(\boldsymbol{\rho},\boldsymbol{\rho}') \cdot a\hat{\mathbf{t}}(\boldsymbol{\rho}')J_0(\boldsymbol{\rho}')\, d\rho' \\ &+ \int\limits_{\partial S} \overline{\overline{G}}_{m\epsilon}(\boldsymbol{\rho},\boldsymbol{\rho}') \cdot b\hat{\mathbf{z}}J_0(\boldsymbol{\rho}')\, d\rho' = \begin{cases} \boldsymbol{E}_{out}(\boldsymbol{\rho}), & \boldsymbol{\rho} \in S_\infty \setminus \partial S, \\ \boldsymbol{E}(\boldsymbol{\rho}), & \boldsymbol{\rho} \in S \setminus \partial S, \end{cases} \end{aligned} \tag{1.27}$$

$$\begin{aligned} &- \int\limits_{\partial S} \overline{\overline{G}}_{m\epsilon}(\boldsymbol{\rho},\boldsymbol{\rho}') \cdot a\hat{\mathbf{t}}(\boldsymbol{\rho}')J_0(\boldsymbol{\rho}')\, d\rho' \\ &i\omega\epsilon \int\limits_{\partial S} \overline{\overline{G}}_{e\epsilon}(\boldsymbol{\rho},\boldsymbol{\rho}') \cdot b\hat{\mathbf{z}}J_0(\boldsymbol{\rho}')\, d\rho' = \begin{cases} \boldsymbol{H}_{out}(\boldsymbol{\rho}), & \boldsymbol{\rho} \in S_\infty \setminus \partial S, \\ \boldsymbol{H}(\boldsymbol{\rho}), & \boldsymbol{\rho} \in S \setminus \partial S. \end{cases} \end{aligned} \tag{1.28}$$

The above expressions are used to derive the single-source integral equation with respect to the fictitious unknown function J_0 defined on the surface ∂S [47] as discussed next.

1.2.4 Traditional outward single-source integral equations

The traditional outward formulation of the E-field SSIE is obtained by constraining of the outer single source E-field representation (1.25) and H-field representation (1.26) with the extinction theorem of the traditional internal equivalence principle (1.17)

$$\begin{aligned} &i\omega\mu_0 \int\limits_{\partial S} \overline{\overline{G}}_{e\epsilon}(\boldsymbol{\rho},\boldsymbol{\rho}') \cdot \hat{\mathbf{n}}' \times \boldsymbol{H}(\boldsymbol{\rho}')\, d\rho' \\ &- \int\limits_{\partial S} \overline{\overline{G}}_{m\epsilon}(\boldsymbol{\rho},\boldsymbol{\rho}') \cdot \hat{\mathbf{n}}' \times \boldsymbol{E}(\boldsymbol{\rho}')\, d\rho' = \mathbf{0}, \qquad \boldsymbol{\rho} \in S_\infty \setminus \partial S. \end{aligned} \tag{1.29}$$

Substitution of the $\boldsymbol{E}$ and $\boldsymbol{H}$ field representations from (1.25) and (1.26) into the tangential component of the external extinction theorem for the E-field (1.29) upon $\boldsymbol{\rho}$ tending to ∂S from S_∞, yields conventional *outward E-field SSIE* with respect to

the unknown current J_0

$$
\begin{aligned}
&i\omega\mu_0\hat{\mathbf{t}}\cdot\int\limits_{\partial S}\overline{\overline{G}}_{e\epsilon}(\boldsymbol{\rho},\boldsymbol{\rho}')\cdot\hat{\mathbf{n}}'\times\left(\int\limits_{\partial S}\overline{\overline{G}}_{m0}(\boldsymbol{\rho}',\boldsymbol{\rho}'')\cdot a\hat{\mathbf{t}}''J_0(\boldsymbol{\rho}'')\;d\rho''-\right.\\
&\left.i\omega\epsilon_0\int\limits_{\partial S}\overline{\overline{G}}_{e0}(\boldsymbol{\rho}',\boldsymbol{\rho}'')\cdot b\hat{\mathbf{z}}J_0(\boldsymbol{\rho}'')\;d\rho''\right)d\rho'\\
&-\hat{\mathbf{t}}\cdot\int\limits_{\partial S}\overline{\overline{G}}_{m\epsilon}(\boldsymbol{\rho},\boldsymbol{\rho}')\cdot\hat{\mathbf{n}}'\times\left(-i\omega\mu_0\int\limits_{\partial S}\overline{\overline{G}}_{e0}(\boldsymbol{\rho}',\boldsymbol{\rho}'')\cdot a\hat{\mathbf{t}}''J_0(\boldsymbol{\rho}'')\;d\rho''-\right.\\
&\left.\int\limits_{\partial S}\overline{\overline{G}}_{m0}(\boldsymbol{\rho}',\boldsymbol{\rho}'')\cdot b\hat{\mathbf{z}}J_0(\boldsymbol{\rho}'')\;d\rho''\right)d\rho'=\\
&-\hat{\mathbf{t}}\cdot i\omega\mu_0\int\limits_{\partial S}\overline{\overline{G}}_{e\epsilon}(\boldsymbol{\rho},\boldsymbol{\rho}')\cdot\hat{\mathbf{n}}'\times\boldsymbol{H}^{\mathrm{inc}}(\boldsymbol{\rho}')d\rho'+\hat{\mathbf{t}}\cdot\int\limits_{\partial S}\overline{\overline{G}}_{m\epsilon}(\boldsymbol{\rho},\boldsymbol{\rho}')\cdot\hat{\mathbf{n}}'\times\boldsymbol{E}^{\mathrm{inc}}(\boldsymbol{\rho}')d\rho',
\end{aligned}
\tag{1.30}
$$

where $\boldsymbol{\rho}\to\partial S$ and $\boldsymbol{\rho}\in S_\infty$.

The extinction theorem of the traditional internal equivalence principle for the H-field (1.18)

$$
\begin{aligned}
&-\int\limits_{\partial S}\overline{\overline{G}}_{m\epsilon}(\boldsymbol{\rho},\boldsymbol{\rho}')\cdot\hat{\mathbf{n}}'\times\boldsymbol{H}(\boldsymbol{\rho}')\;d\rho'\\
&-i\omega\epsilon\int\limits_{\partial S}\overline{\overline{G}}_{e\epsilon}(\boldsymbol{\rho},\boldsymbol{\rho}')\cdot\hat{\mathbf{n}}'\times\boldsymbol{E}(\boldsymbol{\rho}')\;d\rho'=\mathbf{0},\qquad\boldsymbol{\rho}\in S_\infty\setminus\partial S,
\end{aligned}
\tag{1.31}
$$

can also be used for constraining the single source field representations (1.25) and (1.26). To that end the $\boldsymbol{E}$ and $\boldsymbol{H}$ field representations (1.25) and (1.26) are substituted into the external extinction theorem for the only z-component of the H-field (1.31) upon $\boldsymbol{\rho}$ tending to ∂S from S_∞. This yields a conventional *outward H-field*

SSIE with respect to the unknown current J_0

$$
\begin{aligned}
&-\hat{\mathbf{z}}\cdot\int\limits_{\partial S}\overline{\overline{G}}_{m\epsilon}(\boldsymbol{\rho},\boldsymbol{\rho}')\cdot\hat{\mathbf{n}}'\times\left(\int\limits_{\partial S}\overline{\overline{G}}_{m0}(\boldsymbol{\rho}',\boldsymbol{\rho}'')\cdot a\hat{\mathbf{t}}''J_0(\boldsymbol{\rho}'')\;d\rho''-\right.\\
&\left.i\omega\epsilon_0\int\limits_{\partial S}\overline{\overline{G}}_{e0}(\boldsymbol{\rho}',\boldsymbol{\rho}'')\cdot b\hat{\mathbf{z}}J_0(\boldsymbol{\rho}'')\;d\rho''\right)d\rho'\\
&-i\omega\epsilon\hat{\mathbf{z}}\cdot\int\limits_{\partial S}\overline{\overline{G}}_{e\epsilon}(\boldsymbol{\rho},\boldsymbol{\rho}')\cdot\hat{\mathbf{n}}'\times\left(-i\omega\mu_0\int\limits_{\partial S}\overline{\overline{G}}_{e0}(\boldsymbol{\rho}',\boldsymbol{\rho}'')\cdot a\hat{\mathbf{t}}''J_0(\boldsymbol{\rho}'')\;d\rho''-\right.\\
&\left.\int\limits_{\partial S}\overline{\overline{G}}_{m0}(\boldsymbol{\rho}',\boldsymbol{\rho}'')\cdot b\hat{\mathbf{z}}J_0(\boldsymbol{\rho}'')\;d\rho''\right)d\rho'=\\
&i\omega\epsilon\hat{\mathbf{z}}\cdot\int\limits_{\partial S}\overline{\overline{G}}_{e\epsilon}(\boldsymbol{\rho},\boldsymbol{\rho}')\cdot\hat{\mathbf{n}}'\times\boldsymbol{E}^{\mathrm{inc}}(\boldsymbol{\rho}')d\rho'+\hat{\mathbf{z}}\cdot\int\limits_{\partial S}\overline{\overline{G}}_{m\epsilon}(\boldsymbol{\rho},\boldsymbol{\rho}')\cdot\hat{\mathbf{n}}'\times\boldsymbol{H}^{\mathrm{inc}}(\boldsymbol{\rho}')d\rho',
\end{aligned}
\tag{1.32}
$$

where $\boldsymbol{\rho}\to\partial S$ and $\boldsymbol{\rho}\in S_\infty$.

1.2.5 Traditional inward single-source integral equations

The traditional inward formulation of the E-field SSIE is obtained by constraining the inner single source E-field representation (1.27) and H-field representation (1.28) with the extinction theorem of the traditional external equivalence principle (1.13)

$$
\begin{aligned}
&\boldsymbol{E}^{\mathrm{inc}}(\boldsymbol{\rho})-i\omega\mu_0\int\limits_{\partial S}\overline{\overline{G}}_{e0}(\boldsymbol{\rho},\boldsymbol{\rho}')\cdot\hat{\mathbf{n}}'\times\boldsymbol{H}(\boldsymbol{\rho}')\;d\rho'\\
&+\int\limits_{\partial S}\overline{\overline{G}}_{m0}(\boldsymbol{\rho},\boldsymbol{\rho}')\cdot\hat{\mathbf{n}}'\times\boldsymbol{E}(\boldsymbol{\rho}')\;d\rho'=\mathbf{0},\qquad\boldsymbol{\rho}\in S\setminus\partial S.
\end{aligned}
\tag{1.33}
$$

Substitution of the $\boldsymbol{E}$ and $\boldsymbol{H}$ field representations from (1.27) and (1.28) into the external extinction theorem for the tangential E-field (1.33) upon $\boldsymbol{\rho}$ tending to ∂S from S yields conventional *inward E-field SSIE* with respect to the unknown current

$$
\begin{aligned}
&J_0 \\
&\quad - i\omega\mu_0\hat{\mathbf{t}} \cdot \int\limits_{\partial S} \overline{\overline{G}}_{e0}(\boldsymbol{\rho}, \boldsymbol{\rho}') \cdot \hat{\mathbf{n}}' \times \left(- \int\limits_{\partial S} \overline{\overline{G}}_{m\epsilon}(\boldsymbol{\rho}', \boldsymbol{\rho}'') \cdot a\hat{\mathbf{t}}'' J_0(\boldsymbol{\rho}'')\ d\rho'' \right. \\
&\quad \left. + i\omega\epsilon \int\limits_{\partial S} \overline{\overline{G}}_{e\epsilon}(\boldsymbol{\rho}', \boldsymbol{\rho}'') \cdot b\hat{\mathbf{z}} J_0(\boldsymbol{\rho}'')\ d\rho'' \right) d\rho' \\
&\quad + \hat{\mathbf{t}} \cdot \int\limits_{\partial S} \overline{\overline{G}}_{m0}(\boldsymbol{\rho}, \boldsymbol{\rho}') \cdot \hat{\mathbf{n}}' \times \left(i\omega\mu_0 \int\limits_{\partial S} \overline{\overline{G}}_{e\epsilon}(\boldsymbol{\rho}', \boldsymbol{\rho}'') \cdot a\hat{\mathbf{t}}'' J_0(\boldsymbol{\rho}'')\ d\rho'' + \right. \\
&\quad \left. \int\limits_{\partial S} \overline{\overline{G}}_{m\epsilon}(\boldsymbol{\rho}', \boldsymbol{\rho}'') \cdot b\hat{\mathbf{z}} J_0(\boldsymbol{\rho}'')\ d\rho'' \right) d\rho' = -\hat{\mathbf{t}} \cdot \boldsymbol{E}^{\text{inc}}(\boldsymbol{\rho}),
\end{aligned}
\tag{1.34}
$$

where $\boldsymbol{\rho} \to \partial S$ and $\boldsymbol{\rho} \in S$.

The extinction theorem of the traditional external equivalence principle (1.14) is the following

$$
\begin{aligned}
&\boldsymbol{H}^{\text{inc}}(\boldsymbol{\rho}) + \int\limits_{\partial S} \overline{\overline{G}}_{m0}(\boldsymbol{\rho}, \boldsymbol{\rho}') \cdot \hat{\mathbf{n}}' \times \boldsymbol{H}(\boldsymbol{\rho}')\ d\rho' \\
&i\omega\epsilon_0 \int\limits_{\partial S} \overline{\overline{G}}_{e0}(\boldsymbol{\rho}, \boldsymbol{\rho}') \cdot \hat{\mathbf{n}}' \times \boldsymbol{E}(\boldsymbol{\rho}')\ d\rho' = \mathbf{0}, \qquad \boldsymbol{\rho} \in S \setminus \partial S.
\end{aligned}
\tag{1.35}
$$

Substitution of the $\boldsymbol{E}$ and $\boldsymbol{H}$ field representations from (1.27) and (1.28) into the external extinction theorem for the only z-component of the H-field (1.35) upon $\boldsymbol{\rho}$ tending to ∂S from S yields conventional *inward H-field SSIE* with respect to the

unknown current J_0

$$
\begin{aligned}
&-\hat{\mathbf{z}}\cdot\int\limits_{\partial S}\overline{\overline{G}}_{m0}(\boldsymbol{\rho},\boldsymbol{\rho}')\cdot\hat{\mathbf{n}}'\times\left(-\int\limits_{\partial S}\overline{\overline{G}}_{m\epsilon}(\boldsymbol{\rho}',\boldsymbol{\rho}'')\cdot a\hat{\mathbf{t}}''J_0(\boldsymbol{\rho}'')\;d\rho''\right.\\
&\left.+i\omega\epsilon\int\limits_{\partial S}\overline{\overline{G}}_{e\epsilon}(\boldsymbol{\rho}',\boldsymbol{\rho}'')\cdot b\hat{\mathbf{z}}J_0(\boldsymbol{\rho}'')\;d\rho''\right)d\rho'\\
&+i\omega\epsilon_0\hat{\mathbf{z}}\cdot\int\limits_{\partial S}\overline{\overline{G}}_{e0}(\boldsymbol{\rho},\boldsymbol{\rho}')\cdot\hat{\mathbf{n}}'\times\left(i\omega\mu_0\int\limits_{\partial S}\overline{\overline{G}}_{e\epsilon}(\boldsymbol{\rho}',\boldsymbol{\rho}'')\cdot a\hat{\mathbf{t}}''J_0(\boldsymbol{\rho}'')\;d\rho''+\right.\\
&\left.\int\limits_{\partial S}\overline{\overline{G}}_{m\epsilon}(\boldsymbol{\rho}',\boldsymbol{\rho}'')\cdot b\hat{\mathbf{z}}J_0(\boldsymbol{\rho}'')\;d\rho''\right)d\rho'=-\hat{\mathbf{z}}\cdot\boldsymbol{H}^{\mathrm{inc}}(\boldsymbol{\rho}),
\end{aligned}
\tag{1.36}
$$

where $\boldsymbol{\rho}\to\partial S$ and $\boldsymbol{\rho}\in S$.

1.2.6 Volume equivalence principle

The field both inside and outside a penetrable object can be written as an integral over volume polarization current $\boldsymbol{j}$ based on the volume equivalence principle [27]

$$
\boldsymbol{E}(\boldsymbol{\rho})=\boldsymbol{E}^{\mathrm{inc}}(\boldsymbol{\rho})+\int\limits_{S}\overline{\overline{G}}_{e0}(\boldsymbol{\rho},\boldsymbol{\rho}')\cdot\boldsymbol{j}(\boldsymbol{\rho}')ds',\boldsymbol{\rho}\in S,\quad\boldsymbol{\rho}'\in S_\infty \tag{1.37}
$$

where $\boldsymbol{j}=k_0^2(\epsilon-1)\boldsymbol{E}$.

1.2.7 Proposed single-source integral equation

In this work we propose to constrain the internal single source field representation

$$
\begin{aligned}
\boldsymbol{E}(\boldsymbol{\rho})=&-i\omega\mu_0\int\limits_{\partial S}\overline{\overline{G}}_{e\epsilon}(\boldsymbol{\rho},\boldsymbol{\rho}')\cdot a\hat{\mathbf{t}}(\boldsymbol{\rho}')J_0(\boldsymbol{\rho}')\;d\rho'\\
&+\int\limits_{\partial S}\overline{\overline{G}}_{m\epsilon}(\boldsymbol{\rho},\boldsymbol{\rho}')\cdot b\hat{\mathbf{z}}J_0(\boldsymbol{\rho}')\;d\rho',\quad\boldsymbol{\rho}\in S\setminus\partial S,
\end{aligned}
\tag{1.38}
$$

with the volume equivalence principle (1.37) instead of the surface equivalence principle as it was previously done in the traditional SSIEs. For that purpose we substitute (1.38) into (1.37) and enforce the latter for the tangential component of the electric field as we tend the observation point $\boldsymbol{\rho}$ to the boundary ∂S from inside S, which produces the proposed *Surface-Volume-Surface E-field SSIE*

$$
\begin{aligned}
&- i\omega\mu_0\hat{\mathbf{t}} \cdot \int\limits_{\partial S} \overline{\overline{G}}_{e\epsilon}(\boldsymbol{\rho}, \boldsymbol{\rho}') \cdot a\hat{\mathbf{t}}' J_0(\boldsymbol{\rho}')\ d\rho' + \hat{\mathbf{t}} \cdot \int\limits_{\partial S} \overline{\overline{G}}_{m\epsilon}(\boldsymbol{\rho}, \boldsymbol{\rho}') \cdot b\hat{\mathbf{z}} J_0(\boldsymbol{\rho}')\ d\rho' \\
&- k_0^2(\epsilon - 1)\hat{\mathbf{t}} \cdot \int\limits_{S} \overline{\overline{G}}_{e0}(\boldsymbol{\rho}, \boldsymbol{\rho}') \cdot \left(-i\omega\mu_0 \int\limits_{\partial S} \overline{\overline{G}}_{e\epsilon}(\boldsymbol{\rho}', \boldsymbol{\rho}'') \cdot a\hat{\mathbf{t}}'' J_0(\boldsymbol{\rho}'')\ d\rho'' + \right. \\
&\left. \int\limits_{\partial S} \overline{\overline{G}}_{m\epsilon}(\boldsymbol{\rho}', \boldsymbol{\rho}'') \cdot b\hat{\mathbf{z}} J_0(\boldsymbol{\rho}'')\ d\rho'' \right) ds' = \hat{\mathbf{t}} \cdot \boldsymbol{E}^{\text{inc}}(\boldsymbol{\rho}), \quad \boldsymbol{\rho} \in S, \quad \boldsymbol{\rho} \to \partial S.
\end{aligned}
\tag{1.39}
$$

where a and b are arbitrary constants.

For simplicity the derivation were presented here for the case of 2D scattering problem under TE-polarization. Derivation of both the traditional SSIE formulations and the new Surface-Volume-Surface SSIE to the 3D case is done in an analogous manner; however it is beyond the scope of the thesis.

1.3 Scope and Contributions

In this thesis we consider a particular case of (1.39) in which constants a and b are taken to be 1 and 0, respectively, yielding

$$
\begin{aligned}
&- i\omega\mu_0\hat{\mathbf{t}} \cdot \int\limits_{\partial S} \overline{\overline{G}}_{e\epsilon}(\boldsymbol{\rho}, \boldsymbol{\rho}') \cdot \boldsymbol{J}(\boldsymbol{\rho}')\ d\rho' \\
&+ i\omega\mu_0 k_0^2(\epsilon - 1)\hat{\mathbf{t}} \cdot \int\limits_{S} \overline{\overline{G}}_{e0}(\boldsymbol{\rho}, \boldsymbol{\rho}') \cdot \int\limits_{\partial S} \overline{\overline{G}}_{e\epsilon}(\boldsymbol{\rho}', \boldsymbol{\rho}'') \cdot \boldsymbol{J}(\boldsymbol{\rho}'')\ d\rho'' ds' = \hat{\mathbf{t}} \cdot \boldsymbol{E}^{\text{inc}}(\boldsymbol{\rho}),
\end{aligned}
\tag{1.40}
$$

where $\boldsymbol{\rho} \to \partial S$, $\boldsymbol{\rho} \in S$, and $\boldsymbol{J}(\boldsymbol{\rho}) = \hat{\mathbf{t}}(\boldsymbol{\rho}) J_0(\boldsymbol{\rho})$. We term the above equation *Surface-Volume-Surface EFIE* due to the presence of only the E-field operators in it. To make

the reader appreciate the nature of the new equation better we present a simplified derivation of the Surface-Volume-Surface SSIE (1.40) in Chapter 2 and Chapter 3 through the interpretation of the internal single source E-field representation (1.27) as a superposition of the waves emanating from the scatterer's boundary.

The scope of the work presented here is two fold. First the generalization of the new SSIE formulation is presented for the vector case of 2D scattering problem (under TE polarization) and general 3D scattering problem. Second the development of low order and higher order MoM solutions of this novel equation are presented for its scalar and vector forms. Numerical demonstration of the rigorous nature of the proposed SVS-EFIE through error-controllable higher-order solutions is another objective of this work.

The outline of this thesis is as follows. Chapter 2 contains formulations of the vector SVS-EFIE for 2D scattering problems under TE polarization and development of low order MoM scheme for its numerical solution. The MoM solution is based on discretization of the boundaries with line elements and cross-sectional discretization utilizing triangle or quadrilateral elements. The generalization of the new SVS-EFIE formulation to the general 3D scattering problem and its low-order MoM discretization is discussed in Chapter 3. Here, first-order triangle and tetrahedral elements are utilized in the MoM scheme for discretization of the scatterer's boundary and its volume, respectively. Chapters 4 and 5 describe a higher order MoM solution of the scalar SVS-EFIE of magneto-quasi-statics governing current flow in a transmission line formed by a single circular conductor and the multi-conductor transmission lines of complex cross-sections. In Chapter 6, a higher-order MoM solution of the vector SVS-EFIE is developed for the solution of 2D scattering problems under TE polarization. Chapter 7, draws conclusions and makes recommendations for related future work.

2

New Vector Single-Source Surface Integral Equation for Scattering Problems on Dielectric Objects in 2D

2.1 New Vector Surface-Volume-Surface EFIE

The new SVS-EFIE can be derived from the classical Volume-EFIE (V-EFIE) [27]. Consider a time-harmonic 2D TE scattering of the incident field $\boldsymbol{E}^{\text{inc}}$ on a homogeneous dielectric cylinder (Fig. 1.3). Enforcing (1.37) throughout the cylinder we get the classic V-EFIE [27]:

$$\boldsymbol{E}(\boldsymbol{\rho}) - k_0^2\,(\epsilon - 1) \iint\limits_S \overline{\overline{G}}_{e0}(\boldsymbol{\rho}, \boldsymbol{\rho}') \cdot \boldsymbol{E}(\boldsymbol{\rho}')ds' = \boldsymbol{E}^{\text{inc}}(\boldsymbol{\rho}), \tag{2.1}$$

where $\rho \in S$. Consider now the total field representation in S in the form

$$\boldsymbol{E}(\boldsymbol{\rho}') = i\omega\mu_0 \int\limits_{\partial S} \overline{\overline{G}}_\epsilon(\boldsymbol{\rho}', \boldsymbol{\rho}'') \ \cdot \ \boldsymbol{J}(\boldsymbol{\rho}'') \ d\rho'', \boldsymbol{\rho}' \in \ S \tag{2.2}$$

Alternative justification for (2.2) is that the total electric field inside the scatterer satisfies the homogeneous wave equation

$$\boldsymbol{\nabla} \times \boldsymbol{\nabla} \times \boldsymbol{E}(\boldsymbol{\rho}) - k_\epsilon^2 \boldsymbol{E}(\boldsymbol{\rho}) = \mathbf{0}, \quad \boldsymbol{\rho} \in S \setminus \partial S. \tag{2.3}$$

Hence, it can be represented as a superposition (2.2) of the cylindrical waves emanating from the cylinder's boundary ∂S. The tangential vector function $\boldsymbol{J}(\boldsymbol{\rho}') = J(\boldsymbol{\rho}')\hat{\mathbf{t}}(\boldsymbol{\rho}')$ defined on the surface ∂S in (2.2) provides the weights for the waves, and $\hat{\mathbf{t}}(\boldsymbol{\rho}')$ representing the tangential vector to the boundary ∂S. The elementary waves $\overline{\overline{G}}_{e\epsilon}(\boldsymbol{\rho}, \boldsymbol{\rho}')$ are represented by the dyadic Green's function of the cylinder medium that satisfies the same homogeneous wave equation as the total field $\boldsymbol{E}$ everywhere in S excluding the boundary ∂S

$$\boldsymbol{\nabla} \times \boldsymbol{\nabla} \times \overline{\overline{G}}_{e\epsilon}(\boldsymbol{\rho}, \boldsymbol{\rho}') - k_\epsilon^2 \overline{\overline{G}}_{e\epsilon}(\boldsymbol{\rho}, \boldsymbol{\rho}') = \overline{\overline{0}}, \tag{2.4}$$

where $\boldsymbol{\rho} \in S \setminus \partial S$ and $\boldsymbol{\rho}' \in \partial S$. Substitution of (2.2) into (2.1) followed by restriction of the observation domain to the boundary of the scatterer cylinder yield the desired SVS-EFIE with respect to the unknown auxiliary current density $\boldsymbol{J}$. Since $\boldsymbol{J}(\boldsymbol{\rho}'')$ is assumed to be a tangential vector function defined on the boundary ∂S. To balance the range and domain of the resulting operators, the V-EFIE (2.1) must be satisfied only for the tangential component of total electric field at the boundary ∂S. This yields the proposed new SVS-EFIE

$$-i\omega\mu_0\hat{\mathbf{t}}\cdot\int_{\partial S}\overline{\overline{G}}_{e\epsilon}(\boldsymbol{\rho},\boldsymbol{\rho}'')\cdot\boldsymbol{J}(\boldsymbol{\rho}'')d\rho''+i\omega\mu_0 k_0^2\,(\epsilon-1)\,\hat{\mathbf{t}}$$
$$\cdot\iint_S\overline{\overline{G}}_{e0}(\boldsymbol{\rho},\boldsymbol{\rho}')\cdot\int_{\partial S}\overline{\overline{G}}_{e\epsilon}(\boldsymbol{\rho}',\boldsymbol{\rho}'')\cdot\boldsymbol{J}(\boldsymbol{\rho}'')d\rho''ds' \qquad =\hat{\mathbf{t}}\cdot\boldsymbol{E}^{\text{inc}}(\boldsymbol{\rho}),\quad \boldsymbol{\rho}\in\partial S. \tag{2.5}$$

The proposed SSIE (2.5) uses only one unknown $\boldsymbol{J}(\boldsymbol{\rho}'')$, called a single layer ansatz [73]. It is convenient to express the SVS-EFIE in the following operator form

$$-\overline{\overline{\mathcal{T}}}_{\epsilon}^{\partial S,\partial S}\circ\boldsymbol{J}+\overline{\overline{\mathcal{T}}}_{0}^{\partial S,S}\circ\overline{\overline{\mathcal{T}}}_{\epsilon}^{S,\partial S}\circ\boldsymbol{J}=\hat{\mathbf{t}}\cdot\boldsymbol{E}^{\text{inc}}. \tag{2.6}$$

In (2.6), each dyadic integral operators is a sum of two integral operators, one corresponding to the scalar potential contribution and one for the vector potential contribution. These operators are defined, as follows:

$$\mathcal{T}_{\epsilon,\Phi}^{\partial S,\partial S}\circ\boldsymbol{J}=\frac{i\omega\mu_0}{k_\epsilon^2}\int_{\partial S}G_\epsilon(\boldsymbol{\rho},\boldsymbol{\rho}'')\boldsymbol{\nabla}''\cdot\boldsymbol{J}(\boldsymbol{\rho}'')d\rho'',\boldsymbol{\rho}\in\partial S, \tag{2.7}$$

$$\boldsymbol{\mathcal{T}}_{\epsilon,A}^{\partial S,\partial S}\circ\boldsymbol{J}=i\omega\mu_0\hat{\mathbf{t}}\cdot\int_{\partial S}G_\epsilon(\boldsymbol{\rho},\boldsymbol{\rho}'')\boldsymbol{J}(\boldsymbol{\rho}'')d\rho'',\boldsymbol{\rho}\in\partial S, \tag{2.8}$$

$$\boldsymbol{\mathcal{T}}_{\epsilon,\nabla\Phi}^{S,\partial S}\circ\boldsymbol{J}=\frac{i\omega\mu_0}{k_\epsilon^2}\int_{\partial S}\boldsymbol{\nabla}'G_\epsilon(\boldsymbol{\rho}',\boldsymbol{\rho}'')\boldsymbol{\nabla}''\cdot\boldsymbol{J}(\boldsymbol{\rho}'')d\rho'',\boldsymbol{\rho}'\in S, \tag{2.9}$$

$$\mathcal{T}_{\epsilon,A}^{S,\partial S}\circ\boldsymbol{J}=i\omega\mu_0\int_{\partial S}G_\epsilon(\boldsymbol{\rho}',\boldsymbol{\rho}'')\boldsymbol{J}(\boldsymbol{\rho}'')d\rho'',\boldsymbol{\rho}'\in S, \tag{2.10}$$

$$\boldsymbol{\mathcal{T}}_{0,\varphi}^{\partial S,S}\circ\boldsymbol{j}=\frac{1}{k_0^2}\iint_S\boldsymbol{\nabla}G_0(\boldsymbol{\rho},\boldsymbol{\rho}')\cdot\boldsymbol{j}(\boldsymbol{\rho}')ds',\boldsymbol{\rho}\in\partial S, \tag{2.11}$$

$$\boldsymbol{\mathcal{T}}_{0,a}^{\partial S,S}\circ\boldsymbol{j}=\hat{\mathbf{t}}\cdot\iint_S G_0(\boldsymbol{\rho},\boldsymbol{\rho}')\boldsymbol{j}(\boldsymbol{\rho}')ds',\boldsymbol{\rho}\in\partial S, \tag{2.12}$$

where $\boldsymbol{j}$ is a polarization current density and $G_\epsilon(\boldsymbol{\rho},\boldsymbol{\rho}')=\frac{1}{4i}H_0^{(2)}\left(k_0\sqrt{\epsilon}\,|\boldsymbol{\rho}-\boldsymbol{\rho}'|\right)$. With the integral operator notations (2.7)–(2.12), the proposed SSIE (2.5) is written as

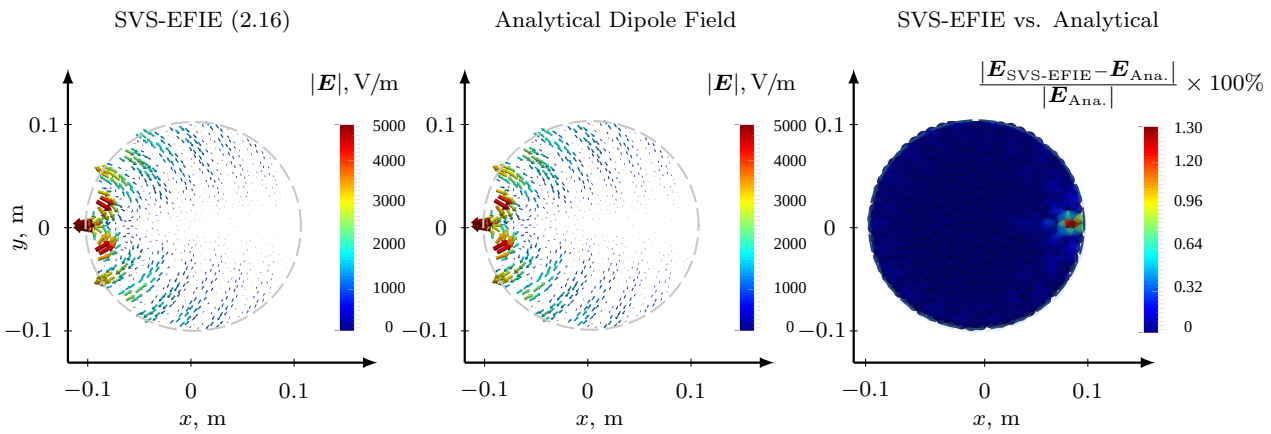

Figure 2.1: A snapshot at time $\mathtt{t} = 0$ s of the electric field at 6 GHz inside a circular cylinder of permittivity $\epsilon = 1$ and cross-section radius 0.1 m centered at the origin produced by x-directed electric dipole situated at $x = -0.105$ m and $y = 0$ m. The electric dipole moment is $I\ell = 1$ A·m. The number of line elements in MoM discretization (2.46) of simplified SVS-EFIE (2.16) on the boundary ∂S is $M = 524$.

$$-\left(\mathcal{T}^{\partial S,\partial S}_{\epsilon,\nabla\Phi}+\boldsymbol{\mathcal{T}}^{\partial S,\partial S}_{\epsilon,A}\right)\circ\boldsymbol{J}\quad+\left(\boldsymbol{\mathcal{T}}^{\partial S,S}_{0,\nabla\varphi}+\boldsymbol{\mathcal{T}}^{\partial S,S}_{0,a}\right)\circ\left(\boldsymbol{\mathcal{T}}^{S,\partial S}_{\epsilon,\nabla\Phi}+\mathcal{T}^{S,\partial S}_{\epsilon,A}\right)\circ\boldsymbol{J}=\hat{\mathbf{t}}\cdot\boldsymbol{E}^{\text{inc}}, \tag{2.13}$$

where

$$\mathcal{T}^{\partial S,\partial S}_{\epsilon,\nabla\Phi}=\hat{\mathbf{t}}\cdot\boldsymbol{\nabla}\mathcal{T}^{\partial S,\partial S}_{\epsilon,\Phi} \tag{2.14}$$

and

$$\boldsymbol{\mathcal{T}}^{\partial S,S}_{0,\nabla\varphi}=\hat{\mathbf{t}}\cdot\boldsymbol{\nabla}\boldsymbol{\mathcal{T}}^{\partial S,S}_{0,\varphi}. \tag{2.15}$$

The integral operators $\left(\boldsymbol{\mathcal{T}}^{S,\partial S}_{\epsilon,\nabla\Phi}+\mathcal{T}^{S,\partial S}_{\epsilon,A}\right)$ translate the unknown tangential weighting source function $\boldsymbol{J}$ from the boundary of the scatterer ∂S to the total field inside the cross-section of the scatterer S. The integral operators $\left(\boldsymbol{\mathcal{T}}^{\partial S,S}_{0,\nabla\varphi}+\boldsymbol{\mathcal{T}}^{\partial S,S}_{0,a}\right)$ map the polarization current $\boldsymbol{j}$ inside the cross-section of the scatterer S to the tangential scattered electric field on the boundary ∂S. The integral operators $\left(\mathcal{T}^{\partial S,\partial S}_{\epsilon,\nabla\Phi}+\boldsymbol{\mathcal{T}}^{\partial S,\partial S}_{\epsilon,A}\right)$ map the tangential weighting sources $\boldsymbol{J}$ defined on the boundary of the scatterer ∂S to the tangential component of the total electric field on the same boundary ∂S. In the case of the free space, i.e. relative permittivity $\epsilon = 1$ in the volume S the SVS-

EFIE (2.5) has an interesting interpretation. Namely, it turns into the EFIE for a perfect electric conductor (PEC) scatterer with the only difference of $\hat{\mathbf{t}} \cdot \boldsymbol{E}^{\text{inc}}$ being in the right hand side instead of $-\hat{\mathbf{t}} \cdot \boldsymbol{E}^{\text{inc}}$

$$-i\omega\mu_0 \hat{\mathbf{t}} \cdot \int\limits_{\partial S} \overline{\overline{G}}_{e0}(\boldsymbol{\rho}, \boldsymbol{\rho}'') \cdot \boldsymbol{J}(\boldsymbol{\rho}'') d\rho'' = \hat{\mathbf{t}} \cdot \boldsymbol{E}^{\text{inc}}(\boldsymbol{\rho}), \quad \boldsymbol{\rho} \in \partial S. \tag{2.16}$$

From the above equation one can see that in the case of $\epsilon = 1$, the weighting function $\boldsymbol{J}$ turns into the negative of the electric current on the surface of the PEC scatterer occupying the same volume S as the original penetrable object under excitation $\boldsymbol{E}^{\text{inc}}$, i.e. $\boldsymbol{J} = -\boldsymbol{J}^e$. This result has a clear physical meaning. While in the case of scattering of $\boldsymbol{E}^{\text{inc}}$ on a PEC body, current $\boldsymbol{J}^e$ produces in S exactly the negative of incident field $-\boldsymbol{E}^{\text{inc}}$ in order to achieve a vanishing total field $\boldsymbol{E}$. The weighting function $\boldsymbol{J}$ in the SVS-EFIE in the case of a vanishing scatterer $\epsilon = 1$ produces in S exactly the incident field $\boldsymbol{E}^{\text{inc}}$. Thus, naturally in the case of a vanishing scatterer, i.e. $\epsilon = 1$, $\boldsymbol{J} = -\boldsymbol{J}^e$ must be true. An example of an incident field representation in S by $\boldsymbol{J}$ is depicted in Fig. 2.1 for the case of the field produced by an electric dipole. One can see that the solution $\boldsymbol{J}$ of the SVS-EFIE (2.16), in the case $\epsilon = 1$, where accurately reproduces the incident field (which could be arbitrary) inside the scatterer volume S. Plug in $\boldsymbol{J}$ into (2.2), followed by substitution of (2.2) into volume-EFIE (2.1) using the condition $\epsilon = 1$ yields

$$-i\omega\mu_0 \int\limits_{\partial S} \overline{\overline{G}}_{e0}(\boldsymbol{\rho}, \boldsymbol{\rho}'') \cdot \boldsymbol{J}(\boldsymbol{\rho}'') d\rho'' = \boldsymbol{E}^{\text{inc}}(\boldsymbol{\rho}), \tag{2.17}$$

where $\boldsymbol{\rho} \in S$. Since the incident field $\boldsymbol{E}^{\text{inc}}$ is arbitrary, the expression (2.17) can be viewed as a representation of an arbitrary field in a volume S by a single-source $\boldsymbol{J}$ localized to the boundary of the volume ∂S and reproducing the field in S through only the electric field dyadic kernel $\overline{\overline{G}}_{e0}$.

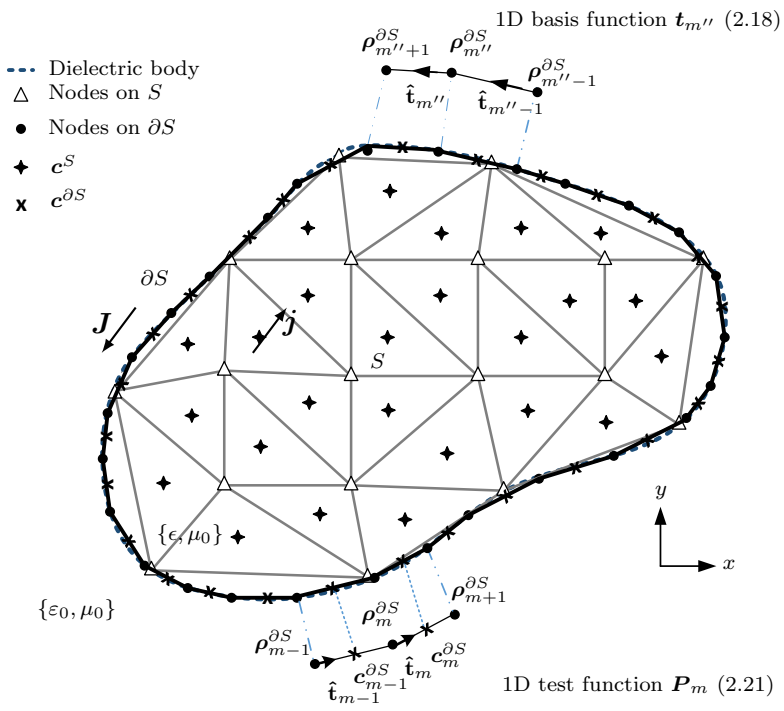

Figure 2.2: Boundary and surface meshes utilized in the MoM discretization of the SVS-EFIE (2.5). The homogeneous cylinder has complex relative permittivity ϵ and magnetic permeability μ_0.

2.2 Method of Moments Discretization of SVS-EFIE Operators

To solve SVS-EFIE numerically, the cross-section of scatterer S is discretized with a 2D mesh consisting of N triangles. The boundary ∂S is discretized with a 1D mesh consisting of M line elements. The number of elements in the 2D mesh N can be independent from the size of 1D mesh M, example meshes are depicted in Fig. 2.2. The position vector on the mth line element is defined parametrically as $\boldsymbol{\rho}^{\partial S}_m(t) = \boldsymbol{\rho}^{\partial S}_m + t(\boldsymbol{\rho}^{\partial S}_{m+1} - \boldsymbol{\rho}^{\partial S}_m)$, where $\boldsymbol{\rho}^{\partial S}_m$ and $\boldsymbol{\rho}^{\partial S}_{m+1}$ are the coordinates of the vertices of the mth line element on the boundary ∂S and $t \in [0, 1]$. The length of the mth line element is defined as $\ell_m = \left|\boldsymbol{\rho}^{\partial S}_{m+1} - \boldsymbol{\rho}^{\partial S}_m\right|$. Tangential vector to the mth line element is defined as $\hat{\mathbf{t}}_m = \frac{\boldsymbol{\rho}^{\partial S}_{m+1} - \boldsymbol{\rho}^{\partial S}_m}{\ell_m}$. The centroid of the mth line element is defined as $\boldsymbol{c}^{\partial S}_m =$

$\frac{\boldsymbol{\rho}^{\partial S}_{m+1}+\boldsymbol{\rho}^{\partial S}_{m}}{2}$. The position vector on the n'th triangle on the cross-section S is defined parametrically as $\boldsymbol{\rho}^{S}_{n'}(\xi',\eta') = \xi'\boldsymbol{\rho}^{S}_{n'(0)}+\eta'\boldsymbol{\rho}^{S}_{n'(1)}+(1-\xi'-\eta')\boldsymbol{\rho}^{S}_{n'(2)}$, where $\boldsymbol{\rho}^{S}_{n'(0)}$, $\boldsymbol{\rho}^{S}_{n'(1)}$, and $\boldsymbol{\rho}^{S}_{n'(2)}$ are the coordinates of the vertices of the n'th triangle on the cross-section and ξ' and η' are barycentric coordinates [25], $\xi' \in [0,1]$, $\eta' \in [0, 1-\xi']$. The centroid of the n'th triangle is defined as $\boldsymbol{c}^{S}_{n'} = \frac{1}{3}(\boldsymbol{\rho}^{S}_{n'(0)} + \boldsymbol{\rho}^{S}_{n'(1)} + \boldsymbol{\rho}^{S}_{n'(2)})$. Discretization of the unknown tangential weighting function $\boldsymbol{J}$ defined on the boundary ∂S is performed using a set of 1D vector roof-top basis functions [27] defined on two adjacent line elements (Fig. 2.2). For example, $\boldsymbol{t}_{m''}$ is m''th basis function, which is positioned on the $(m''-1)$th and m''th line elements and defined as

$$\boldsymbol{t}_{m''}(\boldsymbol{\rho}'') = \begin{cases} \frac{\boldsymbol{\rho}''-\boldsymbol{\rho}^{\partial S}_{m''-1}}{\ell_{m''-1}}, & \boldsymbol{\rho}'' \in \left[\boldsymbol{\rho}^{\partial S}_{m''-1}, \boldsymbol{\rho}^{\partial S}_{m''}\right], \\ \frac{\boldsymbol{\rho}^{\partial S}_{m''+1}-\boldsymbol{\rho}''}{\ell_{m''}}, & \boldsymbol{\rho}'' \in \left[\boldsymbol{\rho}^{\partial S}_{m''}, \boldsymbol{\rho}^{\partial S}_{m''+1}\right]. \end{cases} \tag{2.18}$$

Thus, the discretized form of the unknown tangential weighting function $\boldsymbol{J}$ is

$$\boldsymbol{J}(\boldsymbol{\rho}'') \cong \sum_{m''=1}^{M} I_{m''}\boldsymbol{t}_{m''}(\boldsymbol{\rho}''). \tag{2.19}$$

where, $I_{m''}$ is unknown coefficient of the m''th basis function. The divergence of the set of vector 1D linear basis functions is two pulse functions defined on the adjacent line elements

$$\boldsymbol{\nabla}\cdot\boldsymbol{t}_{m''}(\boldsymbol{\rho}'') = \begin{cases} \frac{1}{\ell_{m''-1}}, & \boldsymbol{\rho}'' \in \left[\boldsymbol{\rho}^{\partial S}_{m''-1}, \boldsymbol{\rho}^{\partial S}_{m''}\right], \\ -\frac{1}{\ell_{m''}}, & \boldsymbol{\rho}'' \in \left[\boldsymbol{\rho}^{\partial S}_{m''}, \boldsymbol{\rho}^{\partial S}_{m''+1}\right]. \end{cases} \tag{2.20}$$

As test functions we use a set of vector piece-wise constant functions positioned between the centroids of the two adjacent line elements [27]. For example $\boldsymbol{P}_m$, mth test function, is defined between line elements $(m-1)$th and mth (Fig. 2.2). It begins at the centroid $\boldsymbol{c}^{\partial S}_{m-1}$ of the $(m-1)$th line element, passes through vertex $\boldsymbol{\rho}^{\partial S}_{m}$, and ends at the centroid $\boldsymbol{c}^{\partial S}_{m}$ of the mth line element. It can be represented, as follows [27]:

$$\boldsymbol{P}_m(\boldsymbol{\rho}) = \begin{cases} \hat{\mathbf{t}}_{m-1}, & \boldsymbol{\rho} \in \left[\boldsymbol{c}^{\partial S}_{m-1}, \boldsymbol{\rho}^{\partial S}_{m}\right], \\ \hat{\mathbf{t}}_{m}, & \boldsymbol{\rho} \in \left[\boldsymbol{\rho}^{\partial S}_{m}, \boldsymbol{c}^{\partial S}_{m}\right]. \end{cases} \tag{2.21}$$

The divergence of the set of the test vector pulse functions is two delta functions [27] defined as

$$\boldsymbol{\nabla} \cdot \boldsymbol{P}_m(\boldsymbol{\rho}) = \delta\left(\boldsymbol{\rho} - \boldsymbol{c}_{m-1}^{\partial S}\right) - \delta\left(\boldsymbol{\rho} - \boldsymbol{c}_{m}^{\partial S}\right). \tag{2.22}$$

Discretization of each of the integral operators (2.7)–(2.12) with the above defined basis and testing functions is presented in the subsections below.

2.2.1 Discretization of the scalar potential surface-to-surface operator $\mathcal{T}_{\epsilon,\nabla\Phi}^{\partial S,\partial S}$

Matrix elements $Z_{\epsilon,\nabla\Phi\, mm''}^{\partial S,\partial S}$ due to MoM discretization of the operator $\mathcal{T}_{\epsilon,\nabla\Phi}^{\partial S,\partial S}$ correspond to the testing of the gradient of the scalar potential produced by $\nabla \cdot \boldsymbol{t}_{m''}$ with test function $\boldsymbol{P}_m$

$$Z_{\epsilon,\nabla\Phi\, mm''}^{\partial S,\partial S} = \left\langle \boldsymbol{P}_m, \mathcal{T}_{\epsilon,\nabla\Phi}^{\partial S,\partial S} \circ \boldsymbol{t}_{m''} \right\rangle = \left\langle \boldsymbol{P}_m, \boldsymbol{\nabla}\mathcal{T}_{\epsilon,\Phi}^{\partial S,\partial S} \circ \boldsymbol{t}_{m''} \right\rangle. \tag{2.23}$$

Subsequently, the div-operator is shifted to the testing function and the 1D divergence theorem mitigating the order of singularity in the pertinent inner product integrals is invoked

$$Z_{\epsilon,\nabla\Phi\, mm''}^{\partial S,\partial S} = -\left\langle \boldsymbol{\nabla} \cdot \boldsymbol{P}_m, \mathcal{T}_{\epsilon,\Phi}^{\partial S,\partial S} \circ \boldsymbol{t}_{m''} \right\rangle = \frac{i\omega\mu_0}{k_\epsilon^2}\Bigg(-\int_0^1 G_\epsilon\left(\boldsymbol{c}_{m-1}^{\partial S}, \boldsymbol{\rho}_{m''-1}^{\partial S}(t'')\right) dt'' + \int_0^1 G_\epsilon\left(\boldsymbol{c}_{m-1}^{\partial S}, \boldsymbol{\rho}_{m''}^{\partial S}(t'')\right) dt'' + \int_0^1 G_\epsilon\left(\boldsymbol{c}_{m}^{\partial S}, \boldsymbol{\rho}_{m''-1}^{\partial S}(t'')\right) dt'' - \int_0^1 G_\epsilon\left(\boldsymbol{c}_{m}^{\partial S}, \boldsymbol{\rho}_{m''}^{\partial S}(t'')\right) dt''\Bigg), \tag{2.24}$$

where $m, m'' = 1, \ldots, M$. The line integrals in (2.24) are computed using 1D quadrature rules after the ln-singularity is extracted from the Green's function G_ϵ. The ln-singular integrals are computed analytically in accord with [74].

2.2.2 Discretization of the vector potential surface-to-surface operator $\boldsymbol{\mathcal{T}}_{\epsilon,A}^{\partial S,\partial S}$

The MoM discretization of the vector potential contribution to the tangential component of the total electric field $\boldsymbol{E}$ on the surface ∂S produced by the unknown weighting function $\boldsymbol{J}$ does not require singularity mitigation. It is composed of four terms corresponding to the interactions of the two test function segments with the two segments of the basis function

$$
\begin{aligned}
Z_{\epsilon,A\,mm''}^{\partial S,\partial S} = \left\langle \boldsymbol{P}_m, \boldsymbol{\mathcal{T}}_{\epsilon,A}^{\partial S,\partial S} \circ \boldsymbol{t}_{m''} \right\rangle = i\omega\mu_0 \Big(\\
\hat{\mathbf{t}}_{m-1} \cdot \hat{\mathbf{t}}_{m''-1} \ell_{m-1} \ell_{m''-1} \int_{0.5}^{1} \int_{0}^{1} t'' G_\epsilon \left(\boldsymbol{\rho}_{m-1}^{\partial S}(t), \boldsymbol{\rho}_{m''-1}^{\partial S}(t'') \right) dt'' dt + \\
\hat{\mathbf{t}}_{m-1} \cdot \hat{\mathbf{t}}_{m''} \ell_{m-1} \ell_{m''} \int_{0.5}^{1} \int_{0}^{1} (1-t'') G_\epsilon \left(\boldsymbol{\rho}_{m-1}^{\partial S}(t), \boldsymbol{\rho}_{m''}^{\partial S}(t'') \right) dt'' dt + \\
\hat{\mathbf{t}}_{m} \cdot \hat{\mathbf{t}}_{m''-1} \ell_{m} \ell_{m''-1} \int_{0}^{0.5} \int_{0}^{1} t'' G_\epsilon \left(\boldsymbol{\rho}_{m}^{\partial S}(t), \boldsymbol{\rho}_{m''-1}^{\partial S}(t'') \right) dt'' dt + \\
\hat{\mathbf{t}}_{m} \cdot \hat{\mathbf{t}}_{m''} \ell_{m} \ell_{m''} \int_{0}^{0.5} \int_{0}^{1} (1-t'') G_\epsilon \left(\boldsymbol{\rho}_{m}^{\partial S}(t), \boldsymbol{\rho}_{m''}^{\partial S}(t'') \right) dt'' dt \Big), \quad (2.25)
\end{aligned}
$$

where $m, m'' = 1, \ldots, M$. In each of the above four integrals the product of a linear function with logarithmic function is extracted from the Green's function G_ϵ and integrated analytically over t'' [74]. The remaining non-singular integrals over t and t'' are computed directly using 1D Gauss-Legendre quadrature rules.

2.2.3 Discretization of the scalar potential surface-to-volume operator $\boldsymbol{\mathcal{T}}_{\epsilon,\nabla\Phi}^{S,\partial S}$

To discretize the contribution of the gradient of the scalar potential to the polarization current $\boldsymbol{j}$ from the divergence of the weighting function $\nabla \cdot \boldsymbol{J}$ represented by the operator $\boldsymbol{\mathcal{T}}_{\epsilon,\nabla\Phi}^{S,\partial S}$,we use pulse functions $p_{n'}(\boldsymbol{\rho}')$, $n' = 1, \ldots, N$, on the triangle elements inside the cross-section as testing functions, where $p_{n'}(\boldsymbol{\rho}')$ is equal to 1, if $\boldsymbol{\rho}' \in S_{n'}$ and to zero otherwise. As the basis functions 1D roof-top functions are used,

yielding

$$\begin{aligned}\boldsymbol{Z}^{S,\partial S}_{\epsilon,\nabla\Phi\, n'm''} &= \left\langle p_{n'}, \boldsymbol{\mathcal{T}}^{S,\partial S}_{\epsilon,\nabla\Phi} \circ \boldsymbol{t}_{m''} \right\rangle \\ &= \frac{i\omega\mu_0}{k_\epsilon^2} \iint_{S_{n'}} \left(\int_0^1 \boldsymbol{\nabla}' G_\epsilon \left(\boldsymbol{\rho}', \boldsymbol{\rho}^{\partial S}_{m''-1}(t'') \right) dt'' \right. \\ &\qquad \left. - \int_0^1 \boldsymbol{\nabla}' G_\epsilon \left(\boldsymbol{\rho}', \boldsymbol{\rho}^{\partial S}_{m''}(t'') \right) dt'' \right) ds',\end{aligned} \tag{2.26}$$

where $n' = 1, \ldots, N$ and $m'' = 1, \ldots, M$. Using 2D gradient theorem [23] for both integrals in (2.26)

$$\iint_{S_{n'}} \boldsymbol{\nabla}' G_\epsilon \left(\boldsymbol{\rho}', \boldsymbol{\rho}'' \right) ds' = - \sum_{i=0}^{2} \hat{\mathbf{m}}_{n',i} \ell_{n',i} \int_0^1 G_\epsilon \left(\boldsymbol{\rho}_{n',i}(t'), \boldsymbol{\rho}'' \right) dt', \tag{2.27}$$

where $\hat{\mathbf{m}}_{n',i}$ is the normal, $\ell_{n',i}$ is the length to the ith edge of the n'th triangle. Hence, $\boldsymbol{Z}^{S,\partial S}_{\epsilon,\nabla\Phi\, n'm''}$ in (2.26) is defined as

$$\begin{aligned}&\boldsymbol{Z}^{S,\partial S}_{\epsilon,\nabla\Phi\, n'm''} \\ &= -\frac{i\omega\mu_0}{k_\epsilon^2} \sum_{i=0}^{2} \hat{\mathbf{m}}_{n',i} \ell_{n',i} \int_0^1 dt' \\ &\qquad \times \left(\int_0^1 G_\epsilon \left(\boldsymbol{\rho}_{n',i}(t'), \boldsymbol{\rho}^{\partial S}_{m''-1}(t'') \right) dt'' \right. \\ &\qquad \left. - \int_0^1 G_\epsilon \left(\boldsymbol{\rho}_{n',i}(t'), \boldsymbol{\rho}^{\partial S}_{m''}(t'') \right) dt'' \right).\end{aligned} \tag{2.28}$$

2.2.4 Discretization of the vector potential surface-to-volume operator $\mathcal{T}^{S,\partial S}_{\epsilon,A}$

The MoM discretization of the weighting function $\boldsymbol{J}$ contribution to the vector potential component of polarization current $\boldsymbol{j}$ determined by the operator $\boldsymbol{\mathcal{T}}^{S,\partial S}_{\epsilon,\nabla\Phi}$ involves inner products

$$\boldsymbol{Z}^{S,\partial S}_{\epsilon,A\, n'm''} = \left\langle p_{n'}, \mathcal{T}^{S,\partial S}_{\epsilon,A} \circ \boldsymbol{t}_{m''} \right\rangle, \tag{2.29}$$

where pulse-functions on the triangles are used as test functions and 1D roof-top functions are used as basis functions, yielding

$$\begin{aligned}\boldsymbol{Z}^{S,\partial S}_{\epsilon,A\,n'm''} = i\omega\mu_0 \quad \times \iint_{S_{n'}} ds' \Bigg(\hat{\mathbf{t}}_{m''-1}\ell_{m''-1} \int_0^1 t'' G_\epsilon\left(\boldsymbol{\rho}', \boldsymbol{\rho}^{\partial S}_{m''-1}(t'')\right) dt'' \\ + \hat{\mathbf{t}}_{m''}\ell_{m''} \int_0^1 (1-t'') G_\epsilon\left(\boldsymbol{\rho}', \boldsymbol{\rho}^{\partial S}_{m''}(t'')\right) dt'' \Bigg),\end{aligned} \tag{2.30}$$

where $n' = 1, \ldots, N$ and $m'' = 1, \ldots, M$. The integrals with the product of a linear function and Green's function are computed similarly with the inner integrals over t'' in (2.25). Namely, the singular part of the integrands corresponding to the linear function product with ln-function is first extracted. Next, the remaining non-singular integrands are computed using 1D Gauss-Legendre quadrature rules.

2.2.5 Discretization of the scalar potential volume-to-surface operator $\boldsymbol{\mathcal{T}}^{\partial S,S}_{0,\nabla\varphi}$

In order to match the discretized range of the $\boldsymbol{\mathcal{T}}^{S,\partial S}_{\epsilon,\nabla\Phi}$ operator with the domain of the $\boldsymbol{\mathcal{T}}^{\partial S,S}_{0,\nabla\varphi}$ operator, which maps the polarization current inside the cross-section S of the scatterer to the tangential scattered electric field on the scatterer's boundary ∂S, we use vector pulse basis functions to expand the polarization current density $\boldsymbol{j}(\boldsymbol{\rho}')$ in the cross-section S

$$\boldsymbol{j}(\boldsymbol{\rho}') \cong \sum_{n'=1}^{N} \boldsymbol{i}_{n'} p_{n'}(\boldsymbol{\rho}') = \sum_{n'=1}^{N} (i^x_{n'}\hat{\mathbf{x}} + i^y_{n'}\hat{\mathbf{y}}) p_{n'}(\boldsymbol{\rho}'), \tag{2.31}$$

where $p_{n'}(\boldsymbol{\rho}')$ is defined as

$$p_{n'}(\boldsymbol{\rho}') = \begin{cases} 1, & \boldsymbol{\rho}' \in S_{n'}, \\ 0, & \boldsymbol{\rho}' \notin S_{n'}, \end{cases} \tag{2.32}$$

$S_{n'}$ being the region inside the n'th triangle. The scattered field is tested with a set of vector pulse test functions $\boldsymbol{P}_m$ similarly with the testing procedure for the

operators $\mathcal{T}^{\partial S,\partial S}_{\epsilon,\nabla\Phi}$ and $\boldsymbol{\mathcal{T}}^{\partial S,\partial S}_{\epsilon,A}$. Therefore,

$$\boldsymbol{Z}^{\partial S,S}_{0,\nabla\varphi\, mn'} = \left\langle \boldsymbol{P}_m, \boldsymbol{\mathcal{T}}^{\partial S,S}_{0,\nabla\varphi} \circ p_{n'} \right\rangle. \tag{2.33}$$

To mitigate the singularity of the integrands, the outer gradient operator is shifted to act on the test function, yielding

$$\begin{aligned} \boldsymbol{Z}^{\partial S,S}_{0,\nabla\varphi\, mn'} &= -\left\langle \boldsymbol{\nabla}\cdot\boldsymbol{P}_m, \boldsymbol{\mathcal{T}}^{\partial S,S}_{0,\varphi} \circ p_{n'} \right\rangle \\ &= -\frac{1}{k_0^2}\left(\iint_{S_{n'}} \boldsymbol{\nabla} G_0\left(\boldsymbol{c}^{\partial S}_{m-1}, \boldsymbol{\rho}^S_{n'}\right) ds' - \iint_{S_{n'}} \boldsymbol{\nabla} G_0\left(\boldsymbol{c}^{\partial S}_{m}, \boldsymbol{\rho}^S_{n'}\right) ds' \right), \end{aligned} \tag{2.34}$$

where $m = 1, \ldots, M$ and $n' = 1, \ldots, N$. The singularity is further mitigated by using 2D gradient theorem [23] taking advantage of the inner gradient operator acting on the Green's function

$$\iint_{S_{n'}} \boldsymbol{\nabla} G_0\left(\boldsymbol{c}^{\partial S}_{m}, \boldsymbol{\rho}^S_{n'}\right) ds' = \; -\sum_{i=0}^{2} \hat{\mathbf{m}}_{n',i}\, \ell^e_{n',i} \int_0^1 G_0\left(\boldsymbol{c}^{\partial S}_{m}, \boldsymbol{\rho}_{n',i}(t')\right) dt', \tag{2.35}$$

where $\ell^e_{n',i}$ is the length of the ith edge of the n'th triangle and $\hat{\mathbf{m}}_{n',i}$ is a normal vector to the ith edge of the n'th triangle defined as

$$\hat{\mathbf{m}}_{n',i} = \frac{\boldsymbol{e}_{n',i} \times \hat{\mathbf{n}}}{|\boldsymbol{e}_{n',i} \times \hat{\mathbf{n}}|}, \tag{2.36}$$

and $\boldsymbol{e}_{n',i}$ is the ith edge of the n'th triangle defined as

$$\boldsymbol{e}_{n',i} = \boldsymbol{\rho}^S_{n',(i+2)\ mod\ 3} - \boldsymbol{\rho}^S_{n',(i+1)\ mod\ 3}, \tag{2.37}$$

where i could be 0, 1, and 2 and *mod* 3 is the *modulo 3* operator. The position vector of the ith edge of the n'th triangle $\boldsymbol{\rho}_{n',i}(t)$ is defined parametrically as

$$\boldsymbol{\rho}_{n',i}(t) = \boldsymbol{\rho}^S_{n',(i+1)\ mod\ 3} + t\, \boldsymbol{e}_{n',i}, \tag{2.38}$$

and $t \in [0,1]$. The above operations provide a definition of the matrix elements $\boldsymbol{Z}^{\partial S,S}_{0,\nabla\varphi\, mn'}$ in the form of integrals featuring ln-singular integrands. These integrals are computed using 1D Gauss-Legendre rule after extracting the ln function. The integral of the 1D elements is computed in closed form according to [74].

2.2.6 Discretization of vector potential volume-to-surface operator $\boldsymbol{\mathcal{T}}^{\partial S,S}_{0,a}$

The MoM discretization of the operator $\boldsymbol{\mathcal{T}}^{\partial S,S}_{0,a}$ mapping volume polarization current $\boldsymbol{j}$ onto the vector potential contribution of the scattered electric field is done with piece-wise basis functions (2.32) on the triangle elements of the volume S expanding the volume current $\boldsymbol{j}$ and the vector pulse test functions (2.21) testing the vector potential as

$$\begin{aligned}\boldsymbol{Z}^{\partial S,S}_{0,a\, mn'} &= \left\langle \boldsymbol{P}_m, \boldsymbol{\mathcal{T}}^{\partial S,S}_{0,a} \circ p_{n'} \right\rangle \\ &= \left(\hat{\mathbf{t}}_{m-1}\ell_{m-1} \int_{0.5}^{1}\int_{0}^{1}\int_{0}^{1-\xi'} G_0\left(\boldsymbol{\rho}^{\partial S}_{m-1}(t), \boldsymbol{\rho}^{S}_{n'}(\xi',\eta')\right) d\eta' d\xi' dt \right. \\ &\left. + \hat{\mathbf{t}}_{m}\ell_{m} \int_{0}^{0.5}\int_{0}^{1}\int_{0}^{1-\xi'} G_0\left(\boldsymbol{\rho}^{\partial S}_{m}(t), \boldsymbol{\rho}^{S}_{n'}(\xi',\eta')\right) d\eta' d\xi' dt \right) 2A_{n'},\end{aligned} \tag{2.39}$$

where $m = 1,\ldots,M$; $n' = 1,\ldots,N$ and $A_{n'}$ is the area of the n'th triangle which is defined as $A_{n'} = \frac{1}{2}\left|(\boldsymbol{\rho}^{S}_{n'(1)} - \boldsymbol{\rho}^{S}_{n'(0)}) \times (\boldsymbol{\rho}^{S}_{n'(2)} - \boldsymbol{\rho}^{S}_{n'(0)})\right|$. The 2D integrals over ξ' and η' in (2.39) are evaluated using 2D quadrature rules after ln-singular part is subtracted from Green's function G_0 and integrated analytically according to [74]. The test integrals over t are computed using 1D Gauss-Legendre quadrature rules.

2.2.7 Discretization of the incident field $\boldsymbol{E}^{\text{inc}}$

The discretization of the incident field is done through the definition of the inner products of the incident field with the vector pulse test functions (2.21)

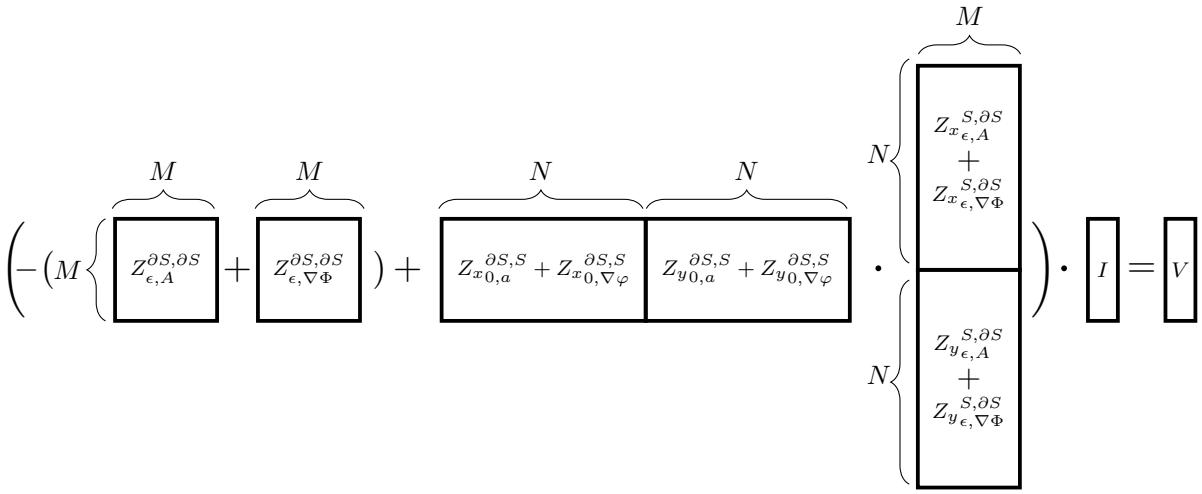

Figure 2.3: Structure of the system of linear algebraic equations (2.42) resulting from MoM discretization of the SVS-EFIE (2.5). The number of line elements on the boundary ∂S is M, and N is the number of triangle cells in cross-section S.

$$V_m \;=\; \left\langle \boldsymbol{P}_m, \boldsymbol{E}^{\text{inc}} \right\rangle \;=\; \ell_{m-1} \int_{0.5}^{1} \hat{\mathbf{t}}_{m-1} \cdot \boldsymbol{E}^{\text{inc}}(\boldsymbol{\rho}) dt \;+\; \ell_m \int_{0}^{0.5} \hat{\mathbf{t}}_{m} \cdot \boldsymbol{E}^{\text{inc}}(\boldsymbol{\rho}) dt, \quad (2.40)$$

where $m = 1, \ldots, M$. The integrals in (2.40) are non-singular and computed to desired precision using 1D Gauss-Legendre quadrature rules.

2.2.8 Resultant MoM matrix assembly

The MoM discretization of the SVS-EFIE reduces it to the following set of linear algebraic equations with respect to the $(M \times 1)$ vector of unknown scalar coefficients I in the expansion of the unknown surface weighting function (2.19)

$$-\left(\left[\ Z_{\epsilon,A}^{\partial S,\partial S}\ \right]+\left[\ Z_{\epsilon,\nabla\Phi}^{\partial S,\partial S}\ \right]\right)\cdot\left[\ I\ \right]+\left(\left(\left[\ \boldsymbol{Z}_{0,a}^{\partial S,S}\ \right]+\left[\ \boldsymbol{Z}_{0,\nabla\varphi}^{\partial S,S}\ \right]\right)\odot\left(\left[\ \boldsymbol{Z}_{\epsilon,A}^{S,\partial S}\ \right]+\left[\ \boldsymbol{Z}_{\epsilon,\nabla\Phi}^{S,\partial S}\ \right]\right)\right)\cdot\left[\ I\ \right]=\left[\ V\ \right]. \tag{2.41}$$

where $\odot$ is dot product of two matrices composed of vector quantities. In the expanded form, the structure of the MoM matrix equation is given by the following expression and is depicted in Fig. 2.3

$$\begin{aligned}-(\left[\ Z_{\epsilon,A}^{\partial S,\partial S}\ \right]+\left[\ Z_{\epsilon,\nabla\Phi}^{\partial S,\partial S}\ \right])\cdot\left[\ I\ \right]+\\ \Big((\left[\ Z_{x0,a}^{\ \partial S,S}\ \right]+\left[\ Z_{x0,\nabla\varphi}^{\ \partial S,S}\ \right])\cdot(\left[\ Z_{x\epsilon,A}^{\ S,\partial S}\ \right]+\left[\ Z_{x\epsilon,\nabla\Phi}^{\ S,\partial S}\ \right])+\\ (\left[\ Z_{y0,a}^{\ \partial S,S}\ \right]+\left[\ Z_{y0,\nabla\varphi}^{\ \partial S,S}\ \right])\cdot(\left[\ Z_{y\epsilon,A}^{\ S,\partial S}\ \right]+\left[\ Z_{y\epsilon,\nabla\Phi}^{\ S,\partial S}\ \right])\Big)\\ \cdot\left[\ I\ \right]=\left[\ V\ \right].\end{aligned} \tag{2.42}$$

The above system of linear algebraic equations (SLAE) with M unknowns can be written in the compact form as $[Z]\cdot[I]=[V]$ with respect to the unknown coefficients $I_1,\ldots,I_M$ in the expansion (2.19) of the sought weighting function $\boldsymbol{J}$.

2.2.9 Computation of electric field inside the scatterer

After solving the system of linear algebraic equations (2.42) for the expansion coefficients $[I]$ in the expansion of weighting function $\boldsymbol{J}$ on ∂S, the electric field $\boldsymbol{E}$ and volume polarization current $\boldsymbol{j}$ in the scatterer volume S can be computed as a superposition of the waves emanating from the boundary ∂S according to (2.2). The MoM matrices $\left[\boldsymbol{Z}_{\epsilon,A}^{S,\partial S}\right]$ and $\left[\boldsymbol{Z}_{\epsilon,\nabla\Phi}^{S,\partial S}\right]$ can be used to compute the electric field $\boldsymbol{E}$ at the centers of the triangle elements in the volume of the scatterer $\boldsymbol{c}_{n'}^{S}$, $n'=1,\ldots,N$, as follows:

$$\left[\boldsymbol{E}(\boldsymbol{c}_{n'}^{S})\right] = -\left(\left[\begin{array}{c} \boldsymbol{Z}_{\epsilon,A}^{S,\partial S} \end{array} \right] + \left[\begin{array}{c} \boldsymbol{Z}_{\epsilon,\nabla\Phi}^{S,\partial S} \end{array} \right] \right) \cdot \left[\begin{array}{c} I \end{array} \right]. \tag{2.43}$$

2.2.10 Computation of electric field outside the scatterer

The total electric field outside the scatterer is computed as $\boldsymbol{E}(\boldsymbol{\rho}) = \boldsymbol{E}^{\text{inc}}(\boldsymbol{\rho}) + \boldsymbol{E}^{\text{scat}}(\boldsymbol{\rho})$, where scattered field is defined by the polarization current in the volume of the scatterer as

$$\boldsymbol{E}^{\text{scat}}(\boldsymbol{\rho}) = k_0^2\,(\epsilon - 1) \iint\limits_{S} \overline{\overline{G}}_{e0}(\boldsymbol{\rho}, \boldsymbol{\rho}') \cdot \boldsymbol{E}(\boldsymbol{\rho}')ds'. \tag{2.44}$$

With the discretized total electric field $\boldsymbol{E}(\boldsymbol{c}_{n'}^{S})$ available at the centroids of triangle elements $\boldsymbol{c}_{n'}^{S}$ in the volume of the scatterer S from (2.43), we compute the scattered field outside S, as follows:

$$\begin{aligned} \boldsymbol{E}^{\text{scat}}(\boldsymbol{\rho}) = k_0^2\,(\epsilon - 1) \sum_{n'=1}^{N} \boldsymbol{E}(\boldsymbol{c}_{n'}^{S}) \iint_{S_{n'}} G_0(\boldsymbol{\rho}, \boldsymbol{\rho}'_{S_{n'}})ds' \\ - (\epsilon - 1) \sum_{n'=1}^{N} \boldsymbol{E}(\boldsymbol{c}_{n'}^{S}) \boldsymbol{\nabla} \iint_{S_{n'}} \boldsymbol{\nabla}' G_0(\boldsymbol{\rho}, \boldsymbol{\rho}'_{S_{n'}})ds'. \end{aligned} \tag{2.45}$$

The first term in (2.45) corresponding to the vector potential contribution into the total electric field is computed using 2D Gauss quadrature rule after the logarithmic singularity is extracted from the Green's function G_0 and the integral $\iint\limits_{S_{n'}} \ln|\boldsymbol{\rho} - \boldsymbol{\rho}'|ds'$ over the area of each triangle is computed analytically according to [74].

The contribution of the gradient of the scalar potential into the total field from each triangle defined by the second term in (2.45) is first reduced using gradient theorem [23] to three line integrals over the edges of the triangles as in (2.35). Subsequently, the line integrals from logarithmic part of the Green's function over the edges of triangle elements $\iint\limits_{\partial S_{n'}} \ln|\boldsymbol{\rho} - \boldsymbol{\rho}'|d\ell'$ are evaluated in closed analytic form according to [74]. The gradient over the observation point of this integral, i.e. $\nabla \iint\limits_{\partial S_{n'}} \ln|\boldsymbol{\rho} - \boldsymbol{\rho}'|d\ell'$, can be subsequently evaluated analytically as well. Extraction of the singular integral

from the second term in (2.45) allows for evaluation of the remaining part using 1D Gauss-Legendre quadrature rules.

2.2.11 Validation of the representation of the total electric field inside the scatterer (2.16)

The simplified SVS-EFIE (2.16) for the case of the free space, i.e. $\epsilon = 1$ in the volume S, can be solved using MoM. To find $\boldsymbol{J}$ numerically the following MoM discretization of simplified SVS-EFIE (2.16) can be used

$$-\left(\left[\; Z_{\epsilon,A}^{\partial S,\partial S} \; \right] + \left[\; Z_{\epsilon,\nabla\Phi}^{\partial S,\partial S} \; \right] \right) \cdot \left[\; I \; \right] = \left[\; V \; \right]. \tag{2.46}$$

Finding discretization coefficients $[I]$ of $\boldsymbol{J}$ and substituting them into discretized form (2.43) of (2.2) produces arbitrary incident field in S at the centers of triangle elements. Numerical reconstruction of electric dipole field in a given volume using (2.46) was demonstrated in Fig. 2.1 and discussed in subsection 2.1.

2.3 Numerical Results

We use GMESH [83] to create our geometries and generate 1D and 2D meshes. Numerical implementation of the MoM solution of the proposed SVS-EFIE has been done using PTC Mathcad [81] tool. All post-process visualizations are performed using Mathlab [85]. To validate the proposed new SSIE we conducted various numerical experiments and compared solutions of the scattering problems obtained using the new SVS-EFIE equation and alternative methods such as analytic Mie series representation and FEM implemented in the commercial software COMSOL [34].

2.3.1 Scattering by circular cylinder

In the first example, we consider the problem of TE-polarized plane wave scattering on a circular dielectric cylinder with cross section radius $R = 0.1\,\mathrm{m}$ and dielectric permittivity $\epsilon = 2$. The cylinder is illuminated by the plane wave incoming

from $\phi = 180$ direction with magnetic field defined as $H_z^{\text{inc}}(\boldsymbol{\rho}) = 1/\eta_0 e^{-i\boldsymbol{k}\cdot\boldsymbol{\rho}}$ [A/m], where $\boldsymbol{k}$ is $k_0\hat{\mathbf{k}}$, $\hat{\mathbf{k}}$ is unit vector in propagation direction $(-cos(\phi)\hat{\mathbf{x}} - sin(\phi)\hat{\mathbf{y}})$, and η_0 is intrinsic impedance of free space. The numerical solution of the scattering problem obtained at 1.5 GHz using the proposed new SVS-EFIE (2.5) is shown in Fig. 2.4. For comparison in the same Fig. 2.4 the solution obtained using analytic Mie series expansion is shown also as well as the relative error between the two solutions. The MoM discretization of the SVS-EFIE involved $M = 64$ line elements discretizing the boundary of the cylinder and $N = 868$ triangle elements discretizing its cross-section. The cross-sectional discretization corresponds to the sampling of the electric field inside the cylinder at approximately 28 elements per wavelength rate. The field inside the cylinder is computed using superposition expression (2.2) after the weighting function $\boldsymbol{J}$ expansion coefficients $[I]$ in (2.19) were obtained from solution of SLAE (2.42). Upon availability of the field distribution in the cross-section of the cylinder the scattered field outside the cylinder was computed using expression (2.45) and added to the incident field. The MoM solution of the SVS-EFIE is seen to match closely with the analytic Mie series solution in accord with the error levels expected from the used discretization density.

In order to demonstrate the behavior of error in the MoM solution of the proposed SVS-EFIE as the density of the discretization per wavelength increases, we next consider the scattering problem on the same circular dielectric cylinder but at the frequency of 300 MHz (Fig. 2.5).

The density of the MoM meshes discretizing the boundary of the scatterer and its volume remained the same as in the previous example, i.e. $M = 64$, $N = 868$, signifying about 140 elements per wavelength discretization rate of the electric field in the cross-section. The Mie series solution and the relative error of the MoM discretization of the proposed SVS-EFIE are shown in the same Fig. 2.5. Substantially increased accuracy in the computed field is observed for the increased MoM sampling rate per wavelength, thus, corroborating the rigorous nature of the proposed new SSIE. The radial component D_ρ of the electric flux $\boldsymbol{D} = \epsilon\epsilon_0\boldsymbol{E}$ inside and outside the cylinder is shown in Fig. 2.6. The ϕ-component of the electric field E_ϕ inside and outside the

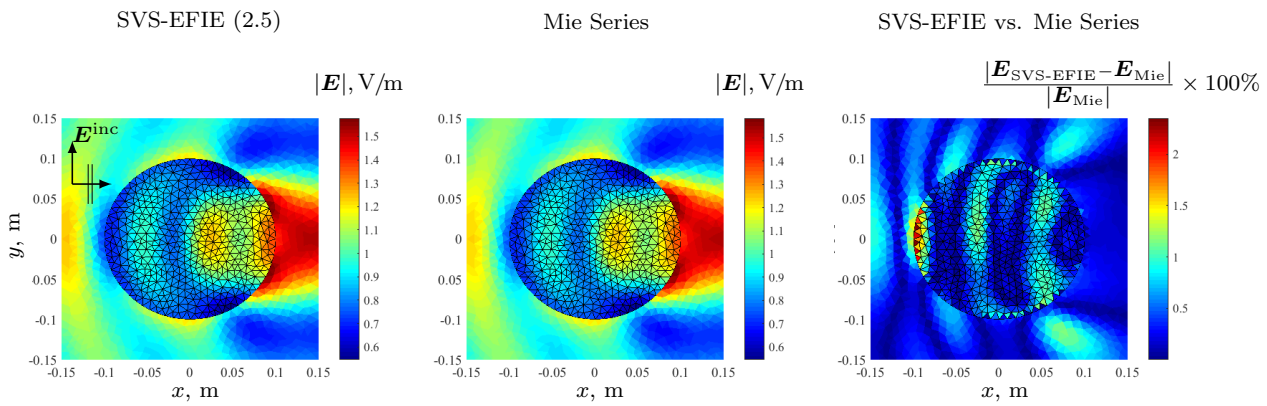

Figure 2.4: Distribution of magnitude of total electric field inside and outside of the dielectric cylinder of radius $R = 0.1$ m and relative permittivity $\epsilon = 2$ in the problem of TE-polarized plane wave scattering at 1.5 GHz. The left sub-figure shows field inside the cylinder obtained using (2.2) after the unknown weighting function $\boldsymbol{J}$ was computed via MoM discretization (2.42) of the SVS-EFIE (2.5) with $M = 64$ elements and $N = 868$ triangle elements. In the same left sub-figure, the total field outside the cylinder computed using the volume equivalence principle (1.37) and (2.45) from the computed volume polarization current $\boldsymbol{j}$ is shown. The analytic Mie series solution for the fields inside and outside the scatterer are shown in center sub-figure. The relative error in the magnitude of the electric field between the SVS-EFIE and Mie series solution is depicted in the right sub-figure.

cylinder is shown in Fig. 2.7. These two figures show that the boundary conditions of the electric field, the tangential component of the electric field and normal component of the electric flux computed, are satisfied via the proposed MoM solution of the SVS-EFIE on the interface between two different media. This can be seen from the plots of error (right sub-figure in Fig. 2.6 and Fig. 2.7) in the SVS-EFIE solution compared to the analytic Mie series solution both inside and outside the cylinder. Indeed, the Mie series analytic solution establishes the continuity of D_ρ and E_ϕ field components. The MoM solution of the SVS-EFIE providing relative error compared to Mie series at 2-3% level demonstrates that the field continuity conditions at the boundary are properly satisfied. Note, that the continuity of the field components at the boundary of the scatterer in SVS-EFIE is established implicitly through the use of the volume equivalence principle (see Appendix 3 for detailed derivations). The computed E- and D-fields obtained from MoM discretization of the SVS-EFIE

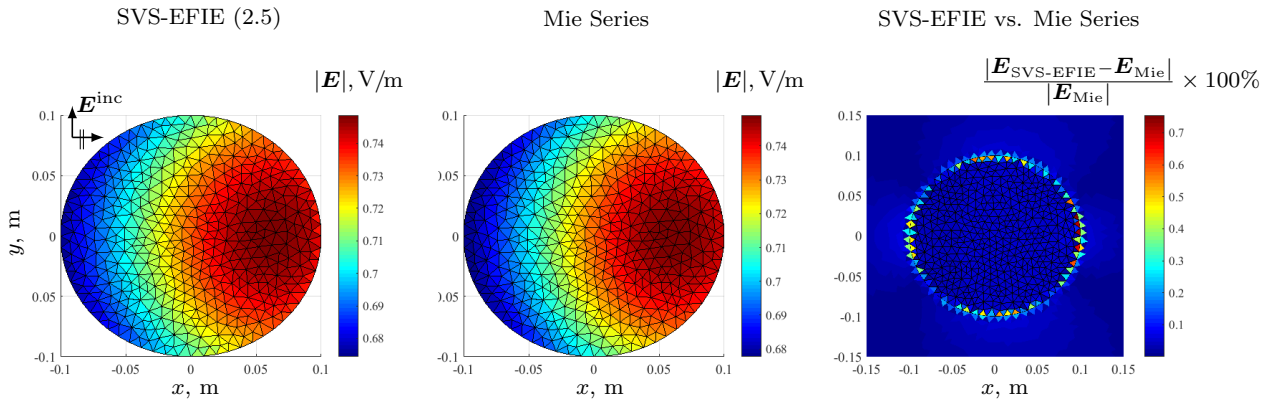

Figure 2.5: Distribution of magnitude of total electric field inside the circular dielectric cylinder of radius $R = 0.1m$ in problem of TE-wave scattering with relative permittivity $\epsilon = 2$ at 300 MHz computed with the 64 of line and 868 triangle elements (same MoM discretization as for the scattering problem in Fig. 2.4). The MoM solution of SVS-EFIE is shown in the left sub-plot. The Mie series solution is shown in the center sub-plot. The relative error in the magnitude of the MoM solution of SVS-EFIE inside and outside of the cylinder is depicted in the right sub-plot.

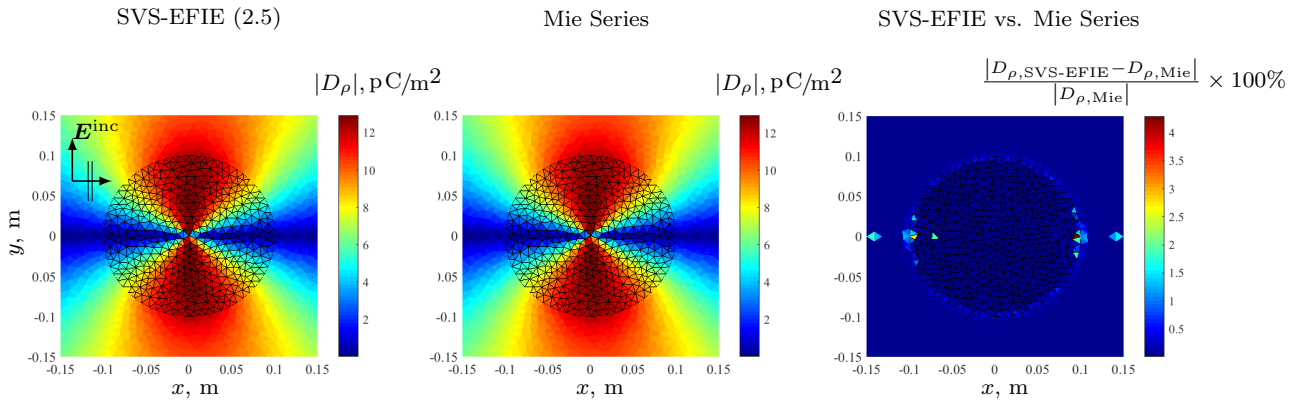

Figure 2.6: Distribution of magnitude of D_ρ component of the electric flux inside and outside of the circular dielectric cylinder with permittivity $\epsilon = 2$ computed via MoM discretization of the SVS-EFIE (left plot) and Mie series solution (center plot). The relative error of the MoM solution is shown in the right sub-plot. Frequency of the incident plane wave is 300 MHz.

demonstrate this effect numerically.

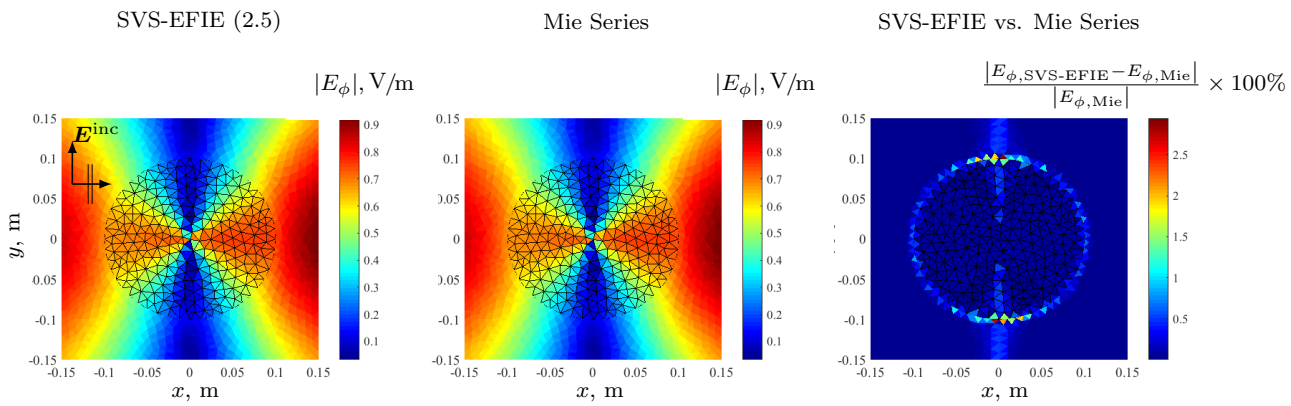

Figure 2.7: Distribution of magnitude of E_ϕ component of the electric field inside and outside of the circular dielectric cylinder with permittivity $\epsilon = 2$ obtained using MoM discretization of the SVS-EFIE (left plot) and Mie series solution (center plot). The relative error of the MoM solution is shown in the right sub-plot. Frequency of incident plane wave is 300 MHz.

2.3.2 Scattering by cylinder of square cross-section

The MoM solution of the SVS-EFIE for a scattering problem on an object featuring sharp corners is depicted in Fig. 2.8. In this example a 300 MHz TE-polarized plane wave is scattered on a dielectric rod of square cross-section with the side length of 0.3 m and relative permittivity $\epsilon = 2$. The MoM discretization of the SVS-EFIE features 128 line elements ($M = 128$) and 256 triangle elements ($N = 256$). In order to validate the MoM solution of the new SVS-EFIE an FEM solution for the same scattering problem is obtained in the COMSOL commercial software [34]. The domain truncation in the FEM requires that the free-space volume outside the scatterer is included in the discretization. In the example under consideration the computational domain is a square with side length of 3.69 m. The outer boundary of the computational domain is set to enforce the absorbing boundary condition (a.k.a the *scattering boundary condition* in the COMSOL software). The magnitude of the electric field inside and outside the scatterer are depicted in Fig. 2.8 for the case of MoM discretization of SVS-EFIE and FEM solution of the COMSOL commercial software. The high-precision FEM solution featuring finite 2D elements with maximum element size 0.007m was obtained with the requested relative error in the field computations

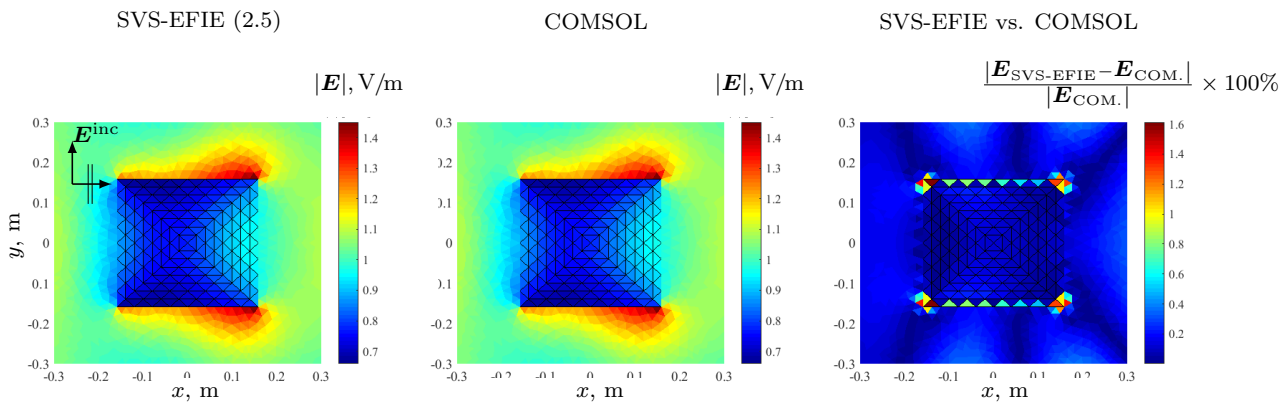

Figure 2.8: Distribution of magnitude of electric field in the square dielectric cylinder obtained from SVS-EFIE (left plot) and COMSOL (center plot). The relative error in SVS-EFIE solution with respect to the COMSOL solution is depicted in right plot. The frequency of incident TE plane wave is 300 MHz.

not exceeding 0.001. The relative error in the MoM solution of the SVS-EFIE compared against the FEM solution is shown in the same Fig. 2.8. The low relative error of the computed fields corroborates that the proposed new SSIE is rigorous in nature.

The MoM solution of the SVS-EFIE for a scattering problem on an object featuring sharp corners in a high frequency field is depicted in Fig. 2.9. In this example, a 1.5 GHz TE-polarized plane wave is scattered on the same dielectric cylinder of square cross-section. The MoM discretization of the SVS-EFIE features 512 line elements ($M = 512$) discretizing the boundary of the scatterer and 1024 triangle elements ($N = 1024$) discretizing its cross section. The parameters of the FEM simulation are set up to be the same as the case of the scattering at 300 MHz. In both 300 MHz and 1.5 GHz scattering problems high-precision FEM solution with relative error in the field computations not exceeding 0.001 was requested.

2.3.3 Behavior of the MoM solution with varying permittivity and discretization density

To demonstrate the behavior of the MoM error in the discretized SVS-EFIE solution with the increased values of the relative permittivity ϵ, we considered the same

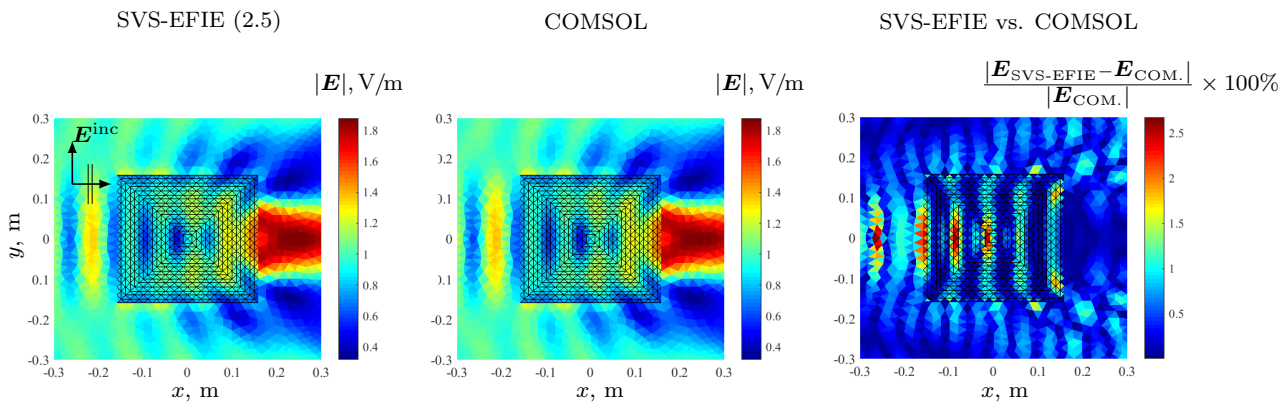

Figure 2.9: Distribution of magnitude of electric field in the square dielectric cylinder obtained from SVS-EFIE (left plot) and COMSOL (center plot). The relative error in SVS-EFIE solution with respect to the COMSOL solution is shown in right plot. The frequency of incident TE plane wave is 1.5 GHz.

case of TE-polarized plane wave scattering on the circular cylinder under a fixed MoM discretization with $M = 128$ and $N = 224$ at 300 MHz. The behavior of average relative error (δ) and its standard deviation (σ) is depicted as a function of relative permittivity ϵ in Table. 2.1. The error increase is due to the reduced electrical sampling rate. The equation was also tested to remain stable at high values of permittivity.

To show error controllability in the MoM solution of the new SVS-EFIE equation, we depict the error behaviour as a function of the cross-sectional mesh density while the contour mesh is fixed (Fig. 2.10(a)) and as a function of the contour mesh density while cross-sectional mesh is fixed (Fig. 2.10(b)). The error in the solution of the SVS-EFIE for the problem of plane wave scattering on a circular cylinder of relative permittivity $\epsilon = 2$ at 300 MHz is seen to consistently reduce upon refinement of the surface and volume mesh densities (Fig. 2.10) to some level dictated by the fixed mesh density. When contour mesh is refined and cross-sectional mesh is fixed, the error can drop only to some level dictated by the fixed cross-sectional mesh. Similar effect takes place in the case of cross-sectional mesh being refined and contour mesh being fixed. Two-dimensional error behaviour here is similar to that in scalar form of the SVS-EFIE [75]. That is, if both the contour and cross-sectional meshes are increased in

Table 2.1: The average relative error δ and its standard deviation σ of the MoM solution of the SVS-EFIE (2.5) with respect to the Mie series solution for TE-polarized plane wave scattering on a circular dielectric cylinder of radius R =0.1 m and relative dielectric permittivity ϵ at 300 MHz.

ϵ	δ	σ
1.5	0.0009	0.0004
4	0.0031	0.0019
8	0.0032	0.0029
12	0.006	0.0037

density, the error consistently reduces. When contour line elements coincide with the edges of the cross-sectional triangular mesh the error is observed to get particularly low.

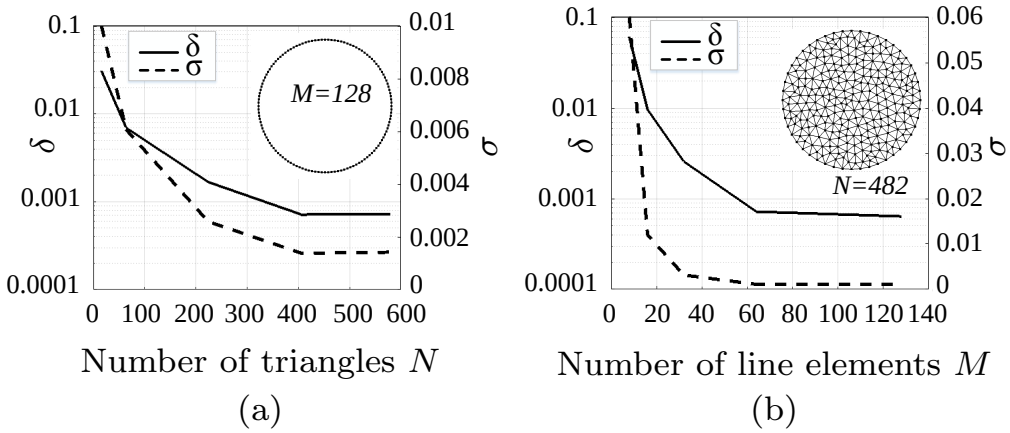

Figure 2.10: Mean relative error δ and its standard deviation σ in the MoM solution of the novel V-SVS-EFIE (2.5) with respect to the Mie series solution for plane wave scattering on a circular dielectric cylinder of radius $R = 0.1\,\mathrm{m}$ with relative permittivity $\epsilon = 2$ at 300 MHz as a function of number of triangles N (a) in the cross-section and number of line elements M (b) on the boundary.

3

Novel Single-Source Surface Integral Equation for Scattering Problems by 3D Dielectric Objects

3.1 SVS-EFIE Formulation in 3D

In this chapter the SVS-EFIE for solution of the general 3D full-wave scattering problems on homogeneous non-magnetic dielectric scatterers is described. Consider the volume equivalence principle [27] written for the time-harmonic electric field $\boldsymbol{E}$ with the cyclic frequency ω on a homogeneous dielectric object of volume V (Fig. 3.1). The time convention $e^{i\omega \mathtt{t}}$ is assumed and suppressed throughout the derivation, $\mathtt{t}$ being time variable and $i = \sqrt{-1}$. The incident electric field is $\boldsymbol{E}^{\text{inc}} = E_x^{\text{inc}}\hat{\mathbf{x}} + E_y^{\text{inc}}\hat{\mathbf{y}} + E_z^{\text{inc}}\hat{\mathbf{z}}$. The classic V-EFIE is written as [27]:

$$\boldsymbol{E}(\boldsymbol{r}) - k_0^2\,(\epsilon - 1)\int\limits_V \overline{\overline{G}}_0(\boldsymbol{r},\boldsymbol{r}')\ \cdot\ \boldsymbol{E}(\boldsymbol{r}')dv' = \boldsymbol{E}^{\text{inc}}(\boldsymbol{r}), \tag{3.1}$$

where $\boldsymbol{r}$ is an arbitrary observation location in space, $\boldsymbol{r}'$ is the position-vector of the total electric field inside the scatterer, and complex relative permittivity $\epsilon = \varepsilon + \sigma/(i\omega\varepsilon_0)$, and $\overline{\overline{G}}_0(\boldsymbol{r}, \boldsymbol{r}')$ is the free space dyadic Green's function defined as

$$\overline{\overline{G}}_0(\boldsymbol{r}, \boldsymbol{r}') = \Big(\frac{\boldsymbol{\nabla}\boldsymbol{\nabla}}{k_0^2} + \overline{\overline{I}}\Big) G_0(\boldsymbol{r}, \boldsymbol{r}'). \tag{3.2}$$

In (3.2), $G_0(\boldsymbol{r}, \boldsymbol{r}') = \frac{e^{-ik_0|\boldsymbol{r}-\boldsymbol{r}'|}}{4\pi|\boldsymbol{r}-\boldsymbol{r}'|}$ is the 3D Green's function of free space, k_0 is the wave number in free space, $\boldsymbol{r}$ and $\boldsymbol{r}'$ are position vectors of the observation and source points, respectively, $\overline{\overline{I}}$ is the idem-factor. The total electric field inside the scatterer satisfies the homogeneous wave equation

$$\boldsymbol{\nabla} \times \boldsymbol{\nabla} \times \boldsymbol{E}(\boldsymbol{r}') - k_\epsilon^2 \boldsymbol{E}(\boldsymbol{r}') = \boldsymbol{0}, \boldsymbol{r}' \in V \setminus \partial V. \tag{3.3}$$

The total electric field inside the scatterer can be written as a superposition of the elementary waves $\overline{\overline{G}}_{e\epsilon}(\boldsymbol{r}, \boldsymbol{r}')$ emanating from the scatterer's boundary ∂V as

$$\boldsymbol{E}(\boldsymbol{r}') = -i\omega\mu_0 \oint_{\partial V} \overline{\overline{G}}_\epsilon(\boldsymbol{r}', \boldsymbol{r}'') \cdot \boldsymbol{J}(\boldsymbol{r}'')\, ds'', \tag{3.4}$$

where tangential vector function $\boldsymbol{J}(\boldsymbol{r}'')$ defined on the surface ∂V plays the role of the weights for the waves $\overline{\overline{G}}_\epsilon$. The elementary waves $\overline{\overline{G}}_\epsilon(\boldsymbol{r}', \boldsymbol{r}'')$ are represented by the dyadic Green's function of the medium

$$\overline{\overline{G}}_\epsilon(\boldsymbol{r}', \boldsymbol{r}'') = \left(\frac{\boldsymbol{\nabla}'\boldsymbol{\nabla}'}{k_\epsilon^2} + \overline{\overline{I}}\right) G_\epsilon(\boldsymbol{r}', \boldsymbol{r}''), \tag{3.5}$$

and produce by point sources and satisfy the same homogeneous wave equation

$$\boldsymbol{\nabla} \times \boldsymbol{\nabla} \times \overline{\overline{G}}_\epsilon - k_\epsilon^2 \overline{\overline{G}}_\epsilon = \overline{\overline{0}}, \tag{3.6}$$

as the total field $\boldsymbol{E}$ everywhere inside the scatterer body V excluding the points situated on its boundary ∂V, thus forcing $\boldsymbol{E}$ to satisfy (3.3).

In (3.5), $G_\epsilon(\boldsymbol{r}', \boldsymbol{r}'') = \frac{e^{-ik_\epsilon|\boldsymbol{r}'-\boldsymbol{r}''|}}{4\pi|\boldsymbol{r}'-\boldsymbol{r}''|}$ is the Green's function of the dielectric media

with the wave number $k_\epsilon = \sqrt{\epsilon} k_0$ and satisfying $\nabla^2 G_\epsilon + k_\epsilon^2 G_\epsilon = 0$. Substitution of (3.2), (3.4) and (3.5) into (3.1) followed by restriction of the observation domain to the boundary of the scatterer yield the desired SVS-EFIE with respect to the unknown auxiliary current density $\boldsymbol{J}$. Since $\boldsymbol{J}$ is assumed to be tangential vector function defined on the boundary ∂V, to balance the range and domain of the resulting operators the V-EFIE has to be satisfied only for tangential component of total electric field at the boundary ∂V. This yields the proposed SVS-EFIE

$$\begin{aligned} -i\omega\mu_0 \hat{\mathbf{t}} \cdot \oint_{\partial V} \overline{\overline{G}}_\epsilon(\boldsymbol{r}, \boldsymbol{r}'') \cdot \boldsymbol{J}(\boldsymbol{r}'') ds'' + i\omega\mu_0 k_0^2 (\epsilon - 1) \hat{\mathbf{t}} \\ \cdot \int_V \overline{\overline{G}}_0(\boldsymbol{r}, \boldsymbol{r}') \cdot \oint_{\partial V} \overline{\overline{G}}_\epsilon(\boldsymbol{r}', \boldsymbol{r}'') \cdot \boldsymbol{J}(\boldsymbol{r}'') ds'' dv' \\ = \hat{\mathbf{t}} \cdot \boldsymbol{E}^{\text{inc}}(\boldsymbol{r}), \quad \boldsymbol{r} \in \partial V, \end{aligned} \tag{3.7}$$

where $\hat{\boldsymbol{t}}$ is the tangential vector to the boundary ∂V.

It is important to emphasize that the integral field representations (3.4) is different from the standard equivalence principle, as shown in [75]. The proposed formulation uses only one unknown $\boldsymbol{J}(\boldsymbol{r}'')$, called a single layer ansatz [73]. It is convenient to express the SVS-EFIE in the following operator form

$$-\overline{\overline{\mathcal{T}}}_\epsilon^{\partial V, \partial V} \circ \boldsymbol{J} + \overline{\overline{\mathcal{T}}}_0^{\partial V, V} \circ \overline{\overline{\mathcal{T}}}_\epsilon^{V, \partial V} \circ \boldsymbol{J} = \hat{\mathbf{t}} \cdot \boldsymbol{E}^{inc}(\boldsymbol{r}) \tag{3.8}$$

In (3.8) each dyadic integral operators is a sum of two integral operators, one corresponding to the scalar potential contribution and one for the vector potential contri-

bution. These operators are defined as follows:

$$\mathcal{T}^{\partial V,\partial V}_{\epsilon,\Phi} \circ \boldsymbol{J} = \frac{i\omega\mu_0}{k_\epsilon^2} \oint_{\partial V} G_\epsilon(\boldsymbol{r},\boldsymbol{r}'')\boldsymbol{\nabla}''_{\mathrm{s}} \cdot \boldsymbol{J}(\boldsymbol{r}'')ds'', \tag{3.9}$$

$$\boldsymbol{\mathcal{T}}^{\partial V,\partial V}_{\epsilon,A} \circ \boldsymbol{J} = i\omega\mu_0\hat{\mathbf{t}} \cdot \oint_{\partial V} G_\epsilon(\boldsymbol{r},\boldsymbol{r}'')\boldsymbol{J}(\boldsymbol{r}'')ds'', \tag{3.10}$$

$$\boldsymbol{\mathcal{T}}^{V,\partial V}_{\epsilon,\nabla\Phi} \circ \boldsymbol{J} = \frac{i\omega\mu_0}{k_\epsilon^2} \oint_{\partial V} \boldsymbol{\nabla}' G_\epsilon(\boldsymbol{r}',\boldsymbol{r}'')\boldsymbol{\nabla}''_{\mathrm{s}} \cdot \boldsymbol{J}(\boldsymbol{r}'')ds'', \tag{3.11}$$

$$\mathcal{T}^{V,\partial V}_{\epsilon,A} \circ \boldsymbol{J} = i\omega\mu_0 \oint_{\partial V} G_\epsilon(\boldsymbol{r}',\boldsymbol{r}'')\boldsymbol{J}(\boldsymbol{r}'')ds'', \tag{3.12}$$

$$\boldsymbol{\mathcal{T}}^{\partial V,V}_{0,\varphi} \circ \boldsymbol{j} = \frac{1}{k_0^2} \int_V \boldsymbol{\nabla} G_0(\boldsymbol{r},\boldsymbol{r}') \cdot \boldsymbol{j}(\boldsymbol{r}')dv', \tag{3.13}$$

$$\boldsymbol{\mathcal{T}}^{\partial V,V}_{0,a} \circ \boldsymbol{j} = \hat{\mathbf{t}} \cdot \int_V G_0(\boldsymbol{r},\boldsymbol{r}')\boldsymbol{j}(\boldsymbol{r}')dv', \tag{3.14}$$

$$\boldsymbol{r} \in \partial V, \quad \boldsymbol{r}' \in V.$$

In (3.13) and (3.14), $\boldsymbol{j}$ is polarization current density, which is defined inside the scatterer as $\boldsymbol{j} = k_0^2(\epsilon - 1)\boldsymbol{E}$ and $\boldsymbol{\nabla}_{\mathrm{s}}\cdot$ denotes surface divergence. With integral operator notations (3.9)–(3.14), the SVS-EFIE (3.8) is written as

$$-\left(\mathcal{T}^{\partial V,\partial V}_{\epsilon,\nabla\Phi} + \boldsymbol{\mathcal{T}}^{\partial V,\partial V}_{\epsilon,A}\right) \circ \boldsymbol{J} + \left(\boldsymbol{\mathcal{T}}^{\partial V,V}_{0,\nabla\varphi} + \boldsymbol{\mathcal{T}}^{\partial V,V}_{0,a}\right) \circ \left(\boldsymbol{\mathcal{T}}^{V,\partial V}_{\epsilon,\nabla\Phi} + \mathcal{T}^{V,\partial V}_{\epsilon,A}\right) \circ \boldsymbol{J} = \hat{\mathbf{t}} \cdot \boldsymbol{E}^{\mathrm{inc}}, \tag{3.15}$$

where $\mathcal{T}^{\partial V,\partial V}_{\epsilon,\nabla\Phi} = \hat{\mathbf{t}} \cdot \boldsymbol{\nabla}\mathcal{T}^{\partial V,\partial V}_{\epsilon,\Phi}$ and $\boldsymbol{\mathcal{T}}^{\partial V,V}_{0,\nabla\varphi} = \hat{\mathbf{t}} \cdot \boldsymbol{\nabla}\boldsymbol{\mathcal{T}}^{\partial V,V}_{0,\varphi}$. Integral operators ($\boldsymbol{\mathcal{T}}^{V,\partial V}_{\epsilon,\nabla\Phi} + \mathcal{T}^{V,\partial V}_{\epsilon,A}$) translate the unknown tangential weighting source function $\boldsymbol{J}$ from the boundary of the scatterer ∂V to the total field inside the the scatterer V. Integral operators ($\boldsymbol{\mathcal{T}}^{\partial V,V}_{0,\nabla\varphi} + \boldsymbol{\mathcal{T}}^{\partial V,V}_{0,a}$) map polarization current $\boldsymbol{j}$ inside of the scatterer V to the tangential scattered electric field on the boundary ∂V. Integral operators $\left(\mathcal{T}^{\partial V,\partial V}_{\epsilon,\nabla\Phi} + \boldsymbol{\mathcal{T}}^{\partial V,\partial V}_{\epsilon,A}\right)$ map tangential weighting sources $\boldsymbol{J}$ defined on the boundary of the scatterer ∂V to the tangential component of the total electric field on the same boundary ∂V.

3.2 Method of Moments Discretization of SVS-EFIE Operators

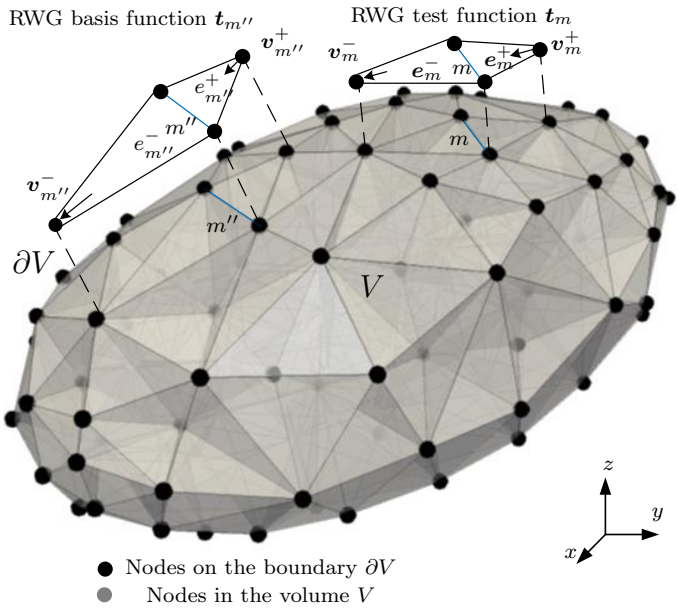

Figure 3.1: Tetrahedral volume mesh and triangle surface mesh utilized in the MoM solution of the SVS-EFIE (3.7) and RWG basis functions on ∂V.

In order to solve the SVS-EFIE (3.7) with MoM, the volume of the V is discretized with a 3D mesh consisting of N tetrahedral elements. The boundary of the scatterer ∂V is discretized with 2D mesh consisting of M triangle elements. The number of elements N in the 3D mesh is independent from the size of 2D mesh M. The meshes are depicted in Fig. 3.1. The position vector on the mth triangle element is defined parametrically as $\boldsymbol{r}^{\partial v}_m(\xi,\eta) = \boldsymbol{r}^{\partial v}_{m(0)}\xi + \boldsymbol{r}^{\partial v}_{m(1)}\eta + \boldsymbol{r}^{\partial v}_{m(2)}(1-\xi-\eta)$, where $\boldsymbol{r}^{\partial v}_{m(0)}$, $\boldsymbol{r}^{\partial v}_{m(1)}$, and $\boldsymbol{r}^{\partial v}_{m(2)}$ are the vertices of the mth triangle element on the boundary ∂V and ξ and η are barycentric coordinates [25] $\xi \in [0,1]$, $\eta \in [0, 1-\xi]$. Centroid of the mth triangle element is defined as $\boldsymbol{c}^{\partial V}_m = \frac{1}{3}(\boldsymbol{r}^{\partial v}_{m(0)} + \boldsymbol{r}^{\partial v}_{m(1)} + \boldsymbol{r}^{\partial v}_{m(2)})$. The position vector on the n'th tetrahedron on the scatterer V is defined parametrically as $\boldsymbol{r}^{v}_{n'}(\xi',\eta',\zeta') = \boldsymbol{r}^{v}_{n'(0)}\xi' + \boldsymbol{r}^{v}_{n'(1)}\eta' + \boldsymbol{r}^{v}_{n'(2)}\zeta' + \boldsymbol{r}^{v}_{n'(3)}(1-\xi'-\eta'-\zeta')$ where $\boldsymbol{r}^{v}_{n'(0)}$, $\boldsymbol{r}^{v}_{n'(1)}$, $\boldsymbol{r}^{v}_{n'(2)}$ and $\boldsymbol{r}^{v}_{n'(3)}$ are the vertices of the n'th tetrahedron, ξ', η', ζ'

being the barycentric coordinates [25] $\xi' \in [0,1]$, $\eta' \in [0, 1-\xi']$, and $\zeta' \in [0, 1-\xi'-\eta']$. The centroid of the n'th tetrahedron is defined as $\boldsymbol{c}^v_{n'} = \frac{1}{4}(\boldsymbol{r}^v_{n'(0)}+\boldsymbol{r}^v_{n'(1)}+\boldsymbol{r}^v_{n'(2)}+\boldsymbol{r}^v_{n'(3)})$. Discretization of the unknown tangential weighting function $\boldsymbol{J}$ defined on the boundary ∂V is performed using a set of Rao-Wilton-Glisson (RWG) basis functions [27] defined on two adjacent triangle elements with a common edge (Fig. 3.1). For example m''th base function is positioned on the common edge m''th between two neighbour triangles $e^+_{m''}$ and $e^-_{m''}$ and is defined as

$$\boldsymbol{t}_{m''}(\boldsymbol{r}'') = \begin{cases} \dfrac{\boldsymbol{r}'' - \boldsymbol{v}^+_{m''}}{2A_{e^+_{m''}}}\ell_{m''}, & \boldsymbol{r}'' \in e^+_{m''}, \\ \dfrac{\boldsymbol{v}^-_{m''} - \boldsymbol{r}''}{2A_{e^-_{m''}}}\ell_{m''}, & \boldsymbol{r}'' \in e^-_{m''}, \end{cases} \tag{3.16}$$

where $\ell_{m''}$ is the length of the common edge between two triangles, $\boldsymbol{v}^+_{m''}$ is non-common vertex in triangle $e^+_{m''}$ and $\boldsymbol{v}_{m''}$ is non-common vertex in triangle $e^-_{m''}$ (Fig. 3.1), $A_{e^+_{m''}}$ and $A_{e^-_{m''}}$ are the areas of triangle $e^+_{m''}$ and $e^-_{m''}$, respectively. Thus, the MoM discretized form of the unknown tangential weighting function $\boldsymbol{J}$ is

$$\boldsymbol{J}(\boldsymbol{r}'') \cong \sum_{m''=1}^{P} I_{m''}\boldsymbol{t}_{m''}(\boldsymbol{r}''), \tag{3.17}$$

where P is the total number of RWG basis functions. Since ∂V is a closed surface, the number of edges P is 1.5 times the number of triangles M, i.e. $P = 1.5M$. The divergence of the set of the RWG basis functions is two pulse functions defined on the adjacent elements

$$\boldsymbol{\nabla}''_{\mathrm{s}} \cdot \boldsymbol{t}_{m''}(\boldsymbol{r}'') = \begin{cases} \dfrac{\ell_{m''}}{A_{e^+_{m''}}}, & \boldsymbol{r}'' \in e^+_{m''}, \\ -\dfrac{\ell_{m''}}{A_{e^-_{m''}}}, & \boldsymbol{r}'' \in e^-_{m''}. \end{cases} \tag{3.18}$$

We use the same set of RWG functions as test functions. Discretization of each of the integral operators (3.9)–(3.14) with the above defined basis and testing functions are presented in the subsections below.

3.2.1 Discretization of scalar potential surface-to-surface operator $\mathcal{T}^{\partial V,\partial V}_{\epsilon,\nabla\Phi}$

The matrix elements $Z^{\partial V,\partial V}_{\epsilon,\nabla\Phi\, mm''}$ in the MoM discretization of the operator $\mathcal{T}^{\partial V,\partial V}_{\epsilon,\nabla\Phi}$ are produced by testing of the gradient of the scalar potential produced by $\boldsymbol{\nabla}''_{\mathrm{s}}\cdot\boldsymbol{t}_{m''}$ with the test function $\boldsymbol{t}_m$ as follows:

$$Z^{\partial V,\partial V}_{\epsilon,\nabla\Phi\, mm''} = \langle \boldsymbol{t}_m, \mathcal{T}^{\partial V,\partial V}_{\epsilon,\nabla\Phi} \circ \boldsymbol{t}_{m''}\rangle = \langle \boldsymbol{t}_m, \boldsymbol{\nabla}\mathcal{T}^{\partial V,\partial V}_{\epsilon,\Phi} \circ \boldsymbol{t}_{m''}\rangle. \tag{3.19}$$

Subsequently, the div-operator is shifted to the testing function

$$\begin{aligned} Z^{\partial V,\partial V}_{\epsilon,\nabla\Phi\, mm''} &= -\langle \boldsymbol{\nabla}_{\mathrm{s}}\cdot\boldsymbol{t}_m, \mathcal{T}^{\partial V,\partial V}_{\epsilon,\Phi} \circ \boldsymbol{t}_{m''}\rangle = \\ -\frac{i\omega\mu_0}{k_\epsilon^2}\Bigg(&\frac{\ell_m\ell_{m''}}{A_{e^+_m}A_{e^+_{m''}}}\int_{e^+_m}\int_{e^+_{m''}} G_\epsilon(\boldsymbol{r},\boldsymbol{r}'')ds''ds \\ &- \frac{\ell_m\ell_{m''}}{A_{e^+_m}A_{e^-_{m''}}}\int_{e^+_m}\int_{e^-_{m''}} G_\epsilon(\boldsymbol{r},\boldsymbol{r}'')ds''ds \\ &- \frac{\ell_m\ell_{m''}}{A_{e^-_m}A_{e^+_{m''}}}\int_{e^-_m}\int_{e^+_{m''}} G_\epsilon(\boldsymbol{r},\boldsymbol{r}'')ds''ds \\ &+ \frac{\ell_m\ell_{m''}}{A_{e^-_m}A_{e^-_{m''}}}\int_{e^-_m}\int_{e^-_{m''}} G_\epsilon(\boldsymbol{r},\boldsymbol{r}'')ds''ds\Bigg), \end{aligned} \tag{3.20}$$

where $m = 1,\ldots,P$ and $m'' = 1,\ldots,P$, and

$$\begin{aligned} &\int_{e^i_m}\int_{e^j_{m''}} G_\epsilon\left(\boldsymbol{r},\boldsymbol{r}''\right) ds''ds = 4A_{e^i_m}A_{e^j_{m''}} \\ &\times\int_0^1\int_0^{1-\xi}\int_0^1\int_0^{1-\xi''} G_\epsilon\left(\boldsymbol{r}^{\partial v}_m(\xi,\eta),\boldsymbol{r}''^{\partial v}_{m''}(\xi'',\eta'')\right) d\eta''d\xi''d\eta d\xi, \end{aligned} \tag{3.21}$$

where i, and j could be $+$ or $-$. The surface integrals in (3.20) are computed using 2D quadrature rules while the $1/R$-singularity is extracted from the Green's function G_ϵ where R is $|\boldsymbol{r}-\boldsymbol{r}''|$. The $1/R$-singular integrals are computed analytically in accord with [74].

3.2.2 Discretization of vector potential surface-to-surface operator $\boldsymbol{\mathcal{T}}_{\epsilon,A}^{\partial V,\partial V}$

The MoM discretization of the vector potential contribution to the tangential component of the total electric field $\boldsymbol{E}$ on the surface ∂V produced by the unknown weighting function $\boldsymbol{J}$ is composed of four terms corresponding to the interactions between the two half-RWG test function segments with the two half-RWG segments of the basis function

$$\begin{aligned} Z_{\epsilon,A\,mm''}^{\partial V,\partial V} &= \left\langle \boldsymbol{t}_m, \boldsymbol{\mathcal{T}}_{\epsilon,A}^{\partial V,\partial V} \circ \boldsymbol{t}_{m''} \right\rangle = i\omega\mu_0 \ell_m \ell_{m''} \\ &\times \Bigg(\int_{e_m^+} \frac{\boldsymbol{r} - \boldsymbol{v}_m^+}{2A_{e_m^+}} \cdot \int_{e_{m''}^+} \frac{\boldsymbol{r}'' - \boldsymbol{v}_{m''}^+}{2A_{e_{m''}^+}} G_\epsilon(\boldsymbol{r}, \boldsymbol{r}'') ds'' ds \\ &+ \int_{e_m^+} \frac{\boldsymbol{r} - \boldsymbol{v}_m^+}{2A_{e_m^+}} \cdot \int_{e_{m''}^-} \frac{\boldsymbol{v}_{m''}^- - \boldsymbol{r}''}{2A_{e_{m''}^-}} G_\epsilon(\boldsymbol{r}, \boldsymbol{r}'') ds'' ds \\ &+ \int_{e_m^-} \frac{\boldsymbol{v}_m^- - \boldsymbol{r}}{2A_{e_m^-}} \cdot \int_{e_{m''}^+} \frac{\boldsymbol{r}'' - \boldsymbol{v}_{m''}^+}{2A_{e_{m''}^+}} G_\epsilon(\boldsymbol{r}, \boldsymbol{r}'') ds'' ds \\ &+ \int_{e_m^-} \frac{\boldsymbol{v}_m^- - \boldsymbol{r}}{2A_{e_m^-}} \cdot \int_{e_{m''}^-} \frac{\boldsymbol{v}_{m''}^- - \boldsymbol{r}''}{2A_{e_{m''}^-}} G_\epsilon(\boldsymbol{r}, \boldsymbol{r}'') ds'' ds \Bigg), \end{aligned} \tag{3.22}$$

where $m = 1, \ldots, P$ and $m'' = 1, \ldots, P$. For example

$$\begin{aligned} &\int_{e_m^+} \frac{\boldsymbol{r} - \boldsymbol{v}_m^+}{2A_{e_m^+}} \cdot \int_{e_{m''}^+} \frac{\boldsymbol{r}'' - \boldsymbol{v}_{m''}^+}{2A_{e_{m''}^+}} G_\epsilon(\boldsymbol{r}, \boldsymbol{r}'') ds'' ds \\ &= \int_0^1 \int_0^{1-\xi} \left(\boldsymbol{r}_m^{\partial v}(\xi, \eta) - \boldsymbol{v}_m^+ \right) \cdot \int_0^1 \int_0^{1-\xi''} \left(\boldsymbol{r}_{m''}^{\prime\prime\partial v}(\xi'', \eta'') - \boldsymbol{v}_{m''}^+ \right) \\ &\qquad G_\epsilon \left(\boldsymbol{r}_m^{\partial v}(\xi, \eta), \boldsymbol{r}_{m''}^{\prime\prime\partial v}(\xi'', \eta'') \right) d\eta'' d\xi'' d\eta d\xi. \end{aligned} \tag{3.23}$$

Each of the above four integrals requires singularity mitigation of $(\boldsymbol{r}'' - \boldsymbol{v}_{m''}^+)/R$ for e_m^+ triangles and $(\boldsymbol{v}_{m''}^- - \boldsymbol{r}'')/R$ for e_m^- triangles. The product of a linear function with a $1/R$ function is extracted from the Green's function G_ϵ and integrated analytically over the element areas e_m^+ and e_m^- [74]. The remaining non-singular integrals are computed directly using 2D quadrature rules.

3.2.3 Discretization of scalar potential surface-to-volume operator $\boldsymbol{\mathcal{T}}^{V,\partial V}_{\epsilon,\nabla\Phi}$

To discretize the contribution of the gradient of the scalar potential to the polarization current $\boldsymbol{j}$ from the surface divergence of the weighting function $\boldsymbol{\nabla}_{\mathrm{s}} \cdot \boldsymbol{J}$ represented by the operator $\boldsymbol{\mathcal{T}}^{V,\partial V}_{\epsilon,\nabla\Phi}$, we use volume pulse-functions on tetrahedron elements as testing functions

$$p_{n'}(\boldsymbol{r}') = \begin{cases} 1, & \boldsymbol{r}' \in V_{n'}, \\ 0, & \boldsymbol{r}' \notin V_{n'}, \end{cases} \tag{3.24}$$

where $n' = 1, \ldots, N$ and RWG functions as the basis functions. This yields

$$\begin{aligned} \boldsymbol{Z}^{V,\partial V}_{\epsilon,\nabla\Phi\, n'm''} = \langle p_{n'}, \boldsymbol{\mathcal{T}}^{V,\partial V}_{\epsilon,\nabla\Phi} \circ \boldsymbol{t}_{m''} \rangle = \frac{i\omega\mu_0}{k_\epsilon^2} \\ \times \int_{V_{n'}} dv' \left(\frac{\ell_{m''}}{A_{e^+_{m''}}} \int_{e^+_{m''}} ds'' \boldsymbol{\nabla}' G_\epsilon(\boldsymbol{r}', \boldsymbol{r}'') \right. \\ \left. - \frac{\ell_{m''}}{A_{e^-_{m''}}} \int_{e^-_{m''}} ds'' \boldsymbol{\nabla}' G_\epsilon(\boldsymbol{r}', \boldsymbol{r}'') \right), \end{aligned} \tag{3.25}$$

where $n' = 1, \ldots, N$ and $m'' = 1, \ldots, P$. To mitigate the singularity in the integrals of (3.25), we use the following gradient theorem [23]

$$\int_{V_{n'}} \boldsymbol{\nabla}' G_\epsilon(\boldsymbol{r}', \boldsymbol{r}'') dv' = 2 \sum_{i=0}^{3} A^e_{n',i} \hat{\mathbf{m}}_{n',i} \int_0^1 \int_0^{1-\xi'} G_\epsilon(\boldsymbol{r}'_{n',i}(\xi', \eta'), \boldsymbol{r}'') d\eta' d\xi'. \tag{3.26}$$

In (3.26), $\hat{\mathbf{m}}_{n',i}$ is the normal vector to the ith face of the n'th tetrahedron, and $A^e_{n',i}$ is the area of the ith face of the n'th tetrahedron. The position vector $\boldsymbol{r}'_{n',i}(\xi', \eta')$ is on the ith face of the n'th tetrahedron. The above operations produce the definition of the matrix elements $\boldsymbol{Z}^{V,\partial V}_{\epsilon,\nabla\Phi\, n'm''}$ in the form featuring $1/R$-singular integrands. These integrals are computed using the 2D Gauss-Legendre rule after extraction of the $1/R$ function. The integral of the latter on 2D triangles forming facets of the tetrahedrons is computed in closed form according to [74].

3.2.4 Discretization of vector potential surface-to-volume operator $\mathcal{T}_{\epsilon,A}^{V,\partial V}$

The MoM discretization of the weighting function $\boldsymbol{J}$ contribution to the vector potential component of polarization current $\boldsymbol{j}$ determined by the operator $\mathcal{T}_{\epsilon,A}^{V,\partial V}$ involves inner products

$$\boldsymbol{Z}_{\epsilon,A\,n'm''}^{V,\partial V} = \langle p_{n'}, \mathcal{T}_{\epsilon,A}^{V,\partial V} \circ \boldsymbol{t}_{m''} \rangle, \tag{3.27}$$

where scalar pulse-functions over tetrahedrons (3.24) are used as test functions and RWG functions are used as basis functions

$$\begin{aligned} \boldsymbol{Z}_{\epsilon,A\,n'm''}^{V,\partial V} = i\omega\mu_0 \ell_{m''} \int_{V_{n'}} dv' \Bigg(& \int_{e_{m''}^{+}} \frac{\boldsymbol{r}'' - \boldsymbol{v}_{m''}^{+}}{2A_{e_{m''}^{+}}} G_\epsilon(\boldsymbol{r}', \boldsymbol{r}'') ds'' \\ & + \int_{e_{m''}^{-}} \frac{\boldsymbol{v}_{m''}^{-} - \boldsymbol{r}''}{2A_{e_{m''}^{-}}} G_\epsilon(\boldsymbol{r}', \boldsymbol{r}'') ds'' \Bigg), \end{aligned} \tag{3.28}$$

where $n' = 1, \ldots, N$ and $m'' = 1, \ldots, P$. The integrals with the product of a linear function and a Green's function are computed similarly with the inner integrals over s'' in (3.22). Namely, the singular part of the integrands corresponding to the linear function product with $1/R$-function is first extracted. Next, the remaining non-singular integrands are computed using 2D Gauss-Legendre quadrature rules.

3.2.5 Discretization of scalar potential volume-to-surface operator $\boldsymbol{\mathcal{T}}_{0,\nabla\varphi}^{\partial V,V}$

In order to match the discretized range of the $\boldsymbol{\mathcal{T}}_{\epsilon,\nabla\Phi}^{V,\partial V}$ operator with the domain of the $\boldsymbol{\mathcal{T}}_{0,\nabla\varphi}^{\partial V,V}$ operator, which maps the polarization current inside the volume V of the scatterer to the tangential scattered electric field on the scatterer's boundary ∂V, we use vector pulse basis functions to expand the polarization current density $\boldsymbol{j}(\boldsymbol{r}')$

in the volume V

$$\boldsymbol{j}(\boldsymbol{r}') \cong \sum_{n'=1}^{N} \boldsymbol{i}_{n'} p_{n'}(\boldsymbol{r}') = \sum_{n'=1}^{N} (i_{n'}^{x}\hat{\mathbf{x}} + i_{n'}^{y}\hat{\mathbf{y}} + i_{n'}^{z}\hat{\mathbf{z}}) p_{n'}(\boldsymbol{r}') \tag{3.29}$$

where $p_{n'}(\boldsymbol{r}')$ is defined as

$$p_{n'}(\boldsymbol{r}') = \begin{cases} 1, & \boldsymbol{r}' \in V_{n'}, \\ 0, & \boldsymbol{r}' \notin V_{n'}, \end{cases} \tag{3.30}$$

and $V_{n'}$ being the region inside the n'th tetrahedron. The scattered field is tested with a set of vector RWG test functions $\boldsymbol{t}_m$ similarly with the testing procedure for the operators $\mathcal{T}_{\epsilon,\nabla\Phi}^{\partial V,\partial V}$ and $\boldsymbol{\mathcal{T}}_{\epsilon,A}^{\partial V,\partial V}$. Therefore,

$$\boldsymbol{Z}_{0,\nabla\varphi\, mn'}^{\partial V,V} = \langle \boldsymbol{t}_m, \boldsymbol{\mathcal{T}}_{0,\nabla\varphi}^{\partial V,V} \circ p_{n'} \rangle. \tag{3.31}$$

To mitigate the singularity of the integrands the outer gradient operator is shifted to act onto the test function, yielding

$$\begin{aligned} \boldsymbol{Z}_{0,\nabla\varphi\, mn'}^{\partial V,V} &= -\langle \boldsymbol{\nabla}_{\mathrm{s}} \cdot \boldsymbol{t}_m, \boldsymbol{\mathcal{T}}_{0,\varphi}^{\partial V,V} \circ p_{n'} \rangle \\ &= -\frac{\ell_m}{k_0^2} \Bigg(\frac{1}{A_{e_m^+}} \int_{e_m^+} \int_{V_{n'}} \boldsymbol{\nabla} G_0(\boldsymbol{r}, \boldsymbol{r}') dv' ds \\ &\qquad - \frac{1}{A_{e_m^-}} \int_{e_m^-} \int_{V_{n'}} \boldsymbol{\nabla} G_0(\boldsymbol{r}, \boldsymbol{r}') dv' ds \Bigg), \end{aligned} \tag{3.32}$$

where $m = 1, \ldots, P$ and $n' = 1, \ldots, N$. The singularity is further mitigated by using the gradient theorem [23] which eliminates the inner gradient operator acting on the Green's function, as follows:

$$\begin{aligned} \int_{V_{n'}} \boldsymbol{\nabla} G_0(\boldsymbol{r}, \boldsymbol{r}') dv' = -\int_{V_{n'}} \boldsymbol{\nabla}' G_0(\boldsymbol{r}, \boldsymbol{r}') dv' = \\ - 2 \sum_{i=0}^{3} A_{n',i}^{e} \hat{\mathbf{m}}_{n',i} \int_0^1 \int_0^{1-\xi'} G_0(\boldsymbol{r}, \boldsymbol{r}'_{n',i}(\eta', \xi')) d\eta' d\xi'. \end{aligned} \tag{3.33}$$

In (3.33), $\hat{\mathbf{m}}_{n',i}$ is normal vector to the ith face of the n'th tetrahedron, and $A^e_{n',i}$ is the area of ith face of the n'th tetrahedron. The position vector $\boldsymbol{r}'_{n',i}(\eta',\xi')$ is on the ith face of the n'th tetrahedron.

The above operations produce the definition of the matrix elements $\boldsymbol{Z}^{\partial V,V}_{0,\nabla\varphi\, mn'}$ in the form of integrals featuring $1/R$-singular integrands. These integrals are computed using the 2D Gauss-Legendre rule after extraction of the $1/R$ function. The integral of the latter on 2D elements is computed in closed form according to [74].

3.2.6 Discretization of vector potential volume-to-surface operator $\boldsymbol{\mathcal{T}}^{\partial V,V}_{0,a}$

The operator $\boldsymbol{\mathcal{T}}^{\partial V,V}_{0,a}$ maps the volume polarization current $\boldsymbol{j}$ onto the vector potential contribution to the scattered electric field.Its MoM discretization is done with pulse basis functions (3.30) on the tetrahedral elements of the volume V expanding the volume current $\boldsymbol{j}$ and the vector RWG test functions (3.16) testing the vector potential as

$$\boldsymbol{Z}^{\partial V,V}_{0,a\, mn'} = \langle \boldsymbol{t}_m, \boldsymbol{\mathcal{T}}^{\partial V,V}_{0,a} \circ p_{n'} \rangle = \int_{e^+_m} \frac{\boldsymbol{r}-\boldsymbol{v}^+_m}{2A_{e^+_m}} \ell_m \cdot \int_{V_{n'}} G_0(\boldsymbol{r},\boldsymbol{r}')dv'ds + \int_{e^-_m} \frac{\boldsymbol{v}^-_m-\boldsymbol{r}}{2A_{e^-_m}} \ell_m \cdot \int_{V_{n'}} G_0(\boldsymbol{r},\boldsymbol{r}')dv'ds, \quad (3.34)$$

where $m = 1,\ldots,P$ and $n' = 1,\ldots,N$. The 3D integral on the tetrahedron is defined as

$$\int_{V_{n'}} G_0(\boldsymbol{r},\boldsymbol{r}')dv' = 6V_{n'} \int_0^1 \int_0^{1-\xi'} \int_0^{1-\xi'-\eta'} G_0(\boldsymbol{r},\boldsymbol{r}'(\xi',\eta',\zeta'))d\xi' d\eta' d\zeta', \quad (3.35)$$

where $V_{n'}$ is the volume of the n' tetrahedron. The 3D integrals over ξ', η' and ζ' in (3.35) are evaluated using 3D quadrature rules after $1/R$-singular part is subtracted from the Green's function G_0 and integrated analytically according to [74]. The test integrals over triangle elements are computed using 2D Gauss-Legendre quadrature rules.

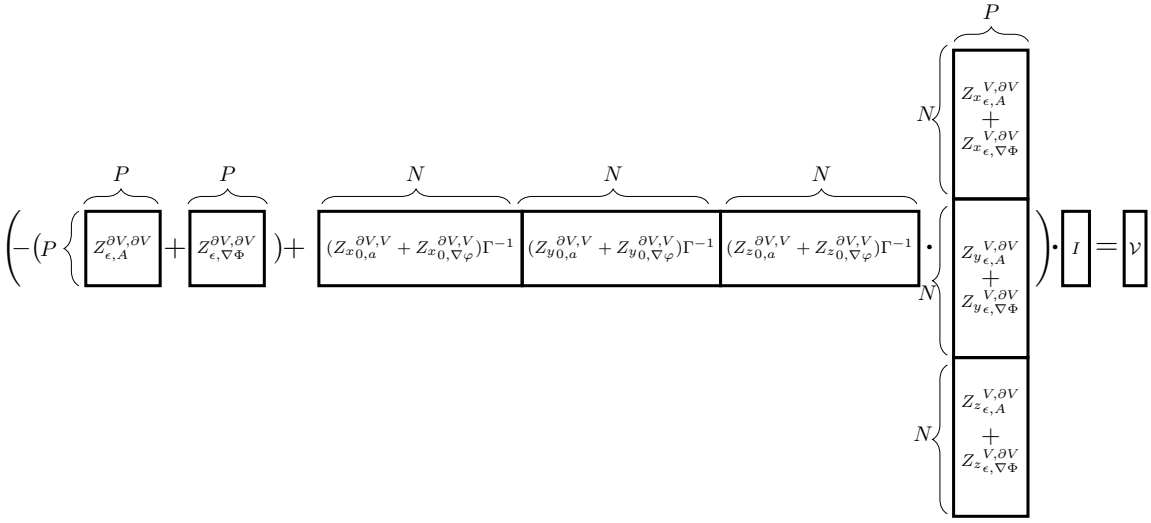

Figure 3.2: Structure of the system of linear algebraic equations resulting from MoM discretization of the SVS-EFIE. The number of RWG basis functions on the boundary ∂V is P and N is the number of tetrahedral cells in volume V.

3.2.7 Discretization of incident field $\boldsymbol{E}^{\text{inc}}$

The discretization of the incident field is done through the definition of the inner products of the incident field with the RWG test functions (3.16)

$$\mathcal{V}_m = \langle \boldsymbol{t}_m, \boldsymbol{E}^{\text{inc}} \rangle = \ell_m \int_{e_m^+} \frac{\boldsymbol{r} - \boldsymbol{v}_m^+}{2A_{e_m^i}} \cdot \boldsymbol{E}^{\text{inc}}(\boldsymbol{r}) ds + \ell_m \int_{e_m^-} \frac{\boldsymbol{v}_m^- - \boldsymbol{r}}{2A_{e_m^-}} \cdot \boldsymbol{E}^{\text{inc}}(\boldsymbol{r}) ds \quad (3.36)$$

where $m = 1, \ldots, P$. The integrals in (3.36) are regular and computed to desired precision using 2D Gauss-Legendre quadrature rules.

3.2.8 MoM matrix assembly

The MoM discretization of the SVS-EFIE is reduced to the following set of linear algebraic equations with respect to the $(P \times 1)$ vector of unknown scalar coefficients I

in the expansion of the unknown surface weighting function (3.17)

$$-\Big(\Big[\ Z_{\epsilon,A}^{\partial V,\partial V}\ \Big]+\Big[\ Z_{\epsilon,\nabla\Phi}^{\partial V,\partial V}\ \Big]\Big)\cdot\Big[\ I\ \Big]$$
$$+\Big(\Big(\Big[\ \boldsymbol{Z}_{0,a}^{\partial V,V}\ \Big]+\Big[\ \boldsymbol{Z}_{0,\nabla\varphi}^{\partial V,V}\ \Big]\Big)\odot\Gamma^{-1}\cdot\Big(\Big[\ \boldsymbol{Z}_{\epsilon,A}^{V,\partial V}\ \Big]+\Big[\ \boldsymbol{Z}_{\epsilon,\nabla\Phi}^{V,\partial V}\ \Big]\Big)\Big)\cdot\Big[\ I\ \Big]=\Big[\ \mathcal{V}\ \Big] \tag{3.37}$$

where $\odot$ is dot product of two matrices composed of vector quantities and Γ is the Gram matrix. Each element of Gram matrix Γ is defined as

$$\Gamma_{n_o,n_s}=\begin{cases}\int_0^1\int_0^{1-\xi'}\int_0^{1-\xi'-\eta'} j_t(n_o)d\xi' d\eta' d\zeta',\ \text{if } n_o=n_s,\\ \\ 0,\ \text{otherwise,}\end{cases} \tag{3.38}$$

where $n_o, n_s = 1,\ldots,N$ and $j_t(n_o)$ is Jacobian of n_oth tetrahedron. In the expanded form the structure of the MoM matrix equation is given by the following expression and is depicted in Fig. 3.2

$$\begin{aligned}&-\left(\left[Z_{\epsilon,A}^{\partial V,\partial V}\right]+\left[Z_{\epsilon,\nabla\Phi}^{\partial V,\partial V}\right]\right)\cdot[I]\\ &+\sum_{d=\{x,y,z\}}\Bigg(\left(\left[Z_{d0,a}^{\partial V,V}\right]+\left[Z_{d0,\nabla\varphi}^{\partial V,V}\right]\right)\cdot\Gamma^{-1}\\ &\qquad\cdot\left(\left[Z_{d\epsilon,A}^{V,\partial V}\right]+\left[Z_{d\epsilon,\nabla\Phi}^{V,\partial V}\right]\right)\Bigg)\cdot[I]=[\mathcal{V}]\,,\end{aligned} \tag{3.39}$$

The above system of linear algebraic equations with P unknowns can be written in the compact form as $[Z]\cdot[I]=[\mathcal{V}]$ with respect to the unknown coefficients I_1,...,I_P in the expansion (3.17) of the sought weighting function $\boldsymbol{J}$.

3.2.9 Computation of electric field inside the scatterer

After solving the system of linear algebraic equations (3.39) for the coefficients $[I]$ in the expansion of weighting function $\boldsymbol{J}$ on ∂V, the electric field $\boldsymbol{E}$ and volume

polarization current $\boldsymbol{j}$ in the scatterer volume V can be computed as a superposition of the waves emanating from the boundary ∂V according to (3.4). The MoM matrices $\boldsymbol{Z}_{\epsilon,A}^{V,\partial V}$ and $\boldsymbol{Z}_{\epsilon,\nabla\Phi}^{V,\partial V}$ can be used to compute the electric field $\boldsymbol{E}$ at the centroid of the tetrahedral elements in the volume of the scatterer $\boldsymbol{c}_{n'}^{v}$, can be calculated as

$$[\boldsymbol{E}(\boldsymbol{c}_{n'}^{v})] = -\Gamma^{-1} \cdot \Big(\Big[\; \boldsymbol{Z}_{\epsilon,A}^{V,\partial V} \; \Big] + \Big[\; \boldsymbol{Z}_{\epsilon,\nabla\Phi}^{V,\partial V} \; \Big] \Big) \cdot \Big[\; I \; \Big], \tag{3.40}$$

$n' = 1, ..., N$, and $\boldsymbol{c}_{n'}^{v}$ are the centroids of the tetrahedral elements in the volume of the scatterer.

3.2.10 Validating the representation of the total electric field inside the scatterer (3.4)

To validate (3.4), we consider the case of the relative permittivity ϵ equal to 1. In this case, the proposed SVS-EFIE (3.7) is simplified to

$$-i\omega\mu_0\hat{\mathbf{t}} \cdot \int_{\partial V} \overline{\overline{G}}_{\epsilon}(\boldsymbol{r}, \boldsymbol{r}'') \cdot \boldsymbol{J}(\boldsymbol{r}'')dr'' = \hat{\mathbf{t}} \cdot \boldsymbol{E}^{\text{inc}}(\boldsymbol{r}), \boldsymbol{r} \in \partial V, \tag{3.41}$$

and the developed MoM solution (3.39) is simplified to

$$-\Big(\Big[\; Z_{\epsilon,A}^{\partial V,\partial V} \; \Big] + \Big[\; Z_{\epsilon,\nabla\Phi}^{\partial V,\partial V} \; \Big] \Big) \cdot \Big[\; I \; \Big] = \Big[\; \mathcal{V} \; \Big]. \tag{3.42}$$

Solving this system of linear algebraic equation results in a solution, which if we plug it back to (3.40) we could obtain the incident field vector at the centroid of each tetrahedron inside the scatterer.

3.2.11 Computation of electric field outside the scatterer

The total electric field outside the scatterer is computed as $\boldsymbol{E}(\boldsymbol{r}) = \boldsymbol{E}^{\text{inc}}(\boldsymbol{r}) + \boldsymbol{E}^{\text{scat}}(\boldsymbol{r})$, where scattered field is defined by the polarization current in the volume of

the scatterer as

$$\boldsymbol{E}^{\text{scat}}(\boldsymbol{r}) = k_0^2\,(\epsilon - 1)\int\limits_V \overline{\overline{G}}_0(\boldsymbol{r},\boldsymbol{r}')\cdot\ \boldsymbol{E}(\boldsymbol{r}')dv'. \tag{3.43}$$

With the discretized total electric field $\boldsymbol{E}(\boldsymbol{c}^v_{n'})$ available at the centroids of tetrahedral elements $\boldsymbol{c}^v_{n'}$ in the volume of the scatterer V from (3.40), we compute the scattered field outside V as a sum of contributions from the scalar and vector potentials $\boldsymbol{E}^{\text{scat}} = \boldsymbol{E}^{\text{scat}}_a + \boldsymbol{E}^{\text{scat}}_\phi$ terms

$$\begin{aligned}\boldsymbol{E}^{\text{scat}}(\boldsymbol{r}) = k_0^2\,(\epsilon - 1)\sum_{n'=1}^{N}\boldsymbol{E}(\boldsymbol{c}^v_{n'})\int_{V_{n'}} G_0(\boldsymbol{r},\boldsymbol{r}'_{V_{n'}})dv' \\ -(\epsilon-1)\sum_{n'=1}^{N}\boldsymbol{E}(\boldsymbol{c}^v_{n'})\boldsymbol{\nabla}\int_{V_{n'}}\boldsymbol{\nabla}' G_0(\boldsymbol{r},\boldsymbol{r}'_{V_{n'}})dv'.\end{aligned} \tag{3.44}$$

The first term in (3.44) corresponding to the vector potential $\boldsymbol{E}^{\text{scat}}_a$ which is computed using 3D Gauss quadrature rule after the $1/R$ singularity is extracted from the Green's function G_0 and the integral $\int\limits_{V_{n'}} \frac{1}{|\boldsymbol{r}-\boldsymbol{r}'|}dv'$ over the volume of each tetrahedron is computed analytically according to [74].

The contribution to the total scattered field from the gradient of scalar potential $\boldsymbol{E}^{\text{scat}}_\phi$ from each tetrahedron is first reduced to four surface integrals using gradient theorem similar with (3.26) with the outer gradient moved to the Green's function as

$$\begin{aligned}\boldsymbol{E}^{\text{scat}}_\phi(\boldsymbol{r}) = -(\epsilon-1)\sum_{n'=1}^{N}\sum_{i=0}^{3} 2A^e_{n',i}[\boldsymbol{E}(\boldsymbol{c}^v_{n'})\cdot\hat{\mathbf{m}}_{n',i}] \\ \int_0^1\int_0^{1-\xi'}\boldsymbol{\nabla}G_0(\boldsymbol{r},\boldsymbol{r}'_{n',i}(\xi',\eta'))d\eta' d\xi'.\end{aligned} \tag{3.45}$$

Integrals over each face of the tetrahedron from the gradient of the singular $1/R$ part of the Green's function are evaluated analytically, i.e. $\nabla\int_{\partial V_{n'}} ds'/|\boldsymbol{r}-\boldsymbol{r}'|$. Extraction of the singular integrals $\nabla\int_{\partial V_{n'}} ds'/|\boldsymbol{r}-\boldsymbol{r}'|$ from the second term in (3.44) allows for use of regular 2D quadrature rules on the remaining non-singular integrands on each of the four tetrahedron's faces.

3.3 Numerical Results

We use GMESH [83] to create our geometries and generate 2D and 3D meshes. Numerical implementation of the MoM solution of the proposed 3D SVS-EFIE has been done using C++ programming language with Intel C++ Compiler. Such implementation allows for either parallel or serial computations. Simulations have been carried out on the advanced computing platform Grex SGI Altix XE 1300 cluster at WestGrid, part of the Compute Canada [82]. All post-process visualizations are performed using paraview [84] and Mathlab [85].

To validate the proposed new SSIE we conducted various numerical experiments and compared solutions of the scattering problems obtained using the new SVS-EFIE equation and alternative methods such as analytic Mie series solution and FEKO commercial software [35].

In the first example, we consider the problem of radiation of a radial electric dipole near a dielectric sphere with radius of $R = 0.1\,\mathrm{m}$ and relative permittivity $\epsilon = 1.5$. The sphere centered at the origin is excited by the electric dipole, which is directed along the positive z-axis and situated above the north pole of the sphere $0.4\,\mathrm{m}$ away from the origin. The electric dipole moment is $I\ell = 1\,\mathrm{A{\cdot}m}$. The numerical solution of the radiation problem computed at $1.5\,\mathrm{GHz}$ using the proposed new SVS-EFIE (3.7) is shown in Fig. 3.3(a), as well as the relative error between the SVS-EFIE solution and analytic Mie series solution in Fig. 3.3(c). The MoM discretization of the SVS-EFIE involved $M = 766$ triangle elements discretizing the boundary ∂V of the sphere, $P = 1,149$ RWG basis functions, and $N = 2,546$ tetrahedral elements discretizing its volume V. The field inside the sphere is computed using the superposition expression (3.4) after the weighting function $\boldsymbol{J}$ expansion coefficients $[I]$ in (3.17)) are obtained from solution of the SLAE (3.39). Upon availability of the field distribution in the volume of the sphere, the scattered field outside the sphere can be computed using (3.44) and added to the incident field. The MoM solution of the SVS-EFIE is seen to match closely with the analytic Mie series solution in accord with the error levels expected from the used discretization density. The average relative error of the SVS-EFIE solution is 0.005 with standard deviation $4.53 \cdot 10^{-3}$ with respect to Mie

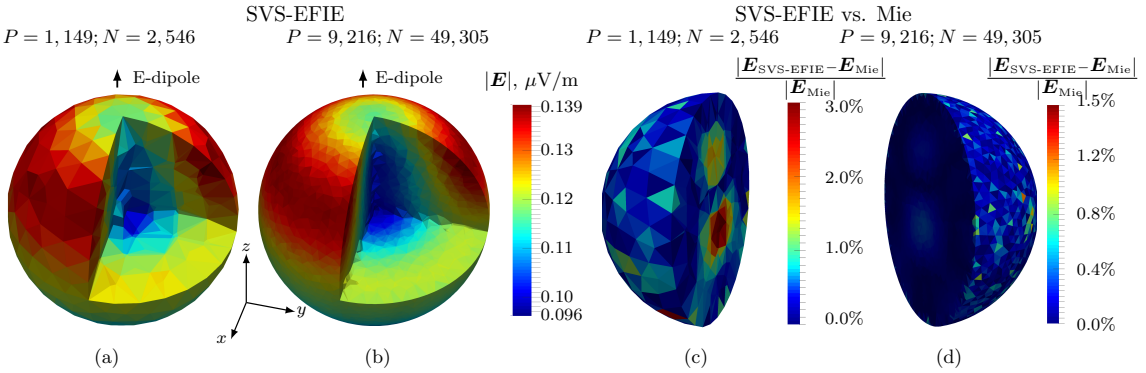

Figure 3.3: Magnitude of total electric field at 1.5 GHz in a dielectric sphere (concave cut is made for improved visibility) with permittivity $\epsilon = 1.5$ and radius 0.1 m centered at the origin produced by z-directed electric dipole situated at $x' = 0\,\text{m}$, $y' = 0\,\text{m}$, $z' = 0.4\,\text{m}$. The electric dipole moment is $I\ell = 1\,\text{A}{\cdot}\text{m}$. The number of triangles in MoM discretization (3.39) of SVS-EFIE (3.7) on the boundary ∂V is M, number of edges is P, and number of tetrahedrons in the volume V is N: (a) $M = 766; P = 1,149; N = 2,456$, (b) $M = 6,144; P = 9,216; N = 49,305$. The relative error distribution of these two solutions with respect to Mie series solution is shown in (c) for $P = 1,149; N = 2,546$ discretization and in (d) for $P = 9,216; N = 49,305$ discretization.

series solution. The discretization corresponds to the sampling of the electric field inside the sphere with approximately 12 samples per linear wavelength.

In order to demonstrate the behavior of the error in the MoM solution of the proposed SVS-EFIE, we next consider the same radiation problem but for the sphere discretized with $N = 49,305$ tetrahedral elements in the volume V and $M = 6,144$ triangle elements on the boundary ∂V. The number of RWG basis functions for this case is $P = 9,216$. The discretization corresponds to the sampling of the electric field inside the sphere with approximately 32 samples per linear wavelength. The numerical solution of the radiation problem obtained using the proposed new SVS-EFIE (3.7) is shown in Fig. 3.3(b) as well as the relative error between the SVS-EFIE solution and analytic Mie series solution in Fig. 3.3(d). The relative error of the SVS-EFIE solution compared to the exact Mie series solution shows that the average relative error of the SVS-EFIE solution decreases below 0.0007 with standard deviation of $8.3 \cdot 10^{-4}$. Increased accuracy in the computed field is observed with the increased

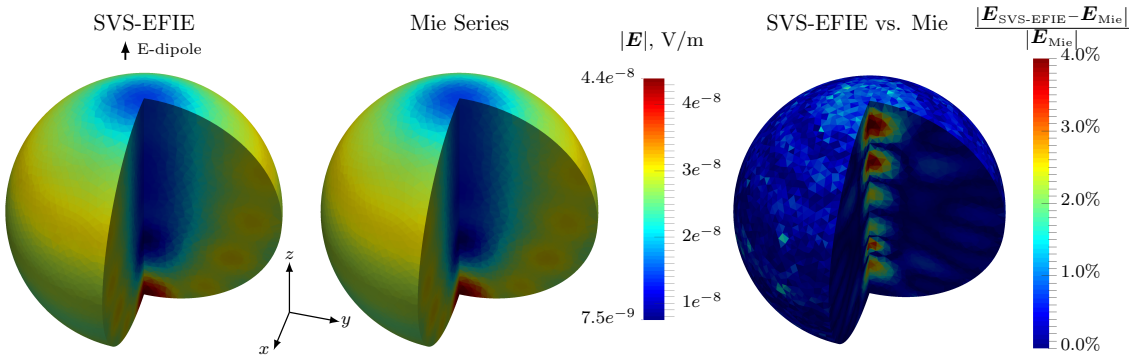

Figure 3.4: Magnitude of total electric field at 3 GHz in a dielectric sphere (concave cut is made for improved visibility) with permittivity $\epsilon = 1.5$ and radius 0.1 m centered at the origin produced by z-directed electric dipole situated at $x' = 0\,\text{m}$, $y' = 0\,\text{m}$, $z' = 0.4\,\text{m}$. The electric dipole moment is $I\ell = 1\,\text{A}\cdot\text{m}$. The number of triangles in MoM discretization (3.39) of SVS-EFIE (3.7) on the boundary ∂V is $M = 12,674$, number of edges is $P = 19,011$ and number of tetrahedra in the volume V is $N = 131,943$. Total electric field in the dielectric obtained from SVS-EFIE is in the left plot and from the Mie series is in the center plot. The relative error distribution of these two solutions with respect to Mie series solution is shown in the right plot.

MoM sampling rate per wavelength corroborates the rigorous nature of the proposed new SSIE.

To demonstrate solution of the proposed SVS-EFIE (3.7) at higher frequencies, we consider the problem of radial dipole radiation near a dielectric sphere at 3 GHz. In the example, a dielectric sphere centered at the origin with a radius of $R = 0.1\,\text{m}$ and dielectric permittivity $\epsilon_r = 1.5$ is excited by an electric dipole directed along z-axis and situated 0.4 m away from the origin above the north pole of the sphere. The electric dipole moment is $I\ell = 1\,\text{A}\cdot\text{m}$. The number of triangles in MoM discretization of the boundary ∂V (3.39) in the SVS-EFIE (3.7) is $M = 12,674$. This surface discretization produces $P = 19,011$ RWG basis functions. The number of elements in the volume V is $N = 131,943$. This discretization corresponds to approximately 26 elements per wavelength sampling rate inside the dielectric. The results of these field computations are depicted in Fig. 3.4. The average relative error of the SVS-EFIE solution is $2.87 \cdot 10^{-3}$ with a standard deviation $3.38 \cdot 10^{-3}$ with respect to

Table 3.1: Error in the MoM solution of the SVS-EFIE (3.7) against Mie series for electric dipole wave scattering at 1.5 GHz on a sphere of radius $R = 0.1$ m and relative permittivity ϵ.

ϵ, rel. permittivity	δ, avg. rel. error	h, tets. perλ
1.5	0.0006	32
4	0.0029	23
8	0.0083	16
12	0.0276	13

Mie series solution. To show the behavior of the MoM error in the discretized SVS-EFIE with the increased values of the relative permittivity ϵ, we considered the same case of electric dipole radiation at 1.5 GHz near a 0.1m radius sphere under a fixed MoM discretization with $M = 6,144$ and $N = 49,305$. The behavior of the average relative error (δ) is shown as a function of ϵ in Table. 3.1. The error increase is due to the reduced electrical sampling rate from 32 tetrahedral per wavelengh to 13. The equation was also tested to remain stable at high values of permittivity. Solution of the SVS-EFIE for analysis of a general problem of dipole radiation near NASA almond [80] target is considered at 3 GHz in order to show its behaviour on a non-smooth geometry featuring a sharp corner. The target has relative permittivity $\epsilon = 1.5$ and a size of 0.252 m, 0.0976 m, and 0.0325 m along x, y, and z axes, respectively. The model is excited by the electric dipole directed along the short axis of the almond (z axis in Fig. 3.5) and situated on the long axis (x axis in Fig. 3.5) of the almond 0.8528 m away for from its tip. The electric dipole moment is $I\ell = 1$ A·m. The number of triangles in the MoM discretization (3.39) of the SVS-EFIE (3.7) on the boundary ∂V is $M = 9,094$, the number of edges is $P = 13,671$, and the number of tetrahedra in the volume V is $N = 44,388$. Distribution of the computed field is depicted in Fig. 3.5. In order to validate the MoM solution of the new SVS-EFIE, a second order FEM solution for the same radiation problem is obtained using FEKO commercial software [35]. The magnitude of the electric field is depicted in Fig. 3.5 for the case of the MoM discretization of SVS-EFIE and FEM solution of the FEKO

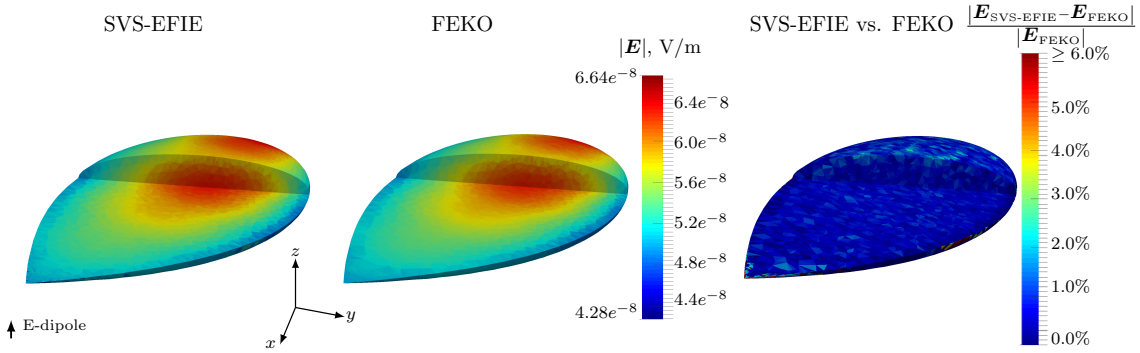

Figure 3.5: Magnitude of total electric field at 3 GHz of a dielectric NASA Almond model with permittivity $\epsilon = 1.5$ and size of 0.252 m, 0.0976 m, and 0.0325 m along x, y, and z axes, respectively. The model is excited by the electric dipole directed along the short axis of the dipole and situated on the long axis of the almond 0.8528 m away for from its tip. The electric dipole moment is $I\ell = 1\,\text{A}\cdot\text{m}$. The number of triangles in MoM discretization (3.39) of SVS-EFIE (3.7) on the boundary ∂V is $M = 9,094$, number of edges is $P = 13,671$, and number of tetrahedra in the volume V is $N = 44,388$. Total electric field in the dielectric obtained from SVS-EFIE is in the left plot and and FEKO-FEM solution is in the center plot. The relative error distribution of these two solutions with respect to FEKO solution is shown in the right plot.

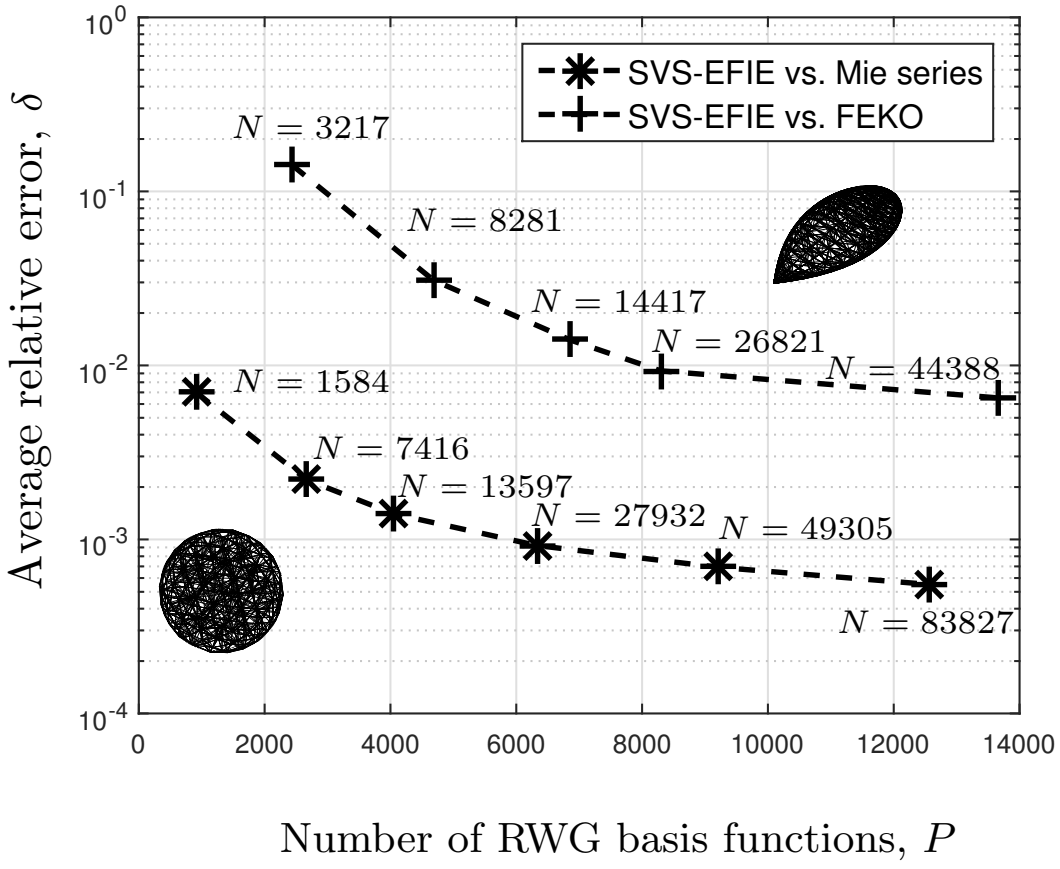

Figure 3.6: Demonstration of the mean relative error δ as a function of number of RWG basis functions P in the MoM solution of the novel SVS-EFIE (3.7) in two radiation problem examples. The error is shown for the problem of radial electric dipole radiation near dielectric sphere of radius $R = 0.1\,\mathrm{m}$ with relative permittivity $\epsilon = 1.5$ at $1.5\,\mathrm{GHz}$ (examples of Fig. 3.3). The mean relative error δ in the MoM solution of the novel SVS-EFIE (3.7) with respect to the FEKO-FEM solution for the problem of electric dipole radiation near dielectric NASA almond with relative permittivity $\epsilon = 1.5$ at $3\,\mathrm{GHz}$ (example of Fig. 3.5) is shown also.

software. The relative error in the MoM solution of the SVS-EFIE compared against the FEM solution is shown in the same Fig. 3.5. Higher than 6.0% relative error is observed in 77 out of 44,388 tetrahedrals located in the regions of the low field levels near the edges of the almond (regions with the highest surface curvature) and the region near the sharp edge. The average relative error of the SVS-EFIE solution is $6.59 \cdot 10^{-3}$ with a standard deviation $7.44 \cdot 10^{-3}$.

To show the behavior of the MoM error in the discretized SVS-EFIE with the increased number of the RWG basis functions P, we considered the case of electric dipole radiation at 1.5 GHz near 0.1 m radius sphere (examples of Fig. 3.3). The behaviour of the average relative error δ with respect to the Mie series solution is depicted as a function of P in Fig. 3.6. The error decrease is due to the increased electrical sampling rate and more accurate geometry representation. In the same Fig. 3.6 mean relative error δ in the MoM solution of the novel SVS-EFIE (3.7) with respect to the FEKO-FEM solution for the problem of the electric dipole radiation near the NASA almond with relative permittivity $\epsilon = 1.5$ at 3 GHz (example of Fig. 3.5) as a function of number of RWG basis functions is demonstrated.

To demonstrate the computational complexity associated with the SVS-EFIE, consider the scattering problem of a sphere dielectric with relative permittivity $\epsilon = 1.5$ and radius of $R = 0.1$ m centered in origin. This scatterer is excited by an electric dipole at 1.5 GHz with electric dipole moment of $I\ell = 1$ A·m directed along z-axis and situated 0.4 m away from the origin. We solve this problem with SVS-EFIE for different number of basis functions P. The results of the matrix fill-time and memory obtained on a system with Intel corei7-4712MQ processor running at 2.30 GHz are shown in Fig. 3.7 as a function of the number of unknowns P. The computational complexity and memory cost of the SLAE including matrix form of the discretized integral operators in SVS-EFIE formulation in a single time-step can be summarized for a computational domain consisting of N tetrahedra in volume V and P RWG basis functions on surface ∂V as follows. For matrix fill and storage associated with the surface to surface operator the $O(P^2)$ time and memory is required (see Fig. 3.7 (a) and Fig. 3.7 (b)). For matrix fill and storage of the surface to volume (see Fig. 3.7 (c) and Fig. 3.7 (d)) and volume to surface operators (see Fig. 3.7 (e) and Fig. 3.7 (f))

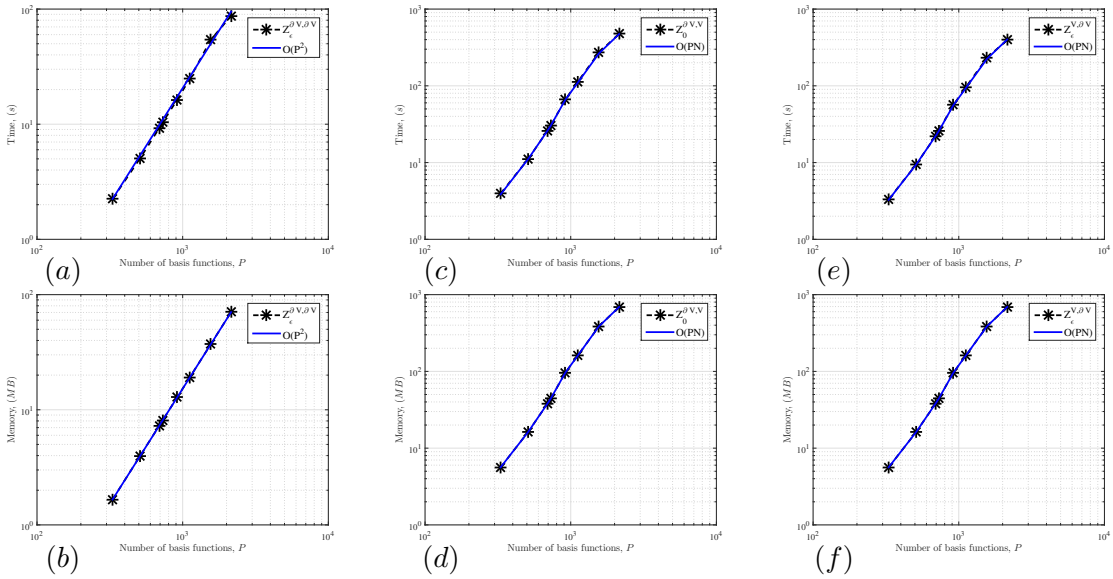

Figure 3.7: Computational complexity and memory associated with the SVS-EFIE integral operators as a function of number of basis functions P for the scattering problem of a sphere dielectric with relative permittivity $\epsilon = 1.5$ and radius of $R = 0.1\,\mathrm{m}$ centered in origin. This scatterer is excited by an electric dipole at $1.5\,\mathrm{GHz}$ with electric dipole moment of $I\ell = 1\,\mathrm{A{\cdot}m}$ directed along z-axis and situated $0.4\,\mathrm{m}$ away from the origin.

the $O(NP)$ time and memory is required. Naive direct solution of the matrix equation also requires the multiplication of the $(P \times N)$ matrix corresponding to the volume to surface operator and $(N \times P)$ matrix corresponding to the surface to volume operator matrix costing $O(P^2N)$ operations. The complexity of the product of these matrices dominates the complexity of the naive direct solution. For a general scatterer the number of volume elements N is related to the number of surface degrees of freedom as $P^{1.5}$, making the dominant term in the CPU time complexity to be $O(P^{3.5})$.

Fast direct solution using arithmetics of the hierarchical matrices can be shown to reduce the CPU complexity to $O(P^{1.5}\log^2 P)$ and memory complexity to $O(P^{1.5}\log P)$. Fast iterative solution with FFT or MLFMA fast algorithms is of $O(P^{1.5}\log P)$ complexity in both CPU time and memory.

3.4 Conclusions

This Chapter presented a new single-source surface-volume-surface integral equation with its solution for 3D scattering problem on homogeneous non-magnetic penetrable dielectrics. The new equation is derived from the classical volume electric field integral equation via representation of the electric field inside the scatterer as a superposition of the spherical waves emanating from its boundary.

Detailed description of Method of Moment (MoM) discretization for the new single source integral equation (SSIE) is provided. The proposed MoM scheme is new compared to the previously known MoM discretizations of the traditional surface integral equations as well as the previously known SSIEs. The MoM basis and testing functions are chosen in such a way that with appropriate shift of the differential operators only $1/R$ singular kernels are featured in the definitions of the MoM inner products. With the proposed new SSIE determining the sought fields is a two-stage process. In the first stage the unknown weighting function on the boundary of the scatterer is determined. This function is subsequently used to obtain the field distribution inside the scatterer. In the second stage the total field outside the scatterer is computed using the volume equivalence principle. The novel equation features only a single unknown on the boundary and is numerically shown to produce an error-controllable solution.

4

Accurate Transmission Lines Characterization via Higher Order Moment Method Solution of Novel Single-Source Integral Equation

4.1 Introduction

Multi-conductor transmission line models are commonly used to analyze signal propagation in high-speed interconnects, transient behaviour in power systems, design of complex aircraft and vehicle cable harnesses and various other applications. Evaluation of the per-unit-length (p.u.l.) inductance and resistance matrices is an essential part of such analysis. It relies on accurate representation of the skin-effect, proximity-effect, and crowding-effect in the current flow through conductor cross-sections. The extraction of R and L matrices must be performed rapidly, accurately, and in a broad range of frequencies. Several issues commonly plague the extraction

process [86]. Insufficient accuracy in numerical solution of the pertinent equations is one of them. At low frequencies the small inductive contribution gets lost in the background of the computed impedance term. At high frequencies, when inductive contribution to the impedance dominates, the accuracy in the extracted resistance matrix gets severely degraded.

Errors associated with inaccurate geometric representation of the curvilinear boundaries of MTL cross-sections typically presents another challenge. To mitigate this error the number of elements discretizing the cross-section often has to be large. This often makes RL-extraction prohibitively long.

The higher-order solution methods offer an effective remedy to both of the above issues. While the higher-order geometric representation of the MTL cross-section allows for only a few elements to accurately represent the curvilinear conductor boundaries, the higher-order discretization of the field quantities results in maintaining a wide dynamic range in accurate extraction of R and L matrices from DC to high frequencies.

In this work we demonstrate such a higher-order (HO) Method of Moment (MoM) solution of a recently proposed single-source integral equation of magneto-quasistatics [75]. The new approach allows for effective error control in extracted R and L matrices of MTL with complex cross-sections at a moderate computational cost. For canonical MTLs allowing for analytic extraction of the R and L matrices, the numerically extracted R and L matrices are shown to exhibit up to 6 digits of precision. The proposed higher-order computational framework enables achieving an analytic-formula-like precision of the RL-extraction in the MTLs of complex cross-sections.

4.2 Single-Source Integral Equation for Magneto-Quasistatics in 2D

New single-source integral equation is derived from the traditional volume electric field integral equation (V-EFIE) for the 2D problems of magneto-quasistatics. Consider the problem of current flow along z-coordinate with volumetric current density

j_z in a 2D conductor having arbitrary cross-section with area S. The V-EFIE with respect to the unknown current density j_z is written as

$$\sigma^{-1} j_z(\boldsymbol{\rho}) + i\omega\mu_0 \iint_S G_0(\boldsymbol{\rho}, \boldsymbol{\rho}') j_z(\boldsymbol{\rho}')\, ds' = V_{\text{p.u.l.}},\ \boldsymbol{\rho} \in S, \tag{4.1}$$

where $G_0(\boldsymbol{\rho}, \boldsymbol{\rho}') = -1/(2\pi)\ln(|\boldsymbol{\rho} - \boldsymbol{\rho}'|)$ is the magneto-static Green's function of free space, σ is the bulk conductivity of the conductor, and $V_{\text{p.u.l.}}$ is the per-unit-length voltage drop.

We represent the distribution of the electric field inside the conductor $E_z = \sigma^{-1} j_z$, which satisfies the Helmholtz equation $\nabla^2 E_z + k_\sigma^2 E_z = 0$, as a superposition of cylindrical waves emanating from the conductor's surface and having the magnitude defined by the surface weighting function $J_z(\boldsymbol{\rho}'')$

$$E_z(\boldsymbol{\rho}') = -i\omega\mu_0 \int_{\partial S} G_\sigma(\boldsymbol{\rho}', \boldsymbol{\rho}'') J_z(\boldsymbol{\rho}'')\, d\boldsymbol{\rho}'',\ \boldsymbol{\rho}' \in S. \tag{4.2}$$

In (4.2), $G_\sigma(\boldsymbol{\rho}', \boldsymbol{\rho}'') = -\frac{i}{4} H_0^{(2)}(k_\sigma |\boldsymbol{\rho}' - \boldsymbol{\rho}''|)$ is the Green's function of the conductor media with the wavenumber $k_\sigma = \sqrt{-i\omega\mu_0\sigma}$ satisfying the Helmholtz equation $\nabla^2 G_\sigma + k_\sigma^2 G_\sigma = 0$ everywhere in S excluding the boundary ∂S.

Substitution of (4.2) into (4.1) followed by the restriction of the observation domain to the surface of the conductor yields the Surface-Volume-Surface (SVS) Electric Field Integral Equation (EFIE) with respect to the weighting surface current J_z

$$\begin{aligned} &- i\omega\mu_0 \int_{\partial S} G_\sigma(\boldsymbol{\rho}, \boldsymbol{\rho}'') J_z(\boldsymbol{\rho}'')\, d\boldsymbol{\rho}'' - \sigma(\omega\mu_0)^2 \times \\ &\iint_S G_0(\boldsymbol{\rho}, \boldsymbol{\rho}') \int_{\partial S} G_\sigma(\boldsymbol{\rho}', \boldsymbol{\rho}'') J_z\,(\boldsymbol{\rho}'')\, d\boldsymbol{\rho}'' ds' = V_{\text{p.u.l.}}(\boldsymbol{\rho}), \end{aligned} \tag{4.3}$$

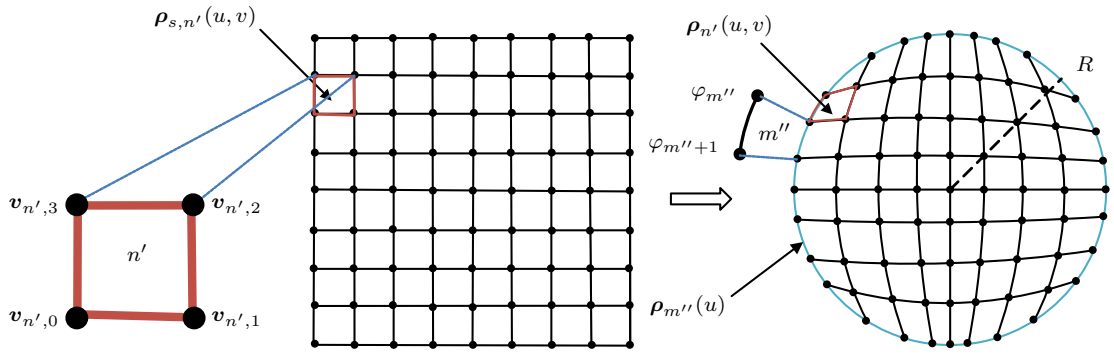

Figure 4.1: Exact mapping from square to circle.

where $\boldsymbol{\rho}\in\partial S$. In the operator form SVS-EFIE (4.3) is

$$\mathtt{T}_{\sigma}^{\partial S,\partial S}\circ J_z+\mathtt{T}_{0}^{\partial S,S}\circ\mathtt{T}_{\sigma}^{S,\partial S}\circ J_z=V_{\text{p.u.l.}}, \tag{4.4}$$

where the integral operators are defined as

$$\mathtt{T}_{\sigma}^{\partial S,\partial S}\circ J_z=-i\omega\mu_0\int_{\partial S}G_{\sigma}(\boldsymbol{\rho},\boldsymbol{\rho}'')J_z(\boldsymbol{\rho}'')\,d\boldsymbol{\rho}'',\ \boldsymbol{\rho}\in\partial S. \tag{4.5}$$

$$\mathtt{T}_{\sigma}^{S,\partial S}\circ J_z=-i\omega\mu_0\int_{\partial S}G_{\sigma}(\boldsymbol{\rho}',\boldsymbol{\rho}'')J_z(\boldsymbol{\rho}'')\,d\boldsymbol{\rho}'',\ \boldsymbol{\rho}'\in S. \tag{4.6}$$

$$\mathtt{T}_{0}^{\partial S,S}\circ j_z=-i\omega\mu_0\sigma\iint_{S}G_0(\boldsymbol{\rho},\boldsymbol{\rho}')j_z(\boldsymbol{\rho}')\,ds',\ \boldsymbol{\rho}\in\partial S. \tag{4.7}$$

4.3 Accurate Geometry Representation

General higher-order representation of cross-sectional geometry has been used in this work. However, to save space and to eliminate the error associated with the geometric representation we consider the case of a single circular conductor for which both cross-section area S and the boundary ∂S can be discretized exactly. The position vector on m''-th line element of the 1D mesh discretizing the circular contour ∂S is defined parametrically as

$$\boldsymbol{\rho}_{m''}(u)=a\ [\cos(\varphi_{m''}(u))\ \hat{\mathbf{x}}+\ \ \sin(\varphi_{m''}(u))\ \hat{\mathbf{y}}], \tag{4.8}$$

where $\varphi_{m''}(u) = \varphi_{m''} + \frac{\varphi_{m''+1}-\varphi_{m''}}{2}(u+1), u \in [-1,1], m'' = 0, 1..., M-1$, M being the total number of line elements, a is the radius of the dielectric cylinder, u is the parametric variable as well as $\varphi_{m''}$ and $\varphi_{m''+1}$ are the starting and ending points of m''-th line element in the contour ∂S.

The exact representation of position-vector on circular cross-section S takes place through a square to circle mapping which is shown in Fig. 4.1. The n'-th square element of the square cross-section is defined parametrically in the barycentric coordinates as $\boldsymbol{\rho}_{Sqr,n'}(u,v) = \sum_{i=0}^{3} \boldsymbol{v}_{n',i}\ S_i(u,v)$. Here $\boldsymbol{v}_{n',i}$ is the i-th vertex of n'-th square patch. Shape functions of the square patches are defined as $S_0(u,v) = 0.25(1-u)(1-v)$, $S_1(u,v) = 0.25(1+u)(1-v)$, $S_2(u,v) = 0.25(1+u)(1+v)$, and $S_3(u,v) = 0.25(1-u)(1+v)$. The position-vector on n'-th curvilinear quadrilateral element in S is defined parametrically in the barycentric coordinates as

$$\boldsymbol{\rho}_{n'}(u,v) = \boldsymbol{\rho}_{Sqr,n'}(u,v)\Big(\sqrt{1-\frac{y^2}{2}}\ \hat{\mathbf{x}} + \sqrt{1-\frac{x^2}{2}}\ \hat{\mathbf{y}}\Big) \tag{4.9}$$

4.4 Higher Order MoM Solution of SVS-EFIE

Discretization of the unknown surface current density $J_z(\boldsymbol{\rho}_{m''}(u))$ on each of the m''-th line element discretizing the conductor's surface ∂S is performed by using Ω monomial basis functions $B_{k''}$ as follows:

$$B_{k''}(u) = u^{k''}, u \in [-1,1], \tag{4.10}$$

where $k'' = 0, ..., \Omega - 1$ and Ω is the maximum order of 1D basis function on each line elements of the contour ∂S. This yields the following expansion of the fictitious current J_z on the contour of the conductor over basis functions $B_{k''}$

$$J_z(u) \cong \sum_{m''=0}^{M-1} \sum_{k''=0}^{\Omega-1} I_{m''k''} B_{k''}(u), \tag{4.11}$$

where k'' is the order of 1D basis function of line elements, and $I_{m''k''}$ is the unknown coefficient of the k''-th order basis function $B_{k''}$ on the m''-th contour element.

Discretization of the unknown volumetric current density $j_z(\boldsymbol{\rho}_{n'}(u,v))$ on each of the n'-th quadrilateral element discretizing conductor's cross-section S is performed by using following basis functions $b_{j'k'}$

$$b_{j'k'}(u,v) = u^{j'} \cdot v^{k'}, u \in [-1,1], v \in [-1,1], \tag{4.12}$$

where $j', k' = 0, 1..., \Psi-1$ and Ψ is the maximum order of 2D basis function of quadrilateral element in the cross-section. Thus, expansion of the volumetric polarization current j_z on the cross-section of the conductor over basis functions $b_{j'k'}$ yields

$$j_z(u,v) \cong \sum_{n'=0}^{N-1} \sum_{j'=0}^{\Psi-1} \sum_{k'=0}^{\Psi-1} j_{n'j'k'}\ b_{j'k'}(u,v), \tag{4.13}$$

where n' is the n'-th 2D quadrilateral element in the volume, N is the total number of quadrilateral elements, j' k' are the order of 2D basis function, and $j_{n'j'k'}$ is the unknown coefficient of $j'k'$-th order basis function $b_{j'k'}$ on n'-th quadrilateral element in the volume. The MoM discretized integral operators $\mathtt{T}_\sigma^{S,S}$, $\mathtt{T}_0^{\partial S,S}$, $\mathtt{T}_\sigma^{S,\partial S}$ and excitation function $V_{p.u.l.}$ is obtained via inner products

$$\begin{aligned} &Z^{S_{n'},\partial S_{m''}}_{j'k',k''} = \langle b_{j'k'}, \langle G_\sigma, B_{k''}\rangle\rangle,\ Z^{\partial S_m,S_{n'}}_{k,j'k'} = \langle B_k, \langle G_0, b_{j'k'}\rangle\rangle, \\ &Z^{\partial S_m,\partial S_{m''}}_{k,k''} = \langle B_k, \langle G_\sigma, B_{k''}\rangle\rangle, \quad V_{m,k} = \langle B_k, V_{p.u.l.}\rangle, \end{aligned} \tag{4.14}$$

where $m, m'' = 0, 1..., M-1,\ k, k'' = 0, 1..., \Omega-1,\ n' = 0, 1..., N-1,$ and $j', k' = 0, 1..., \Psi-1$.

As a result of the HO-MoM discretization of the integral operators $\mathtt{T}_\sigma^{S,\partial S}$, $\mathtt{T}_0^{\partial S,S}$, $\mathtt{T}_\sigma^{\partial S,\partial S}$, and p.u.l. voltage $V_{p.u.l.}$, the SVS-EFIE (4.3) is reduced to the system of linear algebraic equations with respect to the vector $\mathbf{I}$ of unknown coefficients in the expansion of the surface current density J_z in (4.11) as

$$\left(\mathbf{Z}^{\partial S,\partial S} + \mathbf{Z}^{\partial S,S} \cdot \mathbf{\Gamma}^{-1} \cdot \mathbf{Z}^{S,\partial S}\right) \cdot \mathbf{I} = \mathbf{V}. \tag{4.15}$$

The Gram matrix $\mathbf{\Gamma}$ in (4.15) is defined as $\Gamma_{j,k,j',k'} = \langle b_{j,k}, b_{j',k'}\rangle$, where $j, k, j', k' =$

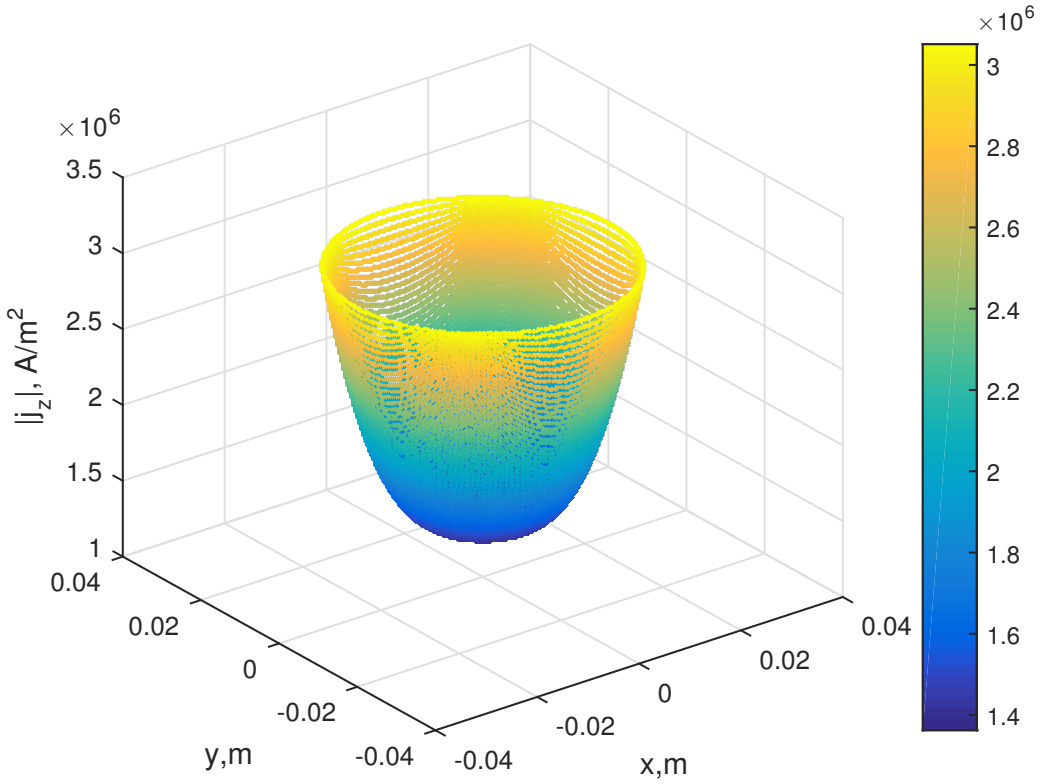

Figure 4.2: Current density j_z at 60Hz in a circular conductor obtained via 4th order HO MoM solution of SVS-EFIE.

$0, 1..., \Psi - 1$.

After solving the system of linear algebraic equations and finding the surface current unknown coefficients $\mathbf{I}$, the vector of expansion coefficients $\mathbf{j}$ in expansion of the polarization current in (4.13) is calculated as $\mathbf{j} = i\omega\mu_0\boldsymbol{\Gamma}^{-1} \cdot \mathbf{Z}^{S,\partial S} \cdot \mathbf{I}$. Addition of the basis functions weighted with coefficients $\mathbf{j}$ yields sought cross-sectional volumetric current density j_z.

4.5 Numerical Results

Numerical implementation of the HO MoM solution of the proposed SVS-EFIE has been done using PTC Mathcad [81] tool. All post-process visualizations are performed

Table 4.1: Values of resistance (R) and inductance (L) extracted via 4th order MoM solution ($\Omega = \Psi = 5$) of new SVS-EFIE equation for circular conductor versus analytic solution.

Analytic		SVS-EFIE	
R, $\mu\Omega/m$	L, $\mu H/m$	R, $\mu\Omega/m$	L, $\mu H/m$
5Hz			
14.32345586	0.787675212	14.32345594	0.787675187
60Hz			
20.012773	0.778065296	20.012782	0.778065260
500Hz			
51.102242	0.75276944	50.91332526	0.75285481

using Mathlab [85]. To demonstrate performance of the proposed HO MoM solution of the SVS-EFIE with $M = 10$ line elements and $N = 25$ cross-sectional elements, the fourth order scheme ($\Omega = \Psi = 5$) was applied to compute the volume current distribution in an aluminum ($\sigma = 3.57 \cdot 10^7$ S/m) circular conductor of 0.025m radius centred at the origin under $V_{p.u.l.} = 1$ V/m excitation at 5Hz, 60Hz, and 500Hz. The solutions $j_z(\boldsymbol{\rho})$ were compared against the analytical result [76] and plotted against radial coordinate $r = \sqrt{x^2 + y^2}$ in Fig. 4.3 alongside with the respective relative error shown in Fig. 4.4. Fig. 4.2 shows cross-sectional distribution of j_z at 60Hz. Values of the extracted p.u.l. resistance R and inductance L at 5Hz, 60Hz, and 500Hz obtained are presented in Table 4.1 where analytic values [76] are provided for reference. One can observe natural degradation of the accuracy in the HO MoM solution with fixed order of the basis functions and discretization meshes as frequency increases. This occurs due to a stronger skin-effect. An increase in orders Ω and Ψ and/or the density of the meshes M and N reduces such error exponentially more effectively than a low order MoM solution [75]. To show the computational complexity of the proposed HO MoM solution of the SVS-EFIE the results also obtained with orders $\Omega = \Psi = 1, 2,$ and 3 at $f = 60$ Hz. The HO MoM solutions of SVS-EFIE obtained from a system with Intel core i7-3370 processor running at 3.4GHz. The computational time of the 1st order of MoM solution of SVS-EFIE including 80 unknowns is 0.4712509679999999 seconds and the accuracy of the extracted values of R and L is up to 4 digits. The computational time of the second order of MoM solution including 120 unknowns is

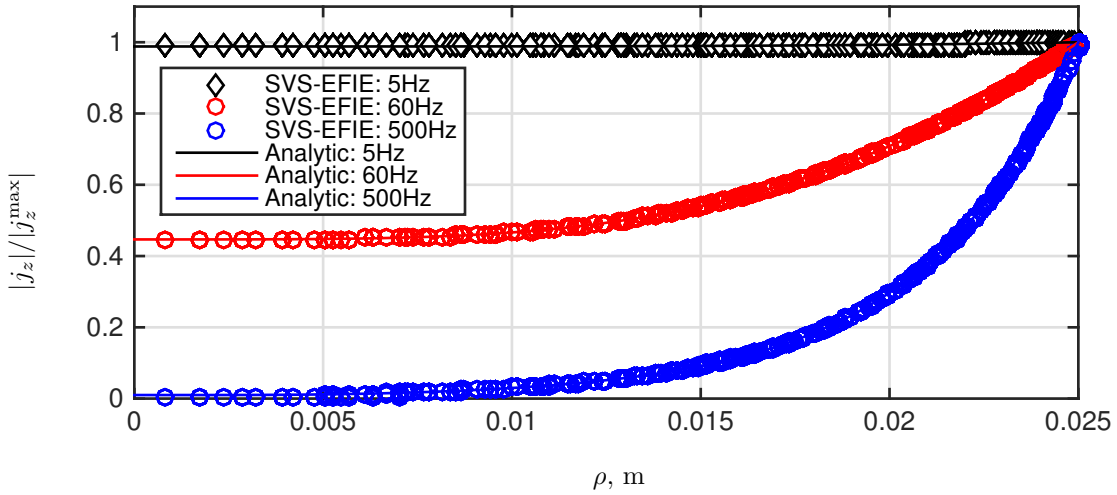

Figure 4.3: Current density j_z at 5Hz, 60Hz, and 500Hz in a circular conductor obtained via 4th order HO MoM solution of SVS-EFIE vs. analytic solution.

2.5548365209999999 seconds and the accuracy of the extracted values of R and L for this solution is up to 7 digits. The computational time of the third order of MoM solution including 160 unknowns is 7.5655723369999999 seconds and the accuracy of the extracted values of R and L for this solution is up to 8 digits.

4.6 Full-Wave Formulation

New single-source integral equation can be derived from the volume electric field integral equation (V-EFIE) for full-wave scattering problems.Consider a 2D TM-scattering problem for a dielectric cylinder directed along z-coordinate and having arbitrary cross-section with area S. The V-EFIE in the electrodynamic case is written as [31], [66]

$$E_z(\boldsymbol{\rho}) - k_0^2(\epsilon - 1)\iint\limits_S G_0(\boldsymbol{\rho}, \boldsymbol{\rho}')E_z(\boldsymbol{\rho}')\, ds' = E_z^{\text{inc}}(\boldsymbol{\rho}),\ \boldsymbol{\rho} \in S \tag{4.16}$$

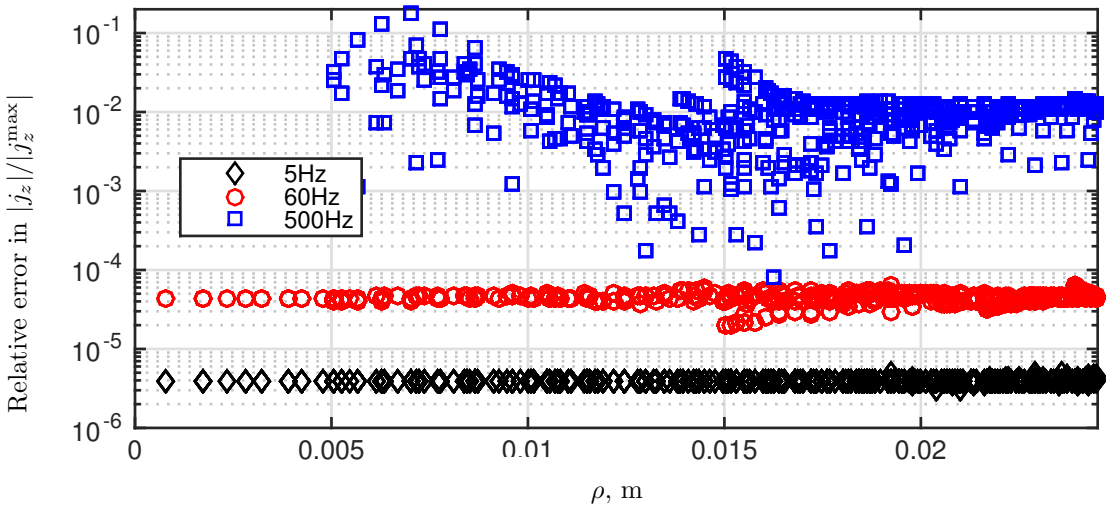

Figure 4.4: Relative error in current density j_z at 5Hz, 60Hz, and 500Hz in circular conductor obtained via 4th order HO MoM solution of SVS-EFIE.

where E_z is the unknown distribution of the electric field inside the cylinder,$G_0(\boldsymbol{\rho},\boldsymbol{\rho}')=-\frac{i}{4}H_0^{(2)}(k_0|\boldsymbol{\rho}-\boldsymbol{\rho}'|)$ is the Green's function of free space, $\epsilon=\varepsilon+\sigma/(i\omega\varepsilon_0)=\varepsilon(1+i\tan\delta)$ is the complex relative permittivity of the dielectric cylinder, and E_z^{inc} is the incident field impinging on the cylinder. We represent the distribution of the electric field inside the cylinder E_z satisfying the Helmholtz equation $\nabla^2 E_z+k_\epsilon^2 E_z=0$ as a superposition of cylindrical waves emanating from the cylinder's surface and having the strength defined with the function $\mathtt{J}_z(\boldsymbol{\rho}'')$ playing the role of an auxiliary surface current density

$$E_z(\boldsymbol{\rho}')=-i\omega\mu_0\int_{\partial S}G_\epsilon(\boldsymbol{\rho}',\boldsymbol{\rho}'')\,\mathtt{J}_z(\boldsymbol{\rho}'')\,d\boldsymbol{\rho}'',\ \boldsymbol{\rho}'\in S. \tag{4.17}$$

In (4.17), $G_\epsilon(\boldsymbol{\rho}',\boldsymbol{\rho}'')=-\frac{i}{4}H_0^{(2)}(k_\epsilon|\boldsymbol{\rho}'-\boldsymbol{\rho}''|)$ is the Green's function of the dielectric media with the wavenumber $k_\epsilon=\omega\sqrt{\mu_0\varepsilon_0\epsilon}$ that satisfies the Helmholtz equation $\nabla^2 G_\epsilon+k_\epsilon^2 G_\epsilon=0$ everywhere in S excluding the boundary ∂S. Substitution of (4.17) into (4.16) followed by the restriction of the observation domain to the surface of the

scatterer yields the desired SVS-EFIE with respect to the unknown current density

$$-i\omega\mu_0 \int_{\partial S} G_\epsilon(\boldsymbol{\rho},\boldsymbol{\rho}'')\mathtt{J}_z(\boldsymbol{\rho}'')\,d\boldsymbol{\rho}'' + i\omega\mu_0 k_0^2(\epsilon-1)\iint_S G_0(\boldsymbol{\rho},\boldsymbol{\rho}')\int_{\partial S} G_\epsilon(\boldsymbol{\rho}',\boldsymbol{\rho}'') \cdot \mathtt{J}_z\,(\boldsymbol{\rho}'')\,d\boldsymbol{\rho}''ds' = E_z^{\text{inc}}(\boldsymbol{\rho}),\ \boldsymbol{\rho}\in\partial S. \quad (4.18)$$

In the operator form SVS-EFIE (4.18) is expressed as follows:

$$\mathtt{T}_\epsilon^{\partial S,\partial S}\circ\mathtt{J}_z + \mathtt{T}_0^{\partial S,S}\circ\mathtt{T}_\epsilon^{S,\partial S}\circ\mathtt{J}_z = E^{\text{inc}} \quad (4.19)$$

where the integral operators are defined as

$$\mathtt{T}_\epsilon^{\partial S,\partial S}\circ\mathtt{J}_z = -i\omega\mu_0\int_{\partial S} G_\epsilon(\boldsymbol{\rho},\boldsymbol{\rho}'')\mathtt{J}_z(\boldsymbol{\rho}'')\,d\boldsymbol{\rho}'',\ \boldsymbol{\rho}\in\partial S \quad (4.20)$$

$$\mathtt{T}_\epsilon^{S,\partial S}\circ\mathtt{J}_z = i\omega\mu_0\int_{\partial S} G_\epsilon(\boldsymbol{\rho}',\boldsymbol{\rho}'')\mathtt{J}_z(\boldsymbol{\rho}'')\,d\boldsymbol{\rho}'',\ \boldsymbol{\rho}'\in S \quad (4.21)$$

$$\mathtt{T}_0^{\partial S,S}\circ E_z = k_0^2(\epsilon-1)\iint_S G_0(\boldsymbol{\rho},\boldsymbol{\rho}')E_z(\boldsymbol{\rho}')\,ds',\ \boldsymbol{\rho}\in\partial S. \quad (4.22)$$

4.7 Discretization of the Scatterer Geometry and Higher Order Method of Moments Solution of SVS-EFIE

4.7.1 Discretization of the scatterer geometry

The position vector of m''-th line element of the 1D mesh discretizing the circular contour ∂S is defined parametrically as

$$\boldsymbol{\rho}_{m''}(u)=R\,[cos(\varphi_{m''}(u))\ \hat{\mathbf{x}} + \ sin(\varphi_{m''}(u))\ \hat{\mathbf{y}}],\ \ -1\leqslant u\leqslant 1 \quad (4.23)$$

where $\varphi_{m''}(u)=\varphi_{m''}+\frac{\varphi_{m''+1}-\varphi_{m''}}{2}(u+1)$ and $m''=0,1...,M-1$. Here M is the total number of line elements, R is the radius of the dielectric cylinder, u is the parametric

variable as well as $\varphi_{m''}$ and $\varphi_{m''+1}$ are the starting and ending points of m''-th line element of the contour. The exact representation of position-vector on circular cross-section S happens through a square to circle mapping, which is shown in Fig. 4.1. The n'-th square element of the square cross-section is defined parametrically in the barycentric coordinates [25] as

$$\boldsymbol{\rho}_{s,n'}(u,v) = \sum_{i=0}^{3} \boldsymbol{v}_{n',i}\ S_i(u,v), \quad -1 \leqslant u,v \leqslant 1 \tag{4.24}$$

where $n' = 0, 1..., N-1$. Here N is the total number of square elements in the volume, u and v are the parametric variables, and $\boldsymbol{v}_{n',i}$ is the i-th vertex of n'-th square patch.

Shape functions of the square patches are defined as $S_0(u,v) = 0.25(1-u)(1-v)$, $S_1(u,v) = 0.25(1+u)(1-v)$, $S_2(u,v) = 0.25(1+u)(1+v)$, and $S_3(u,v) = 0.25(1-u)(1+v)$.

The position-vector on n'-th quadrilateral element of the cross-section S is defined parametrically in the barycentric coordinates as

$$\boldsymbol{\rho}_{n'}(u,v) = x\ \sqrt{1-\frac{y^2}{2}}\ \hat{\mathbf{x}} + y\ \sqrt{1-\frac{x^2}{2}}\ \hat{\mathbf{y}}, \quad -1 \leqslant u,v \leqslant 1 \tag{4.25}$$

where

$$x = \boldsymbol{\rho}_{s,n'}(u,v) \cdot\ \hat{\mathbf{x}}, \tag{4.26}$$

$$y = \boldsymbol{\rho}_{s,n'}(u,v) \cdot\ \hat{\mathbf{y}}, \tag{4.27}$$

and $n' = 0, 1..., N-1$. Here N is the total number of quadrilateral elements in the volume. By using this mapping technique each square patch maps to a quadrilateral element. The reason for mapping is to have an exact analytical representation of the circular scatterer geometry (see: Fig. 4.1). Discretization of the unknown surface current density $\mathtt{J}_z(\boldsymbol{\rho}_{m''}(u))$ on each m''-th line element discretizing the scatterer's surface ∂S is performed by using the following MΩ monomial basis functions

$$B_{k''}(u) = u^{k''}, \quad -1 \leqslant u \leqslant 1 \tag{4.28}$$

where $k'' = 0, 1, ..., \Omega$ and Ω is the maximum order of 1D basis function of line elements in the contour. Thus, expansion of the fictitious current $\mathtt{J}_z$ on the contour of the scatterer over basis function $B_{k''}$ is the following

$$J_z(u) \cong \sum_{m''=0}^{M-1} \sum_{k''=0}^{\Omega} I_{m''k''} B_{k''}(u), \quad -1 \leqslant u \leqslant 1 \tag{4.29}$$

where k'' is the order of 1D basis function of line elements, and $I_{m''k''}$ is the unknown coefficient of k''-th order basis function $B_{k''}$ on m''-th line element in the contour.

Discretization of the unknown volumetric polarization current $j_z(\boldsymbol{\rho}_{n'}(u, v))$ on each n'-th quadrilateral element discretizing the scatterer's volume S is performed by using the basis function $b_{j'k'}$ defined as

$$b_{j'k'}(u, v) = u^{j'} v^{k'}, \quad -1 \leqslant u, v \leqslant 1 \tag{4.30}$$

where $j' = 0, 1, ..., \Psi$, $k' = 0, 1, ..., \Psi - j'$ and Ψ is the maximum order of 2D basis function of quadrilateral element in the cross-section. Thus, expansion of the volumetric polarization current j_z on the cross-section of the scatterer over basis function $b_{j'k'}$ is the following

$$j_z(u, v) \cong \sum_{n'=0}^{N-1} \sum_{j'=0}^{\Psi} \sum_{k'=0}^{\Psi - j'} i_{n'j'k'} \; b_{j'k'}(u, v), \quad -1 \leqslant u, v \leqslant 1 \tag{4.31}$$

where n' is the n'-th 2D quadrilateral element in the volume, N is the total number of quadrilateral elements, j' k' are the order of 2D basis function, and $i_{n'j'k'}$ is the unknown coefficient of $j'k'$-th order basis function $b_{j'k'}$ on n'-th quadrilateral element in the volume.

4.7.2 Higher order method of Moments solution of SVS-EFIE

4.7.2.1 HO-MoM discretization of SVS-EFIE's surface-to-volume operator $\mathrm{T}_{\epsilon}^{S,\partial S}$

The discretized form of the integral operator $\mathrm{T}_{\epsilon}^{S,\partial S}$ is tested by inner product with 2D higher order test function. The matrix elements of the result are defined as

$$\mathcal{Z}_{j'k',k''}^{S_{n'},\partial S_{m''}} = \langle b_{j'k'}, \langle G_\epsilon, B_{k''} \rangle \rangle = -i\omega\mu_0 \left(\frac{\pi R}{M}\right) \int_{-1}^{1}\int_{-1}^{1} du'dv' b_{j'k'}(u',v') f_{n'}(u',v') \cdot \int_{-1}^{1} du'' B_{k''}(u'') G_\epsilon(\boldsymbol{\rho}_{n'}(u',v'), \boldsymbol{\rho}_{m''}(u'')) \quad (4.32)$$

where $f_{n'}(u',v') = \sqrt{|g_{n'}(u',v')|}$ is the determinant of Jacobian matrix on the n'-th quadrilateral element in the volume. Introducing consecutive indexing for all of the $N\Psi^2$ 2D higher-order test functions in the volume and all of the $M\Omega$ 1D higher-order line basis functions on the surface we define the total matrix representation of this operator to be

$$Z_{p',q''}^{S,\partial S} = \mathcal{Z}_{j'k',k''}^{S_{n'},\partial S_{m''}} \quad (4.33)$$

where $p' = \frac{1}{2}[n'(\Psi^2+3\Psi+2)+j'(2\Psi-j'+3)+2k'$ and $q'' = m''\Omega+k''$, $n' = 0,1,...,N-1$, $j' = 0,1,...,\Psi$, $k' = 0,1,...,\Psi-j'$, $m'' = 0,1,...,M-1$, and $k'' = 0,1,...,\Omega$.

4.7.2.2 HO-MoM discretization of SVS-EFIE's volume-to-surface operator $\mathrm{T}_{0}^{\partial S,S}$

The discretized form of the integral operator $\mathrm{T}_{0}^{\partial S,S}$ is tested by inner product with 1D higher order test function. The matrix elements of the result are defined as

$$\mathcal{Z}_{k,j'k'}^{\partial S_m,S_{n'}} = \langle B_k, \langle G_0, b_{j'k'} \rangle \rangle = k_0^2(\epsilon-1) \left(\frac{\pi R}{M}\right) \int_{-1}^{1} du\ B_k(u) \int_{-1}^{1}\int_{-1}^{1} du'dv' \cdot b_{j'k'}(u',v')\ f_{n'}(u',v') G_0(\boldsymbol{\rho}_m(u), \boldsymbol{\rho}_{n'}(u',v')), \quad (4.34)$$

where 1D higher order test function is defined as

$$B_k(u) = u^k, \ \ -1 \leqslant u \leqslant 1. \tag{4.35}$$

Here $k = 0, 1, ..., \Omega$ and Ω is the maximum order of 1D basis function of line elements in the contour. Introducing consecutive indexing for all of the $M\Omega$ 1D higher-order line basis functions on the surface and all of the $N\Psi^2$ 2D higher-order test functions in the volume, we define the total matrix representation of this operator to be

$$Z_{q,p'}^{\partial S,S} = \mathcal{Z}_{k,j'k'}^{\partial S_m, S_{n'}} \tag{4.36}$$

where $m = 0, 1, ..., M-1$, $k = 0, 1, ..., \Omega$, $n' = 0, 1, ..., N-1$, and $j' = 0, 1, ..., \Psi$, $k' = 0, 1, ..., \Psi - j'$.

4.7.2.3 HO-MoM discretization of SVS-EFIE's surface-to-surface operator $\mathtt{T}_\epsilon^{\partial S,\partial S}$

The discretized form of the integral operator $\mathtt{T}_\epsilon^{\partial S,\partial S}$ is tested by inner product with 1D higher order test function. The matrix elements of the result are:

$$\mathcal{Z}_{k,k''}^{\partial S_m, \partial S_{m''}} = \langle B_k, \langle G_\epsilon, B_{k''} \rangle \rangle = -i\omega\mu_0 \left(\frac{\pi R}{M}\right)^2 \int_{-1}^{1} du \ B_k(u) \int_{-1}^{1} du'' B_{k''}(u'') \cdot G_\epsilon(\boldsymbol{\rho}_m(u), \boldsymbol{\rho}_{m''}(u'')). \tag{4.37}$$

Introducing consecutive indexing for all of the $M\Omega$ 1D line basis functions on the surface, we define the total matrix representation of this operator to be

$$Z_{q,q''}^{\partial S,\partial S} = \mathcal{Z}_{k,k''}^{\partial S_m, \partial S_{m''}} \tag{4.38}$$

where $m, m'' = 0, 1, ..., M-1$ $k, k'' = 0, 1, ..., \Omega$, and $q = m\Omega + k$.

4.7.2.4 HO-MoM discretization of $E_z^{\mathbf{inc}}$

The discretized form of the excitation E_z^{inc} is calculated by testing it with 1D higher order test function. Vector elements of the result are defined to be

$$V_{m,k} = \langle B_k, E_z^{\text{inc}} \rangle = \frac{\pi R}{M} \int_{-1}^{1} du \; B_k(u) \; E_{zm}^{\text{inc}}(u). \tag{4.39}$$

Total vector representation of this operator is as

$$[V]_{(m\Omega+k)\times 1} = V_{m,k}, \tag{4.40}$$

where $m = 0, 1, ..., M-1$ and $k = 0, 1, ..., \Omega$.

As a result of the HO-MoM discretization of the integral operators $\mathtt{T}_\epsilon^{S,\partial S}$, $\mathtt{T}_0^{\partial S,S}$, $\mathtt{T}_\epsilon^{\partial S,\partial S}$, and the incident field E_z^{inc}, the SVS-EFIE (4.18) is reduced to a system of linear algebraic equations with respect to the vector of unknown coefficients $I_{[M\Omega,1]}$ in the expansion of the auxiliary surface current density (4.29) as

$$\left(Z^{\partial S,\partial S} + Z^{\partial S,S} \cdot \Gamma^{-1} \cdot Z^{S,\partial S}\right) \cdot I = V, \tag{4.41}$$

where each element of Gram matrix Γ is defined as

$$\Gamma_{p',p'} = \begin{cases} \int_{-1}^{1} \int_{-1}^{1} du \; dv f_{n_o}(u,v) u^{j_o} v^{k_o} u^{j_s} v^{k_s}, \text{ if } n_o = n_s, \\ 0, \text{ otherwise,} \end{cases} \tag{4.42}$$

where $f_{n_0}(u,v) = \sqrt{|g_{n_o}(u,v)|}$, $n_o = 0, 1, ..., N-1$, $j_o, j_s = 0, 1, ..., \Psi$, and $k_o, k_s = 0, 1, ..., \Psi - j_o$. After solving the system of linear algebraic equations and finding the unknown coefficients, the polarization current j at the centroid of quadrilateral patches is calculated using

$$j = i\omega\mu_0 \Gamma^{-1} \cdot Z^{S,\partial S} \cdot I. \tag{4.43}$$

4.8 Numerical Results

Numerical implementation of the HO MoM solution of the proposed SVS-EFIE has been done using PTC Mathcad [81] tool. All post-process visualizations are performed using Mathlab [85].

We consider the problem of TM-polarized plane wave scattering on a circular dielectric cylinder with a cross-sectional radius $R = 1\,\text{m}$ and a dielectric permittivity $\epsilon = 2$. The cylinder is illuminated by the plane wave at f=90 MHz incoming from the $\phi = 180°$ direction with magnetic field defined as $E_z^{\text{inc}}(\boldsymbol{\rho}) = e^{-i\boldsymbol{k}\cdot\boldsymbol{\rho}}$ V/m, where $\boldsymbol{k}$ is $k_0\hat{\mathbf{k}}$, $\hat{\mathbf{k}}$ is the unit vector in propagation direction. The field inside the cylinder is computed after expansion coefficients $[I]$ in (4.29) were obtained from the solution of the HO-MoM discretization of SVS-EFIE (B.24) and is shown in Fig. 4.5. The HO-MoM discretization of the SVS-EFIE used $M = 50$ 1D elements discretizing the exact boundary of the cylinder, $N = 81$ 2D elements discretizing its exact cross-section, $\Omega = 5$ and $\Psi = 5$. Distribution of relative error in the magnitude of total electric field at 90 MHz between the proposed HO-MoM solution of the SVS-EFIE (4.18) and the Mie series solution is shown in Fig. 4.6. The average relative error between the analytic Mie series solutions and the proposed HO-MoM solution of the SVS-EFIE is 3×10^{-5}. Fig. 4.7 shows the average relative error obtained by the HO-MoM discretization of the SVS-EFIE (4.18) with order ($\Omega = \Psi$) refinement and electrical sampling rate refinement from 11 elements per wavelength to 33 elements per wavelength. The accuracy beyond seven digits is obtained. The trade-off, however, is that HO methods are more difficult to implement as they require preservation of the desired accuracy throughout all stages of the numerical scheme including: the mesh based representation of the geometry, choice of basis functions approximating the unknown field, rules for integration of reaction integrals, evaluation of matrix-vector products.

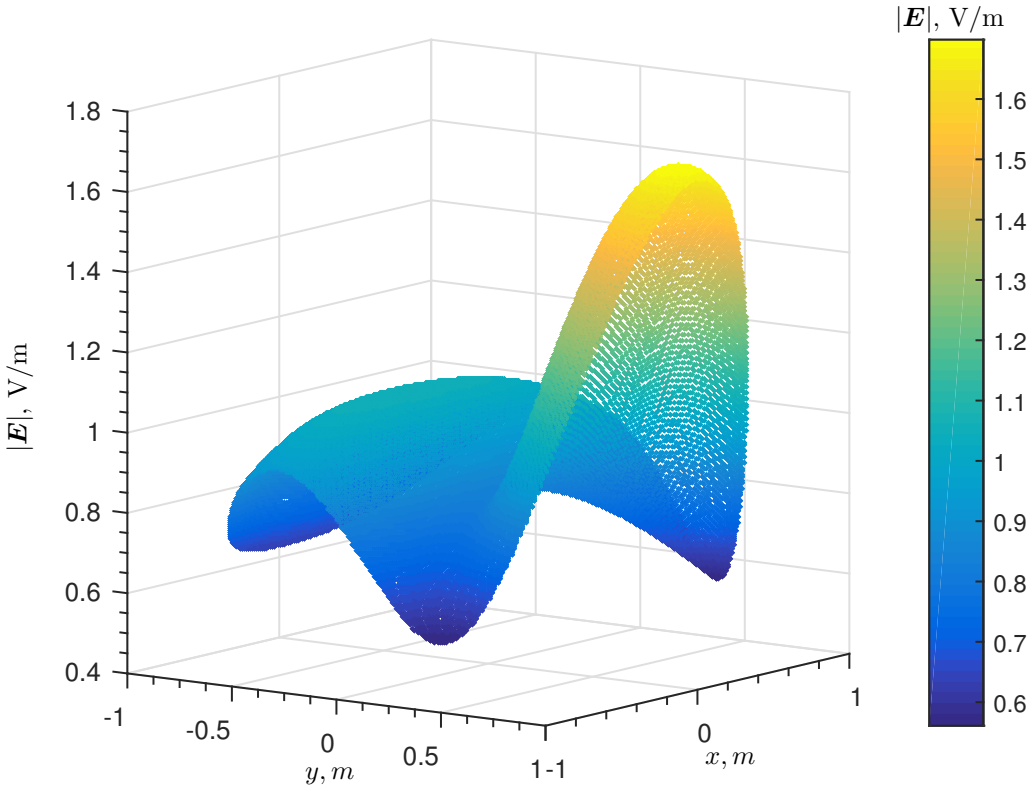

Figure 4.5: Distribution of magnitude of total electric field inside of the dielectric cylinder of radius $R = 1$ m and relative permittivity $\epsilon = 2$ in the problem of TM-polarized plane wave scattering at 90 MHz obtained from the proposed HO-MoM solution of the SVS-EFIE (4.18) with $N = 81$, $M = 50$, $\Omega = 5$ and $\Psi = 5$.

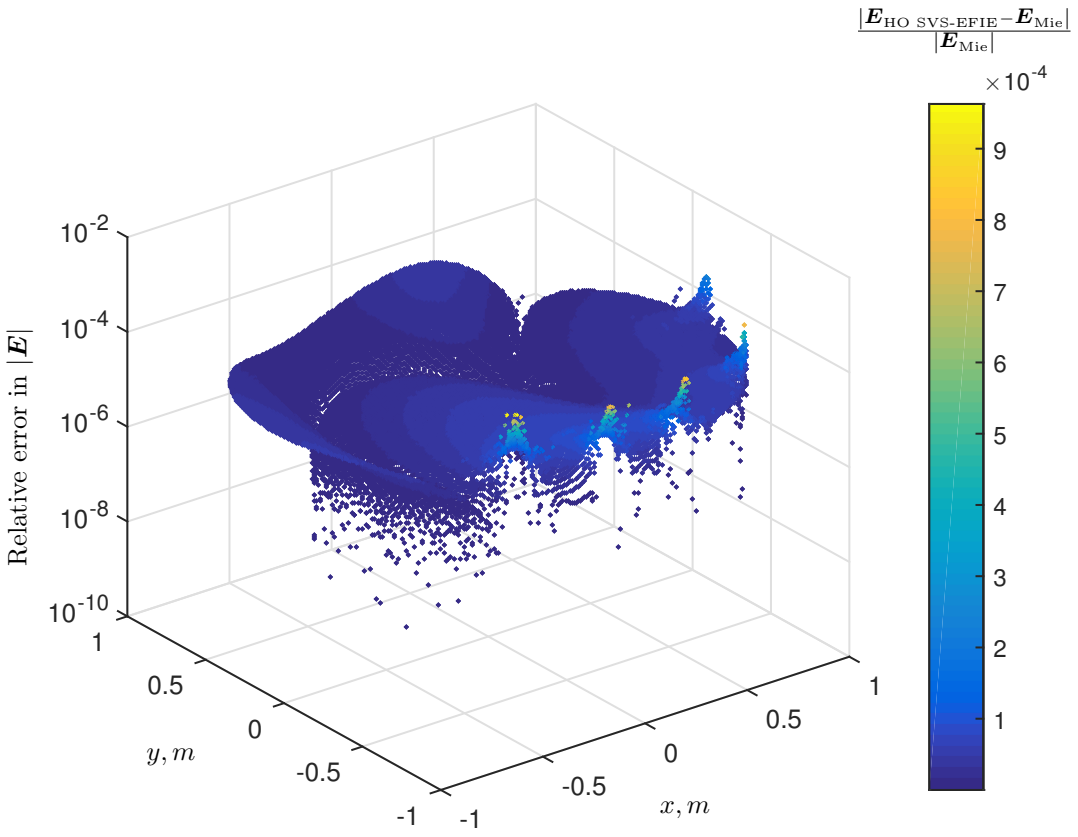

Figure 4.6: Distribution of relative error in the magnitude of total electric field at 90 MHz between the proposed HO-MoM solution of the SVS-EFIE (4.18) with $\Omega = 5$, $\Psi = 5$, $N = 81$, and $M = 50$ and the Mie series solution.

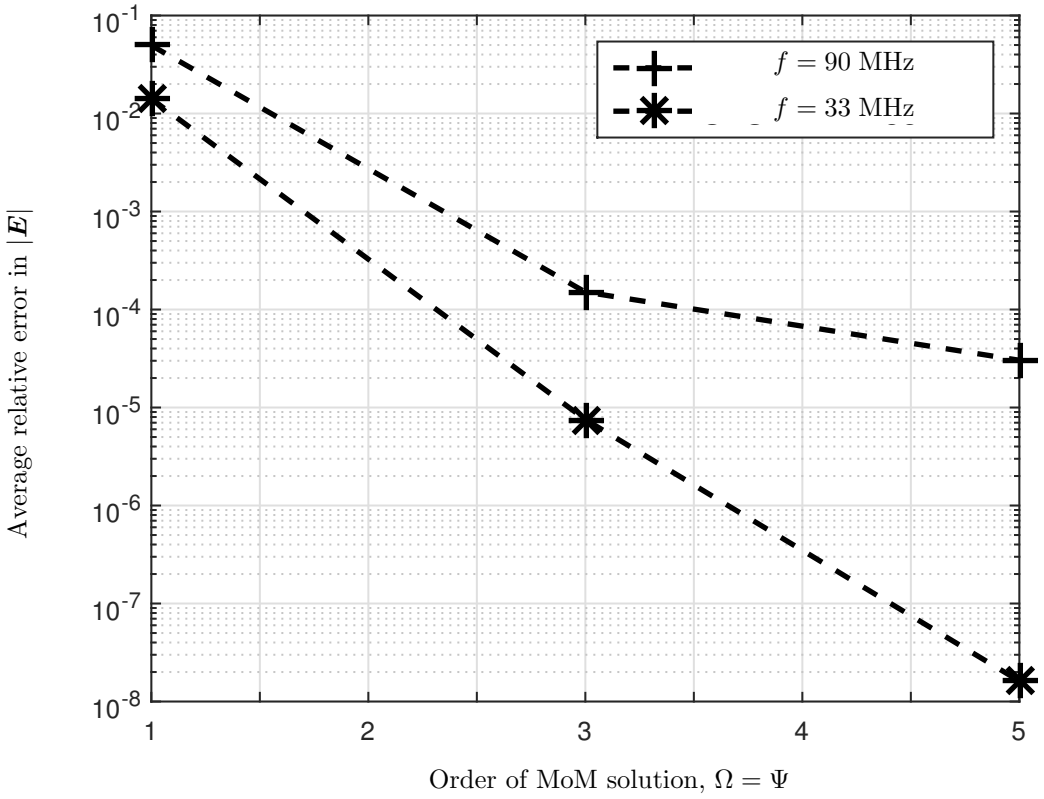

Figure 4.7: Average relative error in the magnitude of total electric field at 90 MHz and 33 MHz between the proposed HO-MoM solution of the SVS-EFIE (4.18) with $N = 81$, $M = 50$ and the Mie series solution as a function of different order of the MoM solution.

5

Accurate Characterization of Coaxial Transmission Lines via Higher Order Moment Method Solution of Novel Single-Source Surface Integral Equations

5.1 Introduction

Coaxial cables are used for transmission of high and low energy signals in a broad variety of electrical and electronic systems. Their applications include high-speed data transmission, high-voltage delivery in power systems, feeds of radio-frequency signals to various types of antennas, and many other. Popularity of the coaxial transmission lines is owed to the ease of their manufacturing, their favourable dispersive characteristics in broad range of frequencies, minimal electromagnetic interference

produced by transmitted signal in differential mode, and other qualities [76].

This work expands on [77] to propose a computational framework that characterizes coaxial cables with analytic like accuracy in the regimes where an analytic solution is unavailable while maintaining low use of the CPU time and memory. The methodology is based on a higher-order (HO) Method of Moments (MoM) solution of a new single-source integral equation (SSIE) under exact meshing of the cross-sectional geometry. Such a numerical scheme answers the stringent requirements on the speed and accuracy imposed on the commercial resistance and inductance extractors [78]. The latter require 1% error tolerance on the extracted per-unit-length (p.u.l.) parameters from near DC frequencies at which the resistive term of the impedance is four orders of magnitude greater than the inductive term to high frequencies at which the inductive term of the impedance exceeds the resistance by four orders of magnitude. This imposes up to a 6 digit accuracy requirement on the numerically evaluated electromagnetic fields. At the same time computations at 100 frequency points within such range must be completed within seconds [79]. To achieve required accuracy under this tight constraint on the CPU time we developed numerical scheme here and in [77], which provides exponentially fast error reduction upon linear increase in degrees of freedom of the discretized problem.

The boundary element formulation of the inductance and resistance extraction problem is enabled by the recently proposed SSIE termed Surface-Volume-Surface Electric Field Integral Equation (SVS-EFIE) [75]. The unknown quantity in SVS-EFIE is a fictitious current playing the role of a weighting function in the single-source integral representation of the volumetric current density in the cross-section of the transmission line. This unknown function on the contours of the cross-sectional geometry is constrained through the classical volume EFIE of magneto-quasi-statics enforced on the same cross-sectional contours. It produces field translations from the conductors boundaries to their cross-sections and back to the boundaries necessitating use of both 1D meshes discretizing boundaries of the conductors and 2D meshes discretizing their cross-sections.

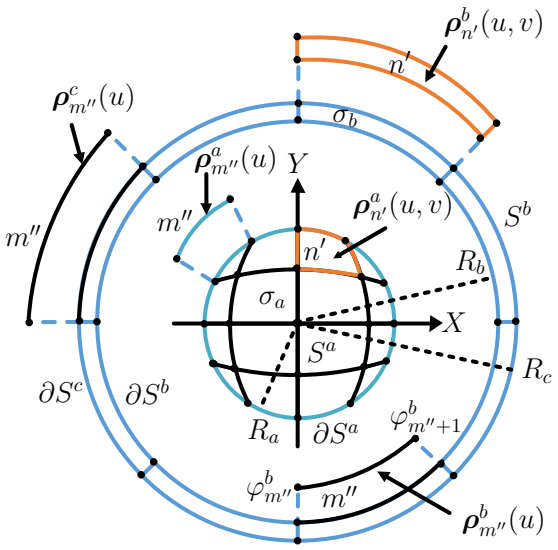

Figure 5.1: Exact discretization of the center conductor of the coaxial cable using square-to-circle mapping and the sheath conductor in cylindrical coordinates.

5.2 SVS-EFIE of Magneto-Quasi-Statics in 2D

Consider a coaxial cable with one inner conductor and a metal sheath. The inner conductor has circular cross-section with area S^a, boundary ∂S^a, and conductivity σ_a. The sheath has conductivity σ_b, cross-section area S^b, inner boundary ∂S^b and outer boundary ∂S^c. The line is infinitely long along the z-coordinate as depicted in Fig. 5.1.

The system of traditional volume electric field integral equations (V-EFIE) for the 2-conductor 2D problems with respect to two unknown volumetric current densities j_a

in the inner conductor and j_b in the sheath is written, as follows:

$$\begin{cases} j_a(\boldsymbol{\rho})/\sigma_a + i\omega\mu_0 \iint\limits_{S^a} G_0(\boldsymbol{\rho},\boldsymbol{\rho}')j_a(\boldsymbol{\rho}')\,ds' \\ \quad + i\omega\mu_0 \iint\limits_{S^b} G_0(\boldsymbol{\rho},\boldsymbol{\rho}')j_b(\boldsymbol{\rho}')\,ds' = V_{a,\text{p.u.l.}}, \quad \boldsymbol{\rho}\in S_a, \\ j_b(\boldsymbol{\rho})/\sigma_b + i\omega\mu_0 \iint\limits_{S^a} G_0(\boldsymbol{\rho},\boldsymbol{\rho}')j_a(\boldsymbol{\rho}')\,ds' \\ \quad + i\omega\mu_0 \iint\limits_{S^b} G_0(\boldsymbol{\rho},\boldsymbol{\rho}')j_b(\boldsymbol{\rho}')\,ds' = V_{b,\text{p.u.l.}}, \quad \boldsymbol{\rho}\in S_b, \end{cases}, \tag{5.1}$$

where $\boldsymbol{\rho}$ is the position vector of the observation point, $G_0(\boldsymbol{\rho},\boldsymbol{\rho}') = -1/(2\pi)\ln(|\boldsymbol{\rho}-\boldsymbol{\rho}'|)$ is the magneto-static Green's function of free space. In (5.1), $V_{a,\text{p.u.l.}}$ and $V_{b,\text{p.u.l.}}$ are the per-unit-length voltage drops in the coaxial cable inner conductor S^a and its sheath S^b, respectively.

The SVS-EFIE [75] represents the distribution of the volumetric current densities j_a and j_b inside the conductors as a superposition of cylindrical waves emanating from the conductor's surface and having the magnitude defined by the surface weighting functions $J_a(\boldsymbol{\rho}'')$ and $J_b(\boldsymbol{\rho}'')$ as

$$j_a(\boldsymbol{\rho}') = -i\omega\mu_0 \oint\limits_{\partial S^a} G_{\sigma_a}(\boldsymbol{\rho}',\boldsymbol{\rho}'')J_a(\boldsymbol{\rho}'')\,d\boldsymbol{\rho}'', \quad \boldsymbol{\rho}'\in S_a, \tag{5.2}$$

and

$$j_b(\boldsymbol{\rho}') = -i\omega\mu_0 \oint\limits_{\partial S^b + \partial S^c} G_{\sigma_b}(\boldsymbol{\rho}',\boldsymbol{\rho}'')J_b(\boldsymbol{\rho}'')\,d\boldsymbol{\rho}'', \quad \boldsymbol{\rho}'\in S_b. \tag{5.3}$$

In (5.2), $G_{\sigma_a}(\boldsymbol{\rho}',\boldsymbol{\rho}'') = -iH_0^{(2)}(k_{\sigma_a}|\boldsymbol{\rho}'-\boldsymbol{\rho}''|)/4$ is the full-wave Green's function of a homogeneous medium with conductivity of σ_a and wavenumber $k_{\sigma_a} = \sqrt{-i\omega\mu_0\sigma_a}$. It satisfies the Helmholtz equation $\nabla^2 G_{\sigma_a} + k_{\sigma_a}^2 G_{\sigma_a} = 0$ everywhere in S^a excluding the boundary ∂S^a. The Green function of the homogeneous medium with conductivity of the sheath conductor, $G_{\sigma_b}(\boldsymbol{\rho}',\boldsymbol{\rho})$, is the same as the inner conductor Green's function but with the wavenumber $k_{\sigma_b} = \sqrt{-i\omega\mu_0\sigma_b}$.

Substitution of (5.2) and (5.3) into (5.1) followed by the restriction of the observation domain to the surface of the conductors yields a system of SVS-EFIEs with respect to weighting surface currents J_a and J_b as

$$\begin{bmatrix} \mathcal{T}_{\sigma_a}^{\partial S^a,\partial S^a}\circ J_a \\ \mathcal{T}_{\sigma_b}^{\partial S^b,\partial S^b}\circ J_b \end{bmatrix}+\begin{bmatrix} \mathcal{T}_{0}^{\partial S^a,S^a} & \mathcal{T}_{0}^{\partial S^a,S^b} \\ \mathcal{T}_{0}^{\partial S^b,S^a} & \mathcal{T}_{0}^{\partial S^b,S^b} \end{bmatrix}\circ\begin{bmatrix} \mathcal{T}_{\sigma_a}^{S^a,\partial S^a}\circ J_a \\ \mathcal{T}_{\sigma_b}^{S^b,\partial S^b}\circ J_b \end{bmatrix}=\begin{bmatrix} \sigma_a V_{a,\text{p.u.l.}} \\ \sigma_b V_{b,\text{p.u.l.}} \end{bmatrix}. \tag{5.4}$$

The integral operators in (5.4) are defined as

$$\mathcal{T}_{\sigma_a}^{\partial S^a,\partial S^a}\circ J_a = -i\omega\mu_0 \oint\limits_{\partial S^a} G_{\sigma_a}(\boldsymbol{\rho},\boldsymbol{\rho}'')J_a(\boldsymbol{\rho}'')\,d\boldsymbol{\rho}'', \tag{5.5}$$

$$\mathcal{T}_{\sigma_b}^{\partial S^b,\partial S^b}\circ J_b = -i\omega\mu_0 \oint\limits_{\partial S^b+\partial S^c} G_{\sigma_b}(\boldsymbol{\rho},\boldsymbol{\rho}'')J_b(\boldsymbol{\rho}'')\,d\boldsymbol{\rho}'', \tag{5.6}$$

$$\mathcal{T}_{\sigma_a}^{S^a,\partial S^a}\circ J_a = -i\omega\mu_0 \oint\limits_{\partial S^a} G_{\sigma_a}(\boldsymbol{\rho}',\boldsymbol{\rho}'')J_a(\boldsymbol{\rho}'')\,d\boldsymbol{\rho}'', \tag{5.7}$$

$$\mathcal{T}_{\sigma_b}^{S^b,\partial S^b}\circ J_b = -i\omega\mu_0 \oint\limits_{\partial S^b+\partial S^c} G_{\sigma_b}(\boldsymbol{\rho}',\boldsymbol{\rho}'')J_b(\boldsymbol{\rho}'')\,d\boldsymbol{\rho}'', \tag{5.8}$$

$$\mathcal{T}_{0}^{\partial S^{a,b},S^a}\circ j_a = i\omega\mu_0\sigma_a \iint\limits_{S^a} G_0(\boldsymbol{\rho},\boldsymbol{\rho}')j_a(\boldsymbol{\rho}')\,ds', \tag{5.9}$$

$$\mathcal{T}_{0}^{\partial S^{a,b},S^b}\circ j_b = i\omega\mu_0\sigma_b \iint\limits_{S^b} G_0(\boldsymbol{\rho},\boldsymbol{\rho}')j_b(\boldsymbol{\rho}')\,ds'. \tag{5.10}$$

In the operators (5.5)–(5.10), $\boldsymbol{\rho}$ is the position vector of an observation point on the boundaries ∂S^a, ∂S^b, and ∂S^c. The next section describes discretization of the SVS-EFIEs (5.4) with HO MoM.

5.3 HO MoM Discretization of the SVS-EFIE

5.3.1 Exact meshing of the cross-section geometry

To eliminate the error associated with meshing of the geometry, exact discretization has been done in this work. The inner conductor has radius of R_a, and the sheath has inner radius of R_b and outer radius of R_c. All the cross-sections and boundaries can be discretized exactly. The exact representation of position-vector $\boldsymbol{\rho}^a_{n'}(u,v)$ on n'th element of the cross-section S^a is obtained through a square to circle mapping [77]. Here, $n' = 0, 1, \ldots, N^a - 1$, N^a being the total number of quadrilateral elements on the cross-section S^a, $u \in [-1, 1]$ and $v \in [-1, 1]$ are parametric variables. Position-vector $\boldsymbol{\rho}^a_{m''}(u)$ exactly defines m''th element of the boundary ∂S^a, where $m'' = 0, 1, \ldots, M^a - 1$, M^a being the total number of line elements on ∂S^a [77]. The exact position vector on the inner boundary ∂S^b is defined as

$$\boldsymbol{\rho}^b_{m''}(u) = R_b \left[\cos(\varphi^b_{m''}(u))\hat{\mathbf{x}} + \sin(\varphi^b_{m''}(u))\hat{\mathbf{y}}\right], \tag{5.11}$$

where $\varphi^b_{m''}(u) = \varphi^b_{m''} + (\varphi^b_{m''+1} - \varphi^b_{m''})(u+1)/2, u \in [-1, 1]$, $m'' = 0, 1, \ldots, M^b - 1$, M^b being the total number of line elements on the inner boundary of metallic shield, $\varphi^b_{m''}$ and $\varphi^b_{m''+1}$ are the starting and ending points of m''th line element in the contour ∂S^b. Exact position vector on the outer boundary ∂S^c is defined similar to (5.11) with replacing R_b with R_c. Position-vector on n'th element of the cross-section S^b is defined as

$$\boldsymbol{\rho}^b_{n'}(u,v) = \left[R_b + \frac{1+v}{2}(R_c - R_b)\right] [\cos(\varphi^b_{m''}(u))\hat{\mathbf{x}} + \sin(\varphi^b_{m''}(u))\hat{\mathbf{y}}]. \tag{5.12}$$

5.3.2 Higher order discretization of surface and volume currents

Discretization of the unknown surface current densities $J_a(\boldsymbol{\rho}_{m''}(u))$ and $J_b(\boldsymbol{\rho}_{m''}(u))$ on the conductor's surfaces ∂S^a, ∂S^b, and ∂S^c is performed by using Ω monomial basis

functions $B_{k''}$, as follows:

$$B_{k''}(u) = u^{k''}, u \in [-1, 1], \tag{5.13}$$

where $k'' = 0, ..., \Omega - 1$ and Ω is the maximum order of 1D basis function on each 1D element. This yields the following expansions of the fictitious current J_a on the contour of the inner conductor over basis functions $B_{k''}$

$$J_a(u) \cong \sum_{m''=0}^{M^a-1} \sum_{k''=0}^{\Omega-1} I^a_{m''k''} B_{k''}(u), \tag{5.14}$$

where k'' is the order of 1D basis function of line elements, and $I^a_{m''k''}$ is the unknown coefficient of k''th order basis function $B_{k''}$ on m''th contour element.

The expansion of the fictitious current J_b on the contours ∂S^b and ∂S^c of the sheath over basis functions $B_{k''}$ is

$$J_b(u) \cong \sum_{m''=0}^{M^b-1} \sum_{k''=0}^{\Omega-1} I^b_{m''k''} B_{k''}(u) + \sum_{m''=0}^{M^c-1} \sum_{k''=0}^{\Omega-1} I^c_{m''k''} B_{k''}(u), \tag{5.15}$$

where k'' is the order of 1D basis function of line elements, and $I^b_{m''k''}$ and $I^c_{m''k''}$ are the unknown coefficients of k''th order basis function $B_{k''}$ on m''th contour elements ∂S^b and ∂S^c. Discretization of the unknown volumetric current density $j_a(\boldsymbol{\rho}_{n'}(u, v))$ on each n'th quadrilateral element that discretizes the conductor's cross-section S^a is performed by using the following basis functions $b_{j'k'}$

$$b_{j'k'}(u, v) = u^{j'} v^{k'}, u \in [-1, 1], v \in [-1, 1], \tag{5.16}$$

where $j', k' = 0, 1, \ldots, \Psi - 1$, Ψ is the maximum order of 2D basis function on quadrilateral element in the cross-section. Thus, expansion of the volumetric polarization current j_a on the inner conductor over basis functions $b_{j'k'}$ is

$$j_a(u, v) \cong \sum_{n'=0}^{N^a-1} \sum_{j'=0}^{\Psi-1} \sum_{k'=0}^{\Psi-1} j^a_{n'j'k'}\ b_{j'k'}(u, v), \tag{5.17}$$

where n' is the index of 2D quadrilateral element in the S^a, N^a is the total number of curvilinear quadrilateral elements, j' k' are the orders of 2D basis functions, and $j^a_{n'j'k'}$ is the unknown coefficient of $j'k'$th order basis function $b_{j'k'}$ on n'th quadrilateral element in the inner conductor.

The expansion of the volumetric polarization current j_b on the cross-section of the sheath conductor over the same type of 2D basis functions $b_{j'k'}$ is performed analogously, as follows:

$$j_b(u,v) \cong \sum_{n'=0}^{N^b-1} \sum_{j'=0}^{\Psi-1} \sum_{k'=0}^{\Psi-1} j^b_{n'j'k'}\ b_{j'k'}(u,v). \tag{5.18}$$

5.3.3 System of linear algebraic equations

The MoM discretized integral operators (5.5)–(5.10) and excitations $V_{a,\text{p.u.l.}}$ and $V_{b,\text{p.u.l.}}$ are obtained via inner products

$$\begin{aligned} &Z_{\sigma_i j'k',k''}^{S^i_{n'},\partial S^j_{m''}} = \langle b_{j'k'}, \langle G_{\sigma_i}, B_{k''}\rangle\rangle, Z_{k,k''}^{\partial S^j_m,\partial S^j_{m''}} = \langle B_k, \langle G_{\sigma_i}, B_{k''}\rangle\rangle, \\ &Z_{k,j'k'}^{\partial S^j_m,S^i_{n'}} = \langle B_k, \langle G_0, b_{j'k'}\rangle\rangle, \quad V^i_{m,k} = \langle B_k, V_{i,\text{p.u.l.}}\rangle, \end{aligned} \tag{5.19}$$

where $m, m'' = 0, 1, \ldots, M^j - 1$, $k, k'' = 0, 1, \ldots, \Omega - 1$, $n' = 0, 1, \ldots, N^i - 1$, $j', k' = 0, 1, \ldots, \Psi - 1$, and $i = a, b$ and $j = a, b, c$. As a result of the HO-MoM discretization of the integral operators (5.5)–(5.10) and the p.u.l. excitation voltages $V_{a,\text{p.u.l.}}$ and $V_{b,\text{p.u.l.}}$, the SVS-EFIE (5.4) is reduced to the system of linear algebraic equations with respect to the unknown coefficients I^a, I^b and I^c in the expansion of the surface current densities J_a and J_b in (5.14) and (5.15) as

$$\begin{bmatrix} Z_{\sigma_a}^{\partial S^a,\partial S^a} & 0 & 0 \\ 0 & Z_{\sigma_b}^{\partial S^b,\partial S^b} & Z_{\sigma_b}^{\partial S^b,\partial S^c} \\ 0 & Z_{\sigma_c}^{\partial S^c,\partial S^b} & Z_{\sigma_c}^{\partial S^c,\partial S^c} \end{bmatrix} \begin{bmatrix} I^a \\ I^b \\ I^c \end{bmatrix} + \begin{bmatrix} Z_0^{\partial S^a,S^a} & Z_0^{\partial S^a,S^b} \\ Z_0^{\partial S^b,S^a} & Z_0^{\partial S^b,S^b} \\ Z_0^{\partial S^c,S^a} & Z_0^{\partial S^c,S^b} \end{bmatrix} \cdot \begin{bmatrix} \Gamma^{S^a,S^a} & 0 \\ 0 & \Gamma^{S^b,S^b} \end{bmatrix}^{-1} \cdot \begin{bmatrix} Z_{\sigma_a}^{S^a,\partial S^a} & 0 & 0 \\ 0 & Z_{\sigma_b}^{S^b,\partial S^b} & Z_{\sigma_b}^{S^b,\partial S^c} \end{bmatrix} \cdot \begin{bmatrix} I^a \\ I^b \\ I^c \end{bmatrix} = \begin{bmatrix} V^a \\ V^b \\ V^c \end{bmatrix} \tag{5.20}$$

The elements of Gram matrices Γ^{S^a,S^a} and Γ^{S^b,S^b} in (5.20) are defined as

$$\Gamma^{S^a,S^b}_{j,k,j',k'} = \int_{-1}^{1}\int_{-1}^{1} dudv\sqrt{g^{a,b}(u,v)}b_{j,k}(u,v)b_{j',k'}(u,v), \tag{5.21}$$

where $j,k,j',k' = 0,1...,\Psi-1$, and $\sqrt{g^{a,b}(u,v)}$ is the Jacobian of coordinate transformation.

After solving the system of linear algebraic equations (5.20) and finding the surface current unknown coefficients I^a, I^b and I^c, the vector of coefficients j^a and j^b in expansion of the polarization currents in (5.14) and (5.15) are calculated as

$$j^a = i\omega\mu_0(\Gamma^{S^a,S^a})^{-1}\cdot Z^{S^a,\partial S^a}_{\sigma_a}\cdot I^a \tag{5.22}$$

and

$$j^b = i\omega\mu_0(\Gamma^{S^b,S^b})^{-1}\cdot (Z^{S^b,\partial S^b}_{\sigma_b}\cdot I^b + Z^{S^b,\partial S^c}_{\sigma_b}\cdot I^c). \tag{5.23}$$

Addition of the basis functions weighted with coefficients j^a and j^b yields the sought cross-sectional volumetric current densities j_a and j_b used in calculation of the coaxial cable's (2×2) admittance matrix.

5.4 Numerical Results

Numerical implementation of the HO MoM solution of the proposed SVS-EFIE has been done using PTC Mathcad [81] tool. All post-process visualizations are performed using Mathlab [85].

To demonstrate performance of the proposed HO MoM solution of the SVS-EFIE (5.4) we consider a coaxial cable of a circular cross-section depicted in Fig. 5.1. The inner conductor is made of copper ($\sigma_a = 5.96\times 10^7\,\mathrm{S/m}$) and has the radius of 0.022 m. The sheath is made of lead ($\sigma_b = 4.55\times 10^6\,\mathrm{S/m}$) and has the inner and outer radii of 0.0395 m and 0.044 m, respectively. The discretization of the inner conductor and the sheath used in HO MoM has $M^a = 20$, $M^b = 10$, and $M^c = 10$ line elements and $N^a = 25$ and $N^b = 10$ cross-sectional elements. The 3rd order scheme

Table 5.1: Values of p.u.l. resistance (R) and inductance (L) extracted via 1st to 3rd order MoM solution of SVS-EFIE (5.4) for coaxial cable (Fig. 5.2). PSCAD [78], COMSOL [34], and V-EFIE (5.1) solutions included for reference.

HO MoM solution of SVS-EFIE (5.4)		
Order	R, mΩ/m	L, μH/m
$\Omega = \Psi = 1$	0.2034487527921641	0.161323480642420
$\Omega = \Psi = 2$	0.2034852366003740	0.161323392288670
$\Omega = \Psi = 3$	0.2034852178263414	0.161323391640562
PSCAD [78]		
—	0.2035	0.1627
COMSOL [34]: highly refined mesh (13556778 elements)		
—	0.2034852446055154	0.161323496678413
COMSOL [34]: standard mesh (7946 elements)		
—	0.2034914913396053	0.161327763020772
Semi-analytical solution of V-EFIE (5.1): 13 digit accurate		
—	0.2034852151141888	0.161323403623543

($\Omega = \Psi = 3$) was applied to compute volume current distributions j_a and j_b. Fig. 5.2 shows the distribution of the computed current density at 60 Hz. The distribution of relative error in j_a and j_b solution of 3th order with respect to semi-analytical solution of V-EFIE (5.1) is shown in Fig. 5.3. The extracted p.u.l. $R = R_a + R_b$ and $L = L_a - L_{ab} - L_{ba} + L_b$ of the cable computed in PSCAD, COMSOL, and V-EFIE (5.1) are presented for reference in Table 5.1 along with the results obtained with the proposed HO MoM solution of the SVS-EFIE with orders $\Omega = \Psi = 1, 2$, and 3. The relative error in the values of R and L in different orders HO MoM solutions with respect to the results of to semi analytical solution of V-EFIE (5.1) are shown in the Fig. 5.4. Exponentially rapid error decrease with the linear increase of the HO MoM degrees of freedom is observed.

5.5 Conclusion

Higher order method of moments solution of a new single-source surface integral equation is presented for extraction of inductance and resistance matrices in coaxial cable. The method effectively controls the numerical error of the values of R and L extractions using significantly reduced computational resources compared to low

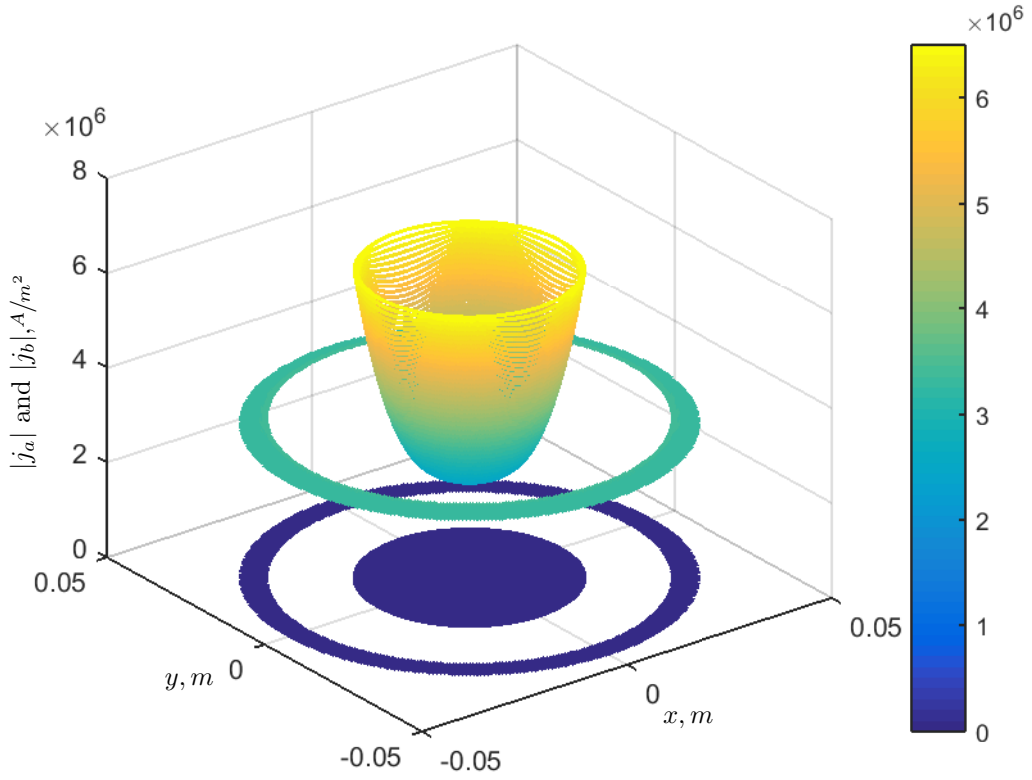

Figure 5.2: Volumetric current densities j_a and j_b at 60 Hz in circular coaxial transmission line obtained via 3rd order HO MoM solution of SVS-EFIE (5.4).

order approaches.

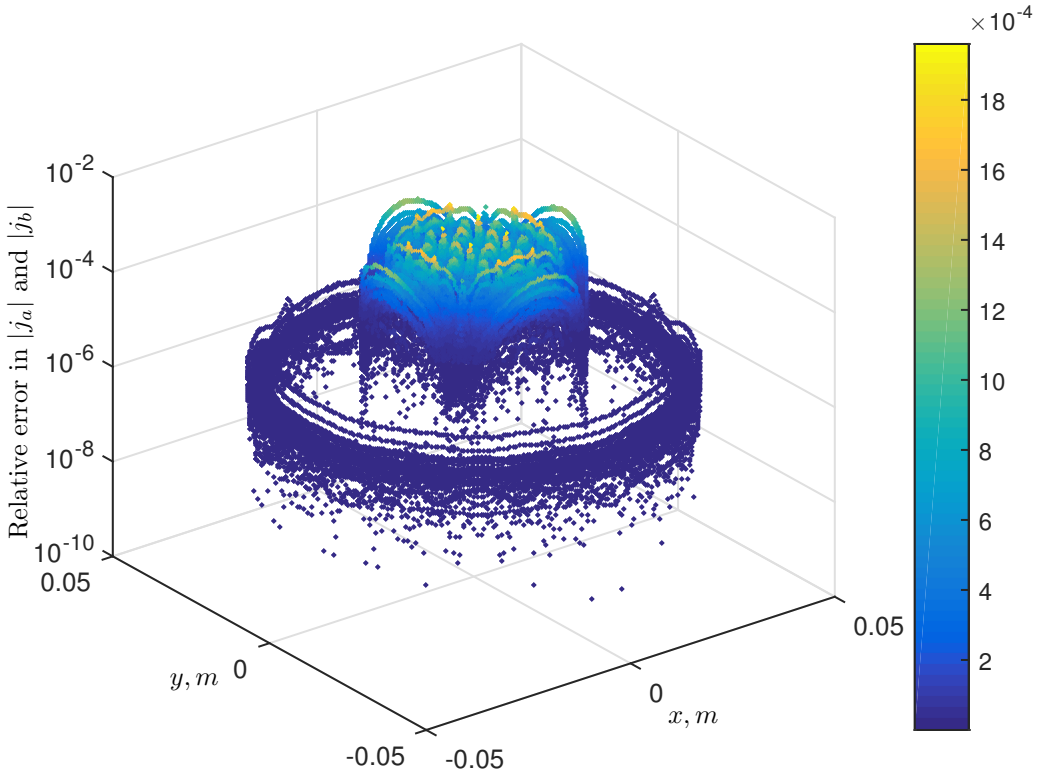

Figure 5.3: Relative error in magnitude of the volumetric current densities j_a and j_b at 60 Hz between the 3rd order HO MoM solutions of SVS-EFIE (5.4) and semi-analytical (13 digit accurate) solution of V-EFIE (5.1).

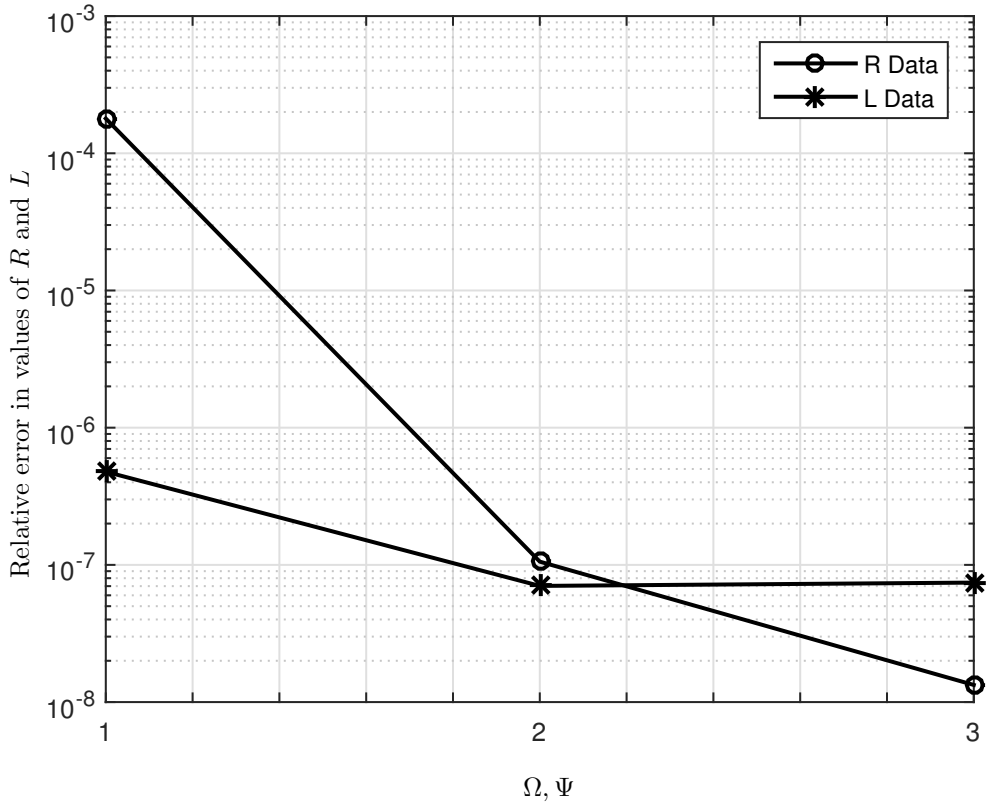

Figure 5.4: Relative error in p.u.l. R and L versus order of HO MoM solutions at 60 Hz in the circular coaxial transmission line (Fig. 5.4) with respect to the semi-analytical solution of V-EFIE (5.1).

6

Higher Order Method of Moments Solution of the New Vector Single-Source Surface Integral Equation for 2D TE Scattering by Dielectric Objects

6.1 Introduction

The single source integral equation (SSIE) termed Surface-Volume-Surface Electric Field Integral Equations (SVS-EFIE) was recently proposed [69] for the solution of scattering problems by homogeneous dielectric objects. Unlike previously known SSIE formulations derived through constraining of the single-source field representation with surface equivalence principle, the new SVS-EFIE is obtained through constraining of the such representation with the volume equivalence principle. The resultant SSIE, therefore, translates the fields from the surface of the scatterer to its

volume and then back to its surface, lending it its name. While additional computations are introduced into the method of moments (MoM) solution of the SVS-EFIE due to discretization of both the surface and the volume of the scatterer, the new SSIE offers several advantages compared to both the previously known SSIEs [47] as well as traditional surface integral equations (SIEs) such as Muller or PMCHWT integral equations [32]. The SVS-EFIE has derivative-free kernels, it features only one unknown function instead of two compared to the traditional SIEs, it exhibits the same computational and memory complexity when accelerated with FFT-based methods compared to traditional SIEs and other SSIEs, and its MoM solution is simpler to implement as it features no double-layer potential terms.

In this work we present a higher-order (HO) MoM for error-controlled solution of the new SVS-EFIE in the case of TE-waves scattering by homogeneous dielectric cylinder. The new HO MoM discretization of the SVS-EFIE shifts the differential operators from the EFIE kernels to the test and basis functions which combined with application of the gradient theorem allows to cast its inner products in the form of integrals having no stronger than 1/R singularities. Proposed HO MoM solution of the SVS-EFIE is compared against analytic Mie series solution for the scattering problem by circular dielectric cylinder to demonstrate its error controllability and to numerically prove the rigorous nature of the new SVS-EFIE.

6.2 Vector Surface Volume Surface-EFIE in 2D

SVS-EFIE is derived from the classical V-EFIE [27] for time-harmonic 2D TE scattering of the incident field $\boldsymbol{E}^{\text{inc}}$ with cyclic frequency ω on a homogeneous dielectric cylinder as

$$\begin{aligned} -i\omega\mu_0\hat{\mathbf{t}}\cdot\int\limits_{\partial S}\overline{\overline{G}}_{e\epsilon}(\boldsymbol{\rho},\boldsymbol{\rho}'')\cdot\boldsymbol{J}(\boldsymbol{\rho}'')d\rho'' + i\omega\mu_0 k_0^2\,(\epsilon-1)\,\hat{\mathbf{t}}\cdot\iint\limits_{S}\overline{\overline{G}}_{e0}(\boldsymbol{\rho},\boldsymbol{\rho}') \\ \cdot\int\limits_{\partial S}\overline{\overline{G}}_{e\epsilon}(\boldsymbol{\rho}',\boldsymbol{\rho}'')\cdot\boldsymbol{J}(\boldsymbol{\rho}'')d\rho''ds' \quad = \hat{\mathbf{t}}\cdot\boldsymbol{E}^{\text{inc}}(\boldsymbol{\rho}), \quad \boldsymbol{\rho},\boldsymbol{\rho}''\in\partial S,\ \boldsymbol{\rho}'\in S, \end{aligned} \tag{6.1}$$

where $\overline{\overline{G}}_{e\epsilon}(\boldsymbol{\rho},\boldsymbol{\rho}') = (\mathbf{I}+k_0^2\boldsymbol{\nabla}\boldsymbol{\nabla})1/_{i4}H_0^{(2)}(k_0\sqrt{\epsilon}|\boldsymbol{\rho}-\boldsymbol{\rho}'|)$ is electric field dyadic Green's function of the homogeneous dielectric having relative permittivity of ϵ, cross-section of S and boundary of ∂S. $\overline{\overline{G}}_{e0}(\boldsymbol{\rho},\boldsymbol{\rho}')$ is the dyadic Green's function of vacuum, $\mathbf{I}$ is the idem-factor, $H_0^{(2)}$ is the Hankel function of second kind and order zero, μ_0 is the permeability of vacuum, i is the imaginary unit, $\hat{\mathbf{t}}$ is the tangential vector to the boundary ∂S and $k_0=\omega\sqrt{\epsilon_0\mu_0}$ is the vacuum wavenumber. The new SSIE (6.1) uses only one unknown $\boldsymbol{J}(\boldsymbol{\rho}'')$ and can be written in the operator form

$$-\left(\mathcal{T}_{\epsilon,\nabla\Phi}^{\partial S,\partial S}+\boldsymbol{\mathcal{T}}_{\epsilon,A}^{\partial S,\partial S}\right)\circ\boldsymbol{J}+\left(\boldsymbol{\mathcal{T}}_{0,\nabla\varphi}^{\partial S,S}+\boldsymbol{\mathcal{T}}_{0,a}^{\partial S,S}\right)\circ\left(\boldsymbol{\mathcal{T}}_{\epsilon,\nabla\Phi}^{S,\partial S}+\mathcal{T}_{\epsilon,A}^{S,\partial S}\right)\circ\boldsymbol{J}=\hat{\mathbf{t}}\cdot\boldsymbol{E}^{\text{inc}}, \tag{6.2}$$

where $\mathcal{T}_{\epsilon,\nabla\Phi}^{\partial S,\partial S}=\hat{\mathbf{t}}\cdot\boldsymbol{\nabla}\mathcal{T}_{\epsilon,\Phi}^{\partial S,\partial S}$ and $\boldsymbol{\mathcal{T}}_{0,\nabla\varphi}^{\partial S,S}=\hat{\mathbf{t}}\cdot\boldsymbol{\nabla}\boldsymbol{\mathcal{T}}_{0,\varphi}^{\partial S,S}$.

6.3 Higher Order Method of Moments Solution

6.3.1 Analytical representation of exact geometry discretization:

To represent analytically the cross-section of an exact circular cylinder with radius R we use the cross-section of a square cylinder with side length $2R$ and a square to circle mapping such that the points along the axes remain unchanged and any point (x,y) in square maps into the point (X,Y) in the circle where $X=x\sqrt{1-\frac{y^2}{2R^2}}$ and $Y=y\sqrt{1-\frac{x^2}{2R^2}}$. As demonstrated in Fig. 4.1 we discretize the square cross-section with N square cells and map each square cell into a square in u,v computational domain where $-1\leqslant u,v\leqslant 1$. The position vector of the n-th square element of the square cross-section is defined parametrically in the barycentric coordinates [25] as

$$\boldsymbol{\rho}_{s,n}(u,v)=\sum_{i=0}^{3}\boldsymbol{v}_{n,i}\;S_i(u,v),\quad -1\leqslant u,v\leqslant 1, \tag{6.3}$$

where $\boldsymbol{v}_{n,i}$ is the i-th vertex of n-th square patch, and $n=0,1,...,N-1$. The shape functions are defined as $S_0(u,v)=0.25(1-u)(1-v)$, $S_1(u,v)=0.25(1+u)(1-v)$, $S_2(u,v)=0.25(1+u)(1+v)$, and $S_3(u,v)=0.25(1-u)(1+v)$. Now

we map the n-th square patch on square cylinder into n-th quadrilateral element on circular cylinder through the square to circle mapping which is shown in Fig. 4.1. The position-vector of the n-th quadrilateral element is defined parametrically in the barycentric coordinates as

$$\boldsymbol{\rho}_n(u,v) = x\ \sqrt{1-\frac{y^2}{2R^2}}\ \hat{\mathbf{x}} + y\ \sqrt{1-\frac{x^2}{2R^2}}\ \hat{\mathbf{y}}, \tag{6.4}$$

where $x = \boldsymbol{\rho}_{s,n}(u,v)\cdot\ \hat{\mathbf{x}}$, and $y = \boldsymbol{\rho}_{s,n}(u,v)\cdot\ \hat{\mathbf{y}}$.

The boundary of the circular cylinder ∂S is discretized equally to M arcs, 1D elements. The position vector of the m-th 1D element is defined parametrically as

$$\boldsymbol{\rho}_m(u)=R\ [\cos(\varphi_m(u))\ \hat{\mathbf{x}} +\ \ \sin(\varphi_m(u))\ \hat{\mathbf{y}}], \tag{6.5}$$

where $\varphi_m(u)=\varphi_m + \frac{(u+1)}{2}(\varphi_{m+1}-\varphi_m)$ and $m = 0, 1..., M-1$. φ_m and φ_{m+1} are the start and end points of the m-th 1D element shown in Fig. 4.1.

6.3.2 Higher order Method of Moments discretization:

Discretization of the unknown single-source weighting function $\boldsymbol{J}$ localized on the boundary ∂S is performed by using the 1D higher order (HO) RWG basis functions. The m-th 1D HO RWG basis function is defined using two neighbours $m-1$ -th and m-th 1D HO elements as follows

$$\boldsymbol{B}_k^m(u) = \begin{cases} \frac{1}{2J}u^k(1+u)\frac{\partial}{\partial u}\boldsymbol{\rho}_{m-1}(u), & \boldsymbol{\rho}\in L_{m-1}, \\ \\ \frac{1}{2\,J}(-1)^k u^k(1-u)\frac{\partial}{\partial u}\boldsymbol{\rho}_m(u), & \boldsymbol{\rho}\in L_m, \end{cases} \tag{6.6}$$

where $J = {}^{\pi R}/_{M}$ is the Jacobian of 1D HO element, k is the k-th order of the 1D HO RWG basis function, L_{m-1} and L_m are ids of the $m-1$-th and the m-th 1D HO

elements. Divergence of the 1D HO RWG basis function is obtained as

$$\boldsymbol{\nabla}\cdot\boldsymbol{B}_k^m(u)=\begin{cases}\frac{1}{2J}\frac{\partial}{\partial u}[u^k(1+u)], & \boldsymbol{\rho}\in L_{m-1},\\ \\ \frac{(-1)^k}{2\,J}\frac{\partial}{\partial u}[u^k(1-u)], & \boldsymbol{\rho}\in L_m.\end{cases}\tag{6.7}$$

Thus, expansion of the fictitious current $\boldsymbol{J}(\boldsymbol{\rho}_m(u))$ on the contour of the scatterer over basis functions $\boldsymbol{B}_k^m$ is the following

$$\boldsymbol{J}(u)\cong\sum_{m=0}^{M-1}\sum_{k=0}^{\Omega-1}I_{mk}\;\boldsymbol{B}_k^m(u),\tag{6.8}$$

where I_{mk} is the unknown coefficient of k-th order basis function $\boldsymbol{B}_k^m$ on m-th 1D element.

Discretization of the unknown volumetric polarization current $\boldsymbol{j}(\boldsymbol{\rho}_n(u,v))$ on scatterer's cross section S is performed by using 2D HO basis functions. The 2D HO basis function is defined as

$$b_{j'k'}(u,v)=u^{j'}v^{k'},\tag{6.9}$$

where $j'=0,1,...,\Psi-1$, $k'=0,1,...,\Psi-1$ and Ψ is the chosen order of the 2D HO basis function of the 2D HO elements. Thus, expansion of the volumetric polarization current $\boldsymbol{j}$ on the cross-section of the scatterer over basis function $b_{j'k'}$ is

$$\boldsymbol{j}(u,v)\cong\sum_{n=0}^{N-1}\sum_{j'=0}^{\Psi-1}\sum_{k'=0}^{\Psi-1}(i^x_{nj'k'}\hat{\mathbf{x}}+i^y_{nj'k'}\hat{\mathbf{y}})\;b_{j'k'}(u,v),\tag{6.10}$$

where $i^x_{nj'k'}$ and $i^y_{nj'k'}$ are the unknown coefficients of the $j'k'$-th order basis function $b_{j'k'}$ of the n-th 2D HO element.

6.3.2.1 HO-MoM discretization of SVS-EFIE's surface-to-volume operators $\mathcal{T}^{S,\partial S}_{\epsilon,A}$ and $\boldsymbol{\mathcal{T}}^{S,\partial S}_{\epsilon,\nabla\Phi}$

The HO MoM discretization of the operator $\mathcal{T}^{S,\partial S}_{\epsilon,A}$ involves inner products

$$\boldsymbol{Z}^{S,\partial S}_{\epsilon A\, p',q''} = \left\langle b_{j'k'}(u,v), \mathcal{T}^{S,\partial S}_{\epsilon,A} \circ \boldsymbol{B}^{m''}_{k}(u'') \right\rangle, \tag{6.11}$$

where $p' = n\Psi^2 + j'\Psi + k'$ and $q'' = m''\Omega + k$ are the indices for row and column of the matrix elements, $n = 0, 1, ..., N-1$, $j' = 0, 1, ..., \Psi - 1$, $k' = 0, 1, ..., \Psi - 1$, and $k = 0, 1, ..., \Omega - 1$.

To discretize $\boldsymbol{\mathcal{T}}^{S,\partial S}_{\epsilon,\nabla\Phi}$, we use (6.6) as basis functions and test this operator with (6.9)

$$\boldsymbol{Z}^{S,\partial S}_{\epsilon\nabla\Phi\, p',q''} = \left\langle b_{j'k'}(u,v), \boldsymbol{\mathcal{T}}^{S,\partial S}_{\epsilon,\nabla\Phi} \circ \boldsymbol{B}^{m''}_{k}(u'') \right\rangle. \tag{6.12}$$

Using the surface gradient theorem [23] one can mitigate the singularity in the matrix elements of $\boldsymbol{Z}^{S,\partial S}_{\epsilon\nabla\Phi\, p',q''}$.

6.3.2.2 HO-MoM discretization of SVS-EFIE's volume-to-surface operators $\boldsymbol{\mathcal{T}}^{\partial S,S}_{0,a}$ and $\boldsymbol{\mathcal{T}}^{\partial S,S}_{0,\nabla\varphi}$

The HO MoM discretization of the operator $\boldsymbol{\mathcal{T}}^{\partial S,S}_{0,a}$ is done by using HO 2D basis functions and testing it by (6.6) as

$$\boldsymbol{Z}^{\partial S,S}_{0a\, q,p'} = \left\langle \boldsymbol{B}^{m}_{k}(u), \boldsymbol{\mathcal{T}}^{\partial S,S}_{0,a} \circ b_{j'k'}(u,v) \right\rangle, \tag{6.13}$$

where $q = m\Omega + k$, $m = 0, 1, ..., M-1$, $k = 0, 1, ..., \Omega - 1$, $n = 0, 1, ..., N-1$, $j' = 0, 1, ..., \Psi - 1$, and $k' = 0, 1, ..., \Psi - 1$.

In order to discretize the $\boldsymbol{\mathcal{T}}^{\partial S,S}_{0,\nabla\varphi}$ operator, we use a 2D HO basis function on each 2D HO element, and then the gradient of the scalar potential contribution to the tangential scattered field is tested with 1D HO RWG basis functions as follows

$$\boldsymbol{Z}^{\partial S,S}_{0\nabla\Phi\, q,p'} = \left\langle \boldsymbol{B}^{m}_{k}(u), \boldsymbol{\mathcal{T}}^{\partial S,S}_{0,\nabla\Phi} \circ b_{j'k'}(u,v) \right\rangle, \tag{6.14}$$

where $m = 0, 1, ..., M-1$, $k = 0, 1, ..., \Omega - 1$, $n = 0, 1, ..., N-1$, and $j' = 0, 1, ..., \Psi - 1$, $k' = 0, 1, ..., \Psi - 1$. The matrix elements of $\boldsymbol{Z}^{\partial S,S}_{0\nabla\Phi\, q,p'}$ can be defined in the form free of hyper singularity by using surface gradient theorem [23].

6.3.2.3 HO-MoM discretization of SVS-EFIE's surface-to-surface operators $\boldsymbol{\mathcal{T}}^{\partial S,\partial S}_{\epsilon,A}$ and $\boldsymbol{\mathcal{T}}^{\partial S,\partial S}_{\epsilon,\nabla\Phi}$

$\boldsymbol{\mathcal{T}}^{\partial S,\partial S}_{\epsilon,A}$ operator's domain and range are discretized with 1D HO RWG basis functions (6.6) as follows:

$$Z^{\partial S,\partial S}_{\epsilon A\ q,q''} = \langle \boldsymbol{B}^m_k(u), \langle \boldsymbol{\mathcal{T}}^{\partial S,\partial S}_{\epsilon,A}, \boldsymbol{B}^{m''}_k(u'')\rangle\rangle, \tag{6.15}$$

where $m'' = 0, 1, ..., M-1$ and $k = 0, 1, ..., \Omega - 1$.

The HO MoM discretization of the operator's $\boldsymbol{\mathcal{T}}^{\partial S,\partial S}_{\epsilon,\nabla\Phi}$ domain is done with HO 1D RWG basis functions on 1D HO elements expanding the current $\boldsymbol{J}$. Testing of the scalar potential gradient is performed with 1D HO RWG test functions (6.6) as

$$Z^{\partial S,\partial S}_{\epsilon\nabla\Phi\ q,q''} = \left\langle \boldsymbol{B}^m_k(u), \mathcal{T}^{\partial S,\partial S}_{\epsilon,\nabla\Phi} \circ \boldsymbol{B}^{m''}_k(u'') \right\rangle. \tag{6.16}$$

6.3.2.4 MoM discretization of the incident field $\boldsymbol{E}^{\text{inc}}$

The discretized form of the excitation $\boldsymbol{E}^{\text{inc}}$ is calculated by testing it with 1D HO test functions as

$$V_{m,k} = \langle \boldsymbol{B}^m_k(u), \boldsymbol{E}^{\text{inc}}_m(u)\rangle. \tag{6.17}$$

The HO-MoM discretization of the dyadic integral operators SVS-EFIE in (6.2) and incident field $\boldsymbol{E}^{\text{inc}}$ in (6.17), produces a system of linear algebraic equations

$$\left(-\left(Z^{\partial S,\partial S}_{\epsilon A} + Z^{\partial S,\partial S}_{\epsilon\nabla\Phi}\right) + \left(\boldsymbol{Z}^{\partial S,S}_{0a} + \boldsymbol{Z}^{\partial S,S}_{0\nabla\Phi}\right) \cdot \Gamma^{-1} \cdot \left(\boldsymbol{Z}^{S,\partial S}_{\epsilon A} + \boldsymbol{Z}^{S,\partial S}_{\epsilon\nabla\Phi}\right) \right) \cdot I = V, \tag{6.18}$$

where each element of Gram matrix Γ is defined as

$$\Gamma_{p,p'}(j,k,j',k') = \int_{-1}^{1}\int_{-1}^{1} du\ dv J_n(u,v) u^j v^k u^{j'} v^{k'}, \tag{6.19}$$

where $n = 0, 1, ..., N-1$, $j, j' = 0, 1, ..., \Psi - 1$ $k, k' = 0, 1, ..., \Psi - 1$, and J_n is the Jacobian of the n-th 2D element.

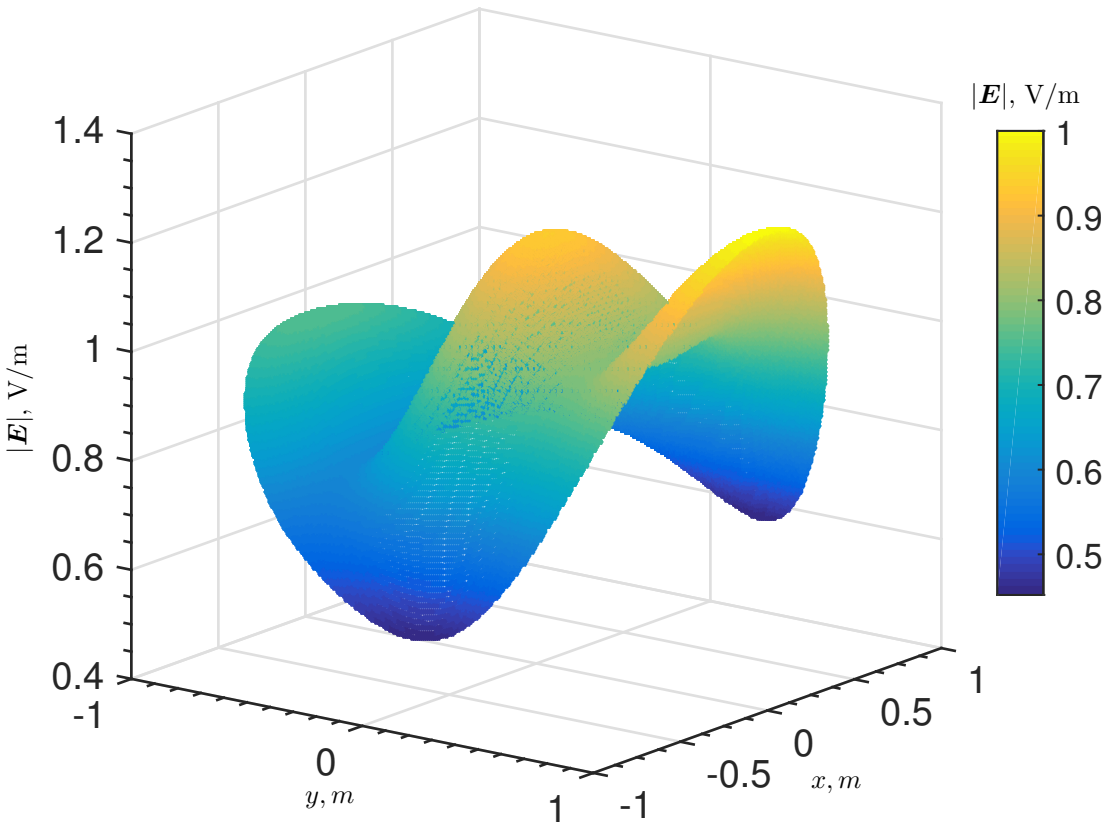

Figure 6.1: Distribution of magnitude of total electric field inside of the dielectric cylinder of radius $R = 1$ m and relative permittivity $\epsilon = 2$ in the problem of TE-polarized plane wave scattering at 120 MHz obtained from the proposed HO-MoM solution of the SVS-EFIE (6.2) with $\Omega = 3$ and $\Psi = 3$.

6.4 Numerical Results

Numerical implementation of the MoM solution of the proposed SVS-EFIE has been done using PTC Mathcad [81] tool. All post-process visualizations are performed using Mathlab [85].

We consider the problem of TE-polarized plane wave scattering on a circular dielectric cylinder with a cross-sectional radius $R = 1\,\text{m}$ and a dielectric permittivity $\epsilon = 2$. The cylinder is illuminated by the plane wave at f=120 MHz incoming from the $\phi = 180°$ direction with magnetic field defined as $H_z^{\text{inc}}(\boldsymbol{\rho}) = e^{-i\boldsymbol{k}\cdot\boldsymbol{\rho}}/\eta_0$ A/m, where $\boldsymbol{k}$ is $k_0\hat{\mathbf{k}}$, $\hat{\mathbf{k}}$ is the unit vector in propagation direction, and η_0 is the intrinsic

impedance of free space. The field inside the cylinder is computed after expansion coefficients $[I]$ in (6.8) were obtained from the solution of the HO-MoM discretization of SVS-EFIE (6.18) and is shown in Fig. 6.1. The HO-MoM discretization of the SVS-EFIE used $M = 80$ 1D elements discretizing the exact boundary of the cylinder, $N = 400$ 2D elements discretizing its exact cross-section, $\Omega = 3$ and $\Psi = 3$. Distribution of relative error in the magnitude of total electric field at 120 MHz between the proposed HO-MoM solution of the SVS-EFIE (6.2) and the Mie series solution is shown in Fig. 6.2. The average relative error between the analytic Mie series solutions and the proposed HO-MoM solution of the SVS-EFIE is 1.904×10^{-5}. Fig. 6.3 shows the average relative error obtained by the HO-MoM discretization of the SVS-EFIE (6.2)with order ($\Omega = \Psi$) and quadrilateral elements N refinements.

6.5 Conclusion

This chapter presents a higher order method of Moments solution of the new single-source surface-volume-surface integral equation for solution of TE-polarized wave scattering by a homogeneous non-magnetic penetrable circular cylinder with analytical exact Geometry representation. By using the proposed HO-MoM, numerical solutions with RMS relative error in the computed fields not exceeding 10^{-5} are achieved, and hence, numerically validates the rigorous nature of the new single source integral equation formulation and its use.

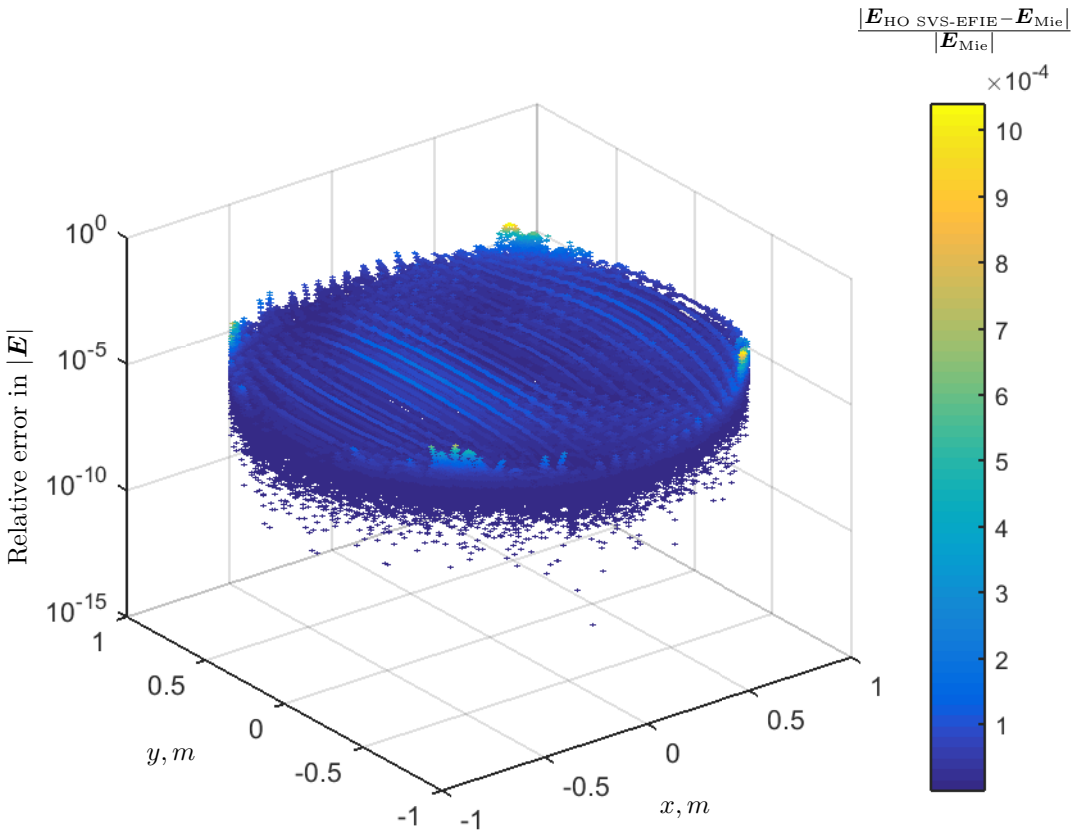

Figure 6.2: Distribution of relative error in the magnitude of total electric field of the dielectric cylinder of radius $R = 1$ m and relative permittivity $\epsilon = 2$ in the problem of TE-polarized plane wave scattering at 120 MHz between the proposed HO-MoM solution of the SVS-EFIE (6.2) with $\Omega = 3$ and $\Psi = 3$, and the Mie series solution.

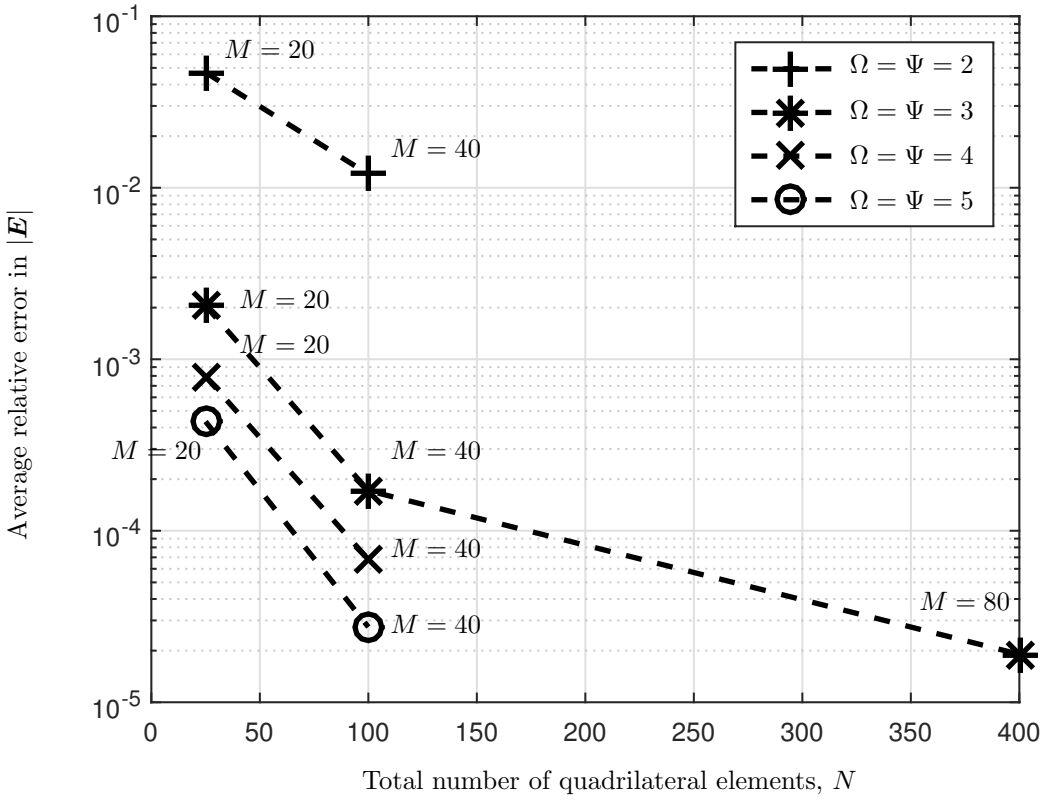

Figure 6.3: Average relative error in the magnitude of total electric field of the dielectric cylinder of radius $R = 1$ m and relative permittivity $\epsilon = 2$ in the problem of TE-polarized plane wave scattering at 120 MHz between the proposed HO-MoM solution of the SVS-EFIE with different order (6.2) and the Mie series solution as a function of total number of quadrilateral elements, N.

7

Conclusions and Future Work

This work presents a novel single source integral equation for solution of scattering and radiation problems in 2D and 3D. Higher order MoM schemes are also developed for the solution of the new equation applied to magneto-quasistatic characterization of the current flow in 2D transmission lines. The new equation is derived from the classical volume electric field integral equation via representation of the electric field inside the scatterer as a superposition of the elementary waves emanating from its boundary. Using the proposed new SSIE to determine the sought fields is a two-stage process. In the first stage an unknown weighting function on the boundary of the scatterer is determined. This function is subsequently used to obtain the field distribution inside the scatterer. In the second stage the total field outside the scatterer is computed using the volume equivalence principle. The novel equation features only a single unknown vector function on the boundary of the scatterer. Unlike previously known SSIEs this novel formulation uses only electric field type of Green's function. Several numerical examples have been used to demonstrate the validity of the equation. Numerical solutions obtained from low order MoM and higher order MoM confirm that the sought solutions are error-controllable and can obtain with high precision and accuracy, therefore demonstrating rigours nature of the novel SSIE.

Future research directions regarding the new formulations are vast. In this thesis we consider a particular case of (1.39) in which constants a and b are taken to be

1 and 0, respectively. We called this particular case as SVS-EFIE. One can study and implement (1.39) using different values of the constants a and b, which could be beneficial in some cases. It is known that EFIE suffers from the existence of a null-space. When operating frequency is exactly at the internal resonance frequency, the solution of the EFIE is not unique since part of the solution belongs to the null-space of the EFIE. We have the same problem with SVS-EFIE. MFIE suffers from the same problem, however, its internal resonance frequency is different from the EFIE one. Hence, there would be a great opportunity to study SVS formulation (1.39) under different values of the weighting coefficients a and b to come up with free internal resonance frequency formulation. It should be possible to get a unique solution without suffering of the internal resonance by choosing different weighting coefficients a and b.

Another future research direction includes applying the novel equation for field computations in composite dielectric/conductor bodies of arbitrary shape embedded in layered media. As the proposed integral equation formulation is derivative free and has only an electric field type of Green's function, it is particularly suitable for analysis in multilayered media. Currently, only the low order MoM solution of the SVS-EFIE for 3D full wave scattering problems has been developed. The new computational framework has been tested and validated against analytical Mie series solutions and commercial full wave computational tools such as FEKO. Other future research direction involves applying the novel SSIE to the solution of large scale problems through fast direct solution of MoM dense matrix equation using hierarchical matrices (H-matrices). Generalization of the HO 3D MoM formulation for the case of general 3D interconnect modelling is currently under development with another member of our group. Rigorous handling of the conductor loss using the SVS-EFIE models requires both volumetric and surface discretization of the interconnect model. Due to high disparity in the skin-depth compared the wavelength in fields variation along the conductors, special meshing of the structure is required. The volumetric elements feature lengths that exceed their thicknesses hundreds of times (e.g. longer one dimension along the line then other dimension along the skin effect). higher-order (HO) discretization is employed to efficiently control the error in the approximation of

the field throughout such elements. This guarantees the smallest number of degrees of freedom required to achieve the desired precision of the computations and flexibility in field representation inside the elements with disparate dimensions. The former is essential for the computationally demanding fast direct MoM analysis [86].

A

Mie Series Analytic Solution for 2D TM Scattering on Circular Dielectric Cylinder

Consider the problem of scattering for TM-polarized electromagnetic wave on the circular dielectric cylinder. The solution of the problem can be obtained analytically through the expansion of the 2π periodic fields over angular coordinate into Fourier series. Such solution is known as the Mie series solution. The Fourier series expansion is defined for a periodic function, $f(t) = f(t+T)$, as

$$f(t) = \sum_{-\infty}^{\infty} A_n e^{jn\theta}, \tag{A.1}$$

where

$$A_n = \frac{1}{T} \int_{-\frac{T}{2}}^{\frac{T}{2}} f(t) e^{-jn\theta} dt, \tag{A.2}$$

$\theta = \frac{2\pi t}{T}$, and $T = 2\pi$. Considering homogeneous and lossless medium and taking the curl of (1.8) yields

$$\boldsymbol{\nabla} \times \boldsymbol{\nabla} \times \boldsymbol{E}(\boldsymbol{r}) = -\boldsymbol{\nabla} \times \boldsymbol{M}^i(\boldsymbol{r}) - j\omega\mu \boldsymbol{\nabla} \times \boldsymbol{H}(\boldsymbol{r}). \tag{A.3}$$

If we plug (1.9) into (A.3), we have

$$\boldsymbol{\nabla} \times \boldsymbol{\nabla} \times \boldsymbol{E}(\boldsymbol{r}) = -\boldsymbol{\nabla} \times \boldsymbol{M}^i(\boldsymbol{r}) - j\omega\mu[\boldsymbol{J}^i(\boldsymbol{r}) + \boldsymbol{J}^c(\boldsymbol{r}) + j\omega\epsilon\boldsymbol{E}(\boldsymbol{r})]. \tag{A.4}$$

Since we are considering a 2D problem with no variation along z axis ($\partial/\partial z = 0$) and cross-section area S, which is a source free region (i.e. $\boldsymbol{J}^i(\boldsymbol{r}) = 0$ and $\boldsymbol{M}^i(\boldsymbol{r}) = 0$), assuming the lossless medium ($\sigma = 0$ $\boldsymbol{J}^c(\boldsymbol{r}, t) = 0$), equation (A.4) is simplified to

$$\boldsymbol{\nabla} \times \boldsymbol{\nabla} \times \boldsymbol{E}(\boldsymbol{r}) - k^2\boldsymbol{E}(\boldsymbol{r}) = 0, \tag{A.5}$$

where wave number, $k = \omega\sqrt{\mu\epsilon}$. By using vector identity $\boldsymbol{\nabla}\times\boldsymbol{\nabla}\times\boldsymbol{A}(\boldsymbol{r}) = -\boldsymbol{\nabla}^2\boldsymbol{A}(\boldsymbol{r}) + \boldsymbol{\nabla}(\boldsymbol{\nabla} \cdot \boldsymbol{A}(\boldsymbol{r}))$ we have,

$$\boldsymbol{\nabla} \times \boldsymbol{\nabla} \times \boldsymbol{E}(\boldsymbol{r}) = -\nabla^2\boldsymbol{E}(\boldsymbol{r}) + \boldsymbol{\nabla}(\boldsymbol{\nabla} \cdot \boldsymbol{E}(\boldsymbol{r})). \tag{A.6}$$

Lack of variation along z axis ($\partial/\partial z = 0$) ensures that only z component of the electric field exist. By using equation(A.6) and the fact that $\boldsymbol{\nabla} \cdot \boldsymbol{E}(\boldsymbol{r}) = 0$ for source free regions, equation (A.5) becomes

$$\nabla^2\boldsymbol{E}(\boldsymbol{r}) + k^2\boldsymbol{E}(\boldsymbol{r}) = 0. \tag{A.7}$$

The vector Helmholtz equation converts to scalar equation for TM mode as

$$\nabla^2 E_z(x, y) + k^2 E_z(x, y) = 0;\ x, y \in S, \tag{A.8}$$

since only E_z component of the electric field in non zero. Equation (A.8) can be written in the cylindrical coordinate system as follows

$$\frac{1}{\rho}\frac{\partial}{\partial\rho}(\rho\frac{\partial}{\partial\rho}E_z(\rho, \phi)) + k_0^2 E_z(\rho, \phi) + \frac{1}{\rho^2}\frac{\partial^2}{\partial\phi^2}E_z(\rho, \phi) = 0;\ \rho, \phi \notin S. \tag{A.9}$$

Since $E_z(\rho, \phi)$ is a periodic function over ϕ we can use Fourier series to represent it as

$$E_z(\rho,\phi) = \sum_{n=-\infty}^{\infty} E_{zn}(\rho)e^{-jn\phi}. \tag{A.10}$$

If we plug in equation (A.10) into equation (A.9) and solve for unknown coefficients $E_{zn}(\rho)$ we have

$$\sum_{n=-\infty}^{\infty} \big[\frac{1}{\rho}\frac{\partial}{\partial\rho}(\rho\frac{\partial}{\partial\rho}E_{zn}(\rho)) + \frac{1}{\rho^2}(-n^2)E_{zn}(\rho) + k^2E_{zn}(\rho)\big]e^{-jn\phi} = 0. \tag{A.11}$$

A property of the Fourier series is that it's coefficients must be equal to zero for all the values of n if it produces a function which is zero for all values of $\phi \in [0, 2\pi]$. Hence, (A.11) becomes

$$\frac{1}{\rho}\frac{\partial}{\partial\rho}(\rho\frac{\partial}{\partial\rho}E_{zn}(\rho)) + (k^2 - {}^{n^2}\!/_{\rho^2})E_{zn}(\rho) = 0. \tag{A.12}$$

Equation (A.12) is the Bessel equation.The solutions of the Bessel equation are

$$E_{zn}(\rho) = \begin{cases} J_n(k,\rho), \\ Y_n(k,\rho), \\ H_n^{(1)}(k,\rho), \\ H_n^{(2)}(k,\rho), \end{cases} \tag{A.13}$$

where J_n is the Bessel function of the first kind, Y_n is the Neumann function or Bessel function of the second kind, $H_n^{(1)}$ is the Hankel function of the first kind, $H_n^{(2)}$ is the Hankel function of the second kind.

Inside the cylinder at the origin $\rho = 0$ the solution must not turn into infinity. Therefore, the Bessel function representation of it must be used. Choosing the impinging such that the solution is even function of ϕ (e.g. a plane wave incoming from $\phi = 0$ direction), we can rewrite field representation as

$$E_z^{\text{in}}(\rho,\phi) = \sum_{n=-\infty}^{\infty} B_nJ_n(k_\epsilon\rho)e^{-jn\phi} = \sum_{n=0}^{\infty} \epsilon_nB_nJ_n(k_\epsilon\rho)\cos(n\phi), \tag{A.14}$$

where

$$\epsilon_n = \begin{cases} 1, \text{ if } n = 0, \\ 2, \text{ otherwise.} \end{cases} \tag{A.15}$$

In the region $a \leq \rho \leq \infty$ or outside the cylinder the solution must satisfy the radiation condition. As a result, it must be taken in the form of expansion of the Hankel functions of the second kind, which satisfy this condition. The expansion in the outer region is taken in the form

$$E_z^{\text{scat}}(\rho, \phi) = \sum_{n=-\infty}^{\infty} C_n H_n^{(2)}(k_0\rho) e^{-jn\phi} = \sum_{n=0}^{\infty} \epsilon_n C_n H_n^{(2)}(k_0\rho) \cos(n\phi). \tag{A.16}$$

Let's assume that the cylinder is illuminated by the incident plane wave which is described as $E_z{}^{\text{inc}}(\boldsymbol{\rho}) = E_0 e^{-j\boldsymbol{k}\cdot\boldsymbol{\rho}}$, where $E_0 = 1$, $\boldsymbol{k}$ is $k_0\hat{\mathbf{k}}$, $\hat{\mathbf{k}}$ is unit vector in the propagation direction and k_0 is the free space wavenumber. Normal to the cross-section is $\hat{\mathbf{n}}$. Assuming the place wave incoming from $\phi = 180$ direction and using Fourier series representation for the plane wave, we can define the incident field as

$$E_z^{\text{inc}} = \sum_{n=0}^{\infty} (-j)^n \epsilon_n J_n(k_0\rho) \cos(n\phi). \tag{A.17}$$

The total field outsider the cylinder E_z is defined as the sum of incident and scattered fields [67]

$$E_z^{\text{out}} = E_z^{\text{inc}} + E_z^{\text{scat}}, \tag{A.18}$$

which can be written as

$$E_z^{\text{out}}(\rho, \phi) = \sum_{n=0}^{\infty} [(-j)^n J_n(k_0\rho) + C_n H_n^{(2)}(k_0\rho)] \epsilon_n \cos(n\phi). \tag{A.19}$$

At radius $\rho = a$ the tangential component of the electric field must be continuous, that is

$$E_z^{\text{in}} = E_z^{\text{out}}. \tag{A.20}$$

By using (A.20) we get the first equation in the system of two linear algebraic equa-

tions with respect to the coefficients of the Fourier series expansion

$$\sum_{n=0}^{\infty} \epsilon_n B_n J_n(k_\epsilon a)\cos(n\phi) = \sum_{n=0}^{\infty}[(-j)^n J_n(k_0 a) + C_n H_n^{(2)}(k_0 a)]\epsilon_n \cos(n\phi). \quad (A.21)$$

Since $E_\rho = E_\phi = 0$, from Maxwell-Ampere law, the ϕ component of magnetic field H_ϕ^{in} component inside the scatterer is calculated as

$$H_\phi^{\text{in}} = \frac{1}{j\omega\mu_0}\left(\frac{\partial E_z^{\text{in}}}{\partial \rho}\right). \quad (A.22)$$

Substituting ${E_z}^{\text{in}}$ from (A.14) into (A.22), we obtain

$${H_\phi}^{\text{in}}(\rho,\phi) = \frac{k_\epsilon}{j\omega\mu_0}\sum_{n=0}^{\infty} B_n J_n'(k_\epsilon\rho)\cos(n\phi). \quad (A.23)$$

Since the magnetic field outside the cylinder is a superposition of the incident and scattered field contributions

$$H_\phi^{\text{out}} = H_\phi^{\text{inc}} + H_\phi^{\text{scat}}, \quad (A.24)$$

its Fourier series expansion becomes

$${H_\phi}^{\text{out}}(\rho,\phi) = \frac{k_0}{j\omega\mu_0}\sum_{n=0}^{\infty}[(-j)^n J_n'(k_0\rho) + C_n H_n^{(2)\prime}(k_0\rho)]\epsilon_n\cos(n\phi). \quad (A.25)$$

We know that, at radius $\rho = a$ tangential component of magnetic field must be continuous

$$H_\phi^{\text{in}} = H_\phi^{\text{out}}. \quad (A.26)$$

By using (A.26) we get the second equation of the system of linear algebraic equation with respect to the unknown coefficients of the Fourier series expansion

$$\frac{k_\epsilon}{j\omega\mu_0}\sum_{n=0}^{\infty} B_n J_n'(k_\epsilon a)\cos(n\phi) = \frac{k_0}{j\omega\mu_0}\sum_{n=0}^{\infty}[(-j)^n J_n'(k_0 a) + C_n H_n^{(2)\prime}(k_0 a)]\epsilon_n\cos(n\phi). \quad (A.27)$$

The system of linear algebraic equations (A.21) and (A.27) can be written in the matrix form as

$$\begin{bmatrix} J_n(k_\epsilon a) & -H_n^{(2)}(k_0 a) \\ k_\epsilon J_n'(k_\epsilon a) & -k_0 H_n'^{(2)}(k_0 a) \end{bmatrix} \begin{bmatrix} B_n \\ C_n \end{bmatrix} = \begin{bmatrix} (-j)^n J_n(k_0 a) \\ k_0 (-j)^n J_n'(k_0 a) \end{bmatrix} \tag{A.28}$$

After solving the system of linear algebraic equations (A.28) we find known coefficients B_n and C_n

$$B_n = \frac{(-j)^n \epsilon_n}{u_n - j\, v_n}, \tag{A.29}$$

$$C_n = j v_n B_n, \tag{A.30}$$

where $k_\epsilon = \sqrt{\epsilon} k_0$ and u_n, v_n are defined as follows:

$$u_n = \frac{\pi a}{2\mu_0}\big(- \mu_0 k_\epsilon J_n'(k_\epsilon a) Y_n(k_0 a) + \mu_0 k_0 J_n(k_\epsilon a) Y_n'(k_0 a)\big), \tag{A.31}$$

$$v_n = \frac{\pi a}{2\mu_0}\big(\mu_0 k_\epsilon J_n'(k_\epsilon a) J_n(k_0 a) - \mu_0 k_0 J_n(k_\epsilon a) J_n'(k_0 a)\big), \tag{A.32}$$

Derivative of the Bessel functions are given as

$$J_n'(k_0 a) = \frac{n J_n(k_0 a)}{k_0 a} - J_{n+1}(k_0 a), \tag{A.33}$$

$$J_n'(k_\epsilon a) = \frac{n J_n(k_\epsilon a)}{k_\epsilon a} - J_{n+1}(k_\epsilon a). \tag{A.34}$$

$$Y_n'(k_0 a) = \frac{n Y_n(k_0 a)}{k_0 a} - Y_{n+1}(k_0 a). \tag{A.35}$$

A.1 Numerical Evaluation

Validation of the Mie series solution against commercial COMSOL Multiphysics software is demonstrated below. As an example, we consider a circular dielectric cylinder with cross section radius of $R = 0.09$ m and relative dielectric permittivity $\epsilon = 4$. The cylinder is illuminated by the incident plane wave with angle $\phi = 180$ which has the harmonic waveform as $E_z^{\,inc}(\boldsymbol{\rho}) = e^{-i\boldsymbol{k}\cdot\boldsymbol{\rho}}$. Frequency of the plane

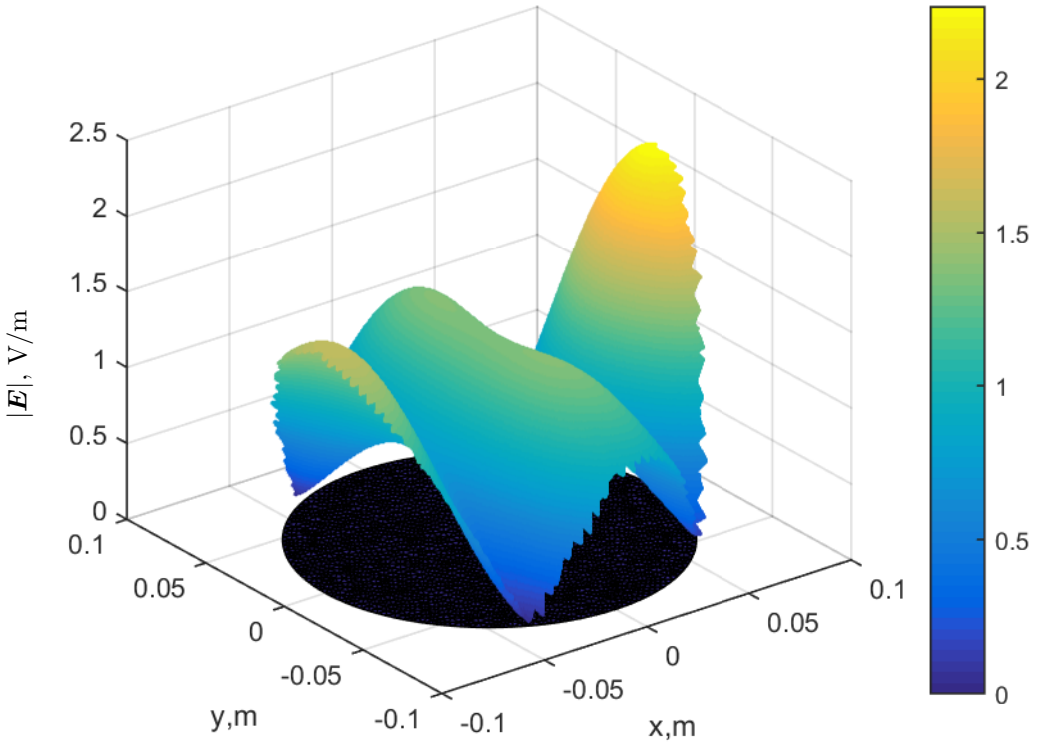

Figure A.1: Volumetric distribution of $|\boldsymbol{E}|$ at 1 GHz TM polarized in circular cylinder with $\epsilon = 4$ obtained from (A.14) Mie series solution.

wave travelling in positive direction x direction is 1GHz. Distribution of magnitude of (A.14) in the Mie series is depicted in Fig. A.1. COMSOL solution and its relative error with respect to the Mie series solution computed to machine precision are depicted in Fig. A.1 and Fig. A.1, respectively.

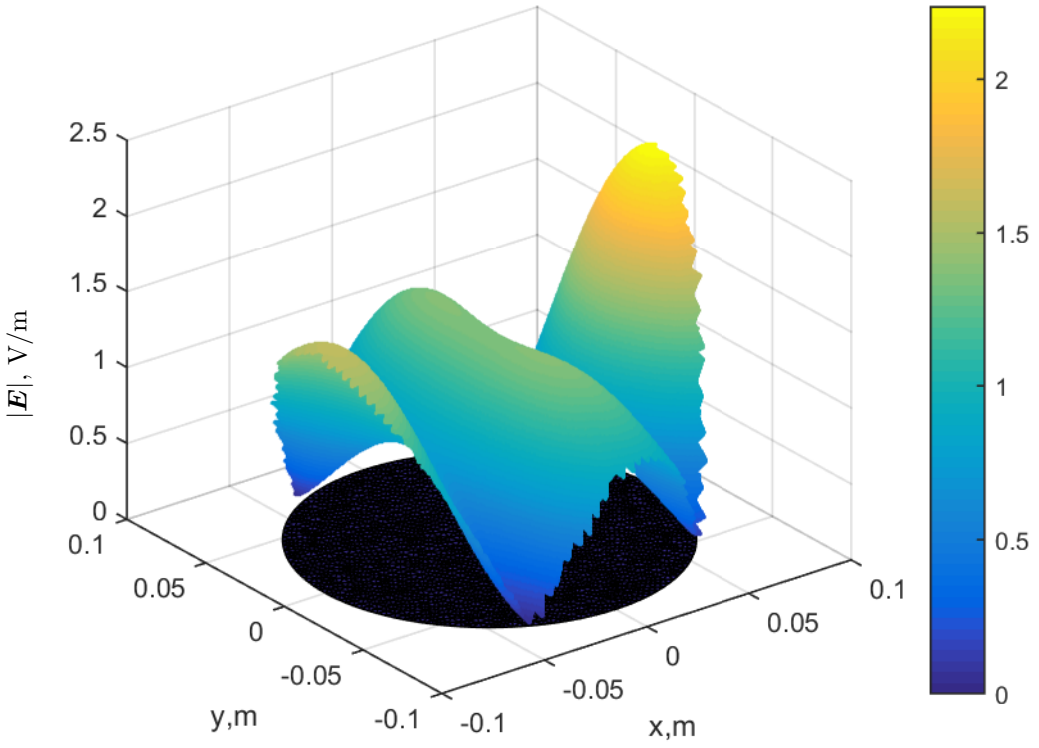

Figure A.2: Volumetric distribution of $|\boldsymbol{E}|$ at 1 GHz TM polarized in circular cylinder with ϵ= 4 obtained from COMSOL.

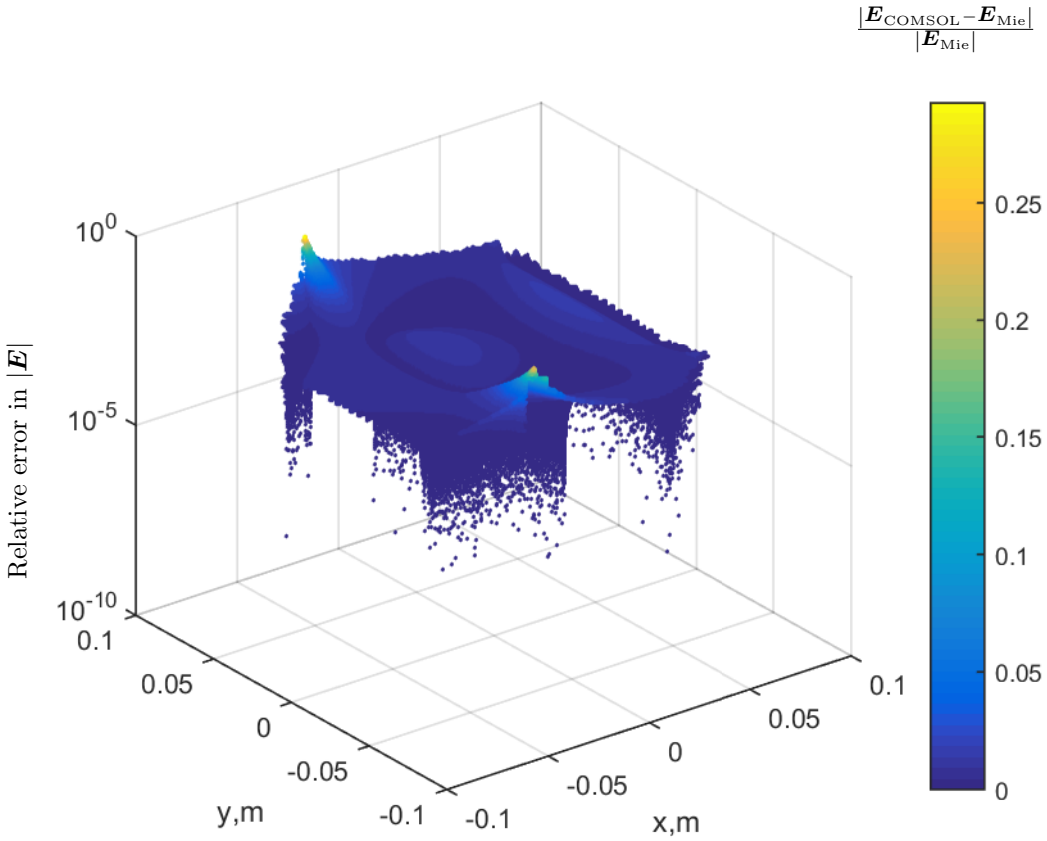

Figure A.3: Relative error in the volumetric density of $|\boldsymbol{E}|$ at 1 GHz in circular cylinder with $\epsilon = 4$ (Fig. 5.4) between Mie series and COMSOL solutions.

B

Mie Series Analytic Solution for 2D TE Scattering on Circular Dielectric Cylinder

For TE case, the cylinder is illuminated by the incident plane wave, which has the harmonic waveform as $H_z^{\text{inc}}(\boldsymbol{\rho}) = \frac{H_0}{\eta_0} e^{-j\boldsymbol{k}\cdot\boldsymbol{\rho}}$, where $E_0 = 1\text{V/m}$, $\boldsymbol{k}$ is $k_0\hat{\mathbf{k}}$, $\hat{\mathbf{k}}$ is unit vector in the propagation direction and k_0 is the free space wavenumber. Normal to the cross-section is $\hat{\mathbf{n}}$. If we take the curl of (1.9) we get

$$\nabla \times \nabla \times \boldsymbol{H}(\boldsymbol{r}) = \nabla \times \boldsymbol{J}^i(\boldsymbol{r}) + \nabla \times \boldsymbol{J}^c(\boldsymbol{r}) + j\omega\epsilon\nabla \times \boldsymbol{E}(\boldsymbol{r}). \tag{B.1}$$

Since we are considering a 2D problem, there is no variation along z axis($\partial/\partial z = 0$). Also, since we are considering the region S which is source free we have $\boldsymbol{J}^i(\boldsymbol{r}, t) = \boldsymbol{M}^i(\boldsymbol{r}, t) = 0$. In the lossless case $\sigma = 0$ making $\boldsymbol{J}^c(\boldsymbol{r}, t) = 0$. Considering the above, plug in (1.8) into equation (B.1) yields the following vector wave equation

$$\nabla \times \nabla \times \boldsymbol{H}(\boldsymbol{r}) - k^2\boldsymbol{H}(\boldsymbol{r}) = 0. \tag{B.2}$$

Using vector identity $\nabla \times \nabla \times \boldsymbol{A}(\boldsymbol{r}) = -\nabla^2\boldsymbol{A}(\boldsymbol{r}) + \nabla(\boldsymbol{\nabla} \cdot \boldsymbol{A}(\boldsymbol{r}))$ we get

$$\nabla \times \nabla \times \boldsymbol{H}(\boldsymbol{r}) = -\nabla^2\boldsymbol{H}(\boldsymbol{r}) + \nabla(\boldsymbol{\nabla} \cdot \boldsymbol{H}(\boldsymbol{r})). \tag{B.3}$$

Since we are solving 2D TE problem $H_x = H_y = 0$ and there is only z component of the magnetic field. Combined with fields independence on z coordinate this results in $\boldsymbol{\nabla} \cdot \boldsymbol{H}(\boldsymbol{r}) = 0$. Using this property and accounting for (B.3) we convert equation (B.2) to

$$\nabla^2 \boldsymbol{H}(\boldsymbol{r}) + k^2 \boldsymbol{H}(\boldsymbol{r}) = 0. \tag{B.4}$$

Due to zero components $H_x = H_y = 0$, vector Helmholtz equation converts to scalar equation for the z component of the magnetic field

$$\nabla^2 H_z(x, y) + k^2 H_z(x, y) = 0. \tag{B.5}$$

Equation (B.5) can be rewritten in cylindrical coordinate system as

$$\frac{1}{\rho}\frac{\partial}{\partial \rho}(\rho \frac{\partial}{\partial \rho} H_z(\rho, \phi)) + k_0^2 H_z(\rho, \phi) + \frac{1}{\rho^2}\frac{\partial^2}{\partial \phi^2} H_z(\rho, \phi) = 0. \tag{B.6}$$

Since $H_z(\rho, \phi)$ is a 2π-periodic function over ϕ we can use Fourier series to represent $H_z(\rho, \phi)$ as

$$H_z(\rho, \phi) = \sum_{n=-\infty}^{\infty} H_{zn}(\rho) e^{-jn\phi}. \tag{B.7}$$

If we plug (B.7) into (B.6) and solve for coefficients $H_{zn}(\rho)$ we have

$$\sum_{n=-\infty}^{\infty} \big[\frac{1}{\rho}\frac{\partial}{\partial \rho}(\rho \frac{\partial}{\partial \rho} H_{zn}(\rho)) + \frac{1}{\rho^2}(-n^2) H_{zn}(\rho) + k^2 H_{zn}(\rho)\big] e^{-jn\phi} = 0. \tag{B.8}$$

Taking into consideration that, if for all the values of ϕ the Fourier series is zero, all its coefficients are zero, we enforce equation (B.8) as

$$\frac{1}{\rho}\frac{\partial}{\partial \rho}(\rho \frac{\partial}{\partial \rho} H_{zn}(\rho)) + (k^2 - {}^{n^2}/_{\rho^2}) H_{zn}(\rho) = 0. \tag{B.9}$$

Equation (B.9) is the Bessel equation. The solutions of the Bessel equation are

$$H_{zn}(\rho) = \begin{cases} J_n(k,\rho), \\ Y_n(k,\rho), \\ H_n^{(1)}(k,\rho), \\ H_n^{(2)}(k,\rho), \end{cases} \tag{B.10}$$

as well as their linear combinations. Since, $\cos(n\phi) = (e^{-jn\phi} + e^{jn\phi})/2$ and the coefficients of the Fourier series are even as function of index n, i.e. $H_{z,n} = H_{z,-n}$ when the field is an even function of ϕ we represent the field inside the cylinder $(0 \leq \rho \leq a)$ as

$$H_z^{\text{in}}(\rho,\phi) = \frac{1}{\eta_0} \sum_{n=-\infty}^{\infty} B_n J_n(k_\epsilon \rho) e^{-jn\phi} = \frac{1}{\eta_0} \sum_{n=0}^{\infty} \epsilon_n B_n J_n(k_\epsilon \rho) \cos(n\phi). \tag{B.11}$$

The choice of $J_n(k_\epsilon \rho)$ as the solution of the Bessel equation is stipulated by the fact that the field should remain finite at the origin.

For the region $a \leq \rho \leq \infty$ outside the cylinder,

$$H_z^{\text{scat}}(\rho,\phi) = \frac{1}{\eta_0} \sum_{n=-\infty}^{\infty} C_n H_n^{(2)}(k_0 \rho) e^{-jn\phi} = \frac{1}{\eta_0} \sum_{n=0}^{\infty} \epsilon_n C_n H_n^{(2)}(k_0 \rho) \cos(n\phi). \tag{B.12}$$

The incident plane wave expansion into Fourier series is the following

$$H_z^{\text{inc}} = \frac{1}{\eta_0} \sum_{n=0}^{\infty} (-j)^n \epsilon_n J_n(k_0 \rho) \cos(n\phi). \tag{B.13}$$

Hence, the representation of H_z outside the dielectric cylinder is defined as [67]

$$H_z^{\text{out}} = H_z^{\text{inc}} + H_z^{\text{scat}}. \tag{B.14}$$

Therefore,

$$H_z^{\text{out}}(\rho,\phi) = \frac{1}{\eta_0}\sum_{n=0}^{\infty}[(-j)^n J_n(k_0\rho) + C_n H_n^{(2)}(k_0\rho)]\epsilon_n \cos(n\phi). \tag{B.15}$$

At the boundary $\rho = a$ continuity of the tangential magnetic field components must hold

$$H_z^{\text{in}} = H_z^{\text{out}}. \tag{B.16}$$

From (B.16) we get the first equation of the system of two linear algebraic equations with respect to the unknowns expansion coefficients

$$\frac{1}{\eta_0}\sum_{n=0}^{\infty}\epsilon_n B_n J_n(k_\epsilon a)\cos(n\phi) = \frac{1}{\eta_0}\sum_{n=0}^{\infty}[(-j)^n J_n(k_0 a) + C_n H_n^{(2)}(k_0 a)]\epsilon_n \cos(n\phi). \tag{B.17}$$

By using the fact that for TE case $H_\rho = H_\phi = 0$, from the Faraday's law the ϕ component of the electric field inside the dielectric cylinder is calculated as

$$E_\phi^{\text{in}} = \frac{-1}{j\omega\epsilon}\left(\frac{\partial H_z^{in}}{\partial \rho}\right). \tag{B.18}$$

If we plug ${H_z}^{\text{in}}$ from equation (B.11) into equation (B.18), we get

$$E_\phi^{\text{in}}(\rho,\phi) = \frac{-k_\epsilon}{j\omega\epsilon\eta_0}\sum_{n=0}^{\infty} B_n J_n'(k_\epsilon\rho)\epsilon_n \cos(n\phi). \tag{B.19}$$

Outside the cylinder the total electric field is superposition of the incident and scattered field contributions

$$E_\phi^{\text{out}} = E_\phi^{\text{inc}} + E_\phi^{\text{scat}}. \tag{B.20}$$

Thus, equation (B.20) turns into

$$E_\phi^{\text{out}}(\rho,\phi) = \frac{-k_0}{j\omega\epsilon\eta_0}\sum_{n=0}^{\infty}[(-j)^n J_n'(k_0\rho) - C_n H_n'^{(2)}(k_0\rho)]\epsilon_n \cos(n\phi). \tag{B.21}$$

At radius $\rho = a$ ϕ component of electric field must be continuous

$$E_{\phi}^{\text{in}} = E_{\phi}^{\text{out}}. \tag{B.22}$$

By using (B.22), we get the second equation of the system of linear algebraic equations with respect to the Fourier series expansion coefficients

$$\frac{-k_{\epsilon}}{j\omega\epsilon\eta_0}\sum_{n=0}^{\infty} B_n J_n'(k_{\epsilon}a)\epsilon_n \cos(n\phi) = \frac{-k_0}{j\omega\epsilon\eta_0}\sum_{n=0}^{\infty}[(-j)^n J_n'(k_0a) + C_n H_n'^{(2)}(k_0a)]\epsilon_n \cos(n\phi). \tag{B.23}$$

The system of linear algebraic equations in the matrix form is the following

$$\begin{bmatrix} J_n(k_{\epsilon}a) & -H_n^{(2)}(k_0a) \\ -k_{\epsilon}J_n'(k_{\epsilon}a) & k_0 H_n'^{(2)}(k_0a) \end{bmatrix}\begin{bmatrix} B_n \\ C_n \end{bmatrix} = \begin{bmatrix} (-j)^n J_n(k_0a) \\ -k_0(-j)^n J_n'(k_0a) \end{bmatrix}. \tag{B.24}$$

Solution of the system of linear algebraic equations (B.24) produces the unknown coefficients B_n and C_n in the form

$$B_n = \frac{(-j)^n \epsilon_n}{u_n - j\ v_n}, \tag{B.25}$$

$$C_n = jv_n B_n. \tag{B.26}$$

In (B.25) and (B.26), coefficients u_n and v_n are defined as

$$u_n = \frac{\pi a}{2\epsilon_r\epsilon_0}\big(-\epsilon_0 k_{\epsilon} J_n'(k_{\epsilon}a)Y_n(k_0a) + \epsilon k_0 J_n(k_{\epsilon}a)Y_n'(k_0a)\big), \tag{B.27}$$

$$v_n = \frac{\pi a}{2\epsilon_r\epsilon_0}\big(\epsilon_0 k_{\epsilon} J_n'(k_{\epsilon}a)J_n(k_0a) - \epsilon k_0 J_n(k_{\epsilon}a)J_n'(k_0a)\big). \tag{B.28}$$

where ϵ_r is the relative permittivity of the dielectric medium.

B.1 Numerical Evaluation

Validation of the numerical implementation of the Mie series solution under TE polarization is conducted via comparison to the results obtained using commercial

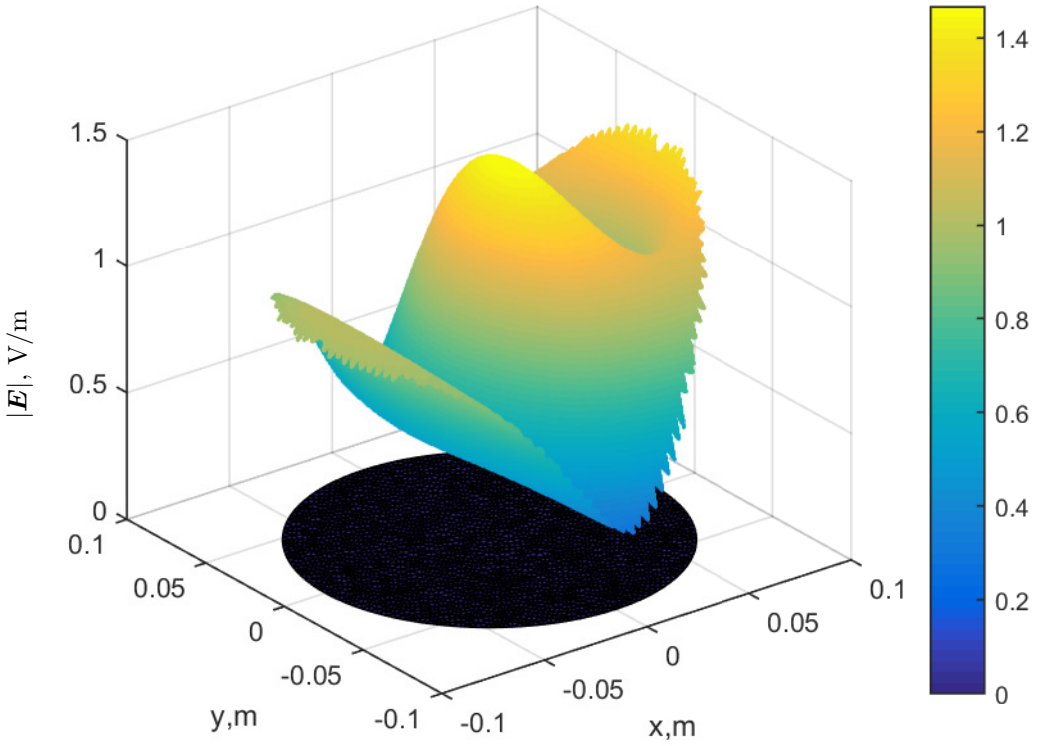

Figure B.1: Volumetric distribution of $|\boldsymbol{E}|$ at 1 GHz in circular cylinder with ϵ= 4 obtained from Mie series solution under excitation with TE-polarized plane wave with magnitude of the electric field $E_0 = 1$V/m.

FEM software COMSOL Multiphysics. As an example, we consider a circular dielectric cylinder with cross section radius of $R = 0.09$ m and relative dielectric permittivity $\epsilon = 4$. The cylinder is illuminated by the incident plane wave incoming from $\phi = 180$ direction with incident magnetic field $H_z{}^{inc}(\boldsymbol{\rho}) = 1/\eta_0 e^{-i\boldsymbol{k}\cdot\boldsymbol{\rho}}$. Frequency of the plane wave is 1GHz. Coefficients B_n from (B.25) substituted into (B.27) and (B.28) produce distribution of magnitude of electric field depicted in Fig. B.1. COMSOL solution and the relative errors between the Mie series and COMSOL solutions are depicted in Fig. B.2 and Fig. B.3, respectively.

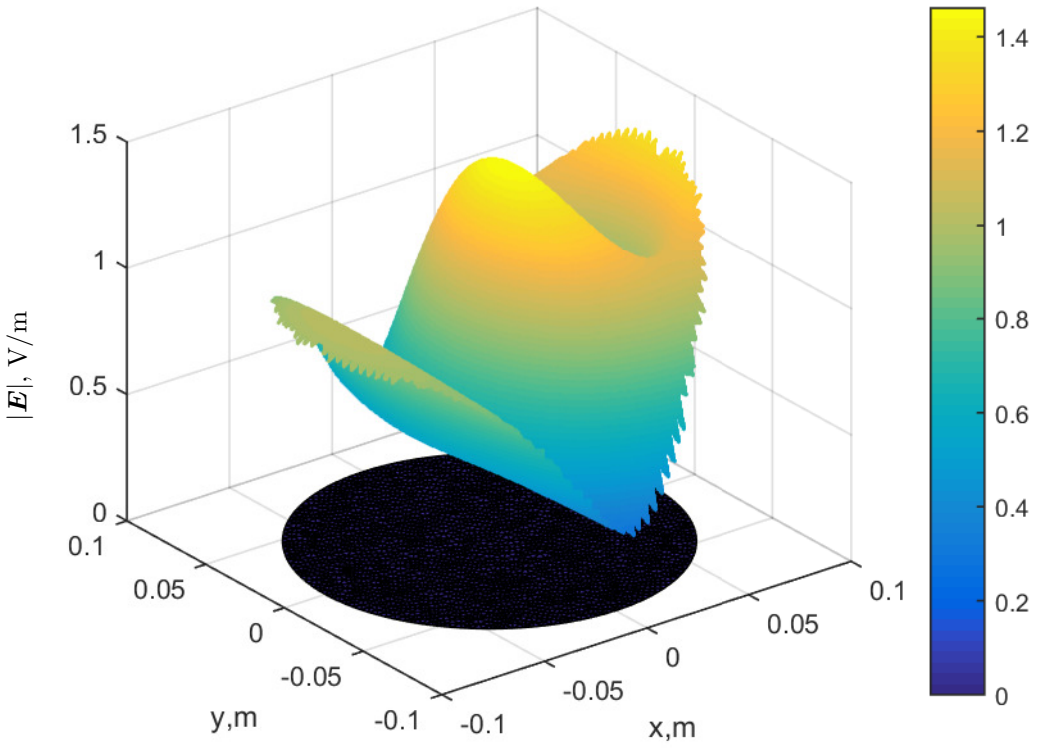

Figure B.2: Volumetric distribution of $|\boldsymbol{E}|$ at 1 GHz in circular cylinder with $\epsilon = 4$ obtained from COMSOL under excitation with TE-polarized plane wave with magnitude of the electric field $E_0 = 1\text{V/m}$.

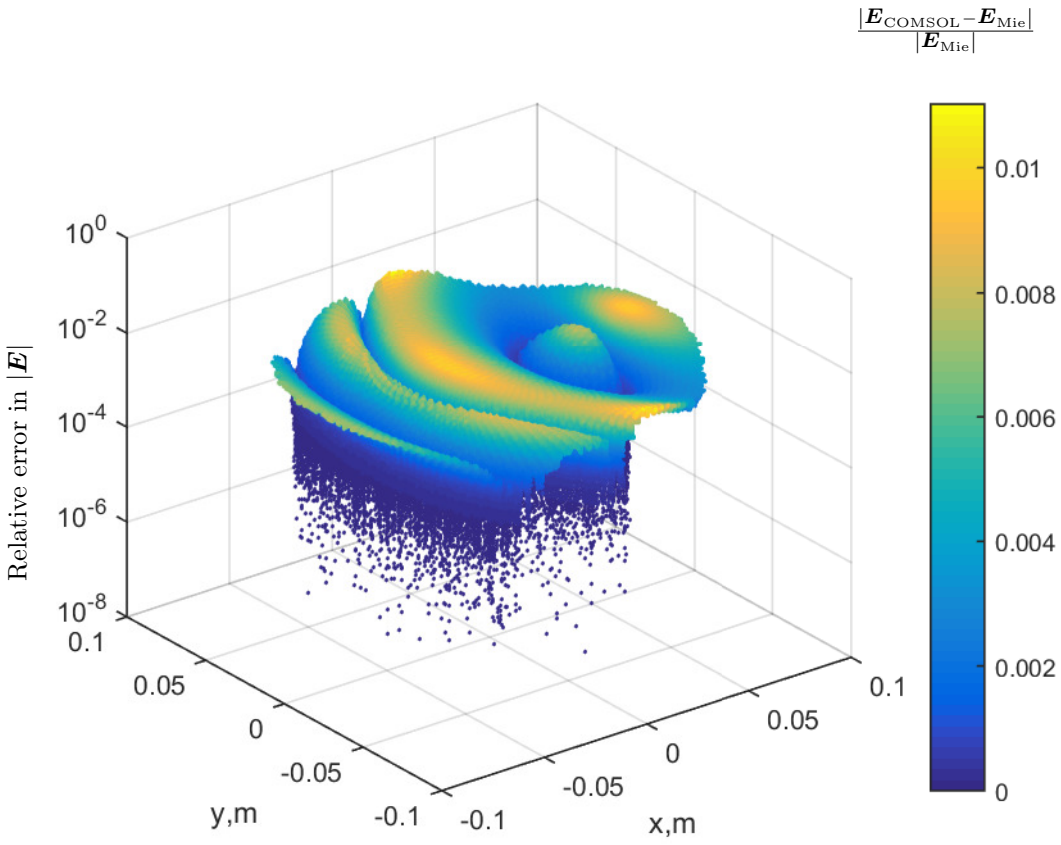

Figure B.3: Relative error in the volumetric distribution of $|\boldsymbol{E}|$ at 1 GHz in circular cylinder with $\epsilon = 4$ between Mie series and COMSOL solutions for the case of TE-polarized plane wave scattering.

C

Continuity of the Tangential Components of the $\boldsymbol{E}$ and $\boldsymbol{H}$ Fields Enforcement in the Volume EFIE

The classic V-EFIE is written as [27]:

$$\boldsymbol{E}(\boldsymbol{r}) = \boldsymbol{E}^{\text{inc}}(\boldsymbol{r}) + k_0^2\,(\epsilon - 1) \int\limits_V \overline{\overline{G}}_0(\boldsymbol{r}, \boldsymbol{r}') \;\cdot\; \boldsymbol{E}(\boldsymbol{r}')dv', \tag{C.1}$$

where $\boldsymbol{E}(\boldsymbol{r})$ is total electric field in observation point $\boldsymbol{r}$, and $\overline{\overline{G}}_0(\boldsymbol{r}, \boldsymbol{r}')$ is free space dyadic Green's function defined as

$$\overline{\overline{G}}_0(\boldsymbol{r}, \boldsymbol{r}') = \Big(\frac{\boldsymbol{\nabla\nabla}}{k_0^2} + \overline{\overline{I}}\Big) G_0(\boldsymbol{r}, \boldsymbol{r}'). \tag{C.2}$$

In (C.2), $G_0(\boldsymbol{r}, \boldsymbol{r}') = \frac{e^{-ik_0|\boldsymbol{r}-\boldsymbol{r}'|}}{4\pi|\boldsymbol{r}-\boldsymbol{r}'|}$ is the 3D Green's function of free space, k_0 is the wave number in free space, $\boldsymbol{r}$ and $\boldsymbol{r}'$ are position vectors of the observation and source points. In order to show that the solution of the (C.1) satisfies the boundary conditions lets calculate the difference $\boldsymbol{E}^+ - \boldsymbol{E}^-$ for the field at outer location $\boldsymbol{r}^+$ and location inside the body $\boldsymbol{r}^-$ along $\hat{\mathbf{n}}$ normal vector to the boundary. Upon crossing the boundary the integrals containing function G_0 and it first derivatives

remain continuous. Only considering the term substantial for this difference we get the following

$$\boldsymbol{E}^{+}(\boldsymbol{r}^{+}) - \boldsymbol{E}^{-}(\boldsymbol{r}^{-}) = \int_{V} (\epsilon - 1)\, \boldsymbol{E}(\boldsymbol{r}')\boldsymbol{\nabla}(G_0(\boldsymbol{r}^{+}, \boldsymbol{r}') - G_0(\boldsymbol{r}^{-}, \boldsymbol{r}'))dv'. \tag{C.3}$$

Therefore, for tangential component of electric field

$$\lim_{\boldsymbol{r}^{+}\to\boldsymbol{r},\boldsymbol{r}^{-}\to\boldsymbol{r}} \left|\boldsymbol{E}_t^{+}(\boldsymbol{r}^{+}) - \boldsymbol{E}_t^{-}(\boldsymbol{r}^{-})\right| = 0, \tag{C.4}$$

where $\boldsymbol{r}$ is a position vector on the boundary between $\boldsymbol{r}^{+}$ and $\boldsymbol{r}^{-}$. For normal component of electric field

$$\lim_{\boldsymbol{r}^{+}\to\boldsymbol{r},\boldsymbol{r}^{-}\to\boldsymbol{r}} \left|\boldsymbol{E}_n^{+}(\boldsymbol{r}^{+}) - \boldsymbol{E}_n^{-}(\boldsymbol{r}^{-})\right| = (\epsilon - 1)\, \boldsymbol{E}_n(\boldsymbol{r}). \tag{C.5}$$

D

Semi-analytical Solution of V-EFIE for the Circular Conductor 2D Problems

Helmholtz equation for the electric field:

$$\nabla^2 E_z + k_\sigma^2 E_z = 0 \tag{D.1}$$

Solution in the core conductor:

$$E_z = C_1 J_0(k_{\sigma 1}\rho) \tag{D.2}$$

Solution in the sheath conductor:

$$E_z = C_2 H_0^{(1)}(k_{\sigma 2}\rho) + C_3 H_0^{(2)}(k_{\sigma 2}\rho) \tag{D.3}$$

E_z is governed by Volume-EFIE:

$$E_z(\boldsymbol{\rho}) + i\omega\mu_0 \iint\limits_{S_1+S_2} G_0(\boldsymbol{\rho}, \boldsymbol{\rho}') E_z(\boldsymbol{\rho}')\, ds' = V_{\text{p.u.l.}}, \quad \boldsymbol{\rho} \in S_1, S_2, \tag{D.4}$$

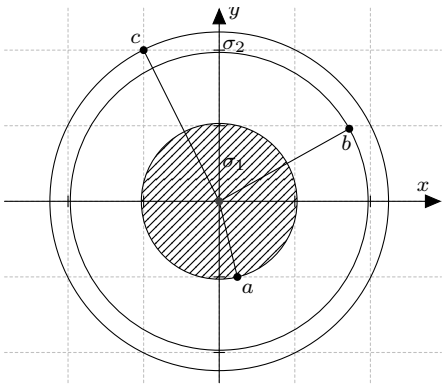

Figure D.1: Coaxial cable cross-sectional geometry view

where $\boldsymbol{\rho}$ is the position vector of the observation point, $G_0(\boldsymbol{\rho},\boldsymbol{\rho}')= -1/(2\pi)\ln(|\boldsymbol{\rho}-\boldsymbol{\rho}'|)$ is the magneto-static Green's function of free space. MoM equations for unknown constants C_1, C_2, and C_3 are computed by enforcing V-EFIE at observation points $\boldsymbol{\rho}=\hat{\mathbf{x}}a$, and $\boldsymbol{\rho}=\hat{\mathbf{x}}b$, and $\boldsymbol{\rho}=\hat{\mathbf{x}}c$. Hence the system of linear algebraic equations is formed as

$$\frac{1}{i\omega\mu_0}\begin{bmatrix}1\\-1\\-1\end{bmatrix}=\begin{bmatrix}J_0\left(k_{\sigma 1}a\right) & 0 & 0\\ 0 & H_0^{(1)}\left(k_{\sigma 2}b\right) & 0\\ 0 & 0 & H_0^{(2)}\left(k_{\sigma 2}c\right)\end{bmatrix}\begin{bmatrix}C_1\\C_2\\C_3\end{bmatrix}+\begin{bmatrix}\alpha & \beta & \gamma\\ \eta & \theta & \vartheta\\ \iota & \kappa & \tau\end{bmatrix}\cdot\begin{bmatrix}C_1\\C_2\\C_3\end{bmatrix}, \tag{D.5}$$

where, $\alpha = \sigma_1\left\langle ln(|\hat{\mathbf{x}}a-\boldsymbol{\rho}'|), J_0\left(k_{\sigma 1}\rho'\right)\right\rangle$, $\beta = \sigma_2\left\langle ln(|\hat{\mathbf{x}}a-\boldsymbol{\rho}'|), H_0^{(1)}\left(k_{\sigma 2}\rho'\right)\right\rangle$, $\gamma = \sigma_2\left\langle ln(|\hat{\mathbf{x}}a-\boldsymbol{\rho}'|), H_0^{(2)}\left(k_{\sigma 2}\rho'\right)\right\rangle$, $\eta = \sigma_1\left\langle ln(|\hat{\mathbf{x}}b-\boldsymbol{\rho}'|), J_0\left(k_{\sigma 1}\rho'\right)\right\rangle$, and
$\theta = \sigma_2\left\langle ln(|\hat{\mathbf{x}}b-\boldsymbol{\rho}'|), H_0^{(1)}\left(k_{\sigma 2}\rho'\right)\right\rangle$, $\vartheta = \sigma_2\left\langle ln(|\hat{\mathbf{x}}b-\boldsymbol{\rho}'|), H_0^{(2)}\left(k_{\sigma 2}\rho'\right)\right\rangle$,
$\iota = \sigma_1\left\langle ln(|\hat{\mathbf{x}}c-\boldsymbol{\rho}'|), J_0\left(k_{\sigma 1}\rho'\right)\right\rangle$, $\kappa = \sigma_2\left\langle ln(|\hat{\mathbf{x}}c-\boldsymbol{\rho}'|), H_0^{(1)}\left(k_{\sigma 2}\rho'\right)\right\rangle$, and
$\tau = \sigma_2\left\langle ln(|\hat{\mathbf{x}}c-\boldsymbol{\rho}'|), H_0^{(2)}\left(k_{\sigma 2}\rho'\right)\right\rangle$. Inner products are defined as

$$\left\langle G_0(\boldsymbol{\rho},\boldsymbol{\rho}'), J_0\left(k_{\sigma 1}\rho'\right)\right\rangle = \frac{-1}{2\pi}\int_0^a\int_0^{2\pi}\ln(|\boldsymbol{\rho}-\boldsymbol{\rho}'|)J_0\left(k_{\sigma 1}\rho'\right)\rho' d\varphi' d\rho', \tag{D.6}$$

and

$$\left\langle G_0(\boldsymbol{\rho},\boldsymbol{\rho}'), H_0^{(i)}\left(k_{\sigma 2}\rho'\right)\right\rangle = \frac{-1}{2\pi}\int_b^c\int_0^{2\pi} \ln(|\boldsymbol{\rho}-\boldsymbol{\rho}'|)H_0^{(i)}\left(k_{\sigma 2}\rho'\right)\rho' d\varphi' d\rho', i=1,2. \tag{D.7}$$

Numerical implementation of the MoM solution of the proposed semi-analytical solution of V-EFIE has been done using PTC Mathcad [81] tool. Getting analytic-like solution requires computation of integrals to machine precision. Hence, the double integrations are calculated using adaptive integration routines to machine precision with error level of 10^{-13}. Adaptive integration is accurate but time consuming as it applies quadrature rules to many small enough intervals in order to produce results with prescribed precision. Mathematical software packages (e.g. PTC Mathcad [81]) use adaptive integrations to compute an integral with an accuracy prescribed by the user.

We consider a coaxial cable of a circular cross-section depicted in Fig. D.1. The inner conductor is made of copper ($\sigma_a = 5.96\times10^7$ S/m) and has the radius of 0.022 m. The sheath is made of lead ($\sigma_b = 4.55\times10^6$ S/m) and has the inner and outer radii of 0.0395 m and 0.044 m, respectively. One solution of SLAE (D.5) MoM equations for unknown constants C_1, C_2, and C_3 is computed by enforcing V-EFIE at observation points $\boldsymbol{\rho} = \hat{\mathbf{x}}0.022\text{m}$, and $\boldsymbol{\rho} = \hat{\mathbf{x}}0.0395\text{m}$, and $\boldsymbol{\rho} = \hat{\mathbf{x}}0.044\text{m}$. Fig. D.2 shows the distribution of the computed current density at 60 Hz. Another solution is computed by enforcing V-EFIE at observation points $\boldsymbol{\rho} = \hat{\mathbf{x}}0.011\text{m}$, and $\boldsymbol{\rho} = \hat{\mathbf{x}}0.04175\text{m}$, and $\boldsymbol{\rho} = \hat{\mathbf{x}}0.044\text{m}$. The distribution of relative error in j_a and j_b between the two solutions is shown in Fig. D.3. The average relative error is $1.1961691980772016\times10^{-15}$. The comparison of the two semi-analytical solutions of V-EFIE computed using two different testing procedures and, therefore, two different SLAEs verifies them to be 13 digit accurate.

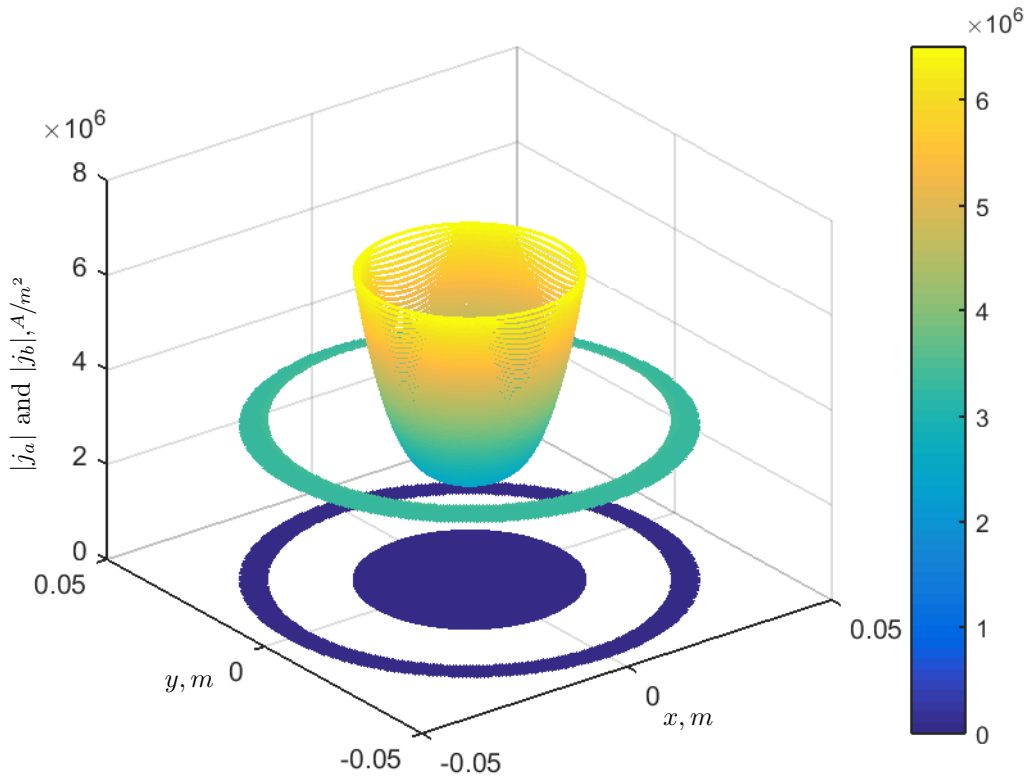

Figure D.2: Volumetric current densities j_a and j_b at 60 Hz in circular coaxial transmission line obtained via semi-analytical solutions (D.2) and (D.3).

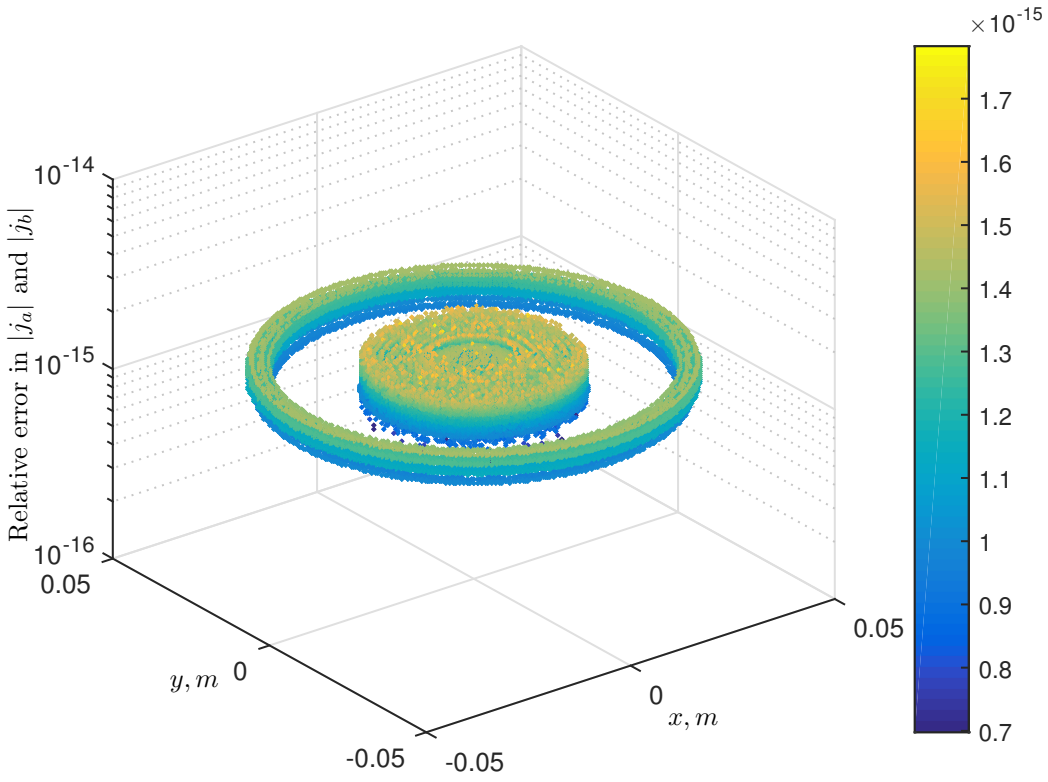

Figure D.3: Relative error in the volumetric current densities j_a and j_b at 60 Hz between two semi-analytical solution of V-EFIE (D.4).

References

[1] J. C. Maxwell, "A dynamical theory of the electromagnetic field," *Phil. Trans. of the Royal Society of London,* vol. 155, pp. 459–512, Jan. 1865.

[2] O. heaviside, "On the forces, stresses and fluxes of energy in the electromagnetic field," *Phil. Trans. of the Royal Society of London,* vol. 50, pp. 126–129, Jan. 1891.

[3] A. Taflove, S. C. Hagness, *Computational electrodynamics the finite-difference time-domain method,* 3rd Ed., Boston, MA: ARTECH HOUSE, 2005.

[4] J. C. Tannehill, D. A. Anderson, and R. H. Pletcher, *Computational Fluid Mechanics and Heat Transfer, First edition,* 2nd ed., Philadelphia: Taylor & Francis, 1997.

[5] P. D. Lax and B. Wendroff, "Systems of conservation laws," Commun. Pure Appl. Math., vol. 13, pp. 217–237, 1960.

[6] P. E. Ceruzzi, *A History of Modern Computing,* Cambridge, MA: MIT Press, 1998.

[7] B. Young, *Digital Signal Integrity,* New York: McGraw-Hill, 2001.

[8] D. M. Pozar, *Microwave Engineering,* 2nd Ed., New York: Wiley, 1997.

[9] S. Ramo, J. R. Whinnery, T. Van Duzer, *Fields and Waves in Communication Electronics,* 2nd Ed., New York, Wiley, 1984.

[10] Weng Cho Chew, Mei Song Tong, and Bin Hu, *Integral Equation Methods for Electromagnetic and Elastic Waves,* Morgan and Claypool, 2009.

[11] J. A. Stratton, *Electromagnetic Theory,* New Yourk: McGraw-Hill, 1941.

[12] J. M. Song, C. C. Lu, W. C. Chew, and S. W. Lee, "Fast Illinois solver code (FISC)," IEEE Antennas Propag. Mag., vol. 40, no. 3, pp. 27–33, 1998.

[13] S. Velamparambil, W. C. Chew, and J. M. Song, "10 million unknowns, is it that large," IEEE Antennas Propag. Mag., vol.45, no.2, pp. 43–58, Apr. 2003.

[14] M. L. Hastriter, "A Study of MLFMA for Large-Scale Scattering Problems," Ph.D. Thesis, Dept. ECE, U. Illinois, Jun. 2003.

[15] A. Menshov, "Novel single-source surface integral equations for scattering on 2-D penetrable cylinders and current flow modeling in 2-D and 3-D conductors," M.Sc. Thesis, Dept. Electr. Comput. Eng, Univ. Manitoba, Winnipeg, Canada, 2012. [Online]. Available: http://hdl.handle.net/1993/23439.

[16] B. M. Notaros, *Electromagnetics,* Pearson Prentice Hall, 2010.

[17] C. A. Balanis, *Advanced Engineering Electromagnetics,* 2nd ed. Hoboken, NJ: Wiley, 2012.

[18] J. S. W. Chew, E. Michielssen and J. Jin, Eds., *Fast and Efficient Algorithms in Computational Electromagnetics,* Norwood, MA, USA: Artech House, 2001.

[19] S. Zouhdi, A. Sihvola, and A. P. Vinogradov, *Metamaterials and Plasmonics: Fundamentals, Modelling, Applications,* New York: Springer-Verlag, 2008.

[20] R. Mittra, Ed., *Computer Techniques for Electromagnetics,* New York: Hemisphere, 1987.

[21] N. Morita, N. Kumagai, and J. R. Mautz, *Integral Equation Methods for Electromagnetics,* Boston: Artech House, 1990.

[22] Andrew F. Peterson, *Mapped Vector Basis Functions for Electromagnetic Integral Equations,* Morgan & Claypool 2005.

[23] C. T. Tai, *Dyadic Green Functions in Electromagnetic Theory,* 2nd ed. New York: IEEE Press, 1994.

[24] G. Green, *An Essay on the Application of Mathematical Analysis to the Theories of Electricity and Magnetism,* T. Wheelhouse, Nottingham, 1828.

[25] J. - M. Jin, *The Finite Element Method in Electromagnetics,* 2nd ed. New York: Wiley, 2002.

[26] A. Taflove and S. C. Hagness, *The Finite-Difference Time-Domain Method,* 3rd ed. Norwood: Artech House, 2005.

[27] A. Peterson, S. Ray, and R. Mittra, *Computational Methods for Electromagnetics,* New York: IEEE Press, 1998.

[28] E. Bleszynski, M. Bleszynski, and T. Jaroszewicz, "Surface integral equations for electro- magnetic scattering from impenetrable and penetrable sheets," *IEEE Antennas Propag. Mag.,* vol. 35, no. 6, pp. 14–26, Dec. 1993.

[29] Jian-Ming Jin, *Theory and Computation of Electromagnetic Fields,* New York: Wiley, 2010.

[30] W. C. Chew, J. - M. Jin, E. Michielssen, and J. Song, (ed.) *Fast and Efficient Algorithms in Computational Electromagnetics,* Norwood: Artech House, 2001.

[31] W. C. Chew, *Waves and Fields in Inhomogeneous Media,* New York: IEEE Press, 1999.

[32] A. Kishk and L. Shafai, "Different formulations for numerical solution of single or multibodies of revolution with mixed boundary conditions," *IEEE Trans. Antennas Propag.,* vol. 34, no. 5, pp. 666–673, May 1986.

[33] *The Sonnet Suite User's Manual,* Sonnet Softw. Inc., North Syracuse, NY, 2014.

[34] *COMSOL Multiphysics RF Module User's Manual,* COMSOL AB, Stockholm, Sweden, 2016.

[35] *FEKO User's Manual,* EM Software & Syst. Inc., Stellenbosch, South Africa, 2014.

[36] E. N. Vasil'ev, "Excitation of a smooth body of revolution," *Izvestiya VUZov of USSR, Radiophysics series,* vol. 2, no. 4, pp. 588-601, 1959.

[37] R. F. Harrington *, Field Computation by Moment Methods.* New York: Macmillan, 1968.

[38] S. M. Rao, D. R. Wilton, and A. W. Glisson, *Electromagnetic scattering by surfaces of arbitrary shape, IEEE Trans. Antennas Propag.,* vol. 30, pp. 409418, 1982.

[39] Ö. Ergül, L. Gürel, *The Multilevel Fast Multipole Algorithm (MLFMA) for Solving Large-Scale Computational Electromagnetics Problems,* Chichester: IEEE Press/Wiley 2014.

[40] V. Okhmatovski, M. Yuan, I. Jeffrey, and R. Phelps "A three-dimensional precorrected FFT algorithm for fast method of moments solutions of the mixed-potential integral equation in layered media," *IEEE Trans. Microw. Theory Techn.,* vol. 57, no. 12, pp. 3505–3517, Dec. 2009.

[41] R. E. Fischer, T. Tadic-Galeb, and P. R. Yoder, *Optical System Design,* 2nd ed. New York: McGraw Hill, 2008.

[42] P. Yang, "Microwave detection of breast tumors using the finite difference time domain method," Ph.D. Thesis, Dept. Electr. Eng., Univ. South Carolina, Columbia, 2006.

[43] B. Young, *Digital Signal Integrity,* New York: McGraw-Hill, 2001.

[44] C. Müller, *Foundations of the Mathematical Theory of Electromagnetic Waves,* New York: Springer-Verlag, 1969.

[45] J. R. Mautz and R. F. Harrington, "H-field, E-field, and combined-field solutions for conducting bodies of revolution," *AEÜ – Int. J. Electron. Commun.,* vol. 32, no. 4, pp. 157–164, Apr. 1978.

[46] D. Maystre and P. Vincent, "Diffraction d'une onde electromagnetique plane par un object cylindrique non inniniment conducteur de section arbitraire," (*in French)*, *Optics Commun.* vol. 5, pp. 327–330, 1972.

[47] D. Swatek, "Investigation of single-source surface integral equation for electromagnetic wave scattering by dielectric bodies," Ph.D. Thesis, Dept. Electr. Comput. Eng, Univ. Manitoba, Winnipeg, Canada, 1999. [Online]. Available: http://hdl.handle.net/1993/1699.

[48] A. W. Glisson, "An integral equation for electromagnetic scattering from homogeneous dielectric bodies," *IEEE Trans. Antennas Propag.,* vol. 32, no. 2, pp. 173–175, Feb. 1984.

[49] R. E. Kleinman and P. A. Martin, "On single integral equation for the transmission problem of acoustics," *SIAM J. Appl. Math.,* vol. 48, no. 2, pp. 307–325, Apr. 1988.

[50] L. F. Knockaert and D. De Zutter, "Integral equations for fields inside a dielectric cylinder immersed in an incident E-wave," *IEEE Trans. Antennas Propag.,* vol. 34, no. 8, pp. 1065–1067, Aug. 1984.

[51] A. W. Glisson, "An integral equation for electromagnetic scattering from homogeneous dielectric bodies," *IEEE Transactions on Antennas and Propagation,* vol. AP-32, no. 2, pp.173-175, 1984.

[52] P. A. Martin and P. Ola, "Boundary integral equations for the scattering of electromagnetic waves by a homogeneous dielectric obstacle," *Proc. Roy. Soc. Minburgh Sect. A,* vol. 123, no. 1, pp. 185–208, Jan. 1993.

[53] E. Marx, "Single integral equation for wave scattering," *J. Math Phys.,* vol. 23, pp. 1057–1065, June 1982.

[54] E. Marx, "Transient fields in dispersive media," *J. Math Phys.,* vol. 24, pp. 2602–2607, Nov. 1983.

[55] E. Marx, "Integral equation for scattering by a dielectric," *IEEE Trans. Antennas Propag.,* vol. 32, no. 2, pp. 166–172, Feb. 1984.

[56] J. Richmond, "TE-wave scattering by a dielectric cylinder of arbitrary cross-section shape," *IEEE Trans. Antennas Propag.,* vol. 14, no. 4, pp. 460–464, July 1966.

[57] L. Mendes and E. Arvas, "TE-scattering from dense homogeneous infinite dielectric cylinders of arbitrary cross-section," *IEEE Trans. Antennas Propag.,* vol. 27, no. 5, pp. 4295–4298, Sep. 1991.

[58] E. Jorgensen, J. L. Volakis, P. Meincke, O. Breinbjerg, "Higher order hierarchical Legendre basis functions for electromagnetic modeling," *IEEE Trans. Antennas Propag.,* vol.52, no.11, pp.2985-2995, Nov. 2004.

[59] M. Djordievic and B. M. Notaros, "Double higher order method of moments for surface integral equation modeling of metalic and dielectric antennas and scatterers," *IEEE Trans. Antennas Propag.,* vol. 52, pp. 2118-2129, Aug. 2004.

[60] B. M. Notaroš, "Higher Order Frequency-Domain Computational Electromagnetics," *IEEE Trans. Antennas Propag.,* vol. 56, no. 8, pp. 2251-2276, Aug. 2008.

[61] R. D. Graglia, D. R. Wilton, and A. F. Peterson, "Higher Order Interpolatory Vector Bases for Computational Electromagnetics," *IEEE Transactions on Antennas and Propagation,* AP-45, 3, March 1997, pp. 329-342.

[62] L. F. Canino, J. J. Ottusch, M. A. Stalzer, J. L. Visher, and S. M. Wandzura, "Numerical solution of the Helmholtz equation in 2D and 3D using a high-order Nyström discretization," *J. Comp. Phys.* vol. 146, no. 2, pp. 627-663, 1998.

[63] S. D. Gedney, "On Deriving a Locally Corrected Nyström Scheme From a Quadrature Sampled Moment Method," *IEEE Trans. Antennas Propag.,* vol. 51, no. 9, p. 2402-2412, September 2003.

[64] A. F. Peterson, M. M. Bibby "an introduction to the locally corrected Nyström Method," *synthesis lectures on computational electromagnetics,* vol. 4, pp. 1-115, 2009.

[65] R. F. Harrington, "Time-Harmonic Electromagnetic Fields," *New York: McGraw-Hill* 1961.

[66] J. Richmond, "Scattering by a dielectric cylinder of arbitrary cross section shape," *IEEE Trans. Antennas Propag.,* Vol. 13, No. 3, pp. 334–341, 1965.

[67] H. Bussey, J. Richmond, "Scattering by a lossy dielectric circular cylindrical multilayer, numerical values," *Proc. Inst. Electr. Eng.,* Vol. 23, No. 5, pp. 723–725, Feb 1975.

[68] K. A. Michalski and D. Zheng, "Electromagnetic scattering and radiation by surfaces of arbitrary shape in layered media, part I: theory," *IEEE Trans. Antennas Propag.,* vol. 38, no. 3, pp. 335–344, Mar. 1990.

[69] V. Okhmatovski, A. Menshov, F. L. S. Hosseini, and S. Zheng, "Novel single-source integral equation in electromagnetics," in *URSI Int. Symp. Electromagnetic Theory (EMTS)*, Espoo, Finland, 2016.

[70] S. Zheng, A. Menshov, and V. Okhmatovski, "Novel single-source integral equation for inductance extraction in transmission lines embedded in lossy layered substrates," in *IEEE/MTT-S Int. Microw. Symp.,* San Francisco, CA, May 2016, to be published.

[71] R. Harrington, *Field Computation by Moment Methods,* New York: IEEE Press, 1993.

[72] N. A. Khizhnyak, "Green's function of Maxwell equations in inhomogeneous media," (*in Russian*), *J. Tech. Phys.*, vol. 28, no. 7, pp. 1592–1609, 1958.

[73] D. Colton and R. Kress, (ed.) *Integral Equation Methods in Scattering Theory,* Malabar, FL: Krieger, 1992.

[74] D. R. Wilton *et al.*, "Potential integrals for uniform and linear source distributions on polygonal and polyhedral domains," *IEEE Trans. Antennas Propag.,* vol. 32, no. 3, pp. 409–418, Mar. 1984.

[75] A. Menshov and V. Okhmatovski, "New single-source surface integral equations for scattering on penetrable cylinders and current flow modeling in 2-D conductors," *IEEE Trans. Microw. Theory Techn.*, vol. 61, no. 1, pp. 341-350, Jan. 2013.

[76] S. Ramo, J.R. Whinnery, T. Van Duzer, *Field and Waves in Communication Electronics,* Hoboken, NJ: Wiley, 1994.

[77] F. Sheikh Hosseini Lori, S. Hosen, A. Menshov, M. Shafieipour, and V. Okhmatovski, "Accurate transmission lines characterization via higher order moment method solution of novel single-source integral equation," in *IEEE MTT-S Int. Microwave Symp.,* 2017.

[78] Manitoba Hydro International Ltd. (Jan. 18, 2017). PSCAD/EMTDC. [Online]. Available: https://hvdc.ca/pscad

[79] M. Shafieipour, J. De Silva, A. Kariyawasam, A. Menshov, V. Okhmatovski, "Fast computation of the electrical parameters of sector-shaped cables using single-source integral equation and 2D moment-method discretization," in *Int. Conf. Power Syst. Transients,* 2017.

[80] A. K. Dominek and H. T. Shamanski, "The almond test body," The Ohio State Univ. Electro-Science Lab., Dept. Electr. Eng., NASA Langley Res. Center, Rep. 721929-9, Mar. 1990.

[81] PTC, Software & Solutions, "PTC Mathcad," Mar. 29, 2016 [Online]. Available: www.ptc.com/engineering-math-software/mathcad.

[82] Compute Canada, WestGrid Canada, "Grex," Oct. 4, 2015 [Online]. Available: www.westgrid.ca/support/systems/Grex/.

[83] C. Geuzaine and J. Remacle, "Gmsh: A 3-D finite element mesh generator with built-in pre-and post-processing facilities," International Journal for Numerical Methods in Engineering, vol. 79, no. 11, pp. 1309–1331, 2009, available: http://geuz.org/gmsh/.

[84] A. Squillacote, The ParaView guide: a parallel visualization application. Kitware, 2007, available: http://www.paraview.org/.

[85] MATLAB and Statistics Toolbox Release 2016, The MathWorks, Inc., Natick, Massachusetts, United States.

[86] M. Shafieipour, J. De Silva, A. Kariyawasam, A. Menshov, and V. Okhmatovski, "Fast Computation of the Electrical Parameters of Sector-Shaped Cables using Single-Source Integral Equation and 2D Moment-Method Discretization," International Conference on Power Systems Transients (IPST2017), Seoul, June 2017.